Manufacturing and characterization of Al matrix composites with nano reinforcements via cold spraying

Xinliang Xie

SPIM

Thèse de Doctorat

école doctorale **sciences pour l'ingénieur et microtechniques**

UNIVERSITÉ DE TECHNOLOGIE BELFORT-MONTBÉLIARD

Manufacturing and characterization of Al matrix composites with nano reinforcements via cold spraying

Xinliang XIE

N° d'ordre : Année : **2019**

Université de Technologie de Belfort-Montbéliard

Ecole doctorale Sciences Pour l'Ingénieur et Microtechniques

THESE

Présentée pour obtenir le grade de

Docteur de l'Université de Technologie de Belfort-Montbéliard en Sciences des Matériaux

Manufacturing and characterization of Al matrix composites with nano reinforcements via cold spraying

Xinliang XIE

Defended in public on 12 December 2019

With the jury composed of

Rapporteurs

Mr. Frank GARTNER, Associate Professor, Helmut Schmidt University

Mr. Jean-François SILVAIN, Professor, Institut de Chimie de la Matière Condensée de Bordeaux (president of the jury members)

Examinateurs

Mr. Michel JEANDIN, Professor, MINES ParisTech.

Mr. Hanlin LIAO, Professor, Université de Technologie de Belfort-Montbéliard

Mr. Gang JI, Senior researcher (HDR), Université de Lille

Acknowledgements

This work was conducted in the cooperation of laboratory of ICB-LERMPS in University of Technology of Belfort-Montbéliard (UTBM) and laboratory of UMET in University of Lille. I would first like to thank you both my supervisors, Prof. Hanlin LIAO from UTBM and Dr. Gang JI from University of Lille, without whom none of this work would been possible. I'm honoured and great lucky to have been under the supervision of Prof. Hanlin LIAO, who is one of the best in the field of thermal spray and additive manufacturing, his creative mind, his incredible experience and wisdom. He can always give me key guidance and great suggestions when I encounter difficulties in experiments, so that my project can be carried out smoothly and completed within three years and half. His patience and attitude as well as the relaxed way of handing problems also impress me a lot. In my mind, he was not only a beacon, guiding us in the direction of progress, but also a ferry, pushing us to the other side. My greatest thank you for him for being the best supervisor I ever hoped. I also owe my sincere gratitude to my supervisor Dr. Gang Ji for his kind help in material characterisation, manuscript correction, and discussion. Thank you for him for spending his weekends in dealing with my EBSD and TEM samples. He is not only my supervisor but also one of my best friends. When I walk too fast, he will remind me to slow down, and when I encounter difficulties, he will always encourage me.

I would like to thank my examiners too, Dr. Frank Gärtner and Prof. Jean-François SILVAIN, for their patience and time in reading my dissertation meticulously and giving me a lot of valuable suggestions. I thank Prof. Michel JEANDIN for his attendance in my defence, and put forward many good questions and suggestions, which are helpful for my future research. How lucky I am to have this opportunity to share my research work and learn from those best researchers in the field.

Thanks to my colleagues at LERMPS, Dr. Christophe Verdy, Mr. Christian Adam, Charles, Joel, Yan, Emmanuelle, for their very kind help with my experiments. Dr. Christophe Verdy helped me a lot in doing cold spraying experiments. Besides, Dr. Chaoyue Chen from Shanghai University, Dr. Yingchun Xie from Guangdong Institute of New Materials, Dr. Yu Ma from University of Lille, Dr. Shuo Yin from University of Dublin, and Dr. Yan Wang Xi'an University of Architecture and Technology, Dr. Bilel Hosni from FCLAB of UTBM, and Prof. Qingdong Zhong from Shanghai University helped me a lot in material characterization, FEA simulation, mechanical and corrosion tests.

I would like to thank you our co-operators, Dr. Zhe Chen, Dr. Zhanqiu Tan, and Prof. Zhiqiang Li from Shanghai Jiao Tong University for providing us the composite powders and help with the tensile tests. My thanks should give to Dr. Frank Gärtner from Helmut Schmidt University for helping me with the single particle compression tests. I appreciate the help in cold spraying by Dr. Sheng Yuan and Prof. Bernard Normand from INSA Lyon.

Thanks also to everyone at LERMPS labo and my friends in UTBM, thanks for their help during my three and a half years living and studying in such a small but beautiful city. I had a happy and unforgettable days here in Belfort.

Finally, I would like to thank my family, my parents for supporting me and giving me a lot of freedom to pressure my dreams. Without your support and encouragement, I couldn't be who I am today.

General introduction

Aluminium matrix composites (AMCs) have the potential to offer desirable properties, including low density, high specific strength and stiffness, excellent wear resistance and controllable expansion coefficient, which make them attractive for numerous applications in the aerospace, automobile, and military industries. So far, various processes have been developed to fabricate AMCs, such as stir casting, spray forming, self-propagating synthesis, powder metallurgy, friction stir processing (FSP) and selective laser melting (SLM). With regards to these processes, extra heating, or even remelting is required in stir casting, powder metallurgy and SLM to acquire the AMC components. This may give rise to problems, such as oxidation, excessive interfacial reaction and grain growth. Furthermore, FSP and spray forming processing are not flexible for net-shape forming.

Cold spray (CS), also known as cold gas dynamic spray or kinetic spray, has attracted increasing attention as a solid-state coating and additive manufacturing technique. The bonding is formed based on severe plastic deformation and following metallurgical bonding or interlocking. Owing to its unique low-temperature feature, in comparison with the laser or electron-beam powder-bed additive manufacturing (AM) processes (e.g. SLM), the adverse effects of oxidation, phase transformation, and grain growth are expected to be minimised or avoided in the CS parts. Also, CS exhibits several other unique advantages, including high production rate, unlimited component size and feasibility in repairing damaged parts. These unique advantages make CS an ideal technique for fabricating coating, repairing and AM of free-standing metal components, especially for temperature-sensitive materials like AMCs.

Until recently, various AMC coatings have been tentatively deposited by CS. By integrating ceramic particles or carbon nanotubes (CNTs) into an Al matrix, microhardness, adhesion strength and tribological performance of the composite coatings were largely improved, in comparison with the unreinforced counterparts. However, previous studies have mainly focused on fabricating AMC coatings and on the coating-related properties. In fact, few attempts have been made to fabricate AMC components from the perspective of cold spray additive manufacturing (CSAM). This is because there are still some considerable challenges in composite powder preparation, CS deposition and post-treatment. First, the CSed composite deposits have a weak inter-splat bonding that can significantly degrade their mechanical performance. Second, the AMCs fabricated from mechanically blended or ball-milled composite powders generally have problems associated with uneven distribution of the reinforcement particles and poor reinforcement/matrix interfacial bonding. Moreover, the post-treatments, including heat treatment, or even FSP, have not shown remarkable improvement on the mechanical performance of CSed AMCs fabricated from the conventional powder preparation processes. This is mainly due to the fact that the above-mentioned problems, such as poor interface bonding and uneven reinforced phase distribution, were not completely resolved. Therefore, new approaches that allow for manufacturing advanced AMC components via CS need to be further explored.

In order to solve the above-mentioned problems, and to obtain CSed AMCs with balanced strength-ductility, efforts have been focused on the aspects of composite powder preparation, processing parameters optimisation, and post-treatments. In terms of composite powder synthesis, different approaches have been developed to disperse the reinforcements, including ceramic particles (TiB_2) and CNTs into Al or Al alloy matrix. Since CNTs are easy to agglomerate, good dispersion of CNTs was the bottleneck to converting their attractive properties to CNT reinforced AMCs. In this dissertation, two distinct methods, namely high shear dispersion (HSD) and shift-speed ball milling (SSBM), were employed to prepare CNTs/Al composite powder for CS deposition. Besides, gas atomised in-situ nanosized TiB_2-reinforced Al composite powders were used as the novel feedstock to fabricate composite components by CS deposition. The use of such composite powders was expected to solve the

above-mentioned problems of uneven distribution of the reinforcement particles, and poor reinforcement/matrix interfacial bonding. Besides, in order to improve the deposition efficiency (DE) of the composite powder, and obtain high-quality AMC components, the main processing parameters, including propellant gas temperature and pressure, gas type and nozzle dimensions were studied by using different CS systems. Moreover, the particle plastic deformation behaviour, as well as the bonding mechanisms of the composite particle, were investigated by the combination of FEA simulation and single particle deposition experiment. Post-treatments, including heat treatment and FSP, were applied to further improve the mechanical properties of the CSed TiB_2 reinforced AMCs. This study provides a potential solid-state manufacturing route to fabricate AMCs with balanced strength-ductility. Moreover, the adhesion strength, wear performance, and corrosion properties of the CSed AMCs were examined as these properties are also important for the applications of damage reparation and coating protection.

This thesis is organised into five chapters, as follows:

Chapter I provides the bibliographic study of the AMCs and their fabrication processes and applications. Next, the principle and setup of the CS process, as well as its main processing parameters and applications, are introduced in detail. More attention has been paid to the developments of CSed AMCs coatings, including composite powder preparation, parameter studies, microstructure characterisation and, mechanical and corrosion properties. Moreover, a review of the influence of post-treatments, including heat treatment and FSP on the microstructure and properties of CSed AMC coatings is also presented. Finally, the objectives of this thesis are clearly declared.

Chapter II introduces the synthesis processes of the three composite powders used in this study, including CNTs/Al, TiB_2/AlSi10Mg and TiB_2/7075Al. It also characterizes the particle size distribution, morphologies and microstructure s of the composite powders. The CS systems and their operation parameters, as well as the material and property characterisation methods are introduced. The single particle compression test is used to obtain the Johnson-Cook parameters of the pure 7075Al and TiB_2/7075Al composite powder. Last, the simulation models including the computational fluid dynamics (CFD) using Fluent/Ansysis and finite element analysis (FEA) using ABAQUS are described in detail.

Chapter III investigates the microstructure and mechanical properties of the CSed CNTs/Al composites. First, two distinct methods, namely HSD and SSBM, were employed to prepare CNTs/Al composite powder for CS deposition. The influence of processing parameters including gas temperature and pressure on the DE, microstructure evolution and the mechanical properties, were investigated. FEA simulation was applied in order to study the plastic deformation behaviour of the spherical and flaky Al particles during CS deposition. Afterwards, the influence of annealing treatments on microstructure evolution, phase stability, as well as mechanical performance-especially the tensile properties of the CNTs/Al composites, were investigated. At last, a fracture model based on micro-scale and submicron-scale observation has been put forward to illuminate the fracture mechanisms of the CSed CNTs/Al composite.

In Chapter IV, a novel in-situ TiB_2 particle reinforced AlSi10Mg composite powder was used as the feedstock to fabricate composite components by CS deposition. Firstl, the effect of the processing parameters on the microstructure and mechanical properties of the composite was investigated. In order to improve the mechanical properties of the as-sprayed deposits, post-treatments, including annealing treatment and FSP were performed using different parameters. It was found that significant improvement in ductility, but a sacrifice of tensile strength, was obtained for both annealed pure AlSi10Mg and TiB_2/AlSi10Mg composite samples due to the enhanced metallurgical bonding between the deformed splats. The presence of TiB_2 particles in the TiB_2/AlSi10Mg composites results in higher tensile strength but lower ductility compared to the pure AlSi10Mg samples. Balanced strength-ductility

was achieved in the FSPed TiB_2/AlSi10Mg composite samples. Fracture mechanisms of the as-sprayed and post-treated deposits were proposed based on morphology observation. Last, the reinforced mechanisms of the TiB_2/AlSi10Mg composite were discussed.

In Chapter V, a gas atomised AlZnMgCu (7075Al) composite powder, reinforced with in-situ nanosized TiB_2 particles, was used as a novel feedstock to fabricate composite parts by CS. The effect of the CS processing conditions (i.e. particle impact velocity and temperature) on the microstructure evolution of the as-sprayed samples was investigated by X-ray diffraction (XRD), scanning electron microscopy (SEM), transmission electron microscopy (TEM), and electron backscatter diffraction (EBSD). Mechanical performance including adhesion strength, microhardness, wear performance and tensile properties of the pure 7075Al and composite deposits was evaluated. Aside from this, corrosion behaviour of the CSed deposits in NaCl solution was investigated in terms of tests for immersion, potentiodynamic polarization, and impedance spectroscopy. The corrosion mechanisms were analyzed based on the results of the electrochemical tests and the microstructure observation. Different post heat treatments were applied to further improve the mechanical performance of the as-sprayed deposits. Microstructure evolution, especially precipitation behaviour and related mechanical performance during heat treatment, was investigated. Finally, strengthening mechanisms were discussed relating to the microstructural evidence.

Content

General introduction I

Content V

List of figures IX

List of tables XXI

Chapter I State-of-the-art of the Al matrix composites fabricated by cold spray process 1

1.1 Al matrix composites 1

1.1.1 Particulate-reinforced Al matrix composites 2

1.1.2 Carbon nanotube-reinforced Al matrix composites 4

1.2 Cold spray process 4

1.2.1 Principle and setup 5

1.2.2 Main processing parameters 5

1.2.3 Advantages and disadvantages 7

1.2.4 Coating formation mechanisms 7

1.2.5 Applications 9

1.3 Fabrication of Al matrix composites via cold spraying 12

1.3.1 Composite powder preparation 12

1.3.2 Composite coating microstructure 27

1.3.3 Composite coating or component properties 33

1.4 Post treatments on as-sprayed Al matrix composites 38

1.4.1 Heat treatment 38

1.4.2 Friction stir processing 39

1.5 Objectives of this study 41

References of Chapter I 42

Chapter II Experimental and numerical simulation details 51

2.1 Materials and powder preparation process 51

2.1.1 CNT/Al composite powder 51

2.1.2 TiB_2/AlSi10Mg composite powder 54
2.1.3 TiB_2/7075Al composite powder 56

2.2 Cold spray process 58
2.2.1 Cold spray systems 58
2.2.2 Processing parameters 60

2.3 Heat treatments 61
2.3.1 CNT/Al composites 61
2.3.2 TiB_2/AlSi10Mg composites 62
2.3.3 TiB_2/7075Al composites 62

2.4 Friction stir treatment on the as-sprayed coatings 62

2.5 Material characterization 63
2.5.1 Deposition efficiency measurement 63
2.5.2 Phase composition characterization 63
2.5.3 Microstructure characterization 63

2.6 Properties characterization 64
2.6.1 Microhardness and nanoindentation test 64
2.6.2 Adhesion test 64
2.6.3 Tribological test 65
2.6.4 Electrochemical corrosion test 65
2.6.5 Tensile tests 65

2.7 Single particle compression test 68

2.8 Numerical simulation methods 70
2.8.1 Simulation of the particle impact velocity and temperature 70
2.8.2 FEA simulation of the particle deformation 71

References of Chapter II 74

Chapter III Cold spraying of CNT/Al composites 75

3.1 Introduction 75

3.2 Effect of propelling gas temperature 75
3.2.1 Particle impact velocity and temperature 75
3.2.2 Deposition efficiency 77
3.2.2 Microstructure 79

3.2.3 Phase composition 84
3.2.4 Adhesion strength 86
3.2.5 Microhardness 87

3.4 Single particle deposition and FEA simulation 89

3.5 Effect of annealing treatment 91

3.5.1 Phase composition 91
3.5.2 Microstructure 93
3.5.3 Microhardness 94
3.5.4 Tensile property 94

3.7 Summary 99

References of Chapter III 100

Chapter IV Cold spraying of TiB_2/AlSi10Mg composites 104

4.1 Introduction 104

4.2 Microstructure characterization of as-sprayed deposits 104

4.3 The effect of annealing treatment 108

4.3.1 Phase composition 108
4.3.2 Microstructure evolution 108
4.3.3 Microhardness 112
4.3.4 Tribological property 114
4.3.5 Tensile property 116

4.4 The effect of FSP process 120

4.4.1 Phase composition 120
4.4.2 Microstructure evolution 121
4.4.3 Microhardness 127
4.4.4 Tribological property 128
4.4.5 Tensile property 130
4.4.6 Strength mechanisms 132

4.5 Summary 133

References of Chapter IV 135

Chapter V Cold spraying of TiB_2/AlZnMgCu composites 138

5.1 Introduction 138

5.2 Particle impact velocity and temperature simulation 138

5.3 Single particle deposition 139

5.3.1 Single particle compression test 139

5.3.3 Particle deformation behavior 143

5.3.3 Single particle deposition experiments 148

5.4 Phase composition and microstructure evolution 150

5.4.1 Phase composition 150

5.4.2 Microstructure evolution 151

5.5 Mechanical properties of the cold sprayed deposits 159

5.5.1 Microhardness 159

5.5.2 Bonding strength 160

5.5.3 Tribological performance 161

5.5.4 Tensile strength 162

5.6 Corrosion properties of the cold sprayed deposits 164

5.6.1 Immersion studies 164

5.6.2 Open circuit potential and polarization studies 166

5.6.3 Electrochemical impedance studies 168

5.6.4 Effect of annealing treatment on the corrosion behavior of the CSed coatings 169

5.6.5 Corrosion mechanisms 170

5.7 Effect of heat treatments on microstructure and mechanical properties 172

5.7.1 Microstructure evolution after heat treatment 172

5.7.2 Mechanical properties after heat treatment 178

5.8 Reinforced mechanisms 183

5.9 Summary 184

References of Chapter V 186

Conclusions and perspectives 190

Abstract 194

Résumé 195

List of figures

Figure 1-1 The schematic diagrams of fabrication processes of P-AMCs: (a) stir casting; (b) powder metallurgy; (c) selective laser melting; (d) thermal spray. *3*

Figure 1-2 (a) Schematic diagram of high-pressure CS systems [34] and (b) comparison of CS with other thermal spray processes [41]..... *5*

Figure 1-3 Schematic of the typical manufacturing parameters used in CS deposition [42]. *6*

Figure 1-4 Deposition characteristics of the single ductile particle impact on metal substrate: (a) deposition window for ductile material [62], (b) Typical morphology of a deformed Al alloy splat [60]; (c) and (d) microstructure evolution within the deformed particle [60]; (e) Schematic diagram of the bonding process of cold-sprayed particles accompanying with the breaking-up and extruding of surface oxide films and the formation of jetting [57]..... *8*

Figure 1-5 In situ observation of micron-sized pure metal particle impact on an metal substrate: (a) the microparticle arrives from the top of the field of view with a speed of 765 m/s, impacts the substrate and subsequently rebounds with a speed of 35 m/s. (b) The microparticle impacts the substrate with a speed of 825 m/s and subsequently adheres to the surface. (c) demonstrates the critical velocities for the deposition of pure Al, Ni, Cu and Zn metals [68, 70]. *9*

Figure 1-6 Key features of CS process for coating, reparation and additive manufacturing [80]..... *11*

Figure 1-7 Comparison between damaged and CSR components: (a) S-92 helicopter gearbox sump, (b) oil tube bores in CH47 helicopter accessory cover, (c) UH-60 helicopter gearbox sump, and (d) UH-60 rotor transmission housing [76] [81]. *11*

Figure 1-8 Application of cold spraying in net-shape forming: (a) high magnetic field magnets ; (b) rapid prototyping of Ti6Al4V axisymmetric bulk part [79]; (c) thick copper coating inside a pressure ring for food processing machine [82]; (d) electronic heat sinks [82]; (e) bulk Ni/Al energetic material [83]; (f) Cu/W cone structure [84]..... *11*

Figure 1-9 Surface morphologies of the blending mixed powders: (a) SiC/5056Al [89]; (b) Al_2O_3/Al [98]; (c) Diamond/Al [99]; (d) Al_2O_3/A380 [100]; (e) B_4C/Al [101]. (f) Al_2O_3/Al [102]..... *13*

Figure 1-10 SEM images showing the morphologies of blended feedstocks (a) TiC/Al and (c) TiC/6061Al, and satellited feedstocks (b) TiC/Al and (d) TiC/6061Al [104, 105]. *14*

Figure 1-11 SEM micrographs of the (a) as-received Al in comparison to nanodiamond/Al composite powders (5 wt.% ND) ball-milled for, (b) 1 h, (c) 4 h and (d) 10 h using a ball-to-powder ratio of 10:1. (e) and (f) Particle size analysis of ND-Al MMC (5 wt.% ND) powders ball-milled for 1, 4 and 10 h using a ball-to-powder ratio of 10:1, in comparison to pure as-received Al. (f) Raman spectra (325 nm excitation) of ND-Al MMCs containing 5 and 10 wt.% ND, in comparison to as-received ND and Al milled with 10:1 ball-to-powder ratio for 1 h [106]. *16*

Figure 1-12 Surface morphologies and cross-section views of the ball-milled composite powder for CS deposition: (a-c) TiB_2/Al [109]; (d-f) TiN/5356Al [110]. *16*

Figure 1-13 SEM micrographs of (a)–(c) morphologies and (d)–(e) cross-sections of powders: (a), and (d) pure Al, (b) and (e) the composite powder (1.0 vol.%), (c) and (f) the composite powder (3.0 vol.%). TEM BF image of composite powder (3.0 vol.%) (black arrows indicate equiaxed NC), (b) SAED pattern of (a), and (c) HREM image of an embedded CNT in the Al matrix (the black arrow indicates bent walls of the CNT) [108]...... *17*

Figure 1-14 SEM micrograph showing a) spray-dried Al-Si agglomerate and b) magnified region within the rectangle in a) showing CNTs within the agglomerate; (c) Schematic of the steps involved in the fabrication of the composite coating [111]. *18*

Figure 1-15 Partial deposition efficiencies evolution during the deposition of Al2O3/Al composite feedstock powders [118]. *28*

Figure 1-16 Three mechanisms proposed in the literature for the DE increase in metal-ceramic mixtures [118]: (a) metallic particles adhere due to peening of ceramic particles upon impact; (b) metallic particles adhere mechanically due to the asperities created by previous ceramic particle impacts; (c) metallic particles adhere to oxide-free surfaces cleaned by previous ceramic particle impacts. (e-f) The PEEQ evolution of Al and Al-Al2O3 impact on 6061Al substrate. *28*

Figure 1-17 Schematic diagrams of two coating mechanisms using: (a) blended feedstock, (b) satellited feedstock [104]. *29*

Figure 1-18 The deposition behavior of the ND/Al composite powder produced from ball milling: (a) Deposition efficiency, (b) particle velocity, and (c) hardness of Al and ND/Al composite powders as a function of milling time [92]. *29*

Figure 1-19 Volume fraction of ceramics in coatings compared to the source powder mixture. *30*

Figure 1-20 Al_2O_3 content in coatings versus feedstock powder Al_2O_3 content with different morphologies (spherical and angular) [127]. Relationship between SiC particles size and SiC content in CSed SiCp/5056Al composite coatings. The SiC contents in the feedstocks were the same (30 vol.%) [123]. *30*

Figure 1-21 (a) Porosity evolution as a function of volume fraction of ceramic particles in the feedstocks and (b) average SiC particle size [100, 123]. *31*

Figure 1-22 Microstructure of the as-sprayed composite coatings obtained from mechanical blending method: (a) Al_2O_3/Al coating [128]; (b) SiC/5056Al coating [122]; (c) SiC/Al coating [116] ; (d) Al_2O_3/Al coating. (e) EBSD pattern quality map on the cross-plane of Al_2O_3/Al coating. (f)TEM micrographs showing the Al/Al_2O_3 interface [116]. *32*

Figure 1-23 SEM cross-section image of (a) TiN//5356Al composite coating [110] and (b) B4C/5356Al composite coating [120] produced from ball-milled composite powder. (c) Bright Field TEM image of (b) showing large B4C particle within the nanostructured Al5356 matrix as confirmed by SAED patterns shown in (d) and (f) respectively [120]. *32*

Figure 1-24 Microstructures of the as-sprayed CNT/Al composite coatings: (a) and (d) SEM micrographs CNT/Al composite coatings; (b) and (e) TEM BF image of CNT/Al composite coatings. (c) SAED pattern of Al matrix in (b). HREM image of embedded MWCNTs in the Al matrix [107, 108]. *32*

Figure 1-25 Coating microhardness as a function of ceramic content in the deposit. *33*

Figure 1-26 Bonding strength as a function of volume fraction of ceramics in the source powder mixture. *34*

Figure 1-27 wear tracks on CSed Al coating (b) CSed Al–50% Al_2O_3 coating and (c) CSed Al–75% Al_2O_3 coating. (d) wear rates of coatings compared to bulk alloys [130]. *35*

Figure 1-28 TEM investigation of the wear mechanisms of CSed Al_2O_3/Al composite coating: (a) technique of TEM foil; (b) and (c) wear track surfaces showing TEM foil locations; (d) TEM micrograph of the cross-section region near the wear track surface; (e) and (f) EDS mapping of Al Kα and O Kα intensities in the third body, the surrounding first body, and interfaces [102]. *36*

Figure 1-29 Tensile properties of the CSed SiC/Al composites:(a) stress-strain curves and (b) Ultimate tensile strength [131] as a function of SiC content; (C) and (d) are the fractured morphologies of the as-sprayed Al-47SiC composite [119]. *36*

Figure 1-30 Microhardness evolution of the annealed (a) TiN/5356Al [88] and (b) CNT/Al composite coatings [108]. *39*

Figure 1-31 Tensile stress-strain plots of as-sprayed and heat-treated B_4C/Al composite samples. Fracture morphologies of (b and c) as-sprayed and heat-treated (500 ℃) B_4C/Al composite samples [101]. *39*

Figure 1-32 (a) Friction-stir modification of CSed titanium coating on the surface of Al substrate. (b) Schematic of FSP process; (c) Schematic representation of FSP as a modifying post-processing technique during CSAM [148]. *40*

Figure 1-33 Microstructure modification for CSed AMCs coatings: (a) macroscopic cross-section of the FSPed Al_2O_3/2024Al [146]; (b) Schematic of reinforcing particle re-distribution in MMC coatings during FSP. [147]; Optical micrographs (e, d) and SEM (e, f) micrographs of CSed (c, e) and FSPed (d, f) Al_2O_3/2024Al/ [146]. *40*

Figure 1-34 Microhardness evolution and the stress-strain curves of the FSP processed Al_2O_3/2024Al composite coatings [146]. *41*

Figure 2-1 Illustration of the (a) HSD process and (b) SSBM process for fabrication of CNT/Al composite powder. *51*

Figure 2-2 The surface morphologies and cross-sectional views of feedstock powders:(a) pure Al powder; (b) CNT/Al composite powder processed by HSD; (c) CNT/Al composite powder processed by SSBM. *52*

Figure 2-3 The magnified views of the morphology of particles: (a) CNT/Al composite particles processed by HSD; (b) CNT/Al composite particles processed by SSBM. The red arrows indicate the shortened CNT. *53*

Figure 2-4 Particle size distributions of the powder feedstocks. *53*

Figure 2-5 Morphologies of the gas atomized powder feedstocks in different magnifications: (a) and (b) AlSi10Mg powder; (c) and (d) TiB_2/AlSi10Mg composite powder. *54*

Figure 2-6 Particle size distributions of powder feedstocks. *55*

Figure 2-7 SEM image and EDS mapping of the magnified area of a composite particle in Figure 2-5d. *55*

Figure 2-8 Cross-sectional microstructure in (a) low and (b) high magnifications and (c-f) the corresponding EDS mapping of a TiB_2/AlSi10Mg composite particle. *56*

Figure 2-9 Particle morphologies of the (a, b) pure 7075Al powder and (c, d) TiB_2/7075Al composite powder in different magnifications; (e) Magnified view of the composite particle surface area marked in (d), showing uniform distribution of TiB_2 nanoparticles (indicated by red arrows) on the surface of an Al micro-particle; (f) displays the particle size distribution of the initial powder feedstocks. *57*

Figure 2-10 BSE/SEM micrographs of the cross-section of (a) a whole TiB_2/7075Al composite particle in the as-received condition and (b) magnified view highlighting the distribution of TiB_2 particles; corresponding EDS element distributions of (c) Al, (d) Mg, (e) Cu, (f) Zn and (g) Ti. *58*

Figure 2-11 SEM/EBSD characterization of the cross-section of the gas-atomized (a-c) 7075Al particle and (d-f) TiB_2/7075Al composite particle: (a) and (d) IPF mapping images, (b) and (e) band contrast images, (c) and (f) Al grain size distributions. The image reveals the grains by cleaning up the nanoparticle TiB_2 phase. *58*

Figure 2-12 Photos of the CS systems: (a) CGT-3000 (LERMPS); (b) Impact 5/8 (INSA-Lyon); (c) Helium circulation CS system (LERMPS). *59*

Figure 2-13 Photos of the as-sprayed AlSi10Mg and TiB_2/AlSi10Mg composite coating (a) before and (b) after FSP treatment. *63*

Figure 2-14 Photos of the CSed CNT/Al composite coatings onto Al substrates using different processing parameters: (a) CC5; (b) CC6. ..... *66*

Figure 2-15 Photos of the CSed TiB_2/AlSi10Mg composite coatings onto Al substrates using different processing parameters: (a) CT1; (b) CT2. ..... *66*

Figure 2-16 Photos of the CSed TiB_2/7075Al composite coatings onto Al substrates using different processing parameters: (a) C1; (b) C2; (c) C3. ..... *67*

Figure 2-17 Specially designed fixture for tensile tests. *67*

Figure 2-18 The size dimensions of the tensile test samples. *67*

Figure 2-19 Schematic diagram of FSP and the dimension size of tensile test samples. *68*

Figure 2-20 Schematic diagram of single particle compression test [14]. *69*

Figure 2-21 The particle morphologies before and after compression tests: (a, b) a 7075Al particle with a size of 51 μm before and after compression tests; (c, d) a TiB_2/7075Al composite particle with a size of 44 μm before and after compression tests. *69*

Figure 2-22 (a) Schematic diagram of the computational domain and boundaries [15]. (b) and (c) display the gas velocity and gas temperature contours during CS deposition. *70*

Figure 2-23 Geometric model and computational domain of spherical 7075Al particle impinging on Al or 7075Al-T6 substrate. *71*

Figure 2-24 Geometric and meshing of flaky Al particle placed in three different posture angles: (a) 0°; (b) 45°; (c) 90°. *71*

Figure 2-25 Geometric model and computational domain of flaky Al particle impinging on Al substrate under the Eulerian frame and (b) the enlarged view of elements around the particle. *72*

Figure 3-1 (a) Particle velocity and (b) particle temperature along the nozzle central line. *76*

Figure 3-2 Particle impact velocity and temperature as a function of propelling gas temperature. *76*

Figure 3-3 (a) Particle velocity and (b) particle temperature along the nozzle central line for the particles with the shape factor (Ψ_{Wa}) from 0.3 to 1; (c) and (d) show particle impact velocity and particle impact temperature as a function of shape factor, respectively. An equivalent average particle size of 25 μm and 45 μm and 62 μm were used for this simulation. *77*

Figure 3-4 DE as a function of propelling gas temperatures *78*

Figure 3-5 Surface morphologies of the pure Al and CNT/Al composite coatings produced at a gas pressure of 3.0 MPa and a temperature of 550 ℃: (a) pure Al coating; (c) HSD composite coating; (e) SSBM composite coatings. (b), (d) and (f) are the corresponding magnified views of (a), (b) and (c), respectively. *79*

Figure 3-6 Optical micrograph of the coatings produced at different propelling gas temperatures: (a-d) pure Al coatings; (e-h) HSD composite coatings; (i-l) SSBM composite coatings. *80*

Figure 3-7 Coating thickness as a function of propelling gas temperature. *80*

Figure 3-8 Etched cross-sectional microstructures of the coatings deposited at a processing gas temperature of 550 ℃: (a, d) pure Al; (b, e) HSD composite; (c, f) SSBM composite. (a-c) are the top areas and (d-f) are the center areas of the corresponding coatings. *81*

Figure 3-9 Etched cross-sectional microstructures of the CNT/Al HSD coatings fabricated at processing gas temperature of (a, c) 500 ℃ and (b, d) 400 ℃. (a, b) top areas and (c, d) center areas of the corresponding coatings. *81*

Figure 3-10 EBSD characterization of the cross-section of the as-sprayed composite coatings at a propelling gas temperature of 550 ℃: (a) IPF mapping and (c) grain size distribution of the HSD composite coating; (b) IPF mapping and (d) grain size distribution of SSBM coating. *82*

Figure 3-11 Optical micrograph and SEM images of the CSed SSBM CNT/Al composite coating in （a-c）CC5 and (d-f) CC6. ..... *83*

Figure 3-12 (a)TEM/EBSD orientation mapping of the SSBM CNT/Al composite (b) grain size distribution; (c) BF TEM images show the laminar structure; (d) magnified TEM image displays the CNTs embedded into the Al matrix. *83*

Figure 3-13 X-ray diffraction patterns of CSed coatings and feedstock powders. *84*

Figure 3-14 Raman spectra mapping of the (a-c) HSD coating and (d-f) SSBM coating fabricated at P_g=600 ℃: (a) and (d) Optical micrographs; (b) and (e) Corresponding confocal Raman maps of G-band intensity (1520~1650 cm^{-1}); (c) and (f) Maps of I_D/I_G ratio value. *85*

Figure 3-15 Raman spectra of the feedstocks and composite coatings. *86*

Figure 3-16 Adhesion strength of CSed pure Al, HSD composite and BBSM composite coatings deposited on SS substrates using different propelling gas temperatures. *87*

Figure 3-17 Microhardness of the as-sprayed coatings. *88*

Figure 3-18 Single splat morphologies of (a) pure Al, (b) HSD and (c) SSBM composite deposited on SS substrate at P_g=3.0 MPa, T_g=550 ℃. *90*

Figure 3-19 Evaluation of effective plastic strain contours and corresponding morphologies of the deposited single Al splat observed by SEM in the cases of the different posture angles: (a) 0°; (b) 45°; (c) 90°. *90*

Figure 3-20 Contours of (a, c) effective plastic strain and (b, d) temperature of several flaky Al particles depositing on a SS substrate at different time: (a) and (b) 15 ns; (c) and (d) 25 ns. *91*

Figure 3-21 Contours of (a, c) effective plastic strain and (b, d) temperature of several spherical Al particles depositing on a SS substrate at 25 ns. *91*

Figure 3-22 XRD patterns of the SSBM CNT/Al composite deposits (obtained from CC5) annealed at different (a) temperatures and (b) duration (annealing temperature kept at 500 ℃). *92*

Figure 3-23 Raman shifts of the SSBM CNT/Al composite coatings annealed under different temperatures (a) and for different durations at a constant temperature of 500 ℃ (b). *92*

Figure 3-24 SEM images of SSBM CNT/Al composite annealed at different temperatures: (a) 300 ℃; (b) 400 ℃; (c) 500 ℃; (d) 550 ℃. *93*

Figure 3-25 TEM images of the CNT/Al composite deposit (CC5) annealed at 500 ℃ for 4 h. *93*

Figure 3-26 Microhardness evolution as a function of (a) annealing temperature and (b) annealing duration (the annealing temperature kept at 500 ℃). *94*

Figure 3-27 (a) Tensile stress-strain curves for SSBM CNT/Al composites annealing treated at different temperatures for 4 h. (b) and (c) summarize the UTS values and elongation of the specimens, respectively. *95*

Figure 3-28 (a) Tensile stress-strain curves for SSBM CNT/Al composites annealing treated at different duration of time. (b) and (c) summarize the UTS values and elongation of the specimens, respectively. *96*

Figure 3-29 (a) Tensile stress-strain curves for SSBM CNT/Al composites in different tensile directions. (b) and (c) summarize the UTS values and elongation of the specimens, respectively. *97*

Figure 3-30 Fracture morphologies of the as-sprayed and annealed CNT/Al composite samples at different conditions (a-c) as-sprayed state; (d-f) 500 ℃/4 h; (g-i) 500 ℃/12 h. *98*

Figure 3-31 Magnified SEM image of the fractured surface: (a) intergranular fracture and (b) pull out of CNTs. *98*

Figure 3-32 Fracture model for the as-sprayed SSBM CNT/Al composite deposit: (a) Fracture through weak inter-splat boundary and intergranular; (b) intergranular fracture by CNT pull out. *98*

Figure 4-1 Surface morphologies of the as-sprayed AlSi10Mg and TiB_2/AlSi10Mg deposits obtained from different conditions: (a) AlSi10Mg-CT1; (b) TiB_2/AlSi10Mg-CT1; (c) AlSi10Mg-CT2; (d) TiB_2/AlSi10Mg-CT2. ..... *104*

Figure 4-2 Cross-sectional morphologies of the CSed AlSi10Mg and TiB_2/AlSi10Mg composite deposits at lower magnification: (a) AlSi10Mg-CT1; (b) TiB_2/AlSi10Mg-CT1; (c) AlSi10Mg-CT2; (b) TiB_2/AlSi10Mg-CT2. (e) and (f) are the magnified views near the substrate/deposit interface showing well bonding state of the deposit and substrate. *105*

Figure 4-3 Cross-sectional morphologies of the CSed AlSi10Mg and TiB_2/AlSi10Mg composite deposits at higher magnification: (a) AlSi10Mg-CT1; (b) TiB_2/AlSi10Mg-CT1; (c) AlSi10Mg-CT2; (b) TiB_2/AlSi10Mg-CT2. ..... *105*

Figure 4-4 SEM micrographs of the etched cross-sections of the as-sprayed AlSi10Mg and TiB_2/AlSi10Mg composite deposits: (a) AlSi10Mg-CT1; (b) TiB_2/AlSi10Mg-CT1; (c) AlSi10Mg-CT2; (b) TiB_2/AlSi10Mg-CT2. (e) and (f) are the magnified regions marked in (c) and (d), respectively. *106*

Figure 4-5 EDS mapping of CSed TiB_2/AlSi10Mg-CT2 deposit. *106*

Figure 4-6 XRD patterns of the (a) pure AlSi10Mg-CT2 and (b) TiB_2/AlSi10Mg-CT2 composite at as-sprayed and annealed states as well as the initial feedstocks. *107*

Figure 4-7 Cross-sectional morphologies of annealed (a-d) AlSi10Mg-CT2 and (e-h) TiB_2/AlSi10Mg-CT2 composite coatings at different temperatures: (a) and (e) 200 °C; (b) and (f) 300 °C; (c) and (g) 400 °C; (d) and (h) 500 °C. *108*

Figure 4-8 Porosity evolution of the AlSi10Mg and TiB_2/AlSi10Mg composite coatings as a function of annealing temperature. *108*

Figure 4-9 SEM micrographs of the etched cross-sections of the annealed (a-d) AlSi10Mg and TiB_2/AlSi10Mg composite samples at a lower magnification: (a) and (e) 200 °C; (b) and (f) 300 °C; (c) and (g) 400 °C; (d) and (h) 500 °C. 109

Figure 4-10 Cross-sectional morphologies (higher magnification) of the annealed (a-d) AlSi10Mg-CT2 and TiB_2/AlSi10Mg-CT2 composite coatings: (a) and (e) 200 °C; (b) and (f) 300 °C; (c) and (g) 400 °C; (d) and (h) 500 °C. 110

Figure 4-11 Schematic of Si particle evolution in morphology and size during annealing treatment. 110

Figure 4-12 Si particle density and particle size evolution as a function of annealing temperatures. 110

Figure 4-13 SEM microstructure and EDS mapping of AlSi10M-CT2 deposits annealed at 500 °C for 4 h. 111

Figure 4-14 SEM microstructure and EDS mapping of TiB_2/AlSi10Mg-CT2 composite deposits annealed at 500 °C for 4 h. 111

Figure 4-15 Microhardness evolution as a function of annealing temperatures. 112

Figure 4-16 Microhardness evolution of the as-sprayed (a) AlSi10Mg-CT2 and (b) TiB_2/AlSi10Mg-CT2 composite as a function of annealing duration and temperatures: 200 ℃; 300 ℃; 400 ℃; 500 ℃. 112

Figure 4-17 Friction coefficient vs. sliding wear distance for (a) AlSi10Mg-CT1 and (b) TiB_2/AlSi10Mg-CT1 composite coatings. (c) and (d) display the average friction coefficient and wear rate as a function of annealing temperatures, respectively. 114

Figure 4-18 The worn morphologies of (a, b) AlSi10Mg-CT1 and (c, d) TiB_2/AlSi10Mg-CT1 deposits at (a, c) as-sprayed state and (b, d) annealed at 500 °C for 4 h. 115

Figure 4-19 EDS mapping of the worn surface of the (a) as-sprayed and (b) annealed (500 °C) TiB_2/AlSi10Mg-CT1 composite deposits. 115

Figure 4-20 Tensile stress-strain curves for pure AlSi10Mg-CT2 and TiB_2/ AlSi10Mg-CT2 composites in as-sprayed state and annealing treated at different temperatures. 116

Figure 4-21 (a) and (b) summarize the UTS values and elongation of the tested specimens, respectively. 116

Figure 4-22 Fracture morphologies of the as-sprayed and annealed AlSi10Mg-CT2 deposits after the tensile test: (a) as-sprayed state; (b) 300 ℃; (c) 400 ℃; (d) 500 ℃. 117

Figure 4-23 Fracture morphologies of the as-sprayed and annealed TiB_2/AlSi10Mg-CT2 composite samples at different temperatures after the tensile test: (a) as-sprayed state; (b) 300 ℃; (c) 400 ℃; (d) 500 ℃. 118

Figure 4-24 Fracture morphologies and EDS mapping of the TiB_2/AlSi10Mg-CT2 composite samples in as-sprayed state and annealed at 400 ℃. 119

Figure 4-25 Schematic of the fractural model for as-sprayed and annealed composite deposits at micro-scale and submicron-scale: (a) micro-scale and (b) submicron-scale fracture model of the as-sprayed composite deposit; (c) micro-scale and (d) submicron-scale fracture model of the annealed composite deposit. 119

Figure 4-26 XRD patterns of the CSed and FSPed deposits: (a) AlSi10Mg-CT2; (b) TiB_2/AlSi10Mg-CT2. 120

Figure 4-27 Optical micrographs showing the cross-section of the FSPed AlSi10Mg deposits: (a) 1 pass; (b) 3 passes. *121*

Figure 4-28 Optical micrographs showing the cross-section of the FSPed TiB_2/AlSi10Mg deposits: (a) 1 pass; (b) 3 passes. *121*

Figure 4-29 Optical micrographs showing the surface morphologies of the FSPed AlSi10Mg deposits: (a) 1 pass (b) 3 passes. *122*

Figure 4-30 Optical micrographs showing the surface morphologies of the FSPed TiB_2/AlSi10Mg deposits: (a) 1 pass; (b) 3 passes. *122*

Figure 4-31 SEM images of the FSPed AlSi10Mg deposit in different regions corresponding to the A, B, C and D as marked in Figure 4-27. ..... *123*

Figure 4-32 Magnified SEM images of the cross-section of the FSPed AlSi10Mg deposits in different regions corresponding to the A, B, C and D as marked in Figure 4-27a. *123*

Figure 4-33 Magnified SEM images of the FSPed AlSi10Mg deposits in different regions as marked in Figure 4-27b. *124*

Figure 4-34 SEM images of the cross-section of the FSPed TiB_2/AlSi10Mg deposits in different regions corresponding to the A, B, C and D as marked in Figure 4-28a. *124*

Figure 4-35 Magnified SEM images of the cross-section of the FSPed TiB_2/AlSi10Mg deposits in different regions corresponding to the A, B, C and D as marked in Figure 4-28a. *125*

Figure 4-36 SEM images of the cross-section of the FSPed TiB_2/AlSi10Mg deposits in SZ as marked in Figure 4-28b. *125*

Figure 4-37 TEM bright-field (BF) images of CSed and FSPed TiB_2/AlSi10Mg-CT2 composite samples; (b) and (d) are the magnified views. *126*

Figure 4-38 Microhardness values of FSPed AlSi10Mg and TiB_2/AlSi10Mg composite samples. *127*

Figure 4-39 Friction coefficient vs. sliding wear distance for FSPed (a) AlSi10Mg-CT2 and (b) TiB_2/AlSi10Mg-CT2 composite deposits. (c) and (d) display the average COF and wear rate values of the CSed and FSPed samples. *128*

Figure 4-40 The worn morphologies of CSed and FSPed pure AlSi10Mg-CT2 and TiB_2/AlSi10Mg-CT2 deposits: (a) AlSi10Mg-CT2; (b) TiB_2/AlSi10Mg-CT2; (g) AlSi10Mg-FSP-1 pass; (d) TiB_2/AlSi10Mg-FSP-1 pass. *128*

Figure 4-41 Tensile stress-strain curves for pure AlSi10Mg and TiB_2/AlSi10Mg composites in as-sprayed state and FSPed with different passes.. ..... *129*

Figure 4-42 (a) and (b) summarize the UTS and elongation values of the tensile specimens, respectively. *130*

Figure 4-43 Comparison of the UTS and elongation of the FSPed TiB_2/AlSi10Mg composite deposits with other FSP fabricated Al matrix composites [21-26] [17, 20, 27-34]. *130*

Figure 4-44 SEM micrographs of the tensile fracture surface of the FSPed AlSi10Mg and TiB_2/AlSi10Mg composites with different magnifications: (a-c) AlSi10Mg-FSP-1 pass; (d-f) TiB_2/AlSi10Mg-FSP-1 pass; (g-i) AlSi10Mg-FSP-3 passes. *131*

Figure 5-1 (a) Particle velocity and (b) particle temperature along the nozzle central line; (c) and (d) show particle impact velocity and particle impact temperature as a function of processing conditions,

respectively. An average particle size of 33 μm and 37 μm corresponding to pure 7075Al and TiB_2/7075Al composite particle respectively were used for this simulation. 138

Figure 5-2 Raw force-displacement data of pure 7075Al particles and TiB_2/7075Al composite particles obtained from single particle compress experiment. 139

Figure 5-3 Nominal stress-strain converted from force-displacement data: (a) 7075Al particles; (b) TiB_2/7075Al composite particle. 139

Figure 5-4 Variations of the nominal stress vs. strain for a 7075Al particle comparing with the fit function. 140

Figure 5-5 UTS values of the pure 7075Al and TiB_2/7075Al composite particle as a function of particle diameter. 141

Figure 5-6 Nanoindentation performance of the (a) pure 7075Al particle and (b) TiB_2/7075Al composite particle. 141

Figure 5-7 Distribution of effective plastic strain (PEEQ) (on the left-hand side) and temperature (on the right-hand side) of the single (a) 7075Al and (b) TiB_2/7075Al composite particles deposited onto pure Al substrate in C1. 144

Figure 5-8 Distribution of PEEQ (on the left-hand side) and temperature (on the right-hand side) of the single (a) 7075Al and (b) TiB_2/7075Al composite particles deposited onto pure Al substrate in C2. 144

Figure 5-9 Distribution of PEEQ (on the left-hand side) and temperature (on the right-hand side) of the single (a) 7075Al and (b) TiB_2/7075Al composite particles deposited onto pure Al substrate in C3. 145

Figure 5-10 Distribution of PEEQ (on the left-hand side) and temperature (on the right-hand side) of the single (a) 7075Al and (b) TiB_2/7075Al composite particles deposited onto 7075Al-T6 substrate in C1. 145

Figure 5-11 Distribution of PEEQ (on the left-hand side) and temperature (on the right-hand side) of the single (a) 7075Al and (b) TiB_2/7075Al composite particles deposited onto 7075Al-T6 substrate in C2. 146

Figure 5-12 Distribution of PEEQ (on the left-hand side) and temperature (on the right-hand side) of the single (a) 7075Al and (b) TiB_2/7075Al composite particles deposited onto 7075Al-T6 substrate in C3. 146

Figure 5-13 Surface and cross-sectional morphologies of single 7075Al and TiB_2/7075Al composite splats deposited onto Al substrate at C1: (a-c) 7075Al; (d-f) TiB_2/7075Al composite. 147

Figure 5-14 Surface and cross-section morphologies of single 7075Al and TiB_2/7075Al composite splats deposited onto Al substrate in C3: (a-c) 7075Al; (d-f) TiB_2/7075Al composite. 148

Figure 5-15 Surface and cross-section morphologies of single 7075Al and TiB_2/7075Al composite splats deposited onto Al substrate in C1: (a-c) 7075Al; (d-f) TiB_2/7075Al composite. 148

Figure 5-16 XRD patterns of the initial feedstocks and as-sprayed components: (a) 7075Al and (b) TiB_2/7075Al composite. 149

Figure 5-17 Surface morphologies of the 7075Al and TiB_2/7075Al composite particles deposited at C1 and C3: (a) and (e) 7075Al-C1; (b) and (f) TiB_2/7075Al-C1; (c) and (g) 7075Al-C3; (d) and (h) TiB_2/7075Al-C3. 150

Figure 5-18 Cross-sectional SEM images of the cold spayed (a-c) 7075Al deposits and (b-d) TiB_2/7075Al composite deposits at different processing parameters: (a) 7075Al-C1, (b) 7075Al-C2, (c)

7075Al-C3, (d) TiB_2/7075Al-C1, (e) TiB_2/7075Al-C2, (f) TiB_2/7075Al-C3. The pores and the typical deformed particles were indicated by white arrows and red dashed outlines, respectively. 151

Figure 5-19 BSE/SEM micrographs of the microstructure of the (a, c) 7075Al and (b, d) TiB_2/7075Al composite coatings: (a) 7075Al-C1, (b) TiB_2/7075Al-C1, (c) 7075Al-C3, (d) TiB_2/7075Al-C3. The white arrows indicate pores in the coatings. 151

Figure 5-20 Porosity evolution of the 7075Al and TiB_2/7075Al composite deposits in different processing conditions. 152

Figure 5-21 Particle flattening ratio evolution of the pure 7075Al and TiB_2/7075Al composite particle under different processing conditions. 152

Figure 5-22 SEM morphologies (a, b) and the corresponding EDS maps of Ti (c, d) of the TiB_2/7075Al-C2 deposit; (e) TiB_2 particle size distribution obtained from SEM images. 153

Figure 5-23 SEM/EBSD characterization of the cross-section of the CSed (a-f) pure 7075Al and TiB_2/7075Al composite deposits in different processing conditions: (a-c) 7075Al-C1; (d-f) 7075Al-C3; (g-i) TiB_2/7075Al-C1; (j-l) TiB_2/7075Al-C3. The first column displays gain orientation maps, and the middle column presents the band contrast. The last column shows gain size distribution of the Al matrix (the TiB_2 phase was eliminated). 154

Figure 5-24 TEM micrographs of the TiB_2/7075Al-C1 deposit in different regions: (a) and (b) particle interior; (c) and (d) near interparticle boundaries. Red arrows show needle-like precipitates dispersed in the Al matrix, while the yellow arrows indicate the spherical precipitates. The blue arrows indicate the in-situ formed TiB_2 nanoparticles in the Al matrix. 155

Figure 5-25 TEM micrographs of the TiB_2/7075Al-C1 deposit showing the precipitate structure. (b) and (d) the magnified micrographs within red dashed boxes of (a) and (c), respectively. Red arrows show needle-like precipitates dispersed in the Al matrix, while the yellow arrows indicate the spherical precipitates. The blue arrows indicate the in-situ formed TiB_2 nanoparticles in the Al matrix. 155

Figure 5-26 TEM micrographs of the TiB_2/7075Al-C3 deposit showing precipitate structures in (a) particle interior, (b) interparticle boundaries with pancake structures and (c) interparticle boundaries with ultrafine grain structures. (b), (d) and (f) are the magnified micrographs within red dashed boxes of (a), (c) and (e), respectively. 157

Figure 5-27 TEM micrographs of the TiB_2/7075Al-C3 deposit showing a pancake structure. (b) and (c) are the corresponding magnified micrographs of area A and B in (a), respectively. 157

Figure 5-28 Microhardness evolution of the pure 7075Al and TiB_2/7075Al composite deposits in different processing conditions. 159

Figure 5-29 Adhesion strength evolution of 7075Al and TiB_2/7075Al composite in C1. 160

Figure 5-30 (a) Coefficient of friction versus wear distance; (b) and (c) average friction coefficients and wear rates at diffident processing conditions. 161

Figure 5-31 Overviews, magnified views and EDS mapping of the worn morphologies of CSed (a-d) 7075Al-C1 and TiB_2/7075Al-C1composite coatings. 161

Figure 5-32 Variation of (a) tensile strength and (b) elongation of the as-sprayed 7075Al and TiB_2/7075Al composite samples in different processing conditions. 162

Figure 5-33 Fracture morphologies of the as-sprayed TiB_2/7075 Al composite tensile samples fabricated using different processing conditions: (a) C1; (b) C2; (c) C3. (a_1), (b_1) and (c_1) are the magnified images of the red dashed area in (a), (b) and (c), respectively. 163

Figure 5-34 SEM images of the 7075Al bulk, 7075 Al and TiB_2/7075Al composite coatings before (first row) and after open circuit immersion in 0.1 M (middle row) and 0.6 M (third row) NaCl for 7 days: (a-c) 7075Al bulk; (d-f) 7075Al-C1; (g-i) TiB_2/7075Al-C1; (j-l) 7075Al-C3; (m-o) TiB_2/7075Al-C3.164

Figure 5-35 Corrosion behavior of the bulk 7075Al , CSed 7075Al coatings and TiB_2/7075Al composite coatings obtained at C1 and C3 in a solution of (a) 0.1 M and (b) 0.6 M NaCl as determined by potentiodynamic polarization. 166

Figure 5-36 Experimental and simulated (a) Nyquist and (b) Bode plots of the bulk 7075Al, and CSed 7075Al and TiB_2/7075Al composite coatings. 167

Figure 5-37 Electrical equivalent circuits used to fit the EIS data. 168

Figure 5-38 Potentiodynamic polarization curves of the CSed and annealed coatings. HT1 refers to annealing procedure of 230 ℃ for 6 h, while HT2 refers to annealing procedure of 412 ℃ for 4 h. 169

Figure 5-39 Cross-sectional SEM images of the pure 7075Al and TiB_2/7075Al composite deposits after T6 treatment: (a) 7075Al-C1, (b) 7075Al-C2, (c) 7075Al-C3, (d) TiB_2/7075Al-C1, (e) TiB_2/7075Al-C2, (f) TiB_2/7075Al-C3. The pores were indicated by white arrows. 172

Figure 5-40 Porosity evolution of the deposits after T6 treatment. 172

Figure 5-41 Optical and SEM micrographs of the etched cross-section of the (a-c) pure 7075Al-C2 and (d-f) TiB2/7075Al-C2 composite deposits after T6 treatment. (a) and (d) optical micrographs; (b, c) and (e, f) are the SEM images. 173

Figure 5-42 EDS mapping of the cross-section of the TiB_2/7075Al composite deposit after T6 treatment. 173

Figure 5-43 Optical and SEM micrographs of the etched cross-section of the (a-c) pure 7075Al-C2 and (d-f) TiB_2/7075Al-C2 composite deposits after 470 ℃/4 h (water quenching) +121 ℃/24 h treatment. (a) and (d) are the optical micrographs; (b, c) and (e, f) are the SEM images. 174

Figure 5-44 Optical and SEM micrographs of the etched cross-section of the (a-c) pure 7075Al-C2 and (d-f) TiB_2/7075Al-C2 composite deposits after 412 ℃/4 h+T6 treatment. (a) and (d) are the optical micrographs; (b, c) and (e, f) are the SEM images. 174

Figure 5-45 EDS mapping of the cross-section of the pure 7075Al-C2 deposit after 412 ℃/4 h + T6 treatment. 175

Figure 5-46 EDS mapping of the cross-section of the TiB_2/7075Al-C2 composite deposit after 412 ℃/4 h+T6 treatment. 175

Figure 5-47 EBSD characterization of the (a-c) pure 7075Al-C1 and (d-f) TiB_2/7075Al-C1 composite deposits after T6 treatment: (a) and (d) band contrast; (b) and (e) IPF mapping; (c) and (f) grain size distribution. 176

Figure 5-48 TEM micrographs of the (a, b) TiB_2/707Al-C1 and (c, d) TiB_2/707Al-C3 composite samples after T6 treatment. 177

Figure 5-49 Microhardness evolution of the deposits as a function of aging duration. 178

Figure 5-50 The fracture morphologies of the TiB_2/7075Al composite deposits after T6 treatment: (a) and (b) TiB_2/7075Al-C1; TiB_2/7075Al-C2. 179

Figure 5-51 The fracture morphologies of the TiB_2/7075Al composite deposits after 412 ℃/4 h + T6 treatment: (a) 7075Al-C2; (b) TiB_2/7075Al-C2. 180

Figure 5-52 SEM morphologies of the TiB_2/7075Al-C3 composite deposit after T6 treatment. 181

List of tables

Table 1-1 Typical deposit properties affected by the manufacturing parameters [42]..... 6

Table 1-2 Comparison of different powder preparation methods [93]..... 12

Table 1-3 Summary of the CS-processed AMCs using mixed/blended composite powders..... 19

Table 1-4 Summary of the CS-processed AMCs using ball-milled composite powders..... 22

Table 1-5 Summary of the wear behavior of CSed AMC coatings..... 23

Table 1-6 Summary of the corrosion behavior of the CSed AMC coatings. 25

Table 2-1 Chemical composition of the 7075Al starting powder..... 56

Table 2-2 Nozzle dimensions and expansion ratios. 59

Table 2-3 Processing parameters used for CS deposition of CNT/Al composite powder feedstocks.... 60

Table 2-4 Processing parameters used for CS deposition of TiB_2/AlSi10Mg composite powder feedstocks. 61

Table 2-5 Processing parameters used for CS deposition of TiB_2/7075Al composite powder feedstocks. 61

Table 2-6 Material parameters for Al, 7075Al-T6 bulk, 7075Al and TiB_2/7075Al composite..... 73

Table 5-1 The main CS processing parameters for the pure 7075Al and TiB_2/7075Al composite powder feedstocks. (This table is also given in Chapter 2)..... 137

Table 5-2 Summary of the UTS values and A, B, n parameters of the pure 7075Al particle obtained from single particle compression tests..... 142

Table 5-3 Summary of the UTS values and A, B, n parameters of the TiB_2/7075Al composite particle obtained from single particle compression tests. 142

Table 5-4 The simulated particle impact velocities and temperatures under different conditions were used for the FEA simulation..... 143

Table 5-5 Results of potentiodynamic corrosion tests in 0.1 M and 0.6 M NaCl solutions. 166

Table 5-6 Fitted EIS parameters for the bulk and as-sprayed coatings..... 168

Table 5-7 Results of potentiodynamic corrosion tests of the annealed samples in a 0.6 M NaCl solution. 169

Table 5-8 The properties of the deposits after heat treatment at different conditions. 178

Table 5-9 Summary of the effect of heat treatments on bubble formation of C3 deposits..... 181

Chapter I State-of-the-art of the Al matrix composites fabricated by cold spray process

Al matrix composites (AMCs) have been widely used in aerospace, automotive and manufacturing industries thanks to their remarkable mechanical properties, such as high specific modulus and strength, superior wear, fatigue and creep resistance. AMCs, fabricated with conventional methods like casting, powder metallurgy and thermal spray, are often accompanied with defects such as porosity, larger grain size, clustering of particles, poor bonding and undesirable interface reaction products, which can have an adverse effect on their final mechanical performance. Recently, as an emerging solid-state deposition technique, cold spray (CS) was proposed as an alternative technology to fabricate AMCs with eliminating these adverse effects brought by high temperature. Differing from high-temperature deposition processes, formation of the CSed deposits relies largely on the particles' kinetic energy at impact rather than on its thermal energy (e.g. conventional thermal spray). Importantly, CS further exhibits several unique advantages in comparison to powder-bed metal additive manufacturing (AM) processes (e.g. selective laser melting), including lower thermal stresses during fabrication, lack of phase transformation, short production time, unlimited component size and capability to repair damaged components. These advantages make CS a potential technique for coating, repairing and additive manufacturing of AMCs.

In this chapter, first of all, we will give a brief introduction about the fabrication processes and applications of AMCs, and then, the principle and setup of CS process, as well as its main processing parameters and applications will be introduced detailly. Afterwards, more attention will be paid on the development of AMCs produced by CS, including the composite powder preparation, processing, microstructure and properties of the CSed AMCs. Moreover, post-treatments on CSed AMC coatings including heat treatment and friction stir process will be introduced. At last, the main objectives and originalities of this thesis will be addressed.

1.1 Al matrix composites

Because of its outstanding comprehensive performance such as high specific strength, good formability and excellent corrosion resistance, aluminum alloys have been widely used in aerospace, automotive and manufacturing industries. Nowadays, in order to meet the increasing service requirements in some special fields (e.g. automobile, aerospace), there has been a strong demand for Al alloys with much higher strength. When a different second-phase material in the shapes of particle, whisker and fiber is integrated into a metal matrix, it actually acts as a reinforcement in order to improve mechanical properties of the matrix. Therefore, metal matrix composites (MMCs) can be regarded as an effective way to produce high-performance metallic materials [1]. It is expected that MMCs can be engineered with combination of metallic matrix (e.g. ductility and toughness) and reinforcement properties (e.g. high strength and modulus, high thermal properties) to obtain tailored mechanical and physical properties in the final composites [1].

The metals and reinforcements used for preparing MMC are usually chosen in accordance with their specific properties and the potential applications. The most commonly used metal matrix is aluminum, magnesium, titanium and their alloys. Al matrix composites (AMCs), which are considered as promising structural materials, have been widely used in the aerospace and automotive industries. This is attributed mainly to their low density, low coefficient of thermal expansion, high strength and stiffness, and good wear resistance [2-4]. AMCs can be classified into four categories depending on the type of reinforcement [5]: i) Particulate-reinforced AMCs (P-AMCs), ii) whisker-or short fibre-

reinforced AMCs, iii) continuous fibre-reinforced AMCs, and iv) mono filament-reinforced AMCs. Numerous studies have been performed related to the fabrication of AMCs using ceramic particles (SiC, B_4C, Al_2O_3, TiB_2, Ti_2N), and carbon based materials, like carbon fibers, synthetic diamond particle, carbon nanotubes, and graphene [5, 6].

1.1.1 Particulate-reinforced Al matrix composites

Recently, P-AMCs have attracted considerable attention as a result of their relatively low costs and characteristic isotropic properties [5]. P-AMCs offer isotropic properties with an increase in strength and stiffness compared to unreinforced materials. Reinforcements include oxides (e.g. Al_2O_3) or carbides (e.g. SiC, B_4C) or borides (TiB_2), nitrides (e.g. AlN) as well as elemental materials (e.g. diamond). They present in volume fraction less than 30% when used for structural and wear resistance applications. However, in electronic packaging applications reinforcement volume fraction could be as high as 70% [1, 5].

A variety of processing techniques have evolved over recent decades in an effort to optimize the structure and properties of P-AMCs [5]. The objectives of the processing techniques are to homogeneously distribute the reinforcement phases and to achieve a defect-free micro-structure as well as economic efficiency. Generally, based on the material state, the processes can be clarified into the following three main groups:

a) Liquid state processing techniques: stir casting, squeeze casting;
b) Solid-state processing techniques: powder metallurgy (PM), friction stir processing (FSP).
c) Deposition process: Spray co-deposition, disintegrated melt deposition (DMD) process, thermal spray.

Among these techniques, stir casting and PM process are the most commonly used for producing P-AMCs in industries. Their schematic diagrams are shown in Figure 1-1a and b.

The stir casting process involves incorporation of ceramic particulate into liquid Al melt by mechanical stirring which is followed by allowing the mixture to solidify [5]. Generally, it is possible to incorporate up to 30% ceramic particles in the size range 5 to 100 μm in a variety of molten Al alloys [3]. The cast composites were further extruded to reduce porosity, refine the microstructure and homogenize the distribution of the reinforcement. The essential thing by this method is to create the good wetting between particulate reinforcement and Al melt. Another challenge associated with this process is segregation of reinforcing particles which is caused by the floating or settling of the reinforcement particles, because of density difference between matrix and reinforcement, during the melting and casting processes.

PM techniques have been developed as promising routes for the fabrication of P-AMCs. In this process, blended fine powdered materials（both the Al matrix and ceramic particles), are compacted into a desired shape and then heated (or sintered) to a desired shape. Moreover, hot rolling or hot extrusion can be applied to further densify and improve mechanical properties of the parts. The PM process allows for the production of complexed shapes with very close dimensional tolerances, with minimum scrap loss and fewer secondary machining operations. Besides, it also allows for producing P-AMCs with high volume fraction of reinforcement which is immiscible in liquid casting.

In recent years, some other advanced technologies have been also developed and applied to fabricate P-AMCs, such as in-situ synthesis [7, 8] and FSP [9, 10]. Compared to the conventional ex-situ process, the in-situ formation of a ceramic second phase in Al matrix provides better control of size and distribution of reinforcements, as well as the matrix reinforcement interface, yielding better improvement in mechanical properties of the composites. FSP as a solid-state process, allows to modify

microstructure and improve mechanical properties of cast or wrought Al-based alloys using a simple and inexpensive tool. Besides, this technique enables to eliminate undesired casting defects, such as porosity and solidification cracking. FSP technology is very effective in microstructure modification of MMCs and has been widely applied for AMCs fabrication as well as coating post-treatment [11, 12].

Moreover, additive manufacturing (AM) as a novel manufacturing method was proposed several years ago and rapidly developed during the last decade. Selective laser melting (SLM), as an AM technology applied to metals and ceramics for decades, has shown promising potential for AMCs fabrication by employing a high power laser system [13]. A series of AMCs have been successfully fabricated by using SLM process, such as TiB_2/AlSi10Mg, AlN/AlSi10Mg [14], Al_2O_3/Al [15, 16], SiC/AlSi10 Mg, TiB_2/Al-12Si [17], TiB_2/Al-3.5Cu-1.5Mg-1Si [18] etc. The as-built composites possess high mechanical performance, even better than composite components made by the conventional techniques [19]. This is attributed to improved laser absorptivity of the Al matrix and enhanced grain refinement with the addition of ceramic particles as well as the fine microstructure result from rapid solidification process [19]. However, up to now, only a few Al alloys which have good formability and high laser absorptivity are suitable for SLM processing of AMCs. Therefore, this process has some limitations in the development of new AMCs.

It can be concluded that extra heat or even remelting are required in stir casting, PM, thermal spray and SLM to acquire the AMC components. This probably gives rise to problems like oxidation, excessive interfacial reaction and grain growth.

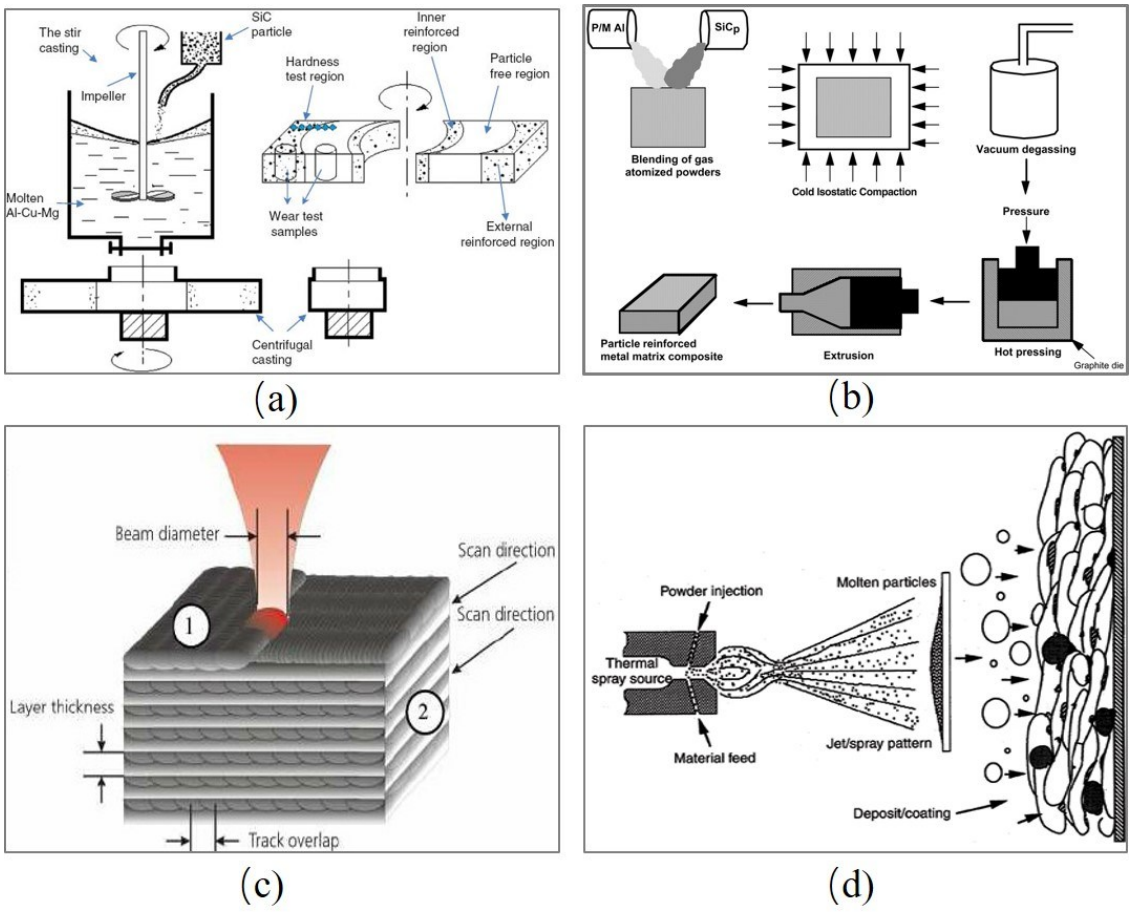

Figure 1-1 The schematic diagrams of fabrication processes of P-AMCs: (a) stir casting; (b) powder metallurgy; (c) selective laser melting; (d) thermal spray.

1.1.2 Carbon nanotube-reinforced Al matrix composites

In addition to the ceramic particles, carbon nanotubes (CNTs) have emerged as the other promising candidates for AMCs. This is due to the fact that the CNTs have many outstanding properties, such as superior strength (up to ~100 GPa), elastic modulus (~1 TPa), stiffness and high thermal and electrical conductivities. Therefore, if CNTs are successfully incorporated into the Al matrix, they are expected to significantly improve both physical and mechanical properties of the composite.

For fabrication of high strength CNT/Al composites, the uniform CNTs dispersion, strong interface bonding and high structural integrity of CNTs have been regarded as the three most important issues [20]. To solve the CNT agglomeration problem, the techniques of nano-scale dispersion [21, 22], high energy ball milling [23, 24], in-situ grown method [25], flake powder metallurgy (flake-PM) [26, 27] and solution coating [28] have been developed in the past decade. Many research efforts have resorted to high energy ball milling to disperse CNTs in the Al matrix powders [24, 29]. However, the structural integrity of the CNTs were often damaged by impacting of the milling balls, which proved to be detrimental for mechanical properties [24]. Very recently, a new flake-PM route via shift-speed ball milling strategy has been proposed by Xu.et al [30]. The coordination of CNTs dispersion, integrity and interfacial bonding could be achieved in the CNT/Al composite powder [30].

Various consolidation processes including casting [31], thermal spraying [32], sintering [25] and hot-extrusion [24] were selectively applied for the fabrication process of CNT/Al composites. However, these methods all have their own limits, for example, the sintering process efficiently produces dense composite structures. But grain growth and aluminum carbide (Al_4C_3) formation due to interfacial reactions between the Al and CNTs are inevitable during hot sintering process, which might result in weakening of the composite [30]. In the thermal spraying like air plasma spraying (APS) and high-velocity oxy-fuel (HVOF), CNTS are exposed to high temperatures and oxygen, and therefore destruction and gasification take place. According to the research work of T. Laha et al [32, 33], the melting and inevitable oxidation of the CNT/Al composite destroyed the structure of the embedded CNTs by gasification of carbon elements.

Recently, cold spray (CS) as an emerging solid-state deposition process, was proposed as an alternative technology to fabricate AMCs with eliminating the adverse effect brought by the high temperature [34]. Compared with thermal spray technologies, such as APS, twin wire-arc spray (TWA), and HVOF, which involve either partial or complete melting of particles during deposition, the formation of the CSed deposits relies largely on the particles' kinetic energy at impact rather than on their thermal energy [35]. In this process, micron-sized particles are accelerated to supersonic velocity (300-1200 m/s) via expansion of a pressurized and ‘hot’ gas through a diverging-converging nozzle, and severe plastic deformation occurs during the impact that leads to success bonding and coating build-up. Since the feedstock used remains in the solid-state during the entire deposition process, the inevitable defects commonly encountered in the high-temperature deposition processes such as oxidation, residual thermal stress, or phase transformation can be minimized or eliminated [36] [37].

1.2 Cold spray process

CS is a relatively new solid-state coating technique based on supersonic fluid dynamics and high-speed impact dynamics. CS was originally developed in the mid-1980s at the Institute of Theoretical and Applied Mechanics of the Russian Academy of Science in Novosibirsk by Papyrin and his colleagues [38, 39]. They successfully deposited a wide range of pure metals, metal alloys, and composites onto a variety of substrate materials [40]. Since then, CS has drawn worldwide attention,

and experienced rapid development in academic laboratories and applied in factory manufacturing as well, especially in the last decade.

1.2.1 Principle and setup

The main technical objective of CS is to ensure that particles of the feedstock powder impinge the substrate at or beyond a critical velocity [34]. This is achieved by means of a pressurized and preheated process gas (air, N_2, He) that expands through a (converging/diverging) de Laval nozzle, reaching supersonic velocities [34]. Figure 1-2a shows an overview of a high-pressure CS system, basically consists of a compressed gas delivery system, a gas heater, a powder feeder, a supersonic de-Laval nozzle, a robot arm, and an operating system. In this system, a fluidized powder feedstock is fed to the process gas upstream, i.e. at high pressure before entering the nozzle. Powder particles are thus accelerated by the process gas, reaching high velocities of up to 1200 m/s or more. Particle temperature upon impact can be 1000 K or more, depending on the process conditions. Additionally, a low-pressure CS system with lower impact velocity and temperature has been developed as a feasible and cheaper method for the restoration of damaged components. Instead of the high-pressure compressed gas, a portable air compressor is used for particle acceleration in a low-pressure CS system; Besides, powder is allowed to be injected at the nozzle divergent section by the pressure difference between atmosphere and nozzle divergent section without using a high-pressured carrier gas. However, only a limited range of materials like Cu, Sn, and Al can be applied by using this low-pressure CS system. As clearly shown in Figure 1-2b, the CS process is featured by high particle impact velocity and low particle temperature compared with other conventional thermal spray processes.

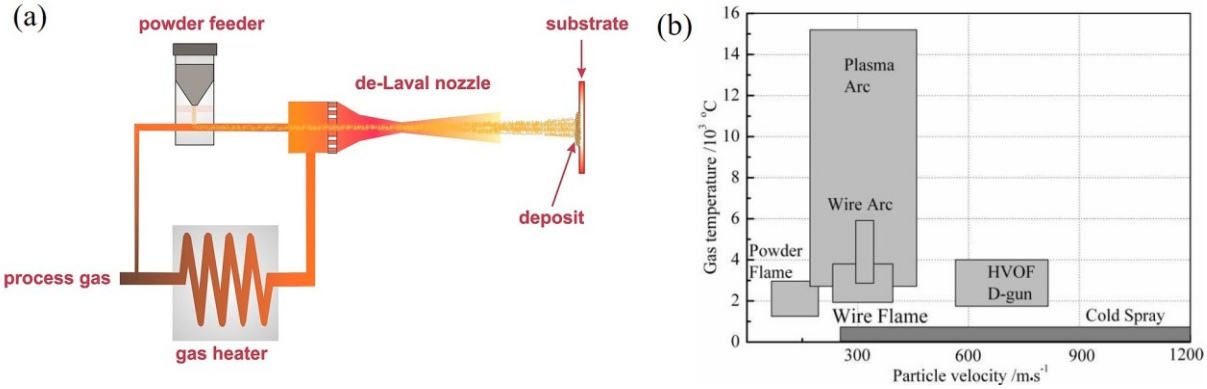

Figure 1-2 (a) Schematic diagram of high-pressure CS systems [34] and (b) comparison of CS with other thermal spray processes [41].

1.2.2 Main processing parameters

Figure 1-3 shows a schematic of the typical manufacturing parameters used in CS deposition, including the propulsive gas parameters (pressure, temperature and type), powder feeder parameters (powder feed rate), and nozzle parameters (traverse speed, scanning step, standoff distance, spray angle and trajectory). All these parameters can affect the deposition process and thus the quality of the coating or component. Influence of these parameters on the coating properties was summarized in

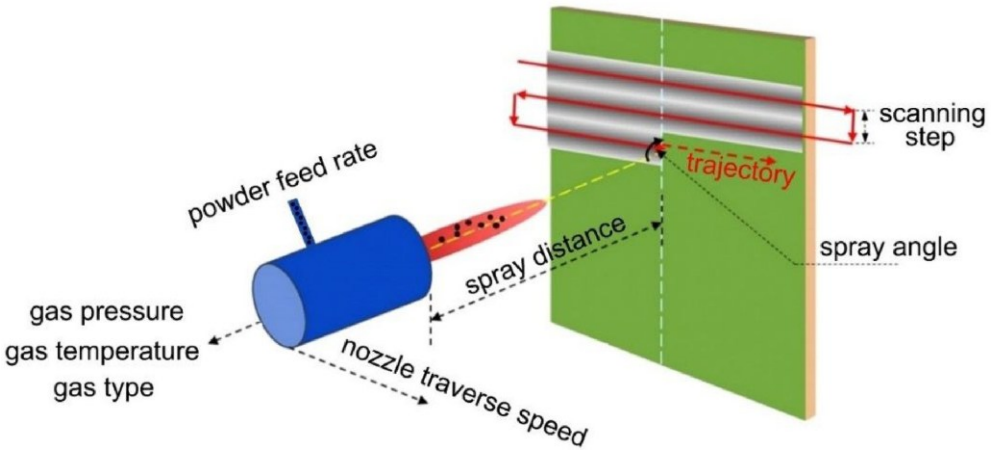

Figure 1-3 Schematic of the typical manufacturing parameters used in CS deposition [42].

Table 1-1 Typical deposit properties affected by the manufacturing parameters [42].

	Porosity	Deposit strength	Adhesion	Residual stress	Deposition efficiency
Gas pressure ↑	↓	↑	↑	↑	↑
Gas temperature ↑	↓	↑	↑	↑	↑
Gas molecular weight ↑	↑	↓	↓	↓	↓
Powder feed rate ↑	↑	↓	↓	↓	↓
Traverse speed ↑	↑	↑	↑	↓	↑
Scanning step ↑	×	×	×	×	×
Standoff distance ↑	o	o	o	o	o
Spray angle ↑	↓	↑	↑	↑	↑
Trajectory	×	×	×	×	×

'↑' increase, '↓' decrease, 'o' relevant but no common view, '×' no data available

Among all these parameters, the propulsive gas parameters, including gas pressure and gas temperature as well as the type of gas, are the most important processing parameters for CS deposition. Because they directly determine the particle impact velocity and the particle impact temperature, and thus quality and properties of the deposit [42, 43]. Previous studies have proved that higher gas pressure, higher gas temperature or lower gas molecular weight causes better gas flow acceleration through de-Laval nozzle [42, 44]. In some cases, using helium (He) instead of N_2 and air is the most effective way to increase particle velocity, but the gas cost of He is also much higher. It has been widely accepted that increasing particle impact velocity and temperature significantly improves deposition efficiency, deposit porosity, deposit strength (cohesion strength or tensile strength) and adhesion strength due to the reduced inherent defects and enhanced metallic bonding [44] [35].

In addition, some other parameters, such as the powder feed rate, gun traverse speed, standoff distance, particle size and morphology, particle preheating temperature, substrate surface roughness and temperature, spray angle, are also important factors which should be taken into account for sound deposition. The detailed review of these factors on CS deposition are summarized by S.Yin et al. [42] and S. Pathak et al. [45].

1.2.3 Advantages and disadvantages

Differing from the high-temperature deposition processes, formation of the CSed deposits relies largely on the particles' kinetic energy at impact rather than on its thermal energy. The feedstock used remains in a solid-state during the entire deposition process. The 'cold' unique feature brings CS process many benefits compared to the thermal spray process, including [45]:

-Almost no oxidation, no phase transformation, no interfacial reaction, no grain growth;

-Flexible in fabrication temperature-sensitive materials, including MMCs;

-Minimum thermal input to the substrate;

-Compressive residual stresses, and fully dense and thick coating

-High deposition efficiency and high deposition rate

However, there are some disadvantages to this technology:

-Pure ceramics and some brittle and hard alloys are difficult or unable to be deposited;

-Cold-sprayed coatings over ceramic substrates show only limited bond strength;

-High-quality coatings are produced with expensive helium as the processing gas in order to achieve the velocities necessary for deposition;

1.2.4 Coating formation mechanisms

In the CS process, the formation of a deposit consists of two different stages. The first stage involves the deposition of an initial layer of particles where bonding occurs between feedstock particles and the substrate material; the second stage is the deposition on top of the layer(s) previously deposited, where bonding occurs between feedstock particles [40].

To reveal the bonding mechanisms of the first stage, the particles/substrate, three different bonding phenomena have been proposed and summarized by W.Y. Li et al. [46]: (1) bonding is by surface adhesion resulted from an interface-instability-induced physical anchoring effect; (2) through partial melting and fusion of materials in a heavily deformed region; and (3) through fracture of the surface oxide (s) which covers sprayed particles and substrate. In addition, from another perspective, metallurgical bonding and mechanical inter-locking are commonly considered to be two mechanisms of the metallic bonding in CS [47] [46]. Mechanical bonding is represented by non-chemical reaction, in which hard particles are mechanically trapped by the soft substrate material to form the interlocking. Mechanical interlocking corresponds to an embedment of particles on the substrate due to a deep penetration as observed in the following particle/substrate combinations: metal/polymer [48, 49], oxide/polymer [50], ceramic/metal [51] and metal/metal [52, 53].

Metallurgical bonding is the consequence of chemical reaction occurring at the inter-particles and coating/substrate interfaces, which requires the oxide-free interface and metal-to-metal contact [54]. Due to the severely localized deformation after impacting on substrate, the occurrence of adiabatic shear instability (ASI) [55, 56] can lead to the adiabatic heating-induced thermal softening at the interface [55]. The thermal softening is dominant over work hardening; thus metals behave like viscous material and form the outward jet feature due to extrusion (Figure 1-4b). As schematically shown in Figure 1-4e, at the ASI region, viscous metal jet due to adiabatic heating-induced thermal softening extrudes from the interface, which results in the extrusion of broken oxide fragments from the interface to the periphery of deformed particle. The cleaning effect by the extrusion of viscous metal jet on the oxide fragments finally provides intimate contact between fresh metal [54, 57]. The adiabatic heating generated within

this highly sheared zone causes rapid rise in local temperature, and some melting phenomena at interface. An amorphous layer is observed in such circumstance and it generally corresponds to an adiabatic shear band across the interface [58]. At the particle interface, the grains are extensive deformed, resulting in dynamic recrystallization and enhanced interface bonding [59] [60], as illustrated in Figure 1-4c and d.

The criterion for effective bonding in CS has been explained based on ASI of the particle. According to Scmidt et al. [61], there is consensus that bonding occurs beyond a critical velocity, and that this velocity generally decreases with increasing particle temperature and particle size. When the particle velocity is inferior to the critical one, the particle rebounds away from the substrate surface due to the rebound energy is higher than 'adhesion energy'. It is also presumed that too high impact velocities result in hydrodynamic erosion of the substrate. The region bound between these two characteristic velocities defines the window of deposition in CS, as shown in Figure 1-4a [62]. That is to say only the particles with the velocity within this window can achieve successful bonding. This theory has been further confirmed by a series of experimental results and simulation results [63-67].

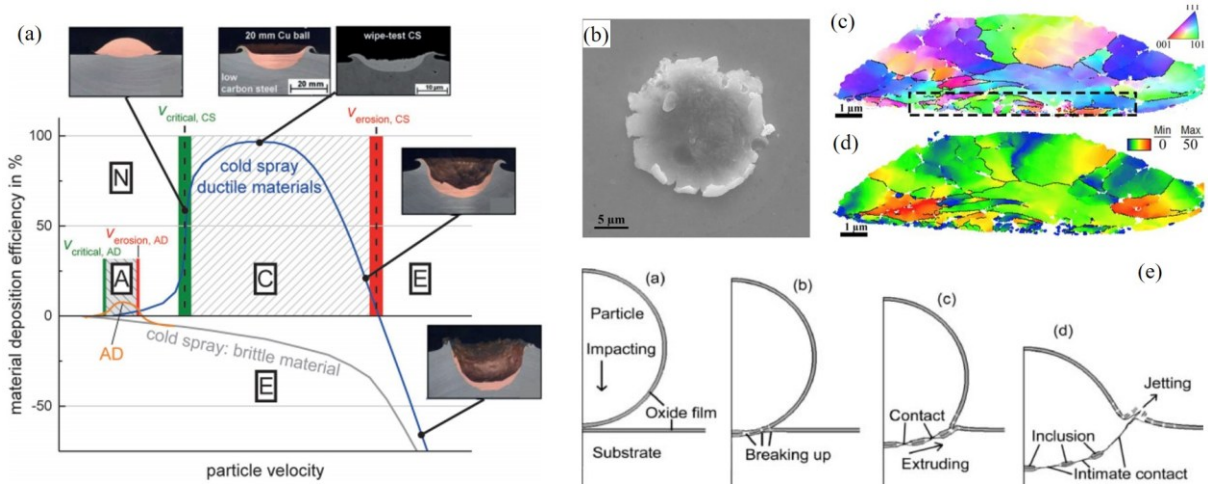

Figure 1-4 Deposition characteristics of the single ductile particle impact on metal substrate: (a) deposition window for ductile material [62], (b) Typical morphology of a deformed Al alloy splat [60]; (c) and (d) microstructure evolution within the deformed particle [60]; (e) Schematic diagram of the bonding process of cold-sprayed particles accompanying with the breaking-up and extruding of surface oxide films and the formation of jetting [57].

Recently, M. Hassani and his colleagues from MIT realized in-situ observation of the microparticle supersonic impact behavior [68, 69]. An example of pure Al single particle impact on Al substrate with different velocities is shown in Figure 1-5a and b [68]. Based on a series of measurements, the critical velocities for successful deposition of pure metals (Al, Ni, Cu, Zn) and alloys (Al2024, Al6061, Al7075) have been determined. It is also proved that the critical velocity is related to particle size. This result is consistent with the accepted notion that larger particles should have lower critical velocities. However, the authors developed a mechanistic framework to estimate the critical velocity for jetting on the basis of a hydrodynamic spall process [69, 70]. Their numerical simulation work revealed that interaction of strong pressure waves with the free surface at the particle edges can cause hydrodynamic plasticity that effects bonding, without requiring shear instability. Then the authors found out a proportionality between the CS critical velocity and the bulk speed of sound. These results provide a new mechanistic view for the process of impact-jetting and adhesion in CS process. But at this moment, there is still debate about this theory [70, 71].

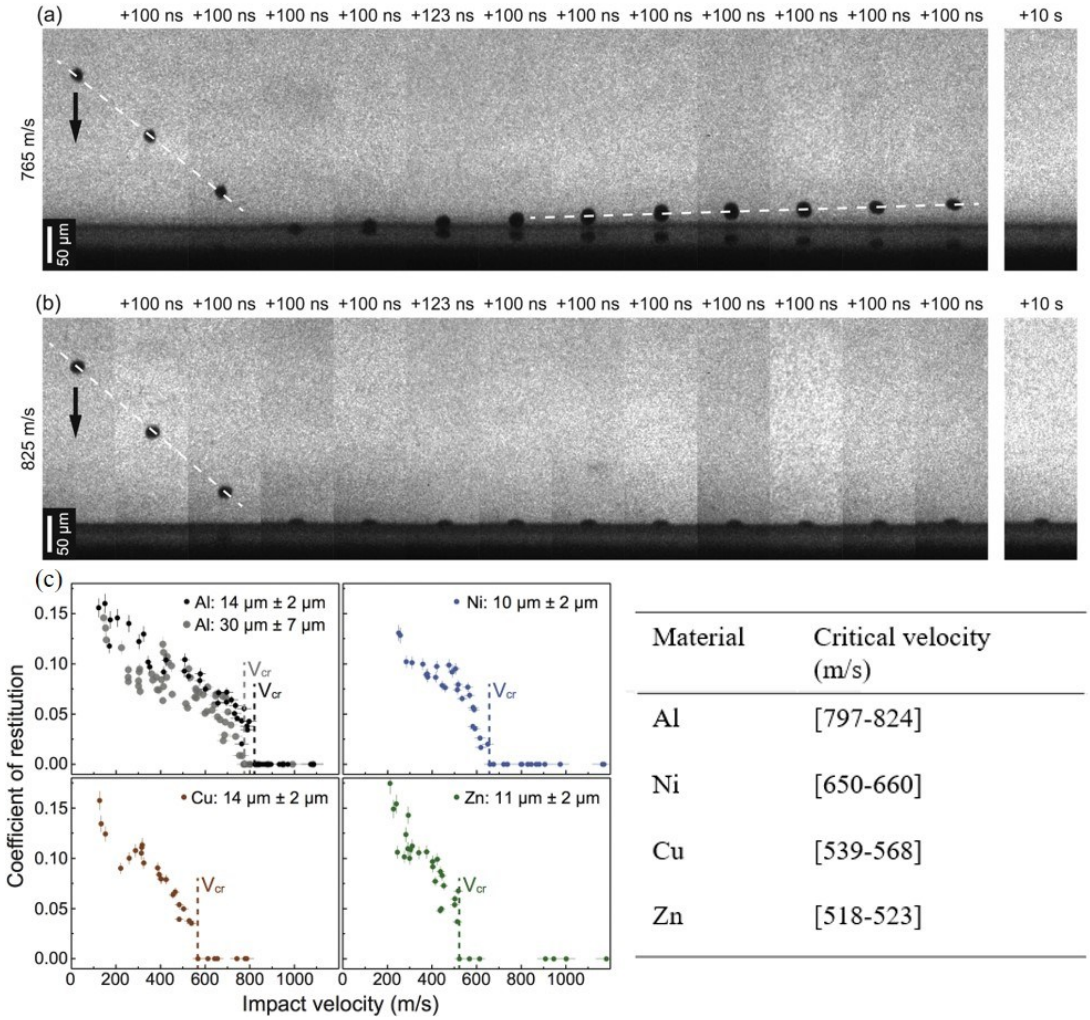

Material	Critical velocity (m/s)
Al	[797-824]
Ni	[650-660]
Cu	[539-568]
Zn	[518-523]

Figure 1-5 In situ observation of micron-sized pure metal particle impact on an metal substrate: (a) the microparticle arrives from the top of the field of view with a speed of 765 m/s, impacts the substrate and subsequently rebounds with a speed of 35 m/s. (b) The microparticle impacts the substrate with a speed of 825 m/s and subsequently adheres to the surface. (c) demonstrates the critical velocities for the deposition of pure Al, Ni, Cu and Zn metals [68, 70].

Once well bonding of the first layer is achieved, the coating built-up depends on the capability of the deposited particles to be joined together [40]. For the ductile particles (e.g. Al), plastic deformation promotes a metallic bonding for the deformed particle and the previously deposited layers. Following this, the plastic deformation of the subsequent particles can further reduce the porosity and enhances the interparticle bonding. The deposition process for coating built-up is described in detail in Ref. [40]. Regarding the non-ductile particles (e.g. ceramic particles), a deposit behavior of these ceramic particles was governed by the interlocking of these hard particles into soft matrix. In some cases, the brittle particles can be broken into fragments during the collision with the deposited hard particles. Then, the fragments are embedded into deposited layers. The coating built-up mechanism on this aspect was well addressed in Ref.[37] [72].

1.2.5 Applications

Up to now, the unique advantages mentioned above make CS a potential technique for coating, repairing and AM of a variety of engineering materials, including pure metals (Cu, Al, Ti, etc.), alloys (Ti64, 7075Al, 6061Al, 316 stainless steel, A380, etc) and composites, nanomaterials, polymers, and

other advanced materials [34, 40, 73]. The main applications of the CS deposition are summarized in Figure 1-6. Globally, there are at least three potential uses of the CS method: surface functionalization, restoration, bulk production. The primary application of the CS process is to fabricate all kinds of coatings for surface functionalization, such as wear-resistant, oxidation resistant, anti-corrosion, conductive/insulation (thermal and electrical), erosion-resistant (cavitation), anti-bacterial; photocatalytic performance, soft magnetic performance and so on. For example, CS deposition of Cu coatings onto ceramics provides an efficient solution for electronic heat sinks and refrigeration units [40]. In U.S. Army Research Laboratory, Cr_3C_2-based coatings were CS deposited on 4140 alloy steel for improving its wear performance [74]. Moreover, metallization of Cu on polymer or polymer composite by CS deposition has attracted wide attention due to its little heat influence on the polymer substrate [49] [48, 75].

CS is a cost-effective process that has shown great potential in the repair of damaged components, due to its capability to avoid any thermal damage to the underlying substrate material, and unique ability to retain the original properties of the feedstock powder. During the past decade, CS has been successfully applied to repair a variety of corroded and damaged components in various fields, such as turbine blades, engine blocks, helicopter propellers and landing gears, pistons, valves, camshafts and gearboxes [46]. For example, researchers from U.S. Army Research Laboratory repaired aircraft actuator and Mg alloy gearbox with CSed Al coatings [76]. Results showed that bonding strength of the coating, hardness and corrosion properties of the CSed coatings were largely improved. In the marine industry, CS has been successfully applied to the repair of corroded internal bore surface of navy Al alloy valve actuator without thermally affecting the base material [77]. Moreover, in the automotive industry, CS has been applied to repair corroded oil pump housings of Caterpillar-3116 and Caterpillar-3126 engines with Al alloy [42].

Besides surface functionalization and repair, CS can produce bulk components with specific functional macroscopic properties for large deposits whose thickness can reach up to 20 mm, even more. CS as an additive method can provide an approximation of real workpiece shape by the use of manufacturing robots systems. Compared to powder-bed metal AM processes (e.g. SLM), CS process exhibits several other unique advantages, including lower thermal stresses during fabrication, lack of phase transformation, short production time, unlimited component size. For example, Eason et al. [78] fabricated dense and strengthened bulk copper thicker than 25 mm with a significant improvement of mechanical performance. Besides, bulk parts in Al alloys, copper alloys, titanium alloys, stainless steels and superalloys have been produced by CS deposition for different functional applications. Figure 1-8a shows an example of functional bulk production: a coil component of high magnetic field magnets. On Figure 1-8b, the CSed forming is used for the rapid prototyping of a more complex shaped body. A Ti6Al4V axisymmetric bulk part was produced from a plate Al substrate with a deposition efficiency of 80% for a short production lead-time (15–30 min) [79]. Moreover, some other components in complexed shapes were fabricated for other applications, as shown in Figure 1-8 (c-f).

Especially with the upgrade of the CS equipment, feedstock powders for deposition are extended from easily cold-sprayable materials to hard-to-deform materials. At the same time, the fabricated parts show high-quality interparticle bonding and good mechanical properties, with the strength comparable with or even superior to the wrought parts. However, the as-sprayed bulk has poor ductility and almost no elongation. In general case, post heat treatment of the as-sprayed component is required for mechanical property improvement.

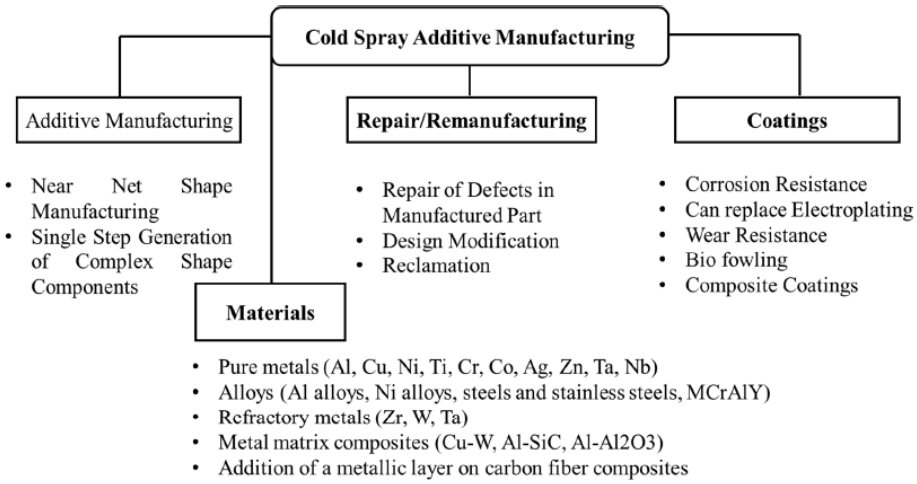

Figure 1-6 Key features of CS process for coating, reparation and additive manufacturing [80].

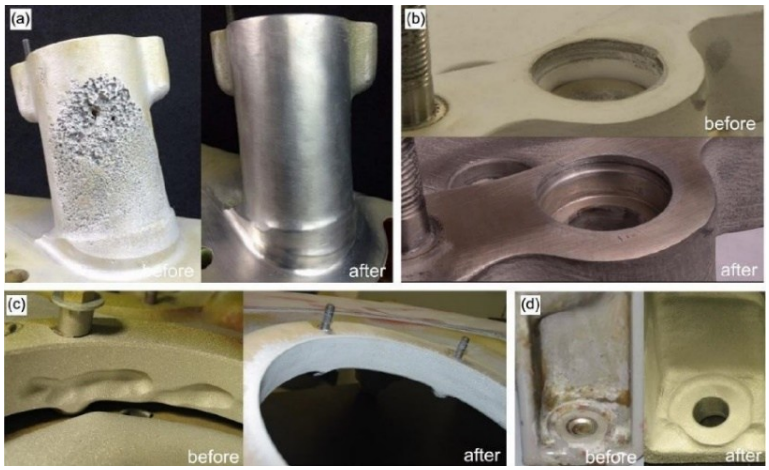

Figure 1-7 Comparison between damaged and CSR components: (a) S-92 helicopter gearbox sump, (b) oil tube bores in CH47 helicopter accessory cover, (c) UH-60 helicopter gearbox sump, and (d) UH-60 rotor transmission housing [76] [81].

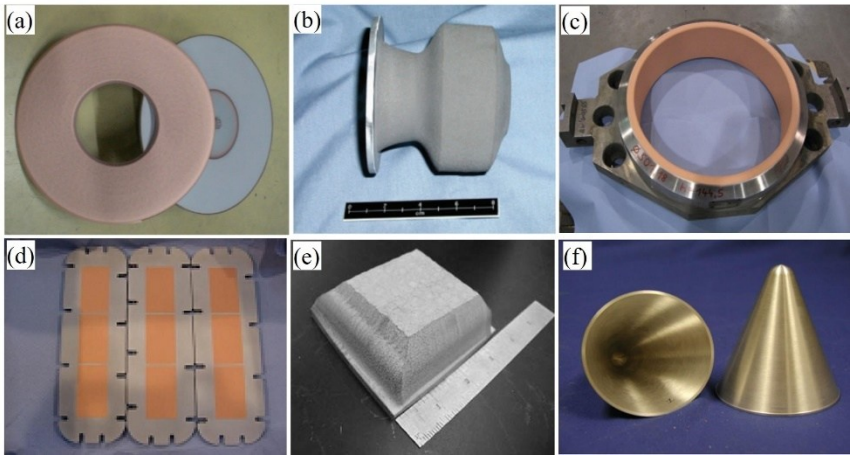

Figure 1-8 Application of cold spraying in net-shape forming: (a) high magnetic field magnets ; (b) rapid prototyping of Ti6Al4V axisymmetric bulk part [79]; (c) thick copper coating inside a pressure ring for food processing machine [82]; (d) electronic heat sinks [82]; (e) bulk Ni/Al energetic material [83]; (f) Cu/W cone structure [84].

1.3 Fabrication of Al matrix composites via cold spraying

In order to improve the mechanical and physical properties, numerous studies have been performed on the AMC coatings with the aim to increase hardness, wear resistance, as well as corrosion resistance. The applications of these CSed AMCs are two folds: first is to improve mechanical and corrosion properties of the substrate, and second is to fabricate high-quality AMCs components.

1.3.1 Composite powder preparation

Up to now, various AMC coatings have been tentatively deposited by CS, such as SiC/Al-12Si [85], Al_2O_3 /Al [86, 87], TiN/Al [88], SiC/Al5056 [89], TiB_2 /Al [90], SiC/7075Al [91], TiB_2/7075Al [91], CNT/Al, Dimond/Al [92] etc.. In these studies, it has been demonstrated that the nature of feedstock powders has a direct influence on microstructure and properties of the CS-processed deposits. In general, AMCs coatings could be deposited by CS in four different ways: (i) deposition of mechanically mixed/blended powder mixtures, (ii) deposition of composite powders obtained by satelliting, (iii) deposition of mechanically ball-milled powders，and (iv) deposition of dry sprayed powders.

Table 1-2 summarizes both the advantages and limitations of these methods. The detailed descriptions of these approaches are given below:

Table 1-2 Comparison of different powder preparation methods [93].

Method	Merit	Shortcoming
Mechanical blending	a) Adjustable range of components, composition of the powders. b) No interface reaction. c) Very easy of operation and very low cost.	a) Particle size limitation b) Loss of refinements during deposition. c) Uneven distribution of reinforcements d) Poor interface bonding between matrix and reinforcement.
Satelliting/wet granulation	a) controlled adherence of small reinforcement particles. b) increased level of ceramic attachment in the CS coatings.	a) Relatively more complex operation process and cost than mechanical blending. b) a little amount of remaining binder. c) Poor interface bonding between matrix and reinforcement.
Ball milling	a) Producing finer and more homogeneous powder mixtures than mechanical blending. b) Effectively control the content, size and distribution of reinforcement c) Formation a stronger interface bonding during ball milling. d) Effective way to produce nanostructured feedstocks	a) Particle morphology change and interfacial reaction b) Relatively more complex operation process and cost than mechanical blending. c) Very low deposition efficiency. d) Introduction of impurities during ball milling
Spray drying	a) Obtaining homogeneous agglomerated composite powders b) Powder with high sphericity, controllable size and low oxygen. c) Not relative complex operation process	a) With poor cohesion strength b) With a low production efficiency and yield of ultra-fine powder. c) High production cost.

1.3.1.1 Mechanical mixing/blending

As summarized in Table 1-3, mechanical mixing/blending has been widely used in many previous studies due to its ease of operation. This approach is mainly devoted to the deposition of ceramic particle reinforced AMCs. By integrating ceramic particles into the Al matrices, microhardness, adhesion strength as well as wear performance of the composite coatings are largely improved in comparison with the unreinforced counterparts. The advantages of such approach are obvious: (a) low cost due to application of mixtures of commercially available powders and (b) possibility of varying easily the composition of coating by controlling the composition of spraying blend. As can been from Table 1-3, the ceramic particles fraction varies from 5-75 vol.%. Besides, as shown in Figure 1-9, the morphology of the ceramics could be near-spherical or irregular, depending on the researchers' purpose. Generally, irregular shaped particles are beneficial for embedding into the deposit and it is capable of obtaining high content of reinforcements in the composite coating, while the spherical particles could have lower content but enhanced in-situ hammering effect due to unsuccessful deposition, which can lead to denser structure and improved grain refinement effect.

Meanwhile, some limits have also been revealed. Firstly, the size of ceramic reinforcement particles needs to reach a threshold value (over around 5 μm) in order to successfully disperse into composite coatings instead of running away with the gas flow [94]. In other words, it is technically difficult to achieve a composite coating reinforced with ultrafine or even nanosized particles. Additionally, using small particles is always accompanying with problem of agglomeration, being quite difficult in achieving uniform distribution of these fine particles. In this case, the dispersion of reinforcements can be improved by using ZrO_2 balls in long roll jar mill duration of long time, as shown in Figure 1-9d. Secondly, the brittle ceramic particles possess lower deposition efficiency than that of ductile metal ones, which results in low retention of reinforcements in the deposited coating, especially when a high content of ceramic particles is mixed in the feedstock powder. Furthermore, because the reinforcements are only distributed at the surface of the deformed matrix particles, the distribution of reinforcements can be considered as nonuniform. The poor bonding between the ceramic particles and metal matrix (mainly mechanical interlocking) is another issue which can largely weaken mechanical properties of the composite coatings. In order to improve both the distribution and interparticle bonding, additional post-treatments such as FSP and hot rolling process are often applied to CS-processed P-AMCs [95-97].

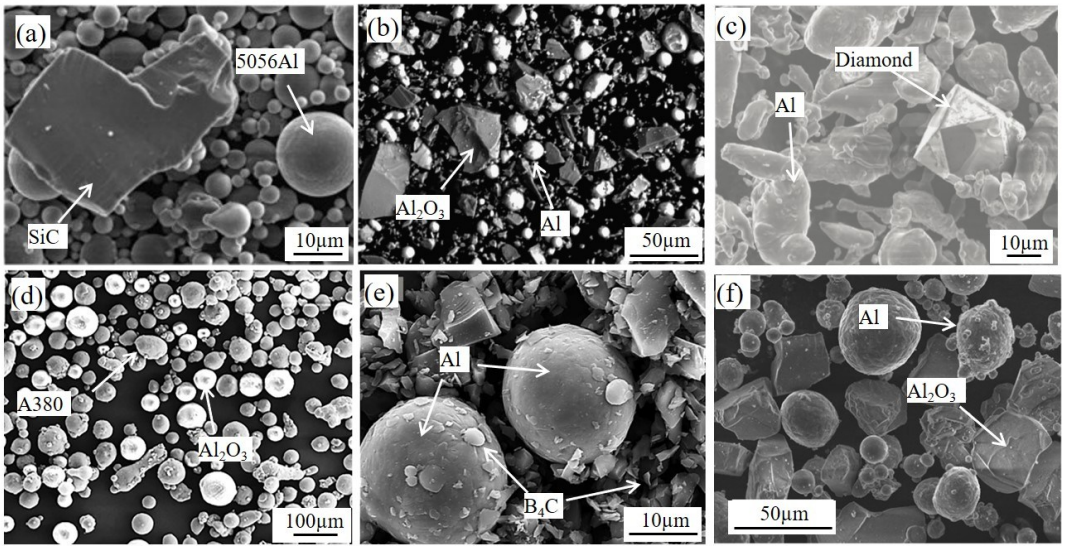

Figure 1-9 Surface morphologies of the blending mixed powders: (a) SiC/5056Al [89]; (b) Al_2O_3/Al [98]; (c) Diamond/Al [99]; (d) Al_2O_3/A380 [100]; (e) B_4C/Al [101]. (f) Al_2O_3/Al [102].

1.3.1.2 Satelliting/wet granulation

In order to improve the dispersion of the reinforced particles, satelliting was recently used as a method for preparing composite feedstocks, depending on using a liquid binder (for example polyvinyl alcohol) to attach fine (satellite) particles onto relatively large metallic particles. Satelliting is a technique which could fall under the umbrella definition of wet granulation [103]. It is specifically well suited to the controlled adherence of small reinforcement particles (<5 μm) to a larger 'planet' particle, which is quite different from the mechanical blending method. Example of TiC/Al and TiC/6061Al composite feedstocks produced by satelliting method is given in Figure 1-10. Significant coating of the large Al particles by TiC can be seen, however some particles are not successfully coated by using the blending mixing process. Experimental results from Kamaal S.et al. [104, 105] found that satelliting of small ceramic particles (TiC) to parent Al particles via use of a binder was demonstrated as an effective method of significantly increasing the level of ceramic attachment in the CS coatings.

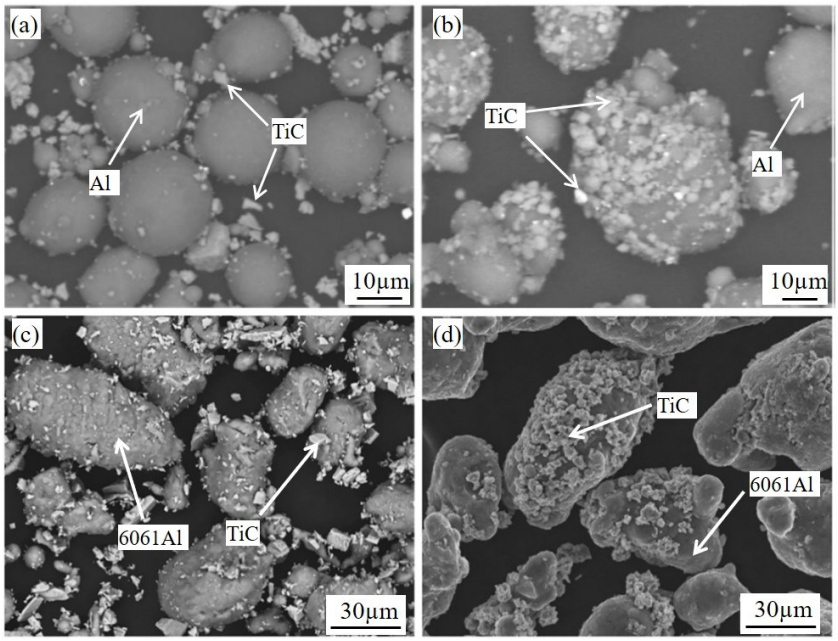

Figure 1-10 SEM images showing the morphologies of blended feedstocks (a) TiC/Al and (c) TiC/6061Al, and satellited feedstocks (b) TiC/Al and (d) TiC/6061Al [104, 105].

1.3.1.3 Ball milling

On the other hand, ball milling of a powder mixture is another effective way to improve the distribution of reinforcement particles and to enhance reinforcement/matrix interfacial bonding. Ball milling is a feasible technique for the synthesis of composite feedstock powders as it provides the control of content, size, and distribution of the two phases in an acceptable way [94]. As summarized in Table 1-4, many authors have reported the acquisition of Al nanocrystalline composites via high-energy ball milling. It was found that the ball-milled powder yields a denser and homogeneous coating with super fine ceramic particles dispersed into the Al matrix, leading to a higher microhardness due to the "constraint effect" of ceramic particulates on the deformation of the soft Al matrix. However, the powders experience work hardening effect and grain refinement during the milling process, which effectively increase its hardness and result in very low particle deposition efficiency [90]. The production of a composite coating using milled powders typically requires higher operating temperatures and pressures and often expensive He as the main gas, making the process less appealing for industrial applications [94]. Besides, annealing treatment was regarded as an effective method to reduce the work hardening effect of the composite particles produced from ball milling process.

Therefore, lower processing parameter is required but a higher deposition efficiency can be acquired in CS deposition. Additionally, impurities like oxygen are inevitably introduced into composite powders during ball milling process, which can have an adverse impact on metallic bonding of the deformed splats and mechanical performance of the composite coating.

The composite particle morphology, size distribution, microstructure and phase composition could be changed during ball milling process, which later can affect the deposition behavior of the particle, microstructure and properties of the CSed composite. A systematic study of the effect of various milling conditions on structure and properties of the resulting AMC powders was carried out by researchers [92, 106]. Figure 1-11 shows an example of nanodiamond-reinforced AMC (ND/AMC) powders synthesized by means of high energy ball milling for CS deposition. In the scope of their study, a full-factorial series of 27 different ND/Al composites were produced by varying ND content and critical milling parameters, including milling time and ball-to-powder ratio. It can be seen that both particle size and shape change notably upon milling. The average particle size decreases with milling time but remains larger for all milled samples as compared to the as-received powder. The size distribution of the powder particles also narrows significantly as the milling time increases. During the initial phase of the milling process, powder particles are cold-welded together and flattened by the milling media, leading to a substantial increase in particle size. With increasing milling time, particles are work hardened, start to fracture, and become more rounded, leading to a decrease in particle size and a more homogeneous powder with respect to shape and size distribution. It was also found that higher ball-to-powder ratios are less effective in ND dispersion and particle size reduction of ND/Al composites, rendering low ball-to-powder ratios and longer milling times more suitable for MMC synthesis. Raman spectroscopy revealed a homogeneous dispersion of ND in the individual MMC powder particles and the formation of a thin Al_4C_3 film at the ND surface, which may serve as an interfacial bonding layer between the reinforcement agent and the metal matrix. Both the ball-to-powder ratio and processing time can have significant effect on the crystal size and hardness of the composite powder, which is important factor that can influence the deposition behavior in CS process. Two other samples processed by ball milling are given in Figure 1-12. In the former case, TiB_2 particles were distributed inside the Al matrix through high energy ball-milling process. The composite powder fabricated by using this method always has a very low deposition efficiency (DE) due to the enhanced work hardening effect. In the latter case, after ball-milling, one can notice that the fine reinforcements were uniformly dispersed not only on the surface of the particle but also inside the particle. However, when the relative low processing energy was applied in ball milling, a core-shell structure can be obtained. The out layer is composed of the composite structure with uniformly distributed ceramic particles in Al matrix, while the inner core remains the initial structure of Al particle with little embedment of reinforcements. Therefore, the composite particle structure can be well controlled by varying the ball milling parameters.

In addition, ball milling process is a commonly used method for dispersing CNTs or graphene into a metal matrix to produce CNTs reinforced MMC for CS deposition [107, 108]. The dispersion of CNTs into metal particles becomes more difficult than that of ceramic particles, because the CNTs have much higher specific surface area. Therefore, before mechanical ball milling, the blended mixtures are commonly ultrasonicated within ethanol for homogeneous dispersion. Figure 1-13 show surface morphologies and cross-sectional views of the pure Al and CNT/Al composite powders with 1.0 and 3.0 vol.% CNTs, respectively. As revealed by the transmission electron microscopy (TEM) bright field, Al equiaxed nanocrystalline grains was formed. CNTs embedded in the NC Al matrix was observed in Figure 1-13i. However, outer walls of the CNTs were bent or fractured as a result of severe deformation caused by mechanical milling. Therefore, the balling milling process is effective in dispersion of CNTs into Al matrix; meanwhile, it can bring some damage to the integrity structure of CNTs.

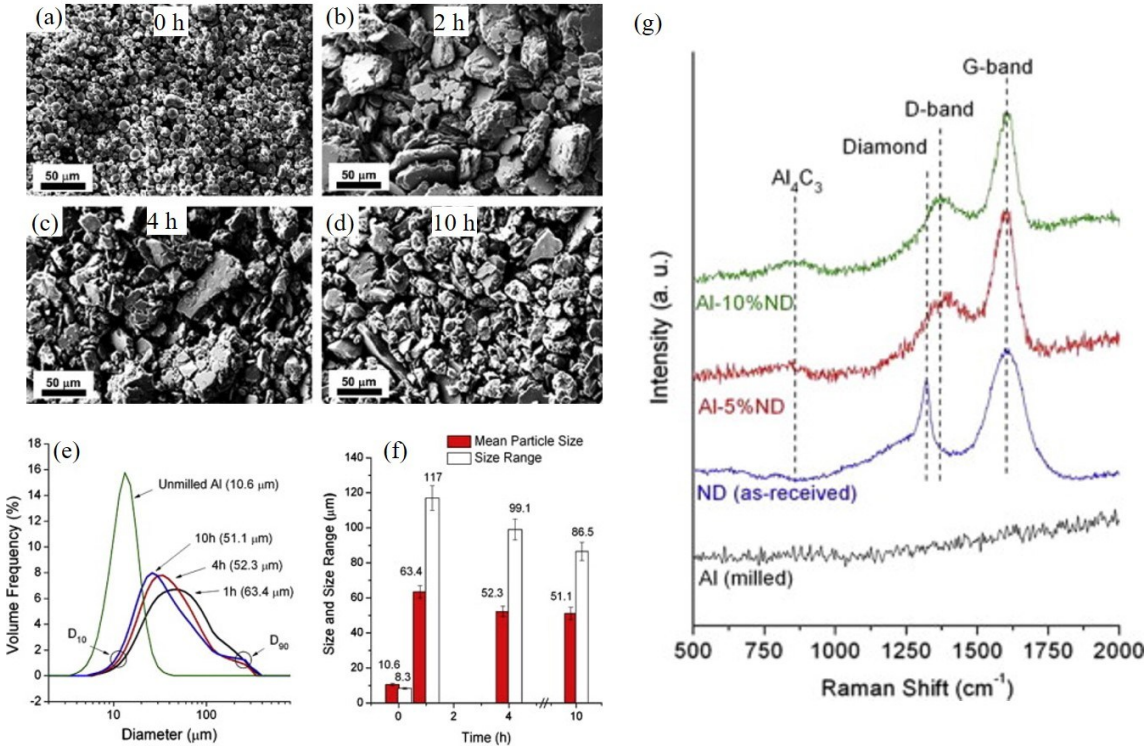

Figure 1-11 SEM micrographs of the (a) as-received Al in comparison to nanodiamond/Al composite powders (5 wt.% ND) ball-milled for, (b) 1 h, (c) 4 h and (d) 10 h using a ball-to-powder ratio of 10:1. (e) and (f) Particle size analysis of ND-Al MMC (5 wt.% ND) powders ball-milled for 1, 4 and 10 h using a ball-to-powder ratio of 10:1, in comparison to pure as-received Al. (f) Raman spectra (325 nm excitation) of ND-Al MMCs containing 5 and 10 wt.% ND, in comparison to as-received ND and Al milled with 10:1 ball-to-powder ratio for 1 h [106].

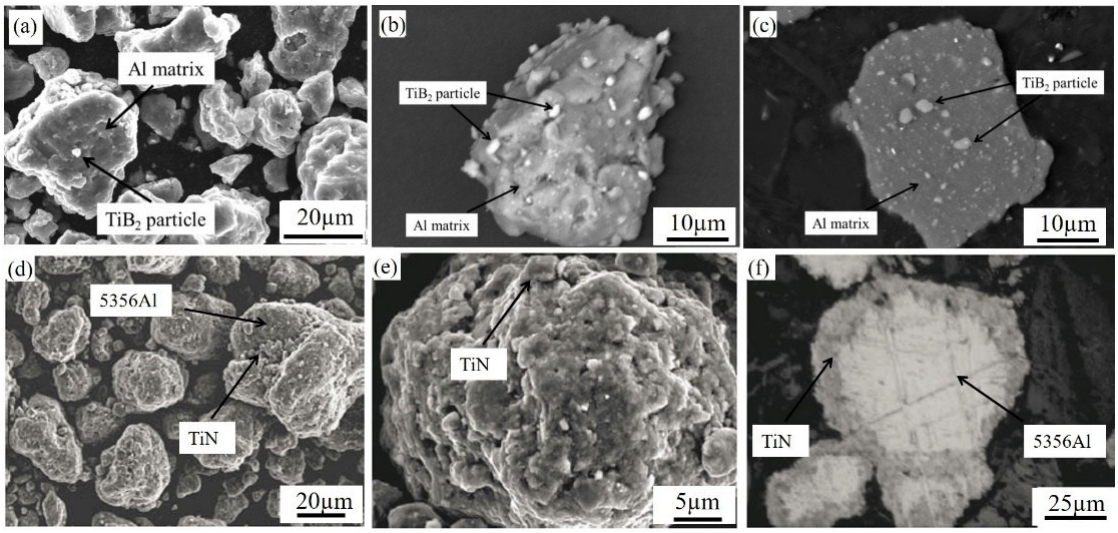

Figure 1-12 Surface morphologies and cross-section views of the ball-milled composite powder for CS deposition: (a-c) TiB_2/Al [109]; (d-f) TiN/5356Al [110].

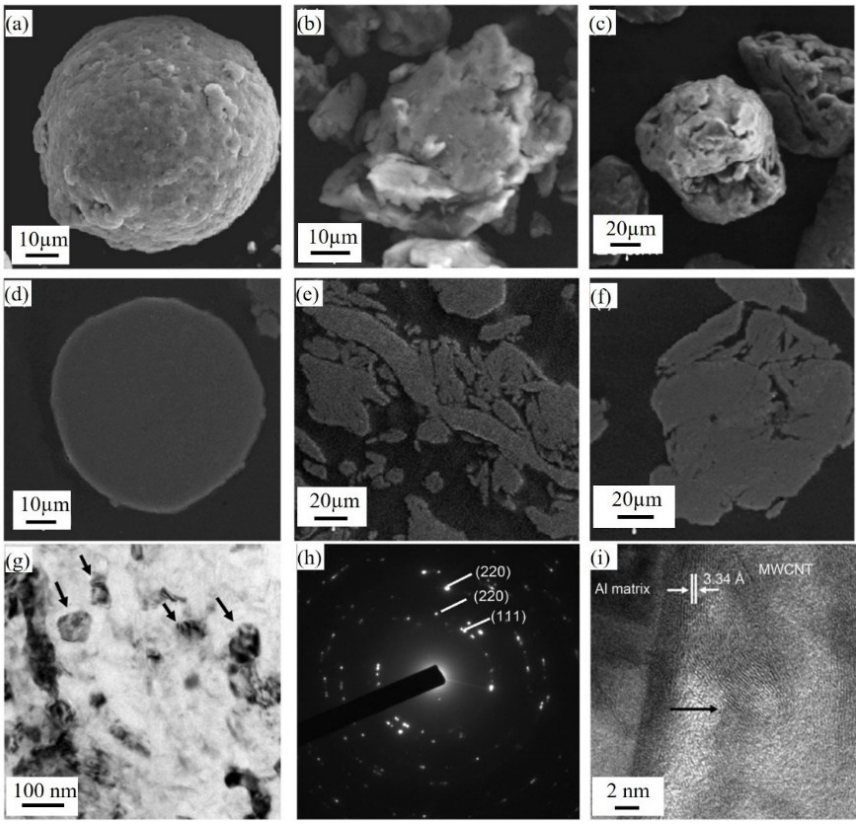

Figure 1-13 SEM micrographs of (a)–(c) morphologies and (d)–(e) cross-sections of powders: (a), and (d) pure Al, (b) and (e) the composite powder (1.0 vol.%), (c) and (f) the composite powder (3.0 vol.%). TEM BF image of composite powder (3.0 vol.%) (black arrows indicate equiaxed NC), (b) SAED pattern of (a), and (c) HREM image of an embedded CNT in the Al matrix (the black arrow indicates bent walls of the CNT) [108].

1.3.1.4 Spray drying

In spray drying, the ingredients are fully mixed with a liquid forming slurry, and then atomized and dried by hot gas, obtaining homogeneous composite powders with a near-spherical shape. Bakshi et al. [111] applied this method to ensure a good dispersion of CNTs in a micron-sized gas-atomized Al-Si eutectic powder as shown in Figure 1-14. The spray-dried powder forms as a result of the evaporation of water from the atomized droplet. Therefore, the CNTs which are dispersed in the slurry appear relatively uniformly distributed on the Al-Si particle surface. The spray-dried agglomerates contain a significant amount of porosity since they are formed by packing of rigid spheres. Coatings up to 500 μm thick were successfully sprayed onto Al alloy substrate with overall nominal CNT compositions of 0.5 and 1 wt.%. CNTs are successfully retained and located both between the splat interfaces and also embedded in the matrix. However, CNTs are shortened in length due to fracture that occurs due to impact and shearing between Al-Si eutectic particles and the Al matrix. However, this method is not widely used to prepare composite powder for CS due to its low production efficiency and high cost.

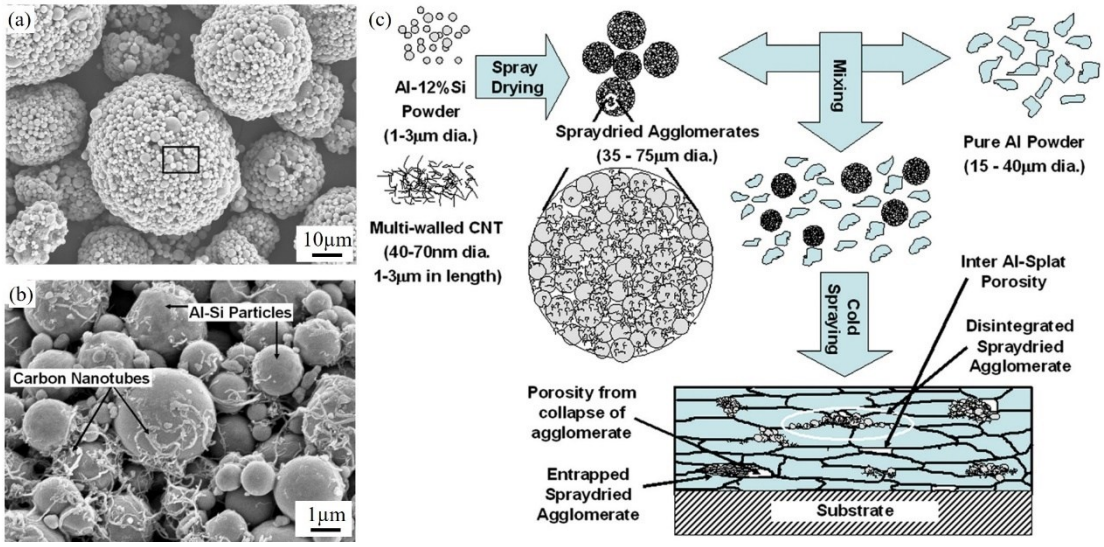

Figure 1-14 SEM micrograph showing a) spray-dried Al-Si agglomerate and b) magnified region within the rectangle in a) showing CNTs within the agglomerate; (c) Schematic of the steps involved in the fabrication of the composite coating [111].

Table 1-3 Summary of the CS-processed AMCs using mixed/blended composite powders.

Composites	Main processing parameters	Substrate material	Ceramic particle size	Ceramic particle content in powders, vol.%	Ceramic particle content in coatings, vol.%	Composite coating hardness, HV	Adhesion strength (MPa)	Reference
SiC/Al12Si	He, P_g=3.0 MPa T_g=500 ℃	Al6061-T6	5-45	0	0	110 ± 25 ($HV_{0.3}$)	21.7 ± 3.8	[112] [85]
				20.0	10.0	145 ± 14	20.9 ± 4.3	
				30.0	14.0	163 ± 16	--	
				40.0	17.0	175 ± 19	16.7 ± 3.6	
				60.0	20.0	205 ± 25	--	
Al_2O_3/Al	N_2, P_g=0.62 MPa T_g=500 ℃	7075Al	25.5	0	0	52 ± 2 ($HV_{0.3}$)	40 ± 5	[86] [113]
				7.1	7.2	60 ± 2.3	53 ± 4	
				24.1	11.7	62 ± 2.3	60 ± 1	
				40.6	16.5	75 ± 4.5	>60	
				67.2	19.2	94 ± 10.2	>60	
Al_2O_3/6061Al	He, P_g =0.62 MPa T_g=125 ℃	Cast AZ91E alloy	20	0	0	112 ± 10 ($HV_{0.2}$)	36.2 ± 2.9	[87]
				25	11	160 ± 10	40.4 ± 3.1	
				50	19	168 ± 15	--	
				75	29	190 ± 20	42.0 ± 0.2	
α-Al_2O_3/Al	Compressed air P_g=1.6 MPa T_g=230 ℃	AZ91 Mg alloy	1-30	0	0	53 ± 3 ($HV_{0.025}$)	18	[114]
				18.6	15.1	65 ± 5	25	
				40.6	29.3	--	32	
TiN/5356Al	Compressed air P_g=2.7 MPa T_g=510 ℃	Pure Al	10-45	0	0	53 ± 2 ($HV_{0.2}$)	32 ± 4	[88]
				13.9	17	146 ± 10	--	
				32.7	26	175 ± 10	>50	
				59.3	60	245 ± 25	--	
TiN/2319	Compressed air, P_g=2.6 MPa T_g=490 ℃	Al	10-45	0	0	106 ± 7.8 ($HV_{0.2}$)	--	[115]
				32.7	38.7	154 ± 18.9	--	
Al_2O_3/Al	He, P_g=0.62 MPa T_g=200 ℃	AZ91 Mg alloy	25	0	0	0.96 GPa	--	[116]
				40.3	15	1.1	--	
SiC/5056Al	Compressed air, P_g=2.5-2.6 MPa T_g=600 ℃	Pure Al	66.9	0	0	110.4 ($HV_{0.3}$)	--	[89]
				15	21.2	135 ± 20	--	
				30	26.4	156 ± 15	--	
				45	33.6	170 ± 30	--	

				60	41.4	213.8 ± 25	--	
SiC/7075Al	He, P_g=0.98 MPa T_g=300 ℃	Al6061-T6	7	0	0	136 ± 10.5 ($HV_{0.3}$)	--	[91]
				10	8	179 ± 8	--	
				20	16	190 ± 8	--	
B_4C/7075Al			15	10	7.4	167 ± 8	--	
				20	12	178 ± 8	--	
Al_2O_3/A380	Compressed air, P_g =2.5 MPa T_g=450 ℃	AZ31	48.3	0	0	105 ± 6 ($HV_{0.3}$)		[100]
				7.4	1.2	135 ± 3	--	
				15	2.5	130 ± 5	--	
				26	4.8	136 ± 4	--	
				33	5.3	124 ± 8	--	
Al_2O_3/Al	He, P_g=0.62 MPa T_g=125 ℃	AZ91D Mg alloy	20	0	0	62.0 ± 4 ($HV_{2.5}$)	20 ± 3	[98]
				15	8.9	76 ± 2	28 ± 6	
				25	13.9	74 ± 2	39 ± 6	
				35	19.8	83 ± 3	38 ± 7	
				50	26.4	88 ± 4	43 ± 8	
				75	39.8	120 ± 6	32 ± 4	
Al_2O_3/Al	N_2, P_g=3.0 MPa T_g=400 ℃	6061Al	25.5 (angular)	0	0	43 ± 3 ($HV_{0.2}$)	--	[117]
				7.1	7.0	58 ± 5	--	
				40.6	16.1	75 ± 6	--	
			24.26 (spherical)	7.1	2.7	47 ± 5	--	
				40.6	8.5	59 ± 4	--	
Al_2O_3/Al	N_2, P_g=1.65 MPa T_g=250 ℃	6061Al	22	0	0	45.0 ± 8.9 ($HV_{0.3}$)	19 ± 2	[118]
				7	6.3	52.3 ± 1.3	30 ± 2	
				15	10.8	64.4 ± 1.6	30 ± 2	
				23	16.1	68.5 ± 2.8	32 ± 2	
				31	21.0	72.3 ± 7.1	40 ± 2	
				41	22.7	78.1 ± 5.7	43 ± 4	
				51	25.2	79.9 ± 4.3	43 ± 2	
				61	30.4	86.1 ± 8.1	62 ± 7	
				73	34.0	89.5 ± 3.9	>70	
				86	41.6	114.2 ± 12.1	>70	
SiC/Al	Compressed air, P_g =1.5 MPa T_g=300 ℃	-	11-34	0	0	50 ± 3 ($HV_{0.3}$)	--	[119]
				23	23	62 ± 4	--	
				46	47	75 ± 8	--	
				71	52	88 ± 4	--	

B_4C/Al	Compressed air, P_g =2.2 MPa T_g=300~350 ℃	Al6061-T6	5	42	23	58 ± 2.8	__	[96]

Table 1-4 Summary of the CS-processed AMCs using ball-milled composite powders.

Materials	Main processing parameters	Substrate material	Ceramic particle size	Ceramic particles content in powders, vol.%	Ceramic particles content in coatings, vol.%	Composite coating hardness	Reference
B_4C/5356Al	He, P_g =3.0 MPa T_g=500 ℃ Preheating powder (150 ℃)	Al6061-T6	3-14	0 20	0 17.5 ± 1.8	133.1 ± 6.5 ($HV_{0.3}$) 251.4 ± 7.8	[120]
Diamond/Al	N_2, P_g=1.73 MPa T_g=450 ℃	1018 steel substrate	nanosized	0 10	0 ~10	1.10 GPa 3.02	[92]
TiB_2/Al	He, P_g =2.9 MPa	Al6061	5-100 nm	20 wt.%	~20 wt.%	132 ± 22 HV	[90]
TiN/Al5356	Compressed air, P_g=2.7 MPa T_g=510 ℃	Al	-	0 60.8±7.7	0 53.2 ± 10.8	68.7 ± 11.6 $HV_{0.2}$ 250 ± 33.8	[110]
Al_2O_3/Al	He, P_g =0.78 MPa T_g=500 ℃ annealed powder (450 ℃/15min)	Mild steel	4 nm	0 5	0 5	0.96 ± 0.09 GPa 1.3 ± 0.3	[121]
MWCNT/Al	He, P_g =2.4 MPa T_g=300 ℃	Al 1050	20–50 nm	0 0.5 wt% 1.0 wt.%	0 0.5 wt.% 1.0 wt.%	58.6 $HV_{0.1}$ 131.2 172.1	[107]

P_g and T_g represent the propelling gas pressure and temperature, respectively

Table 1-5 Summary of the wear behavior of CSed AMC coatings.

Materials	Substrate material	Test method	Testing conditions	Main finding	Reference
Al_2O_3/Al	7075Al	Dry abrasive test	A load of 45 N during 10 min.	Abrasion resistance was found to be independent of the alumina mass fraction in the coatings. The poor cohesion between Al and Al_2O_3 limits improvement of the abrasion resistance of the composite coatings.	[86]
Al_2O_3/6061Al	Cast AZ91E alloy	Ball-on-disc	A load of 3 N, a linear speed of 20 cm s^{-1}; a wear length of 500 m and the counter material 6 mm ball bearing steel	Significant in reduce the wear rate of the composite coating. Increasing Al_2O_3 additions to the coating gradually changes the wear mode from adhesive to abrasive.	[87]
TiN/Al5356	Pure Al	Ball-on-disc	A load of 2 N and 0.2 m/s, sliding distance of 50 m, 6 mm diameter steel ball	Wear rates of the ball-milled composites is lower than the blend mixed composite. Third-body abrasion effect by the fine TiN particulates benefits the decrease of COF.	[88]
SiC/5056Al	Pure Al	Ball-on-disc	Loads of 2 N and 10 N, A peed of 20cm/s, sliding distance of 500 m, 6 mm diameter WC/Co ball	The SiC particle and its content in the coating obviously influence the tribological behavior of the composite coating, and ware tracks indicate that the wear mechanism is the delaminating wear.	[89]
SiC/7075Al B_4C/7075Al	6061Al-T6	Reciprocating wear test	A normal load of 1 N, sliding stroke, total sliding distance and sliding velocity were 0.002 m, 10 m and 0.002 m/s, 6 mmAl_2O_3 ball	The effect of level of the ceramic particle content on the wear performances is not that significant; B_4C reinforced composite coatings exhibited higher wear resistance when compared to SiC reinforced composite coatings.	[91]
Al_2O_3/A380	AZ31	Ball-on-disc	A load of 3 N, a speed of 180 rpm wear length was 37.7 m, 6 mm diameter Al_2O_3 ball	With increase in Al_2O_3 content in the composite coatings, the wear mechanism of the coating is changed from adhesive wear to a combination of delamination and abrasive wear.	[100]
Al_2O_3/Al	6061Al	Sliding wear tests	A normal load of 1 N, sliding speed of 3 mm/s, a track length of 10mm, α-Al_2O_3 ball of 6.35 mm diameter	The spherical Al_2O_3 morphology was associated with improved tribological behaviour compared to the angular morphology.	[117]
Al_2O_3/Al	6061Al	Sliding wear test	A load of 25 N, three different travel lengths: 25, 50, and 100 m. Al_2O_3 ball.	Coating with higher alumina content did not show an increment in wear resistance.	[118]

SiC/Al	--	Sliding wear test	Different sliding velocities (0.5m/s, 1 m/s and 2 m/s) and loads (1 kg, 5 kg, and 10 kg). sliding time was 15 min. WC-Co discs	Increasing SiC particulate volume greatly enhances the wear performance of the coatings. Further improvement in wear performance was observed by heat treating the coatings.	[119]
B_4C/5356Al	6061Al-T6	Reciprocating sliding wear test	The normal load of 16.25 N, a linear 10 mm/s velocity, sliding distance of 500 m	The presence of homogeneously distributed fine B_4C reinforcement particles within matrix could significantly improve the dry sliding wear resistance. High dry sliding wear resistance was observed when cryomilled composite material was used.	[120]
MWCNT/Al	1050Al	Pin-on-disc tests	A load of 100 N duration of 300 s. The rotating diameter of the pin was 20 mm under 100 rpm. a cylindrical bearing steel of 3 mm diameter.	The wear loss decreased, and COF decreased with an increase in the MWCNT fractions. The surface fractures of the composite coatings were reduced by strengthening or toughening of the MWCNTs by bridge or anchor effect.	[107]
TiC/6061Al	6082Al	Ball-on-flat reciprocating dry-sliding wear tests	A normal load of 5N, a linear displacement of 5mm and 1 Hz frequency for a duration of 10 min	Using a satellited feedstock is more efficient in reducing coating swear rate in comparison to coatings made using pure 6061 and blended 6061-TiC, respectively.	[105]

Table 1-6 Summary of the corrosion behavior of the CSed AMC coatings.

Materials	Main processing parameters	Substrate material	Ceramic particle size, μm	Ceramic particles content in powders,vol.%	Corrosion test conditions	Corrosion behavior	Reference
Al-αAl_2O_3	Air, P_g =1.6 MPa T_g=230 ℃	AZ91D Mg alloy	1-30	25, 50	3.5 wt.% NaCl solution	The addition of α-Al_2O_3 has no passive effect on anti-corrosion ability of the composite coatings.	[114]
Al-Al_2O_3	N_2, P_g =0.62MPa T_g=500 ℃	mild steel and Al7075	25.5	10,30,50,75	3.5 wt.% NaCl solution	Composite coatings were as efficient as pure Al coatings in providing a corrosion protection against alternated immersion in saltwater and against salt spray environment.	[86]
Al-Al_2O_3	He, P_g 0.62 MPa T_g=125 ℃	AZ91E Mg alloy	20	25,50,75	5 wt % NaCl solution	Neither the Al_2O_3 content nor a post-spray heat treatment had any significant effect on the polarization behavior of the coatings.	[87]
6061Al-Al_2O_3							
5056Al-SiC	Air, P_g =2.6 MPa T_g=600 ℃	Al	48-92.6	15,30,60	0.1M Na_2SO_4 solution	Composite coatings showed better corrosion resistance than Al 5056 coating. The volume fraction of SiC has no significant effect on the anodic polarization behavior.	[122, 123]
7075-SiC	He, P_g= 0.98 MPa Tg=300 ℃	T6 6061 Al alloy	28	20	3.5 wt.% NaCl solution	Addition of ceramic particles increased corrosion current densities when compared to that of unreinforced 7075 Al coating.	[91]
7075Al-B_4C			7				
Al-$Mg_{17}Al_{12}$	He, P_g =0.98 MPa Tg=300 ℃	AZ91D Mg alloy	48.5	50,70	3.5 wt.% NaCl solution	The anti-corrosion performance was degraded by adding the hard particles to the Al matrix.	[124]
Al-Al_2O_3/Al	N_2, P_g =2.5 MPa T_g=350 ℃	Low carbon steel	2-180 (63)	25	5 wt % NaCl solution	The reinforced coating showed a slightly higher corrosion resistance compared to the pure Al coatings.	[125]
Al-Al_2O_3	He, P_g 0.62 MPa T_g=125 ℃	AZ91 Mg alloy	20 μm	25, 50,75	3.5 wt% NaCl solution	Corrosion potentials lower than the bulk Al.	[126]

1.3.2 Composite coating microstructure

1.3.2.1 Co-deposition behavior

The co-deposition behavior during CS of the composite coating varied with the powder preparation methods. When CS deposition of the composite powders obtained from mechanical blending method, the soft metal Al phase deforms significantly, acting as matrix, while the hard ceramic phase can hardly deform but embed in the Al matrix, acting as reinforcement. One of the most dramatic changes in deposition behavior observed with the addition of ceramic particles to ductile feedstock powder is the increase in DE, as shown in Figure 1-15. The possible mechanisms for the increase in DE were summarized by R. Fernandez et al. [118]. Firstly, the hard ceramic particle acts as shot peening balls, impacting on the soft particles, increasing its plastic deformation. Consequently, DE of the softer metallic particles increases. Secondly, grit blasting effect of the impacting ceramic particles can increase roughness of the substrate or previously deposited coating surface. The formation of asperities can promote bonding more particles, increasing the DE of the mixture due to a higher probability of obtaining mechanical anchoring. Finally, the last potential mechanism suggested in the literature is referred to as the oxide cleaning effect of ceramic particles impacting the metallic particles/substrate. This explanation describes the ceramic particles deforming and removing the native oxide film of the metallic particles/substrate upon impact, exposing new fresh metal surfaces and leaving them ready for the impact of the next metallic particle for the creation of a favorable metallurgical bonding site. These three mechanisms potentially explaining the increase in DE are illustrated in Figure 1-16.

Besides, increase in DE was also obtained for the satellited 6061-TiC composite powder, which has been presented in Figure 1-10. It was suggested that the satellited particles gained 20% higher momentum than the non-satellited Al particles with the same particle size. Thus, the satellited particle that has a layer of hard particles with higher momentum has the ability to produce a higher level of plastic deformation in the coating, increasing material deposition. Figure 1-17 illustrates the proposed mechanisms for the CS deposition process using blended and satellited powders. In the case of the blended feedstock, the majority of the small TiC particles arrive separately from the Al particles and predominantly rebound from the substrate surface. Accordingly, a high proportion of ceramic which was attached to the satellited powder will be embedded in the coating, which explains the high presence of ceramic in the associated composite coating.

However, the deposition behavior of ball-milled composite powder is quite different from the blended mixture and satellited powders, where the ceramic particles are distributed on the surface of the Al matrix. In this case, the ceramic particles were primary embedded inside the composite particle, which allows to regard as an entire particle to be deposited. The reinforcement of ceramic particles, together with the work hardening effect produced from ball-milling process, can significantly increase the hardness of the particle, depending on the ceramic content and the ball milling processing parameters. The increased hardness of the composite powder leads to a lower DE because a higher critical velocity is required for deposition. Besides, the size and morphology change of the particle during ball-milling can influence the particle impact velocity which in turn can also affect the DE of the composite powder. Figure 1-18 shows the deposition behavior of the ND/Al composite powder produced by ball milling. Increasing the milling time resulted in a lower DE. This trend was more distinct in the case of ND/Al MMCs, likely due to an additional hardness increase resulting from dispersion strengthening, in addition to crystal size refinement. It should be noticed that the DE values in Figure 1-18 were obtained from the powders after annealing at 420 ℃ for 24 h in an argon atmosphere. Without annealing, DE values were significantly lower, measuring only 1.0% and 0.5% for the milled (3 h) Al and ND/Al powders. Therefore, annealing is an effective method in increasing the DE of composite powders.

Moreover, the presence of the hard phase allows the working gas to reach high temperatures without nozzle clogging or blocking, which in consequence improves the coating compactness as it increases particle deformation and bonding due to the thermal softening effect at elevated temperatures.

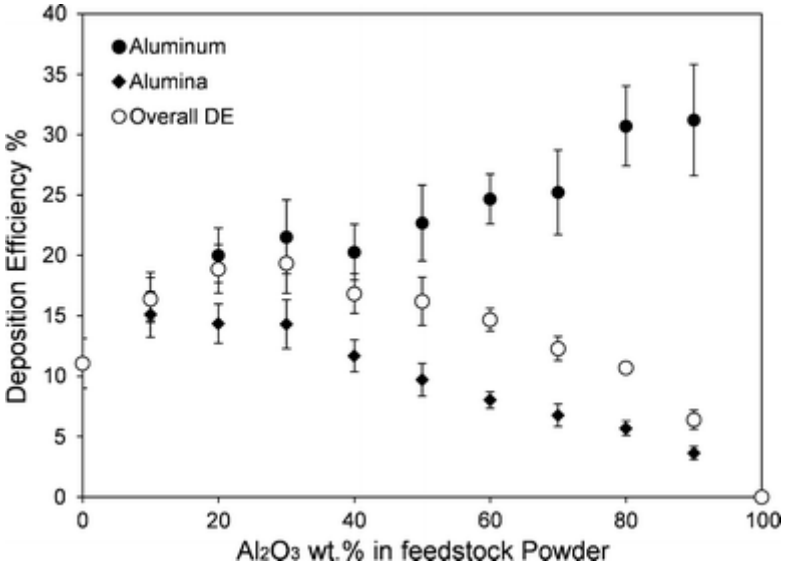

Figure 1-15 Partial deposition efficiencies evolution during the deposition of Al2O3/Al composite feedstock powders [118].

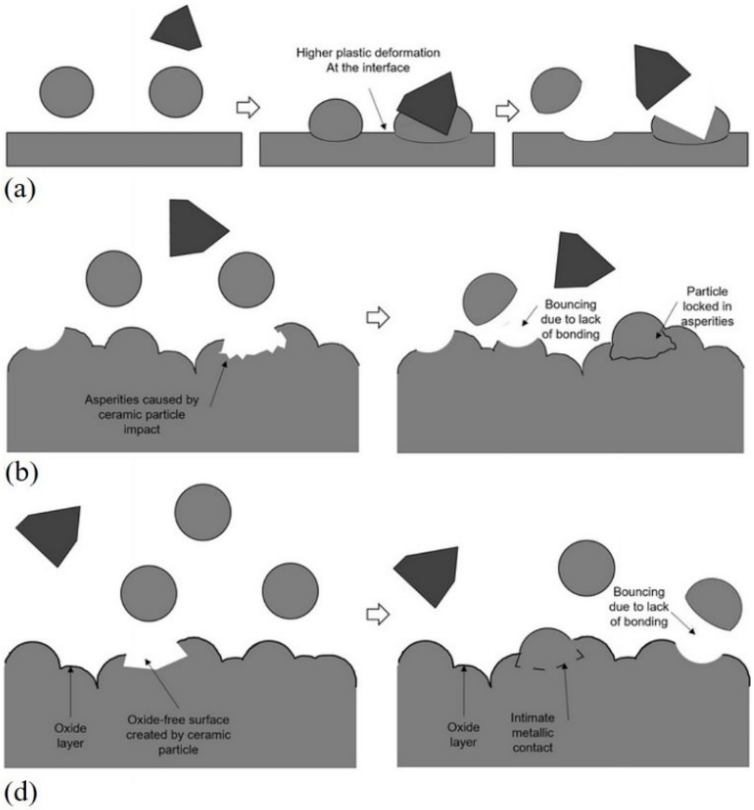

Figure 1-16 Three mechanisms proposed in the literature for the DE increase in metal-ceramic mixtures [118]: (a) metallic particles adhere due to peening of ceramic particles upon impact; (b) metallic particles adhere mechanically due to the asperities created by previous ceramic particle impacts; (c) metallic particles adhere to oxide-free surfaces cleaned by previous ceramic particle impacts. (e-f) The PEEQ evolution of Al and Al-Al2O3 impact on 6061Al substrate.

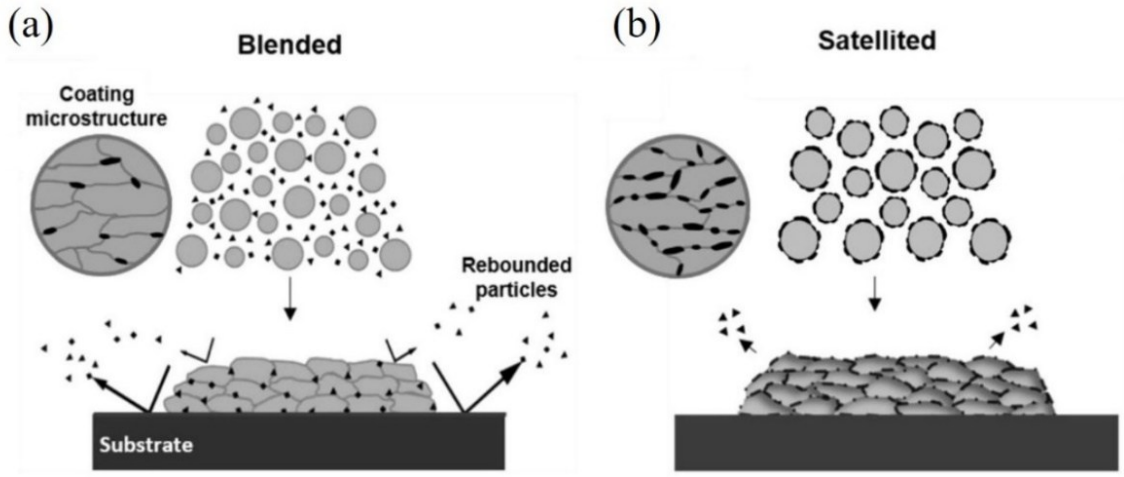

Figure 1-17 Schematic diagrams of two coating mechanisms using: (a) blended feedstock, (b) satellited feedstock [104].

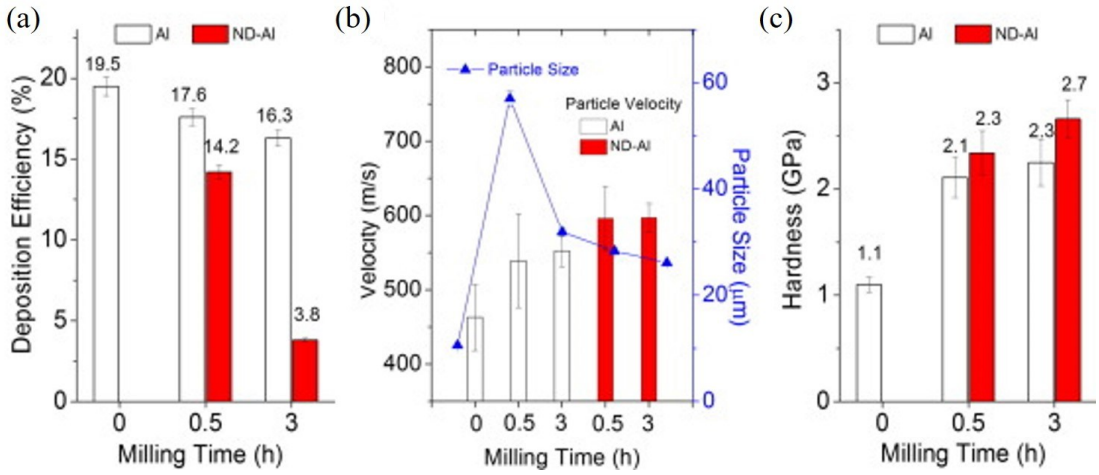

Figure 1-18 The deposition behavior of the ND/Al composite powder produced from ball milling: (a) Deposition efficiency, (b) particle velocity, and (c) hardness of Al and ND/Al composite powders as a function of milling time [92].

1.3.2.2 Volume fraction of reinforcement

Figure 1-19 summarizes the contents of ceramics in the mechanically blended feedstocks and their volume fractions in the final coatings. It clearly shows that the content of ceramics in the composite is generally lower than that in the feedstock because of their relatively different DEs. The slopes of four dotted lines in Figure 1-19 are 1, 0.7, 0.5 and 0.3, which correspond to the percentages of ceramics in the coating as well as in the feedstock of 100 %, 70 %, 50 % and 30 %, respectively. Based on these values, it can be seen that most of the composite systems have DE values of ceramic particles between 30 % and 70 %. It should be noticed that several composite systems (SiC/Al, SiC/5056Al and TiN/5356Al) possess very high retaining of ceramic particles in the coating, with DE values higher than 90%. Besides, one can notice that at a low concentration, the fraction of ceramics in the coating may be higher than that in the feedstock due to the relatively high DE of the reinforcement phase. Moreover, it can be found from Figure 1-20 that the DE depends on the size and morphology of the ceramic particles. Normally, angular shaped ceramics are more favorable for deposition into the Al matrix compared to the spherical ones. According to the study from M.Yu et al. [89], a larger SiC is beneficial for deposition and the highest DE was obtained when the ceramic particle sizes reached about 20 μm. However, further

increase the SiC particle size can hardly affect the DE anymore. Experiments clearly show that the fraction of ceramics can be controlled by adjusting feedstocks.

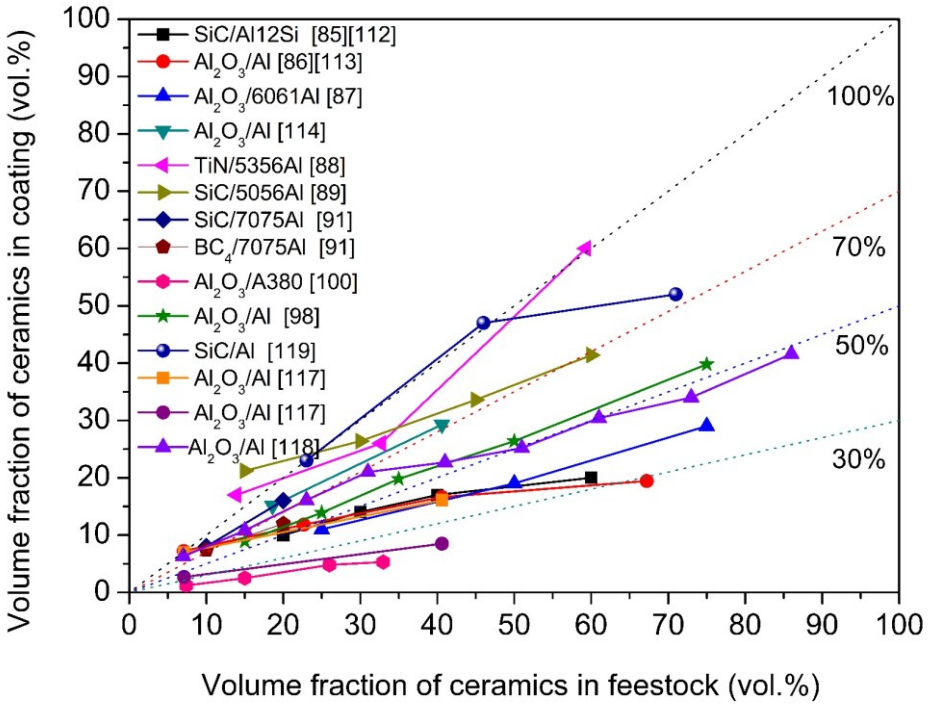

Figure 1-19 Volume fraction of ceramics in coatings compared to the source powder mixture.

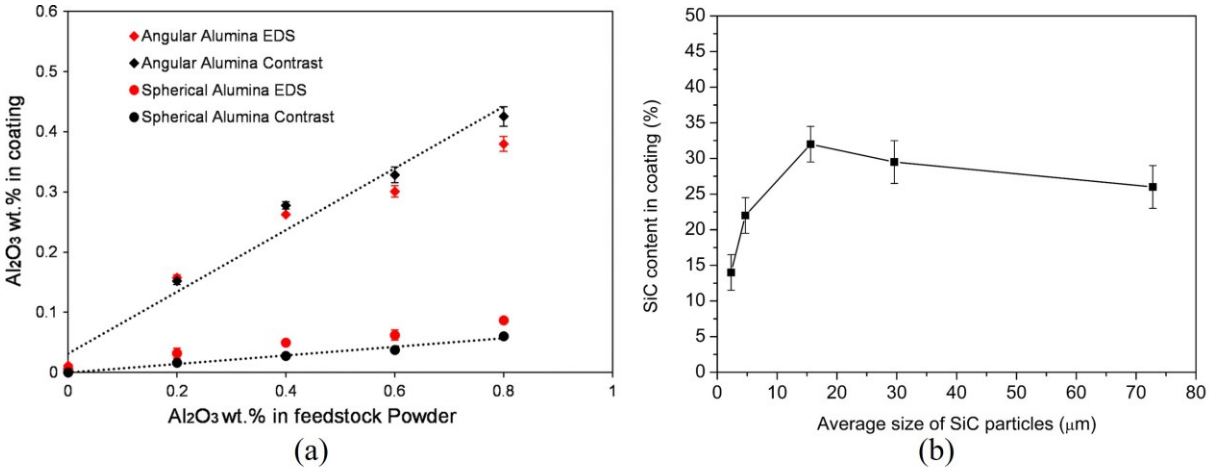

Figure 1-20 Al_2O_3 content in coatings versus feedstock powder Al_2O_3 content with different morphologies (spherical and angular) [127]. Relationship between SiC particles size and SiC content in CSed SiCp/5056Al composite coatings. The SiC contents in the feedstocks were the same (30 vol.%) [123].

1.3.2.3 Porosity evolution

Generally, the addition of ceramic in the feedstock can reduce the porosity in the coating. As shown in Figure 1-21a, a prevalent opinion indicates that the addition of hard ceramic particles increases the deformation of Al particles, so that the porosity of composite coatings becomes lower than that of Al coating due to the enhanced peening effects of ceramic particles. Besides, the different morphologies and sizes of Al matrix powders and the mixed ceramic particles also play an important role. As shown

in Figure 1-21, the porosity of the SiC/5056Al composite coating decreases slightly with the increase of ceramic particle size. According to X.Qiu et al. [100], the spherical-shaped ceramic particle is more efficient in reducing the porosity compared to the irregular shaped particle due to the enhanced in-situ peening effect. However, some researchers found out that increasing the percentage of the reinforced particles content in the feedstock powder resulted in increase in the coating porosity. Due to the presence of a large number of voids at grain boundaries, particularly between ceramic particles, microcracks within the coating and also at the interface with the substrate were observed.

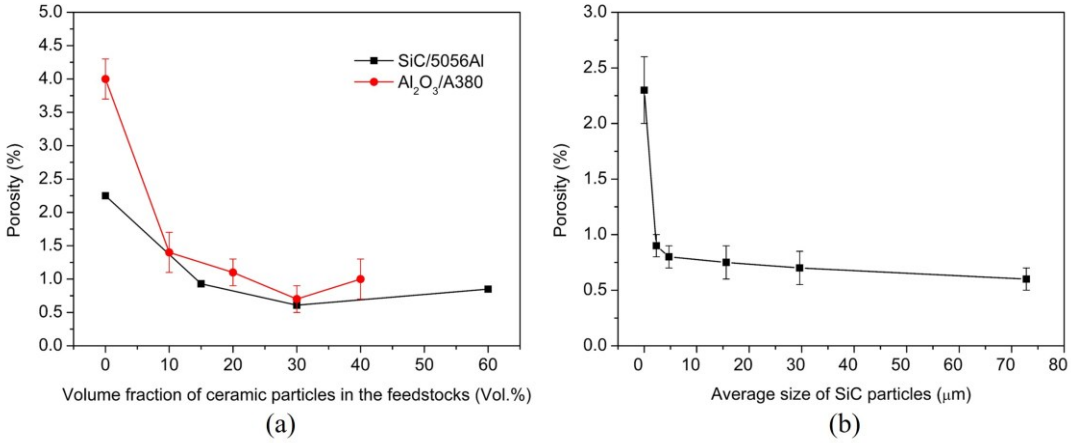

Figure 1-21 (a) Porosity evolution as a function of volume fraction of ceramic particles in the feedstocks and (b) average SiC particle size [100, 123].

1.3.2.4 Microstructure evolution

Typical cross-sections of a few CS metal-ceramic composite coatings obtained from mechanically blended powders are shown in Figure 1-22. All the coatings present a dense microstructure. The soft metals deform severely acting as matrix, while the ceramic particles remain undeformed acting as reinforcement. The ceramic particles are not uniformly distributed in the composite coatings, with most of them located at the particle-particle boundaries. Besides, some large ceramic particles were fractured into small ones during deposition. According to electron backscattered diffraction (EBSD) analysis of the composite coating, the Al particles trapped between Al_2O_3 particles underwent more severe plastic deformation due to the hammering effect [116]. Besides, bent slip bands and refined grains can be observed. Detailed TEM investigation (as shown in Figure 1-22f) shows an intimate interface (indicated by the red dash line) formed between Al and Al_2O_3 particles. At the Al side near the interface, similar to the pure Al coating, severe plastic deformation led to grain refinement, even though no trace of deformation was observed at the Al_2O_3 side.

Figure 1-23 presents some typical cross-section microstructures of the composite coatings obtained from ball-milled composite powder. The composite coatings obtained from ball-milling present a uniform nanocrystalline structure. Compared to the composite from mechanical blended powder, the ceramic particles are smaller in size after ball milling and they are much more uniformly dispersed in the Al matrix. Besides, the structure of the composite powder is well retained in the composite coating. Figure 1-24 shows the cross-sectional views of the CSed CNT/Al composite coatings. A dense structure with intimate bonding at inter-particle boundaries was obtained. Equiaxed NC grains with a mean size of 34 nm were observed, which is very similar to that of the initial composite powder. In contrast, at the interface region of the as-sprayed composited coating, elongated grains were formed along the direction of shear stress propagation. The CNTs were not agglomerated but arranged mostly parallel to each other after CS deposition.

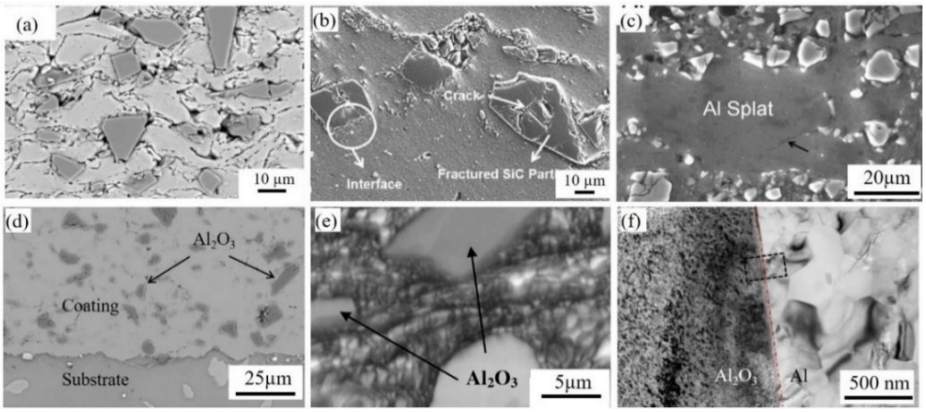

Figure 1-22 Microstructure of the as-sprayed composite coatings obtained from mechanical blending method: (a) Al_2O_3/Al coating [128]; (b) SiC/5056Al coating [122]; (c) SiC/Al coating [116] ; (d) Al_2O_3/Al coating. (e) EBSD pattern quality map on the cross-plane of Al_2O_3/Al coating. (f)TEM micrographs showing the Al/Al_2O_3 interface [116].

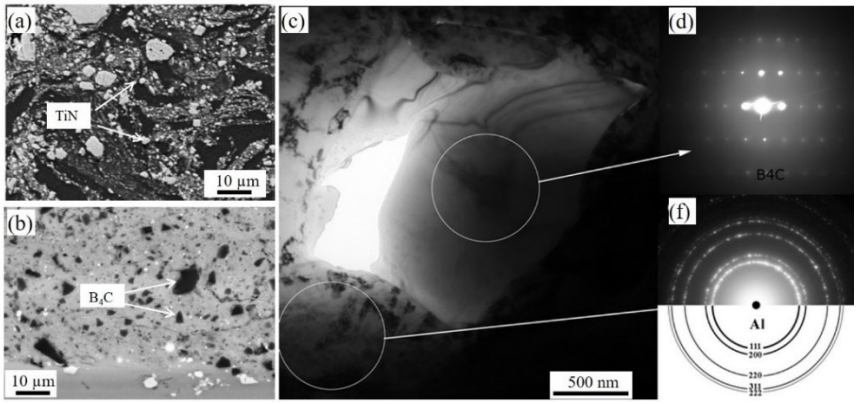

Figure 1-23 SEM cross-section image of (a) TiN//5356Al composite coating [110] and (b) B4C/5356Al composite coating [120] produced from ball-milled composite powder. (c) Bright Field TEM image of (b) showing large B4C particle within the nanostructured Al5356 matrix as confirmed by SAED patterns shown in (d) and (f) respectively [120].

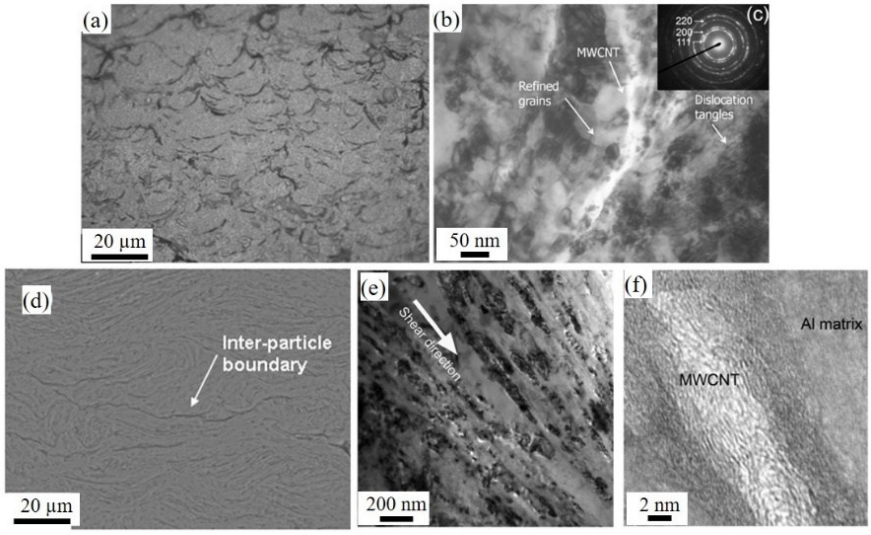

Figure 1-24 Microstructures of the as-sprayed CNT/Al composite coatings: (a) and (d) SEM micrographs CNT/Al composite coatings; (b) and (e) TEM BF image of CNT/Al composite coatings. (c) SAED pattern of Al matrix in (b). HREM image of embedded MWCNTs in the Al matrix [107, 108].

1.3.3 Composite coating or component properties

1.3.3.1 Hardness

Figure 1-25 summarizes the microhardness of the AMC coatings deposited from mechanical blended mixtures. The hardness of the Al coating can be improved through incorporating micro-sized SiC, B_4C, TiN, and Al_2O_3 hard particles. This is due to severe plastic deformation of the Al matrix and the tamping effect of hard ceramics during deposition. Besides, the ceramic particles can restrict further deformation of the soft Al matrix during the loading process. Therefore, a higher microhardness was obtained in these composite coatings. Moreover, it clearly shows that hardness of the composite increases as the volume fraction of ceramic particles in the coating increases. Even though the ceramic content is very influential on the hardness of composite coatings, it is not the only mechanism acting to strengthen it. R.Fernandez et al. [129] reported that spherical alumina showed to be harder than the ones achieved with angular Al_2O_3 even with lower ceramic content. This was attributed to high deformation of Al particles, arising from the low DE seen in coatings sprayed with spherical Al_2O_3.

Additionally, achieving the uniform distribution of reinforcements and reducing the ceramic particle size to nanoscale are also important to enhance strengthening effect. Generally, the composite coatings obtained from ball milling feedstock have higher microhardness due to the enhanced work hardening effect, grain refinement and the strengthening effect of fine particles. As reported by D.J. Woo et al. [92], significant improvement in both hardness and Young modulus was achieved by adding the homogenous nano-diamond particles in Al coating through ball-milling. It was also found that the microhardness of the CSed CNT/Al coatings was highly influenced by dispersion hardening of the CNTs. The CNTs in the coatings inhibit plastic stress flow due to their high strength, leading to active dislocation accumulation and intersection. In addition, fine subgrain formation and higher dislocation density in the coatings also contributed to the strengthening.

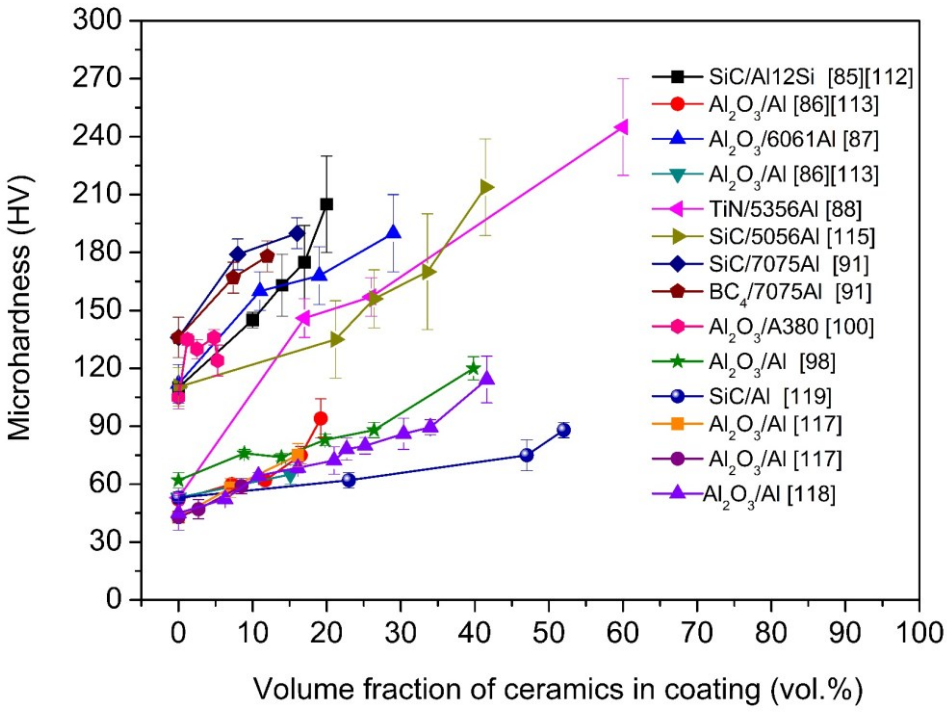

Figure 1-25 Coating microhardness as a function of ceramic content in the deposit.

1.3.3.2 Bonding strength

Variation of the coating adhesion strength as a function of the ceramic particle content in the coating is shown in Figure 1-26. In most cases, the addition of ceramic particles can increase the bonding strength of the coating, and it increases with the content of the ceramic particles in the feedstock. However, when their volume fraction reaches a high level, the bonding strength remains stable or even starts to decrease. The addition of ceramic particles has two major effects on the bonding behavior of the composite coating. On the one hand, the presence of ceramic particles results in increased plastic deformation in the Al particles on impact. This will result in stronger interfaces between the Al particles in the coating (higher cohesive strength), and between Al particles and the substrate (higher adhesive strength). On the other hand, further increase volume fractions of ceramic particles, these gains will be offset by an increased proportion of weak Al/ceramic particles and substrate/ceramic interfaces. Therefore, a maximum is expected in both the adhesive and cohesive coating strength as a function of ceramic content. Q.Wang et al. [129] studied the influence of ceramic particles on bond strength of CSed Al_2O_3/Al composite coatings on AZ91 alloy substrate by using a lug shear test. It was found that with an increase of Al_2O_3 content, a transition from an adhesive to a cohesive fracture mode occurred. Similar results were also reported in other CSed AMCs systems [89]. However, according to M. Yandouzi et al. [85], an increase of the SiC content in the Al12Si coating slightly reduced the level of adhesion of the coatings on the substrates, as marked by the black line in Figure 1-26. The authors believed that the presence of SiC particles at the interface may reduce the surface area available for the Al matrix to deform around the surface irregularities of the substrate and bond to the latter. As more SiC particles impinged on the substrate, fewer Al alloy particles came in contact with the substrate.

Besides, it was reported that the bonding strength of the composite coating is also related to the morphology of ceramic particles [100] [129]. Generally, spherical shaped ceramic particles showed more efficient in enhancing bonding strength of the coating compared to the ones sprayed with angular ceramic [129]. This is because enhanced peening effect from the spherical ceramic particle can lead to high deformation of the first layer of Al particles, resulting in swirling at the interface, strengthening the bonding between the coating and the substrate.

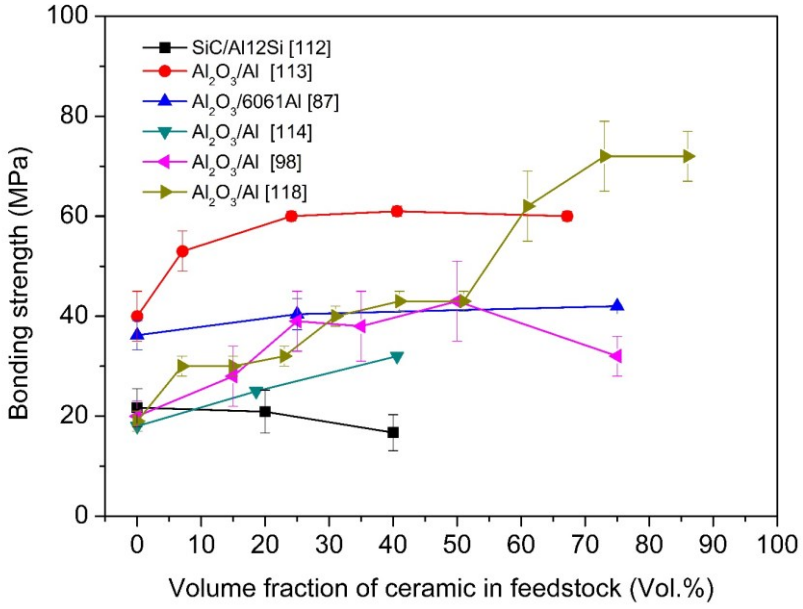

Figure 1-26 Bonding strength as a function of volume fraction of ceramics in the source powder mixture.

1.3.3.3 Wear performance

The wear performance of the CSed AMCs is summarized in Table 1-5. It can be clearly seen that the addition of ceramic particles or CNTs can significantly improve the wear performance of the Al or Al alloy coatings by lowering their coefficient of friction (COF) values and reducing wear rates as more as an order of magnitude. This is mainly due to the increased coating hardness and the effect of third-body abrasion by ceramic particles. The ceramic content in the composite coating can influence the wear behavior. Generally, increase the ceramic content in the coating can enhance the wear performance, since increasing their additions can increase the microhardness and gradually change the wear mode from adhesive to abrasive. An example indicating this evolution is shown in Figure 1-27. However, according to some other researchers, the wear resistance was found to be independent of the ceramic mass fraction in the coatings. Their explanation on this is that the poor cohesion between Al and ceramic particles limits improvement of the abrasion resistance of the composite coatings. Besides, R. J.M. Shockley et al. [130] reported that the spherical Al_2O_3 morphology was associated with improved tribological behavior compared to the angular morphology. Tribological mechanisms were investigated by them using in-situ tribometry and ex-situ analysis of worn material. It was found that forming a thin highly oxidized coherent layer comprising refined grains is of great importance to the wear resistance. The "critical" concentration of Al_2O_3 required to form this layer was strongly dependent on the morphology of Al_2O_3 particles, with less spherical Al_2O_3 being needed compared to angular [130] [102].

Moreover, using different ceramic powders or different synthesis methods can produce different reinforcing effect on the wear resistance. It was reported that the 7075Al composite coating reinforced by the B_4C powder exhibited slightly better wear property than that reinforced by the SiC powder. The B_4C particles in the coating promoted strain localization during reciprocating sliding and produced more uniform third-body microstructures than the SiC particles. According to [120], the B_4C/5356Al composite coatings produced from ball-milling show high dry sliding wear resistance compared to that from mechanical blending when the same content of reinforcements was used. Additionally, K.S.Hamdania found that using a satellited feedstock is more efficient in reducing coating swear rate in comparison to coatings made from blended TiC/6061Al [105].

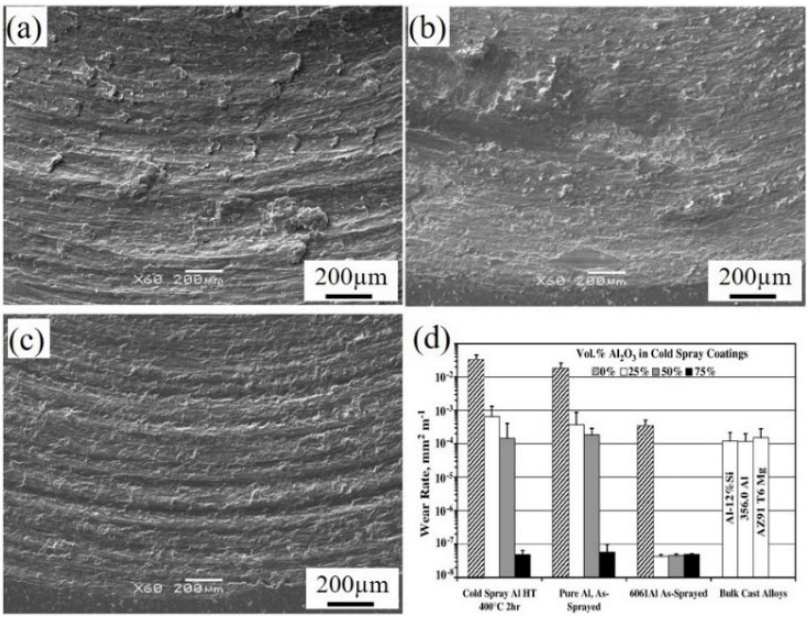

Figure 1-27 Wear tracks on CSed Al coating (b) CSed Al–50% Al_2O_3 coating and (c) CSed Al–75% Al_2O_3 coating. (d) wear rates of coatings compared to bulk alloys [130].

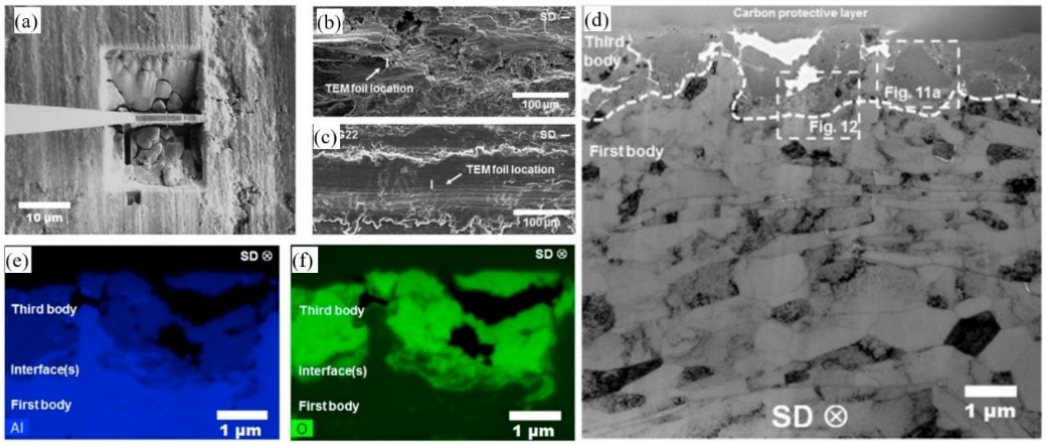

Figure 1-28 TEM investigation of the wear mechanisms of CSed Al_2O_3/Al composite coating: (a) technique of TEM foil; (b) and (c) wear track surfaces showing TEM foil locations; (d) TEM micrograph of the cross-section region near the wear track surface; (e) and (f) EDS mapping of Al Kα and O Kα intensities in the third body, the surrounding first body, and interfaces [102].

1.3.3.4 Tensile properties

Up to now, only a few studies focus on tensile properties of the CSed AMCs. This is mainly due to the fact that it's difficult to obtain high tensile performance owing to the poor interface bonding (interface between Al matrix and ceramic particles or interparticle interface) as well as some defaults within the composite coating. An example on tensile properties of CSed SiC/Al coating is shown in Figure 1-29. It clearly shows that fracture occurred at a very early stage, indicating a brittle feature of the as-sprayed composite. As shown in the fractured morphologies, the smooth cavity indicated by the arrow shows the location of SiC particulate revealing the absence of bonding between the Al splat and the SiC particulate. Therefore, post-treatment is of great necessity to improve the mechanical performance of the as-sprayed coating.

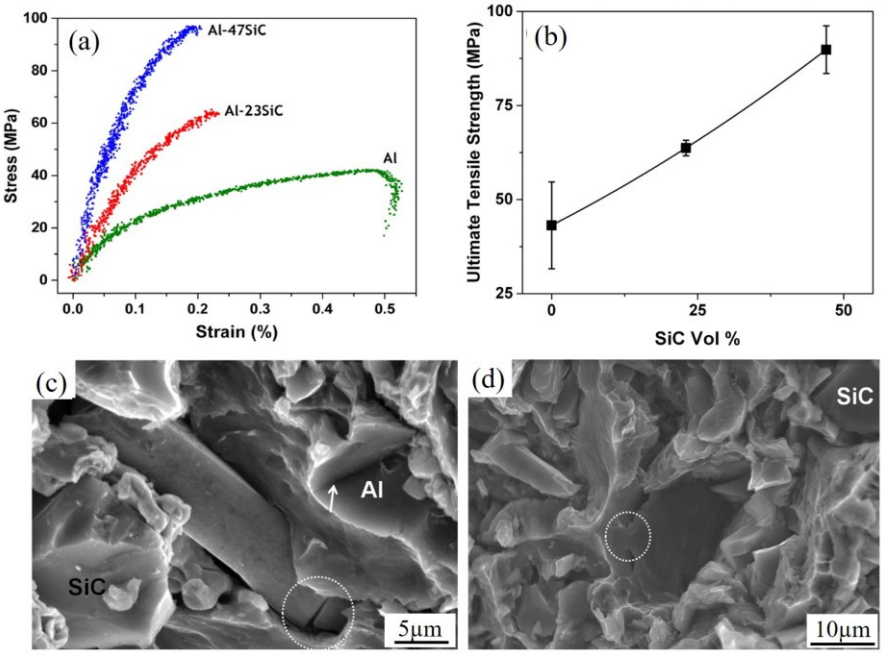

Figure 1-29 Tensile properties of the CSed SiC/Al composites:(a) stress-strain curves and (b) Ultimate tensile strength [131] as a function of SiC content; (C) and (d) are the fractured morphologies of the as-sprayed Al-47SiC composite [119].

1.3.3.5 Corrosion property

Al coatings have been a good alternative for the corrosion protection of components due to the formation of a very thin and impervious aluminum oxide layer [132]. Recently, considerable research [125, 133-137] has been conducted on coating metallic parts with Al or its alloys using CS technique and on studying associated corrosion resistance and mechanical properties. For instance, Karthikeyan et al. [132] studied the electrochemical characteristics of CSed 1100 Al onto an 1100Al substrate using pure He and a mixture of He-20 vol.% N_2 as carrier gases. They found out that the cold-sprayed coatings portrayed better corrosion resistance under electrochemical studies when compared to that of 1100 Al substrate. He (100 vol.%) processing generated higher hardness values but inferior corrosion resistance due to greater particle deformation in comparison to processing with addition of 20 vol.% N_2. It was also reported by Y.S Tao et al [134] that the CSed pure Al coating had better pitting corrosion resistance than bulk pure Al with similar purity in neutral 3.5 wt.% NaCl solution. Sieglind Ngaia et al. [137] studied the saltwater corrosion behavior of CSed 7075Al prepared by using He and N_2 as carrier gases. They found that both He and N_2 sprayed coatings exhibited lesser corrosion resistance than the AA7075-T651 substrate, while inferior corrosion resistance was found in the N_2 sprayed samples due to the limited particle deformation and a high degree of porosity. Therefore, the effects of porosity and plastic deformation on corrosion behavior of the CSed Al coatings is still unclear and needs further investigation.

Although Al-based coatings increase the corrosion resistance of metallic parts, these coatings usually do not protect adequately the coated surface from mechanical forces applied during operation due to their poor mechanical properties [91]. The addition of hard ceramic particles into Al matrix is an effective approach to improve their mechanical properties without sacrificing their corrosion resistance [138].Up to now, many efforts have been made to produce Al matrix composites using cold spray techniques. Previous studies revealed that the addition of ceramic particles into Al matrix led to denser coatings, improved hardness and bond strength without any phase transformation during spraying [126]. As summarized in Table 1, many studies reported the corrosion behavior of the CSed Al matrix composites deposited on different substrates. It can be concluded from these studies that cold spraying of composite coatings is an effective approach to protect the substrate (Mg alloys) from corrosion since the deposited coatings show better anti-corrosion resistance. However, according to previous studies, the addition of ceramic particles into Al matrix via cold spraying can lead to different corrosion behaviors. E. Irissou et al. [86] found that the Al-Al_2O_3 composite coatings proved to be as efficient as pure Al coatings in providing corrosion protection against alternated immersion in saltwater and against salt spray environment. S.Y. Tao et al. [114] reported that the addition of α-Al_2O_3 into Al matrix has no passive effect on anti-corrosion ability of the composite coatings. Similar findings were also reported by Spencer et al. [87]. However, F. S. daSilva et al. [125] reported that the Al-Al_2O_3 composite coating showed a slightly higher corrosion resistance compared to the pure Al coatings. The reason for this could be the decrease of the active area in the composite coating due to the replacing of some Al particles by Al_2O_3 particles on the electrode surface. Y.Y. Wang et al. [123] also found that Al5056-SiC composite coatings showed better corrosion resistance than Al 5056 coating, while the volume fraction of SiC has no significant effect on the anodic polarization behavior. On the other hand, according to the investigation of O. Meydanoglu et al. [91], the addition of ceramic particles increased corrosion current densities when compared to that of unreinforced 7075 Al coating. The higher corrosion current densities of the CSed composite coatings can be attributed to the presence of more active sites for corrosion as a result of higher degree of deformation in comparison with unreinforced 7075 Al coating. Furthermore, the investigation of CSed Al-$Mg_{17}Al_{12}$ composite coating indicated that the bonding among the Al splats and the $Mg_{17}Al_{12}$ particles is mechanical interlocking rather than metallurgical bonding [124]. As such, the interfaces among the particles in the composite coatings usually have a higher strain rate and could

act as a preferential reaction zone for pitting or galvanic corrosion, especially when some defects are present at the interface [136]. Therefore, the corrosion performance of CS composite coatings was found closely related to the porosity, microstructure, and interaction between matrix and reinforcing materials.

1.3.3.6 Other properties

It was found that the CSed CNT/Al composite coatings showed lower electrical resistivity than the Al coating [108]. In addition, the CSed Al coating shows an improved thermal property after the addition of Al_2O_3 particles; thus, it has a potential application in harsh serving environment. Heimann et al. [139] reported that the CSed Al2O3/Al composite coating possess low thermal conductivity, low solar absorbance, comparatively, high infrared emittance and oxidation stability, which has the potential for the outer space application. In addition, according to N.H. Tariq et al. [101], B_4C/Al composites as an effective neutron shielding material have been fabricated by CS for wet storage applications in the nuclear industry.

1.4 Post treatments on as-sprayed Al matrix composites

1.4.1 Heat treatment

Heat treatments are commonly used to relieve the strain stress and further improve the mechanical properties of the as-sprayed coatings or components. As indicated in Figure 1-30, the observation of decreased microhardness in CSed TiN/5356lAl at low annealing temperature is mainly due to the elimination of work hardening effect in the as-sprayed state. Besides, the dispersion strengthening effect of TiN particles, playing a greater role in microhardness increment, is independent of the annealing temperatures. However, as for the CNT/Al composite coating produced from ball-milled powders (Figure 1-30b), the microhardness of the composite coatings increased slightly after annealing treatment, whereas that of pure Al decreased significantly due to grain growth and a decrease in dislocation density. This is mainly due to the preservation of the nanocrystalline structure by CNTs and solid solution hardening effect of the dissociated C atoms. Besides, heat treatments have been also applied for improving the corrosion and wear performance of the CSed AMCs. The improved corrosion properties are mainly attributed to residual stress relief, the elimination of defects through recovery and recrystallization, and the reduction of voids by rearranging grains. Reported by K.S. Al-Hamdania et al. [105], the specific wear rate of the heat-treated TiC/6061Al cold-sprayed coating against a steel ball was reduced by 25% in comparison to the as-sprayed coating. This was explained by the contribution of the improved toughness and enhanced structure cohesion after heat treatment, resulting in reduced fracture during wear.

By annealing the as-fabricated pure Al deposits, both tensile strength and ductility can be largely improved, due to the mitigation of defects in the deposits. It has been found that post-heat treatment can enhance the adhesion and compactness of the coating but bonding strength between metallic particle and ceramic particle can hardly be improved with atomic diffusion during heat treatment. Therefore, it is still a challenge to achieve high tensile strength and good ductility of the CSed AMCs. As shown in Figure 1-31, even slight improvement in the tensile properties can be obtained by using a relative high annealing temperature. The fracture morphologies of heat-treated samples still show limited dimples, and the ceramic/matrix interfaces are still the weakest sites for crack or fracture initially. Moreover, heat treatment has no effect on the size and distribution of the ceramic particles in the composite coating, which is also important for strengthening mechanical properties.

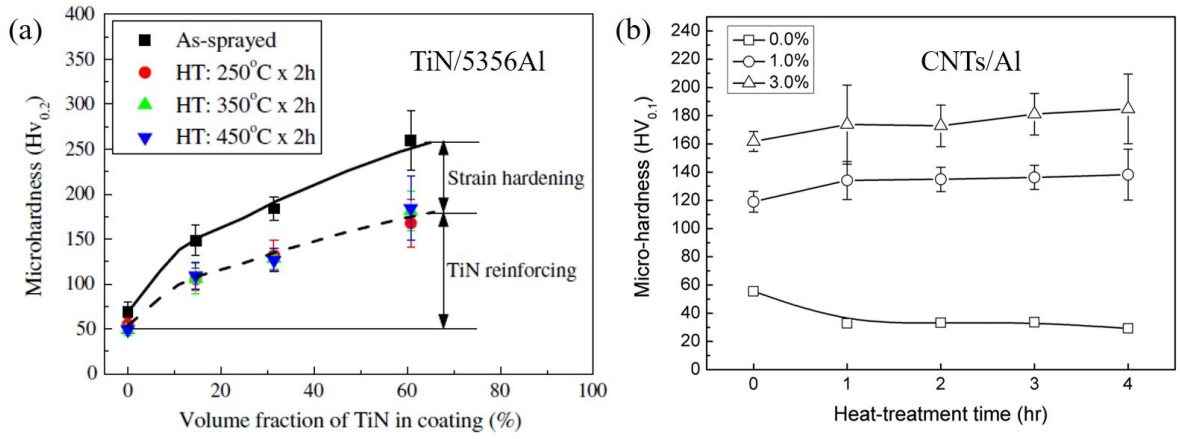

Figure 1-30 Microhardness evolution of the annealed (a) TiN/5356Al [88] and (b) CNT/Al composite coatings [108].

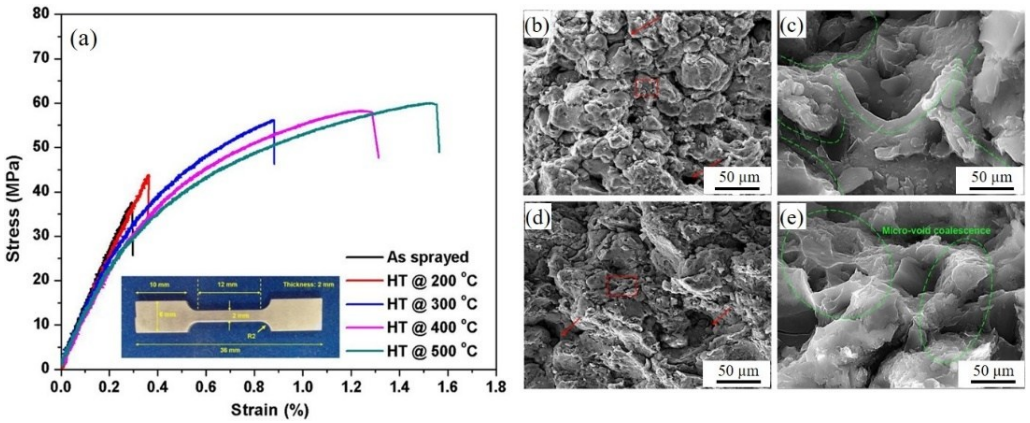

Figure 1-31 Tensile stress-strain plots of as-sprayed and heat-treated B_4C/Al composite samples. Fracture morphologies of (b and c) as-sprayed and heat-treated (500 ℃) B_4C/Al composite samples [101].

1.4.2 Friction stir processing

FSP as an effective solid-state surface modification technique has been widely applied for post-treatment of coatings or deposited materials produced with other processes such as thermal spray, electro-deposition, surface adhesive binding and CS etc. In this technique, a non-consumable rotating tool, consisting mainly of a probe and shoulder, is plunged into a metal plate and then the tool is traversed in the desired direction. During FSP, severe plastic deformation of the material can create a microstructure with fine, equiaxed grains, which is beneficial for mechanical properties. Nowadays, FSP has been employed on the CS coatings to provide the following functions (i) severe plastic deformation to promote mixing and refining of the constituent phases in the CSed bi-materials structure, (ii) elevated temperature deformation to facilitate the formation of intermetallic phases and chemical bonding at the interface, and (iii) hot consolidation to form a fully dense solid coating layer after CS. Owing to these advantages, many attempts have been made to modify CS coatings, such as Ti [140], CuZn alloy [141], 7075Al alloy [142], NiTi alloy, and MMCs [143-146].

In the recent few years, FSP has been used for CS AMCs in order to refine the distribution of reinforcement particles and to improve bonding between deposited particles. For example, Hodder et al. [147] investigated the effects of FSP on a CS deposited Al_2O_3/Al composite. It was found that re-distribution and Al_2O_3 particle size refinement during FSP improved the hardness of the composite

coatings. Huang et al. [143] investigated the effect of FSP on 5056Al reinforced with SiC particles. Moreover, Yang et al. [144] studied the effect of rotation speeds during FSP process on microstructure evolution, ceramic particle distribution, and mechanical properties of the CSed Al_2O_3/2024Al composites. It was found that a higher rotation rate can lead to more significant Al_2O_3 particle refinement and improved particle distribution. Figure 1-33 shows the microstructure of the Al_2O_3/2024Al composite coatings after FSP. It can be seen that some large Al_2O_3 particles were fractured into small ones and the particle-particle interfaces were absent. As a result, higher microhardness, wear resistance and tensile strength were acquired for the FSP processed composite samples, as shown in Figure 1-34. However, ductility didn't show too much improvement, being still much less than that prepared by other traditional processes (e.g. PM). This is mainly due to the factor that some large ceramic particles are still retained in the composite coating and interface bonding between the ceramic and Al matrix is not strong enough. Besides, this group [145] also studied the effect of FSP passes on corrosion behavior of the as-sprayed Al_2O_3/2024Al composite coating. The results demonstrated improved corrosion resistance of the Al_2O_3/2024 Al coatings for the low pass number FSP (1 and 2 passes), with the best corrosion performance occurring at 2-pass FSP. These results show that the FSP has great potential in modifying the CSed AMCs coatings and to improve both their mechanical and corrosion properties. However, more efforts are still required to further improve tensile properties through powder design and process optimization.

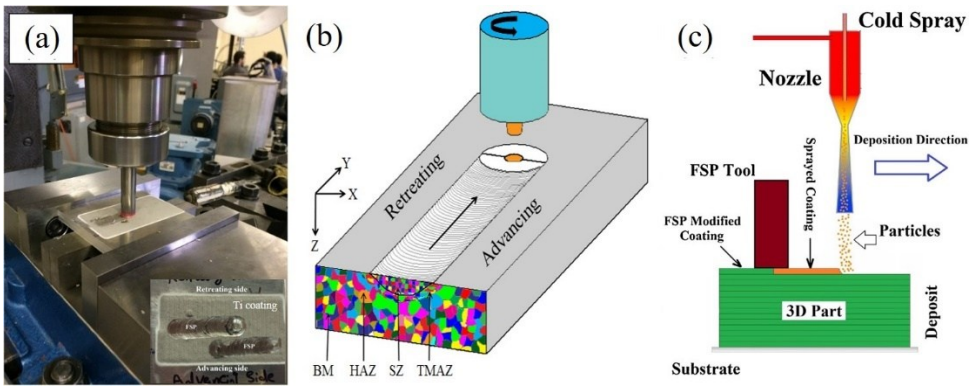

Figure 1-32 (a) Friction-stir modification of CSed titanium coating on the surface of Al substrate. (b) Schematic of FSP process; (c) Schematic representation of FSP as a modifying post-processing technique during CSAM [148].

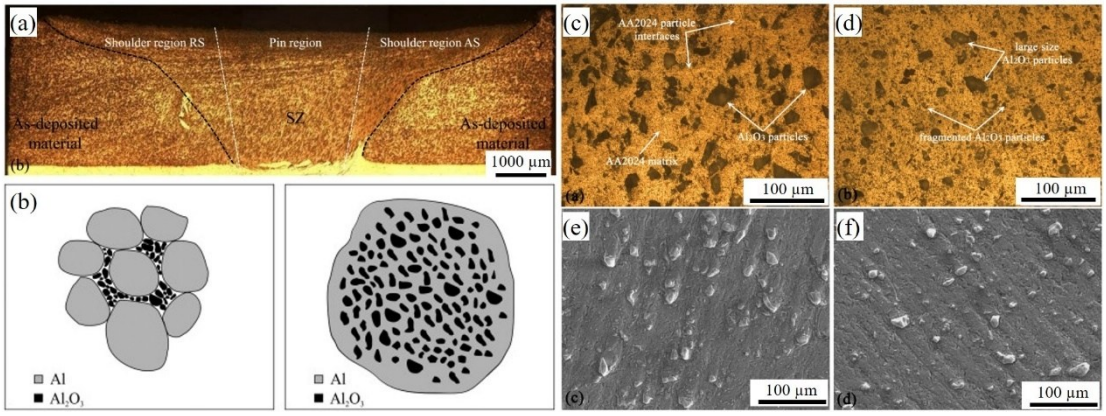

Figure 1-33 Microstructure modification for CSed AMCs coatings: (a) macroscopic cross-section of the FSPed Al_2O_3/2024Al [146]; (b) Schematic of reinforcing particle re-distribution in MMC coatings during FSP. [147]; Optical micrographs (e, d) and SEM (e, f) micrographs of CSed (c, e) and FSPed (d, f) Al_2O_3/2024Al/ [146].

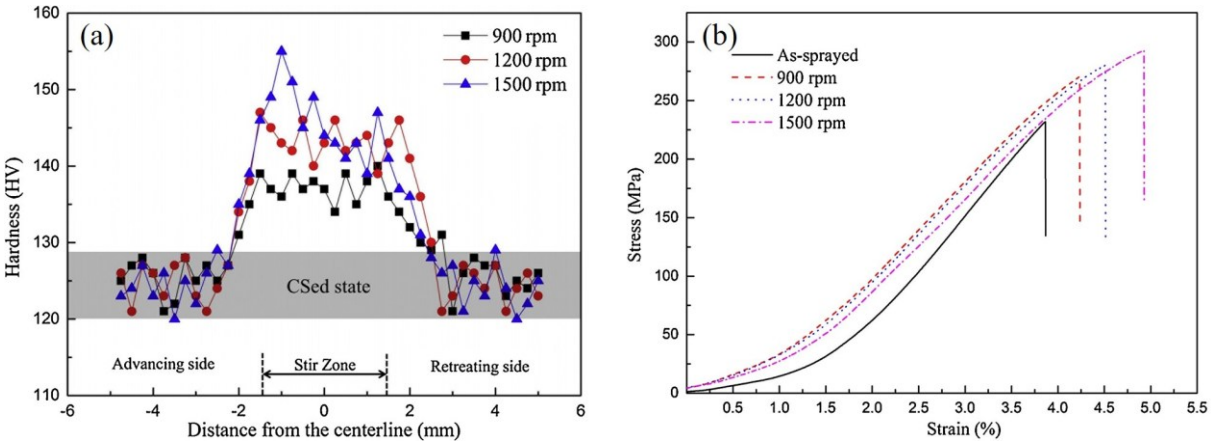

Figure 1-34 Microhardness evolution and the stress-strain curves of the FSP processed Al_2O_3/2024Al composite coatings [146].

1.5 Objectives of this study

Based on the literature investigation, using solid-state CS technique to fabricate AMCs for the applications of damage reparation and net-shape forming has become a hotspot in this field. Up to now, many efforts have been made to fabricate AMC coatings by CS. There are, however, still some challenges that need to be overcome in order to obtain high-quality AMC components. First, the CSed AMCs fabricated using mechanically blended or ball-milled composite powders generally have problems associated with uneven distribution of the reinforcement particles, poor reinforcement/matrix interfacial bonding, as well as low DE. Second, the post-treatments, including heat treatment and FSP did not show significant improvement on the tensile properties of the CSed AMCs mainly due to the fact that the above-mentioned problems such as poor interface bonding and uneven reinforced phase distribution, have not completely been resolved. Therefore, new approaches allowing for the manufacturing of advanced AMC components via CS need to be further explored.

The four objectives of this thesis are given as-follows:

i) Synthesis of nanosized in-situ TiB_2 particles or CNTs reinforced AMC powders by newly-developed methods, that allow for uniform distribution of reinforcements, strong reinforcement/matrix interfacial bonding, and good processability for CS.
ii) Optimization of CS processing parameters to obtain high-quality AMC components of several millimeters in thickness; meanwhile, the specific deposition behavior of the composite particles will be investigated by coupling experimental with numerical simulation methods.
iii) Investigation of the effects of heat treatments and FSP on microstructure evolution, corrosion and mechanical properties of the as-sprayed AMC components.
iv) Development of an understanding of the possible strengthening mechanisms involved in the as-sprayed and post-treated AMC components.

References of Chapter I

[1] Bala G Narasimha, Vamsi M Krishna, Anthony M Xavior, A review on processing of particulate metal matrix composites and its properties, International Journal of Applied Engineering Research, 8 (2013), 647-666.
[2] Kazi Md Shorowordi, Tahar Laoui, ASMA Haseeb, Jean-Pierre Celis, Ludo Froyen, Microstructure and interface characteristics of B4C, SiC and Al2O3 reinforced Al matrix composites: a comparative study, J. Mater. Process. Technol., 142 (2003), 738-743.
[3] MK Surappa, Aluminium matrix composites: Challenges and opportunities, Sadhana, 28 (2003), 319-334.
[4] Toru Kuzumaki, K Miyazawa, Hideki Ichinose, Kunio Ito, Processing of carbon nanotube reinforced aluminum composite, J. Mater. Res., 13 (1998), 2445-2449.
[5] IA Ibrahim, FA Mohamed, EJ Lavernia, Particulate reinforced metal matrix composites—a review, J. Mater. Sci., 26 (1991), 1137-1156.
[6] Riccardo Casati, Maurizio Vedani, Metal matrix composites reinforced by nano-particles—a review, Metals, 4 (2014), 65-83.
[7] S Lakshmi, L Lu, M Gupta, In situ preparation of TiB2 reinforced Al based composites, J. Mater. Process. Technol., 73 (1998), 160-166.
[8] TG Durai, Karabi Das, Siddhartha Das, Synthesis and characterization of Al matrix composites reinforced by in situ alumina particulates, Mater. Sci. Eng., A, 445 (2007), 100-105.
[9] Namrata Gangil, Arshad Noor Siddiquee, Sachin Maheshwari, Aluminium based in-situ composite fabrication through friction stir processing: A review, J. Alloys Compd., 715 (2017), 91-104.
[10] I. S. Lee, C. J. Hsu, C. F. Chen, N. J. Ho, P. W. Kao, Particle-reinforced aluminum matrix composites produced from powder mixtures via friction stir processing, Compos. Sci. Technol., 71 (2011), 693-698.
[11] A Shafiei-Zarghani, SF Kashani-Bozorg, A Zarei-Hanzaki, Microstructures and mechanical properties of Al/Al2O3 surface nano-composite layer produced by friction stir processing, Mater. Sci. Eng., A, 500 (2009), 84-91.
[12] A Dolatkhah, P Golbabaei, MK Besharati Givi, F Molaiekiya, Investigating effects of process parameters on microstructural and mechanical properties of Al5052/SiC metal matrix composite fabricated via friction stir processing, Mater. Des., 37 (2012), 458-464.
[13] WH Yu, SL Sing, CK Chua, CN Kuo, XL Tian, Particle-Reinforced metal matrix nanocomposites fabricated by selective laser melting: A state of the art review, Progress in Materials Science, (2019),
[14] Donghua Dai, Dongdong Gu, Influence of thermodynamics within molten pool on migration and distribution state of reinforcement during selective laser melting of AlN/AlSi10Mg composites, International Journal of Machine Tools and Manufacture, 100 (2016), 14-24.
[15] Quanquan Han, Rossitza Setchi, Sam L Evans, Synthesis and characterisation of advanced ball-milled Al-Al2O3 nanocomposites for selective laser melting, Powder Technology, 297 (2016), 183-192.
[16] Jiubin Jue, Dongdong Gu, Kun Chang, Donghua Dai, Microstructure evolution and mechanical properties of Al-Al2O3 composites fabricated by selective laser melting, Powder technology, 310 (2017), 80-91.
[17] L Xi, P Wang, KG Prashanth, H Li, HV Prykhodko, S Scudino, I Kaban, Effect of TiB2 particles on microstructure and crystallographic texture of Al-12Si fabricated by selective laser melting, J. Alloys Compd., 786 (2019), 551-556.
[18] P Wang, C Gammer, F Brenne, T Niendorf, J Eckert, S Scudino, A heat treatable TiB2/Al-3.5 Cu-1.5 Mg-1Si composite fabricated by selective laser melting: Microstructure, heat treatment and mechanical properties, Composites Part B, 147 (2018), 162-168.

[19] Xiao Peng Li, Gang Ji, Z Chen, Ahmed Addad, Y Wu, HW Wang, Jef Vleugels, Jan Van Humbeeck, Jean-Pierre Kruth, Selective laser melting of nano-TiB2 decorated AlSi10Mg alloy with high fracture strength and ductility, Acta Mater., 129 (2017), 183-193.
[20] B Chen, K Kondoh, H Imai, J Umeda, M Takahashi, Simultaneously enhancing strength and ductility of carbon nanotube/aluminum composites by improving bonding conditions, Scripta Mater., 113 (2016), 158-162.
[21] Toru Noguchi, Akira Magario, Shigeru Fukazawa, Shuichi Shimizu, Junichi Beppu, Masayuki Seki, Carbon nanotube/aluminium composites with uniform dispersion, Mater. Trans., 45 (2004), 602-604.
[22] Hansang Kwon, Mehdi Estili, Kenta Takagi, Takamichi Miyazaki, Akira Kawasaki, Combination of hot extrusion and spark plasma sintering for producing carbon nanotube reinforced aluminum matrix composites, Carbon, 47 (2009), 570-577.
[23] A Esawi, K Morsi, Dispersion of carbon nanotubes (CNTs) in aluminum powder, Composites Part A, 38 (2007), 646-650.
[24] Amal MK Esawi, K Morsi, A Sayed, A Abdel Gawad, P Borah, Fabrication and properties of dispersed carbon nanotube–aluminum composites, Mater. Sci. Eng., A, 508 (2009), 167-173.
[25] Chunnian He, Naiqin Zhao, Chunsheng Shi, Xiwen Du, Jiajun Li, Haipeng Li, Qingran Cui, An approach to obtaining homogeneously dispersed carbon nanotubes in Al Powders for preparing reinforced Al‐matrix composites, Adv. Mater., 19 (2007), 1128-1132.
[26] Lin Jiang, Zhiqiang Li, Genlian Fan, Linlin Cao, Di Zhang, The use of flake powder metallurgy to produce carbon nanotube (CNT)/aluminum composites with a homogenous CNT distribution, Carbon, 50 (2012), 1993-1998.
[27] Zan Li, Qiang Guo, Zhiqiang Li, Genlian Fan, Ding-Bang Xiong, Yishi Su, Jie Zhang, Di Zhang, Enhanced mechanical properties of graphene (reduced graphene oxide)/aluminum composites with a bioinspired nanolaminated structure, Nano Lett., 15 (2015), 8077-8083.
[28] Biao Chen, Shufeng Li, Hisashi Imai, Lei Jia, Junko Umeda, Makoto Takahashi, Katsuyoshi Kondoh, An approach for homogeneous carbon nanotube dispersion in Al matrix composites, Mater. Des., 72 (2015), 1-8.
[29] SR Bakshi, D Lahiri, Arvind Agarwal, Carbon nanotube reinforced metal matrix composites-a review, Int. Mater. Rev., 55 (2010), 41-64.
[30] Run Xu, Zhanqiu Tan, Dingbang Xiong, Genlian Fan, Qiang Guo, Jie Zhang, Yishi Su, Zhiqiang Li, Di Zhang, Balanced strength and ductility in CNT/Al composites achieved by flake powder metallurgy via shift-speed ball milling, Composites Part A, 96 (2017), 57-66.
[31] Hisao Uozumi, Kenta Kobayashi, Kota Nakanishi, Tadashi Matsunaga, Kenji Shinozaki, Hiroki Sakamoto, Takayuki Tsukada, Chitoshi Masuda, Makoto Yoshida, Fabrication process of carbon nanotube/light metal matrix composites by squeeze casting, Mater. Sci. Eng., A, 495 (2008), 282-287.
[32] T Laha, Y Chen, D Lahiri, Arvind Agarwal, Tensile properties of carbon nanotube reinforced aluminum nanocomposite fabricated by plasma spray forming, Composites Part A, 40 (2009), 589-594.
[33] T. Laha, A. Agarwal, Tim McKechnie, S. Seal, Synthesis and characterization of plasma spray formed carbon nanotube reinforced aluminum composite, Mater. Sci. Eng., A, 381 (2004), 249-258.
[34] H Assadi, H Kreye, F Gärtner, T Klassen, Cold spraying–A materials perspective, Acta Mater., 116 (2016), 382-407.
[35] Tobias Schmidt, Hamid Assadi, Frank Gärtner, Horst Richter, Thorsten Stoltenhoff, Heinrich Kreye, Thomas Klassen, From particle acceleration to impact and bonding in cold spraying, J. Therm. Spray Technol., 18 (2009), 794.
[36] Wenya Li, Kang Yang, Shuo Yin, Xiawei Yang, Yaxin Xu, Rocco Lupoi, Solid-state additive manufacturing and repairing by cold spraying: A review, J. Mater. Sci. Technol., 34 (2018), 440-457.

[37] Wen-Ya Li, Chao Zhang, Hanlin Liao, Jinglong Li, Christian Coddet, Characterizations of cold-sprayed Nickel–Alumina composite coating with relatively large Nickel-coated Alumina powder, Surf. Coat. Technol., 202 (2008), 4855-4860.
[38] AP Alkhimov, Sov. Phys. Dokl., 1990, pp. 1047-1049.
[39] V Champagne, D Helfritch, The unique abilities of cold spray deposition, Int. Mater. Rev., 61 (2016), 437-455.
[40] RN Raoelison, Ch Verdy, H Liao, Cold gas dynamic spray additive manufacturing today: Deposit possibilities, technological solutions and viable applications, Mater. Des., 133 (2017), 266-287.
[41] Anatolii Papyrin, Vladimir Kosarev, Sergey Klinkov, Anatolii Alkhimov, Vasily M Fomin, Cold spray technology, Elsevier, 2006.
[42] Shuo Yin, Pasquale Cavaliere, Barry Aldwell, Richard Jenkins, Hanlin Liao, Wenya Li, Rocco Lupoi, Cold spray additive manufacturing and repair: Fundamentals and applications, Addit. Manuf., 21 (2018), 628-650.
[43] RC Dykhuizen, MF Smith, Gas dynamic principles of cold spray, J. Therm. Spray Technol., 7 (1998), 205-212.
[44] DL Gilmore, RC Dykhuizen, RA Neiser, MF Smith, TJ Roemer, Particle velocity and deposition efficiency in the cold spray process, J. Therm. Spray Technol., 8 (1999), 576-582.
[45] Sunil Pathak, Gobinda Saha, Development of sustainable cold spray coatings and 3D additive manufacturing components for repair/manufacturing applications: a critical review, Coatings, 7 (2017), 122.
[46] Wenya Li, Kang Yang, Shuo Yin, Xiawei Yang, Yaxin Xu, Rocco Lupoi, Solid-state additive manufacturing and repairing by cold spraying: A review, J. Mater. Sci. Technol., (2017),
[47] Chaoyue Chen, Yingchun Xie, Shuo Yin, Marie-Pierre Planche, Sihao Deng, Rocco Lupoi, Hanlin Liao, Evaluation of the interfacial bonding between particles and substrate in angular cold spray, Mater. Lett., 173 (2016), 76-79.
[48] XL Zhou, AF Chen, JC Liu, XK Wu, JS Zhang, Preparation of metallic coatings on polymer matrix composites by cold spray, Surf. Coat. Technol., 206 (2011), 132-136.
[49] Chaoyue Chen, Xinliang Xie, Yingchun Xie, Xincheng Yan, Chunjie Huang, Sihao Deng, Zhongming Ren, Hanlin Liao, Metallization of polyether ether ketone (PEEK) by copper coating via cold spray, Surf. Coat. Technol., 342 (2018), 209-219.
[50] DM Chun, MH Kim, JC Lee, SH Ahn, TiO2 coating on metal and polymer substrates by nano-particle deposition system (NPDS), CIRP annals, 57 (2008), 551-554.
[51] Guan-Jun Yang, Chang-Jiu Li, Feng Han, Wen-Ya Li, Akira Ohmori, Low temperature deposition and characterization of TiO2 photocatalytic film through cold spray, Appl. Surf. Sci., 254 (2008), 3979-3982.
[52] Shuo Yin, Yingchun Xie, Xinkun Suo, Hanlin Liao, Xiaofang Wang, Interfacial bonding features of Ni coating on Al substrate with different surface pretreatments in cold spray, Mater. Lett., 138 (2015), 143-147.
[53] Yingchun Xie, Shuo Yin, Chaoyue Chen, Marie-Pierre Planche, Hanlin Liao, Rocco Lupoi, New insights into the coating/substrate interfacial bonding mechanism in cold spray, Scripta Mater., 125 (2016), 1-4.
[54] Chaoyue Chen, Yingchun Xie, Renzhong Huang, Sihao Deng, Zhongming Ren, Hanlin Liao, On the role of oxide film's cleaning effect into the metallurgical bonding during cold spray, Mater. Lett., 210 (2018), 199-202.
[55] Hamid Assadi, Frank Gärtner, Thorsten Stoltenhoff, Heinrich Kreye, Bonding mechanism in cold gas spraying, Acta Mater., 51 (2003), 4379-4394.
[56] Mica Grujicic, CL Zhao, WS DeRosset, D Helfritch, Adiabatic shear instability based mechanism for particles/substrate bonding in the cold-gas dynamic-spray process, Mater. Des., 25 (2004), 681-688.

[57] Wen-Ya Li, Chang-Jiu Li, Hanlin Liao, Significant influence of particle surface oxidation on deposition efficiency, interface microstructure and adhesive strength of cold-sprayed copper coatings, Appl. Surf. Sci., 256 (2010), 4953-4958.
[58] Xiao-Tao Luo, Cheng-Xin Li, Fu-Lin Shang, Guan-Jun Yang, Yu-Yue Wang, Chang-Jiu Li, High velocity impact induced microstructure evolution during deposition of cold spray coatings: a review, Surf. Coat. Technol., 254 (2014), 11-20.
[59] Atanu Chaudhuri, Y Raghupathy, Dheepa Srinivasan, Satyam Suwas, Chandan Srivastava, Microstructural evolution of cold-sprayed Inconel 625 superalloy coatings on low alloy steel substrate, Acta Mater., 129 (2017), 11-25.
[60] Tian Liu, Jeremy D Leazer, Luke N Brewer, Particle deformation and microstructure evolution during cold spray of individual Al-Cu alloy powder particles, Acta Mater., (2019), 13-23.
[61] Tobias Schmidt, Frank Gärtner, Hamid Assadi, Heinrich Kreye, Development of a generalized parameter window for cold spray deposition, Acta Mater., 54 (2006), 729-742.
[62] Dominik Hanft, Jörg Exner, Michael Schubert, Thomas Stöcker, Paul Fuierer, Ralf Moos, An overview of the aerosol deposition method: Process fundamentals and new trends in materials applications, J. Ceram. Sci. Technol, 6 (2015), 147-182.
[63] Xuemei Wang, Feng Feng, Michael A Klecka, Matthew D Mordasky, Jacquelynn K Garofano, Tahany El-Wardany, Aaron Nardi, Victor K Champagne, Characterization and modeling of the bonding process in cold spray additive manufacturing, Addit. Manuf., 8 (2015), 149-162.
[64] Peter C King, Gyuyeol Bae, Saden H Zahiri, Mahnaz Jahedi, Changhee Lee, An experimental and finite element study of cold spray copper impact onto two aluminum substrates, J. Therm. Spray Technol., 19 (2010), 620-634.
[65] T Hussain, DG McCartney, Philip H Shipway, D Zhang, Bonding mechanisms in cold spraying: the contributions of metallurgical and mechanical components, J. Therm. Spray Technol., 18 (2009), 364-379.
[66] Mica Grujicic, CL Zhao, Chenning Tong, WS DeRosset, D Helfritch, Analysis of the impact velocity of powder particles in the cold-gas dynamic-spray process, Mater. Sci. Eng., A, 368 (2004), 222-230.
[67] Mica Grujicic, John R Saylor, Donald E Beasley, WS DeRosset, D Helfritch, Computational analysis of the interfacial bonding between feed-powder particles and the substrate in the cold-gas dynamic-spray process, Appl. Surf. Sci., 219 (2003), 211-227.
[68] Mostafa Hassani-Gangaraj, David Veysset, Keith A Nelson, Christopher A Schuh, In-situ observations of single micro-particle impact bonding, Scripta Mater., 145 (2018), 9-13.
[69] Mostafa Hassani-Gangaraj, David Veysset, Victor K Champagne, Keith A Nelson, Christopher A Schuh, Adiabatic shear instability is not necessary for adhesion in cold spray, Acta Mater., 158 (2018), 430-439.
[70] Mostafa Hassani-Gangaraj, David Veysset, Victor K Champagne, Keith A Nelson, Christopher A Schuh, Response to Comment on "Adiabatic shear instability is not necessary for adhesion in cold spray", Scripta Mater., 162 (2019), 515-519.
[71] H Assadi, F Gärtner, T Klassen, H Kreye, Comment on 'Adiabatic shear instability is not necessary for adhesion in cold spray', Scripta Mater., 162 (2019), 512-514.
[72] Shuo Yin, Yingchun Xie, Jan Cizek, Emmanuel J Ekoi, Tanvir Hussain, Denis P Dowling, Rocco Lupoi, Advanced diamond-reinforced metal matrix composites via cold spray: properties and deposition mechanism, Composites Part B, 113 (2017), 44-54.
[73] Zahra Khalkhali, Wanting Xie, Victor K. Champagne, Jae-Hwang Lee, Jonathan P. Rothstein, A comparison of cold spray technique to single particle micro-ballistic impacts for the deposition of polymer particles on polymer substrates, Surf. Coat. Technol., 351 (2018), 99-107.

[74] Douglas E Wolfe, Timothy J Eden, John K Potter, Adam P Jaroh, Investigation and characterization of Cr 3 C 2-based wear-resistant coatings applied by the cold spray process, J. Therm. Spray Technol., 15 (2006), 400-412.
[75] Hanqing Che, Xin Chu, Phuong Vo, Stephen Yue, Metallization of various polymers by cold spray, J. Therm. Spray Technol., 27 (2018), 169-178.
[76] Victor K Champagne, The repair of magnesium rotorcraft components by cold spray, Journal of Failure Analysis and Prevention, 8 (2008), 164-175.
[77] CA Widener, MJ Carter, OC Ozdemir, RH Hrabe, B Hoiland, TE Stamey, VK Champagne, Timothy John Eden, Application of high-pressure cold spray for an internal bore repair of a navy valve actuator, J. Therm. Spray Technol., 25 (2016), 193-201.
[78] Paul D Eason, Jason A Fewkes, Shane C Kennett, Timothy J Eden, Karem Tello, Michael J Kaufman, Murat Tiryakioğlu, On the characterization of bulk copper produced by cold gas dynamic spray processing in as fabricated and annealed conditions, Mater. Sci. Eng., A, 528 (2011), 8174-8178.
[79] RE Blose, BH Walker, RM Walker, SH Froes, New opportunities to use cold spray process for applying additive features to titanium alloys, Metal Powder Report, 61 (2006), 30-37.
[80] Sunil Pathak, Gobinda C. Saha, Development of Sustainable Cold Spray Coatings and 3D Additive Manufacturing Components for Repair/Manufacturing Applications: A Critical Review, Coatings, 7 (2017), 122.
[81] C Howe, CSAT Workshop. Worcester, USA, 2014.
[82] C May, Proc. CSAT Conf., Worcester, MA, USA, 2013.
[83] Steven W Dean, John K Potter, Richard A Yetter, Timothy J Eden, Victor Champagne, Matthew Trexler, Energetic intermetallic materials formed by cold spray, Intermetallics, 43 (2013), 121-130.
[84] T Briefing, CSAT Workshop. Worcester, USA, 2013.
[85] M Yandouzi, P Richer, B Jodoin, SiC particulate reinforced Al–12Si alloy composite coatings produced by the pulsed gas dynamic spray process: Microstructure and properties, Surf. Coat. Technol., 203 (2009), 3260-3270.
[86] Eric Irissou, Jean-Gabriel Legoux, Bernard Arsenault, Christian Moreau, Investigation of Al-Al 2 O 3 cold spray coating formation and properties, J. Therm. Spray Technol., 16 (2007), 661-668.
[87] K Spencer, DM Fabijanic, M-X Zhang, The use of Al–Al2O3 cold spray coatings to improve the surface properties of magnesium alloys, Surf. Coat. Technol., 204 (2009), 336-344.
[88] Wen-Ya Li, Changlin Yang, Hanlin Liao, Effect of vacuum heat treatment on microstructure and microhardness of cold-sprayed TiN particle-reinforced Al alloy-based composites, Mater. Des., 32 (2011), 388-394.
[89] M Yu, XK Suo, WY Li, YY Wang, HL Liao, Microstructure, mechanical property and wear performance of cold sprayed Al5056/SiCp composite coatings: effect of reinforcement content, Appl. Surf. Sci., 289 (2014), 188-196.
[90] H Chen, Z Pala, T Hussain, DG McCartney, Fabrication and microstrain evolution of Al-TiB2 composite coating by cold spray deposition, Proceedings of the institution of mechanical engineers, Part L: Journal of Materials: Design and Applications, (2017), 1044-1052.
[91] Onur Meydanoglu, Bertrand Jodoin, E Sabri Kayali, Microstructure, mechanical properties and corrosion performance of 7075 Al matrix ceramic particle reinforced composite coatings produced by the cold gas dynamic spraying process, Surf. Coat. Technol., 235 (2013), 108-116.
[92] DJ Woo, FC Heer, LN Brewer, JP Hooper, S Osswald, Synthesis of nanodiamond-reinforced aluminum metal matrix composites using cold-spray deposition, Carbon, 86 (2015), 15-25.
[93] Wenya Li, Hamid Assadi, Frank Gaertner, Shuo Yin, A review of advanced composite and nanostructured coatings by solid-state cold spraying process, Critical Reviews in Solid State and Materials Sciences, 44 (2019), 109-156.

[94] Wenya Li, Hamid Assadi, Frank Gaertner, Shuo Yin, A review of advanced composite and nanostructured coatings by solid-state cold spraying process, Critical Reviews in Solid State and Materials Sciences, (2018), 1-48.
[95] Lawrence Gyansah, Xiang Qiu, Chunni Jia, Hasan Bin Awais, Chengwu Zheng, Hao Du, Jiqiang Wang, Tianying Xiong, Achieving strength-ductility synergy in cold spray additively manufactured Al/B4C composites through a hybrid post-deposition treatment, J. Mater. Sci. Technol., (2019), 1053-1063.
[96] NH Tariq, L Gyansah, X Qiu, H Du, JQ Wang, B Feng, DS Yan, TY Xiong, Thermo-mechanical post-treatment: A strategic approach to improve microstructure and mechanical properties of cold spray additively manufactured composites, Mater. Des., 156 (2018), 287-299.
[97] Kang Yang, Wenya Li, Chunjie Huang, Xiawei Yang, Yaxin Xu, Optimization of cold-sprayed AA2024/Al2O3 metal matrix composites via friction stir processing: Effect of rotation speeds, J. Mater. Sci. Technol., (2018), 2167-2177.
[98] Qiang Wang, Kevin Spencer, Nick Birbilis, Ming-Xing Zhang, The influence of ceramic particles on bond strength of cold spray composite coatings on AZ91 alloy substrate, Surf. Coat. Technol., 205 (2010), 50-56.
[99] Hansang Kwon, Seungchan Cho, Akira Kawasaki, Diamond-Reinforced Metal Matrix Bulk Materials Fabricated by a Low-Pressure Cold-Spray Process, Mater. Trans., 56 (2015), 108-112.
[100] Xiang Qiu, Ji-qiang Wang, Jun-rong Tang, Lawrence Gyansah, Zhi-po Zhao, Tian-ying Xiong, Microstructure, microhardness and tribological behavior of Al2O3 reinforced A380 aluminum alloy composite coatings prepared by cold spray technique, Surf. Coat. Technol., 350 (2018), 391-400.
[101] NH Tariq, L Gyansah, JQ Wang, X Qiu, B Feng, MT Siddique, TY Xiong, Cold spray additive manufacturing: A viable strategy to fabricate thick B4C/Al composite coatings for neutron shielding applications, Surf. Coat. Technol., 339 (2018), 224-236.
[102] J Michael Shockley, EF Rauch, RR Chromik, Sylvie Descartes, TEM microanalysis of interfacial structures after dry sliding of cold sprayed Al-Al2O3, Wear, 376 (2017), 1411-1417.
[103] Veronica De Simone, Diego Caccavo, Gaetano Lamberti, Matteo d'Amore, Anna Angela Barba, Wet-granulation process: Phenomenological analysis and process parameters optimization, Powder technology, 340 (2018), 411-419.
[104] KS Al-Hamdani, JW Murray, T Hussain, A Kennedy, AT Clare, Cold sprayed metal-ceramic coatings using satellited powders, Mater. Lett., 198 (2017), 184-187.
[105] Kamaal S Al-Hamdani, James W Murray, Tanvir Hussain, Adam T Clare, Heat-treatment and mechanical properties of cold-sprayed high strength Al alloys from satellited feedstocks, Surf. Coat. Technol., 374 (2019), 21-31.
[106] DJ Woo, B Sneed, F Peerally, FC Heer, LN Brewer, JP Hooper, S Osswald, Synthesis of nanodiamond-reinforced aluminum metal composite powders and coatings using high-energy ball milling and cold spray, Carbon, 63 (2013), 404-415.
[107] Kicheol Kang, Gyuyeol Bae, Juyeon Won, Changhee Lee, Mechanical property enhancement of kinetic sprayed Al coatings reinforced by multi-walled carbon nanotubes, Acta Mater., 60 (2012), 5031-5039.
[108] Kicheol Kang, Jaeick Kim, Hyungkwon Park, Changhee Lee, Formation and heat treatment of kinetic sprayed nanocrystalline al coatings reinforced with multi-walled carbon nanotubes: the relationship between microstructural features and physical properties, Surf. Coat. Technol., 289 (2016), 124-135.
[109] H Chen, Z Pala, T Hussain, DG McCartney, Fabrication and microstrain evolution of Al-TiB2 composite coating by cold spray deposition, Proceedings of the institution of mechanical engineers, Part L: Journal of Materials: Design and Applications, 233 (2019), 1044-1052.

[110] W-Y Li, G Zhang, C Zhang, O Elkedim, H Liao, C Coddet, Effect of ball milling of feedstock powder on microstructure and properties of TiN particle-reinforced Al alloy-based composites fabricated by cold spraying, J. Therm. Spray Technol., 17 (2008), 316-322.
[111] Srinivasa R Bakshi, Virendra Singh, Kantesh Balani, D Graham McCartney, Sudipta Seal, Arvind Agarwal, Carbon nanotube reinforced aluminum composite coating via cold spraying, Surf. Coat. Technol., 202 (2008), 5162-5169.
[112] E Sansoucy, P Marcoux, L Ajdelsztajn, B Jodoin, Properties of SiC-reinforced aluminum alloy coatings produced by the cold gas dynamic spraying process, Surf. Coat. Technol., 202 (2008), 3988-3996.
[113] JM Shockley, HW Strauss, RR Chromik, N Brodusch, R Gauvin, E Irissou, J-G Legoux, In situ tribometry of cold-sprayed Al-Al2O3 composite coatings, Surf. Coat. Technol., 215 (2013), 350-356.
[114] Yongshan Tao, Tianying Xiong, Chao Sun, Huazi Jin, Hao Du, Tiefan Li, Effect of α-Al2O3 on the properties of cold sprayed Al/α-Al2O3 composite coatings on AZ91D magnesium alloy, Appl. Surf. Sci., 256 (2009), 261-266.
[115] W-Y Li, G Zhang, HL Liao, C Coddet, Characterizations of cold sprayed TiN particle reinforced Al2319 composite coating, J. Mater. Process. Technol., 202 (2008), 508-513.
[116] Qiang Wang, Nick Birbilis, Han Huang, Ming-Xing Zhang, Microstructure characterization and nanomechanics of cold-sprayed pure Al and Al-Al2O3 composite coatings, Surf. Coat. Technol., 232 (2013), 216-223.
[117] JM Shockley, Sylvie Descartes, P Vo, Eric Irissou, RR Chromik, The influence of Al2O3 particle morphology on the coating formation and dry sliding wear behavior of cold sprayed Al–Al2O3 composites, Surf. Coat. Technol., 270 (2015), 324-333.
[118] Ruben Fernandez, Bertrand Jodoin, Cold spray aluminum–alumina cermet coatings: effect of alumina content, J. Therm. Spray Technol., 27 (2018), 603-623.
[119] S Kumar, Sai Kiran Reddy, Shrikant V Joshi, Microstructure and performance of cold sprayed Al-SiC composite coatings with high fraction of particulates, Surf. Coat. Technol., 318 (2017), 62-71.
[120] M Yandouzi, H Bu, M Brochu, B Jodoin, Nanostructured Al-based metal matrix composite coating production by pulsed gas dynamic spraying process, J. Therm. Spray Technol., 21 (2012), 609-619.
[121] Dominique Poirier, Jean-Gabriel Legoux, Robin AL Drew, Raynald Gauvin, Consolidation of Al 2 O 3/Al nanocomposite powder by cold spray, J. Therm. Spray Technol., 20 (2011), 275-284.
[122] Yingying Wang, Bernard Normand, Nicolas Mary, Min Yu, Hanlin Liao, Microstructure and corrosion behavior of cold sprayed SiCp/Al 5056 composite coatings, Surf. Coat. Technol., 251 (2014), 264-275.
[123] Yingying Wang, Bernard Normand, Nicolas Mary, Min Yu, Hanlin Liao, Effects of ceramic particle size on microstructure and the corrosion behavior of cold sprayed SiCp/Al 5056 composite coatings, Surf. Coat. Technol., 315 (2017), 314-325.
[124] Hengyong Bu, Mohammed Yandouzi, Chen Lu, Daniel MacDonald, Bertrand Jodoin, Cold spray blended Al+ Mg17Al12 coating for corrosion protection of AZ91D magnesium alloy, Surf. Coat. Technol., 207 (2012), 155-162.
[125] FS da Silva, J Bedoya, S Dosta, N Cinca, IG Cano, JM Guilemany, AV Benedetti, Corrosion characteristics of cold gas spray coatings of reinforced aluminum deposited onto carbon steel, Corros. Sci., 114 (2017), 57-71.
[126] Qiang Wang, Qi Sun, Ming-Xing Zhang, Wen-Juan Niu, Chang-Bin Tang, Kuai-She Wang, Xing Rui, Le Zhai, Lu Wang, The influence of cold and detonation thermal spraying processes on the microstructure and properties of Al-based composite coatings on Mg alloy, Surf. Coat. Technol., 352 (2018), 627-633.

[127] Ruben Fernandez, Bertrand Jodoin, Cold Spray Aluminum–Alumina Cermet Coatings: Effect of Alumina Morphology, J. Therm. Spray Technol., 1-19.
[128] Dalong Cong, Zhongsheng Li, Qingbing He, Hanbin Chen, Zipeng Zhao, Longping Zhang, Hulin Wu, Wear behavior of corroded Al-Al2O3 composite coatings prepared by cold spray, Surf. Coat. Technol., 326 (2017), 247-254.
[129] Ruben Fernandez, Bertrand Jodoin, Cold Spray Aluminum–Alumina Cermet Coatings: Effect of Alumina Morphology, J. Therm. Spray Technol., 28 (2019), 737-755.
[130] K. Spencer, D. M. Fabijanic, M. X. Zhang, The use of Al–Al2O3 cold spray coatings to improve the surface properties of magnesium alloys, Surf. Coat. Technol., 204 (2009), 336-344.
[131] Jean-Pierre Kruth, Ludo Froyen, Jonas Van Vaerenbergh, Peter Mercelis, Marleen Rombouts, Bert Lauwers, Selective laser melting of iron-based powder, J. Mater. Process. Technol., 149 (2004), 616-622.
[132] Kantesh Balani, T Laha, Arvind Agarwal, J Karthikeyan, N Munroe, Effect of carrier gases on microstructural and electrochemical behavior of cold-sprayed 1100 aluminum coating, Surf. Coat. Technol., 195 (2005), 272-279.
[133] Brian S DeForce, Timothy J Eden, John K Potter, Cold spray Al-5% Mg coatings for the corrosion protection of magnesium alloys, J. Therm. Spray Technol., 20 (2011), 1352-1358.
[134] Yongshan Tao, Tianying Xiong, Chao Sun, Lingyan Kong, Xinyu Cui, Tiefan Li, Guang-Ling Song, Microstructure and corrosion performance of a cold sprayed aluminium coating on AZ91D magnesium alloy, Corros. Sci., 52 (2010), 3191-3197.
[135] Mohammad Diab, Xin Pang, Hamid Jahed, The effect of pure aluminum cold spray coating on corrosion and corrosion fatigue of magnesium (3% Al-1% Zn) extrusion, Surf. Coat. Technol., 309 (2017), 423-435.
[136] Chunchun Ma, Xiaofang Liu, Chungen Zhou, Cold-sprayed Al coating for corrosion protection of sintered NdFeB, J. Therm. Spray Technol., 23 (2014), 456-462.
[137] Sieglind Ngai, Tungwai Ngai, Florian Vogel, William Story, Gregory B Thompson, Luke N Brewer, Saltwater corrosion behavior of cold sprayed AA7075 aluminum alloy coatings, Corros. Sci., 130 (2018), 231-240.
[138] HR Lashgari, AR Sufizadeh, M Emamy, The effect of strontium on the microstructure and wear properties of A356–10% B4C cast composites, Mater. Des., 31 (2010), 2187-2195.
[139] Robert B Heimann, Jacob I Kleiman, Efim Litovsky, Steffen Marx, Richard Ng, Srebri Petrov, Michael Shagalov, Rana NS Sodhi, Agnes Tang, High-pressure cold gas dynamic (CGD)-sprayed alumina-reinforced aluminum coatings for potential application as space construction material, Surf. Coat. Technol., 252 (2014), 113-119.
[140] Farzad Khodabakhshi, Bahareh Marzbanrad, Hamid Jahed, Adrian P Gerlich, Interfacial bonding mechanisms between aluminum and titanium during cold gas spraying followed by friction-stir modification, Appl. Surf. Sci., 462 (2018), 739-752.
[141] CJ Huang, XC Yan, WY Li, WB Wang, C Verdy, MP Planche, HL Liao, G Montavon, Post-spray modification of cold-sprayed Ni-Ti coatings by high-temperature vacuum annealing and friction stir processing, Appl. Surf. Sci., 451 (2018), 56-66.
[142] F Khodabakhshi, B Marzbanrad, LH Shah, H Jahed, AP Gerlich, Friction-stir processing of a cold sprayed AA7075 coating layer on the AZ31B substrate: structural homogeneity, microstructures and hardness, Surf. Coat. Technol., 331 (2017), 116-128.
[143] Chunjie Huang, Wenya Li, Zhihan Zhang, Maosen Fu, Marie-pierre Planche, Hanlin Liao, Ghislain Montavon, Modification of a cold sprayed SiCp/Al5056 composite coating by friction stir processing, Surf. Coat. Technol., 296 (2016), 69-75.

[144] Kang Yang, Wenya Li, Chunjie Huang, Xiawei Yang, Yaxin Xu, Optimization of cold-sprayed AA2024/Al2O3 metal matrix composites via friction stir processing: Effect of rotation speeds, J. Mater. Sci. Technol., 34 (2018), 2167-2177.
[145] Kang Yang, Wenya Li, Yaxin Xu, Xiawei Yang, Using friction stir processing to augment corrosion resistance of cold sprayed AA2024/Al2O3 composite coatings, J. Alloys Compd., 774 (2019), 1223-1232.
[146] Kang Yang, Wenya Li, Pengliang Niu, Xiawei Yang, Yaxin Xu, Cold sprayed AA2024/Al2O3 metal matrix composites improved by friction stir processing: Microstructure characterization, mechanical performance and strengthening mechanisms, J. Alloys Compd., 736 (2018), 115-123.
[147] KJ Hodder, H Izadi, AG McDonald, AP Gerlich, Fabrication of aluminum–alumina metal matrix composites via cold gas dynamic spraying at low pressure followed by friction stir processing, Mater. Sci. Eng., A, 556 (2012), 114-121.
[148] F Khodabakhshi, AP Gerlich, Potentials and strategies of solid-state additive friction-stir manufacturing technology: a critical review, Journal of Manufacturing Processes, 36 (2018), 77-92.

Chapter II Experimental and numerical simulation details

2.1 Materials and powder preparation process

2.1.1 CNT/Al composite powder

2.1.1.1 Composite powder fabrication process

As illustrated in Figure 2-1, two distinct approaches, namely high shear dispersion (HSD) and shift-speed ball milling (SSBM), were applied for obtaining the CNT/Al composite powders with spherical and cake-like morphologies, respectively. These two kinds of CNTs/Al composite powders were produced by our partner Dr. Zhe Chen from Shanghai Jiao Tong University.

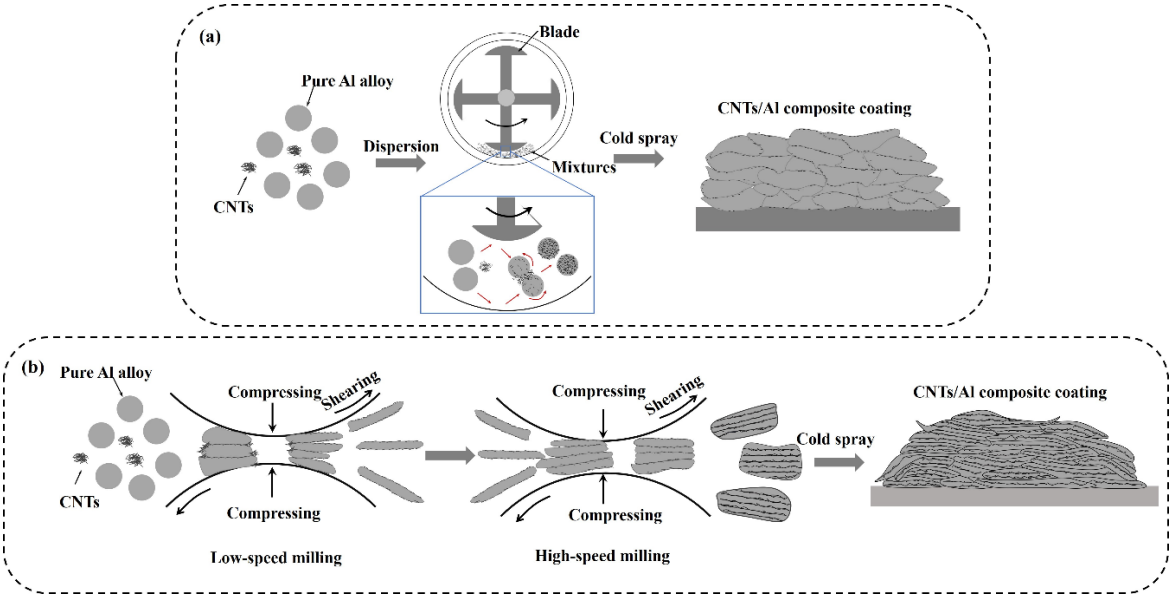

Figure 2-1 Illustration of the (a) HSD process and (b) SSBM process for fabrication of CNT/Al composite powder.

(1) HSD processing of the CNT/Al composite powder. During this process, the near-spherical Al powder (about 30 μm in diameter) and 1.5 wt.% multi-walled CNT were first blended in a mixer for 30 min at a speed of 300 rpm. According to the previous reports [1, 2], 1.5 wt.% CNT was found to be an appropriate content and exhibited reasonable enhancement efficiency, and thus in this work 1.5 wt.% CNT/Al composite was chosen as an example. The mixture was then processed in a high-speed mechanical powder processor (Nobilta, Hosokawa Micron Corporation, Japan) at a speed of 1800 rpm for 15 min. As illustrated in Figure 2-1a, the mixture was processed in a specially designed container in which a rotating four-way blade was almost touching the inner wall of the container with only a 3 mm gap. The application of controlled shear stress between the mixture of CNT and Al powders allows the uniform coating of the Al powder with CNT. More details on this process can be found in the literature [3].

(2) SSBM processing of the CNT/Al composite powder. Alternatively, the 1.5 wt.% CNT/Al powders were prepared using flake powder metallurgy combined with shift-speed ball milling (SSBM) [2]. As shown in Figure 2-1b, CNT and pure Al powders were used as the starting materials, and stearic acid (3 wt.%) was used as the process control agent. They were firstly mixed using a 3D blender, and

then the mixed powders were ball milled in a planetary ball mill at a speed of 200 rpm for 4 h with a ball-to-powder ratio of 10:1. Afterwards, the mixed powders were heat-treated at 400 ºC for 7 h to remove the stearic acid, and then milled at 270 rpm for 1 h to obtain cake-like CNT/Al powders for CS.

2.1.1.2 Powder morphology

Figure 2-2 shows the morphologies of the pure Al powder, and the 1.5 wt.% CNT/Al composite powders that were processed by the HSD and SSBM processes. As shown in Figure 2-2b, the HSD composite powder is near-spherical, which is similar to the raw pure Al powder (Figure 2-2a). As indicated by the red arrows in Figure 2-3b, the CNT clusters are de-agglomerated and are uniformly dispersed onto the surface of Al powder. The principle of dispersing CNT onto Al powder by using the HSD process is similar to the dry particle coating process [4]. First, with the collision between the Al particles and CNT clusters in the container, CNT clusters were de-agglomerated into smaller ones. Then these smaller CNTs were coated onto the surface of pure Al particles subjected to severe shear stress. Last, uniform dispersion of CNTs spread over the Al particle surface was achieved by the repeating collision between the Al particles. The comparison of the cross-sectional views of a pure Al particle (see Figure 2-2d) and a HSD composite particle (see Figure 2-2e) reveals that an equiaxed grain structure of the pure Al particle is well retained in the HSD composite particle, which suggests that the HSD process is capable of dispersing the CNTs onto the surface of Al particle without changing the initial structure of the pure Al particle.

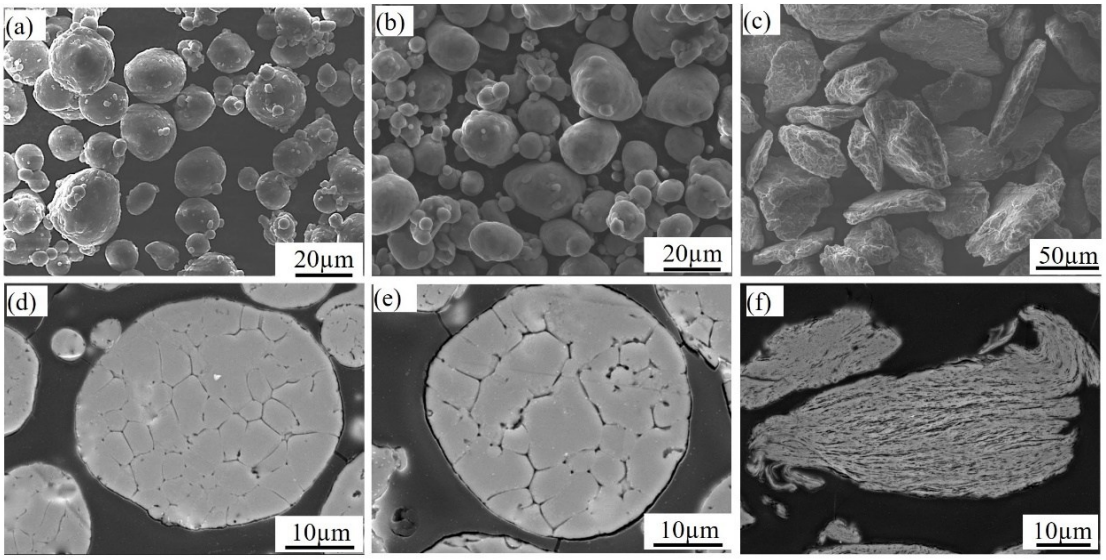

Figure 2-2 The surface morphologies and cross-sectional views of feedstock powders:(a) pure Al powder; (b) CNT/Al composite powder processed by HSD; (c) CNT/Al composite powder processed by SSBM.

Figure 2-2c shows the morphology of the 1.5 wt.% CNT/Al composite powders produced by SSBM process. Unlike the pure Al powder or HSD powder, the ball-milled composite particles exhibit a cake-like shape with sharp edges and flat surfaces. The cross-sectional view of a composite particle showed an internal lamellar structure (Figure 2-2f). The cake-like morphology and lamellar internal microstructure of the composite powder are the results of the two opposing processes-the continual fracturing and cold welding. Different from the commonly used high speed ball milling process (HSBM), an SSBM strategy i.e 4 h starting low-speed ball milling (LSBM) and 1 h following HSBM was used to fabricate the CNT/Al composite powder. As illustrated in Figure 2-1b, the LSBM/4h flattened the composite powder into nano-flakes, meanwhile CNT uniformly dispersed on their surface; then, nano-flakes could be cold-welded into lamellar structured particles during the short HSBM process. Therefore,

the coordination of CNT dispersion, integrity and interfacial bonding could be achieved by using such a special design strategy [2]. As can be seen from Figure 2-3d, CNT are uniformly dispersed onto the surface of the flaky-shaped composite particles.

Figure 2-4 shows the particle size distributions of these three different powder feedstocks measured by a laser diffraction sizer (Mastersizer 2000, Malvern Instruments Ltd., UK). It can be seen that the CNT/Al composite powder obtained by the HSD process exhibited a similar particle size distribution with pure Al powders, having an average particle size of ~25 μm. The CNT/Al composite powder obtained by the SSBM process has an average particle size of ~62 μm due to the flattening and welding effect.

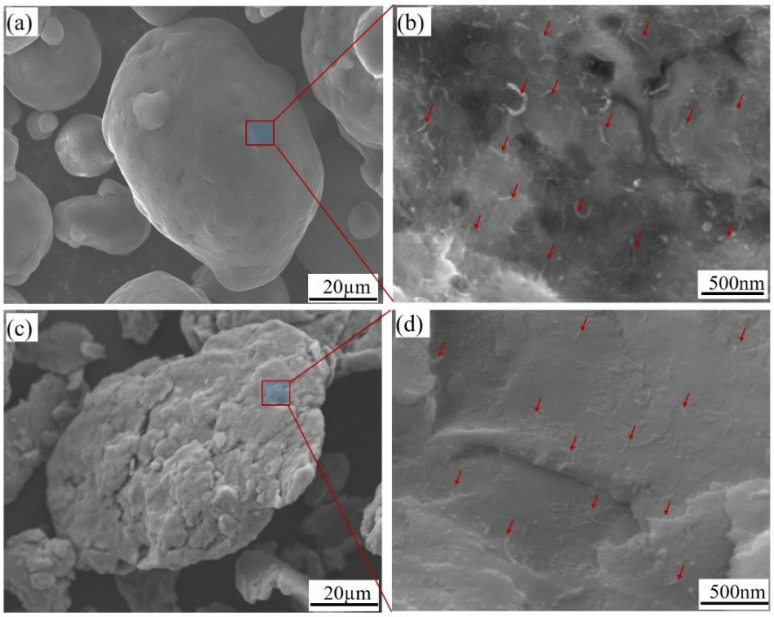

Figure 2-3 The magnified views of the morphology of particles: (a) CNT/Al composite particles processed by HSD; (b) CNT/Al composite particles processed by SSBM. The red arrows indicate the shortened CNT.

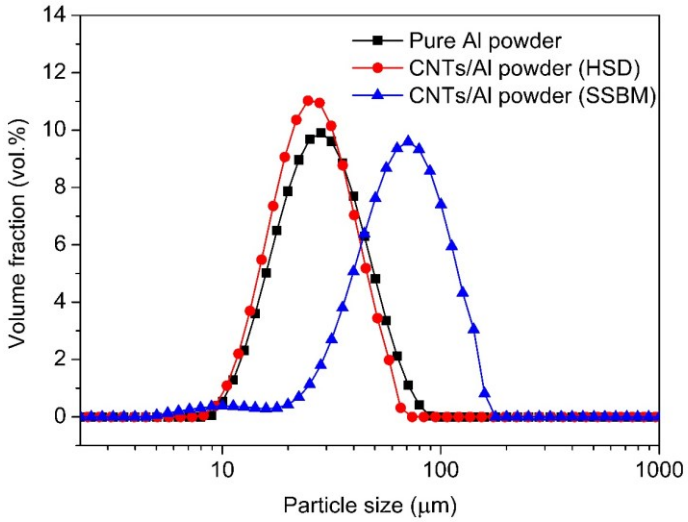

Figure 2-4 Particle size distributions of the powder feedstocks.

2.1.2 TiB_2/AlSi10Mg composite powder

2.1.2.1 Fabrication of in-situ TiB_2 reinforced AlSi10Mg powder

The TiB_2 reinforced AlSi10Mg composite powder used in this study was fabricated in two steps by our partner from Shanghai Jiao Tong University. First, TiB_2 was introduced into pure Al (99.99 %, CHALCO) in a high-purity graphite crucible in air using an electrical resistance furnace at 900 ºC via the in-situ reaction method. Reactive salts of K_2TiF_6 and KBF_4 with high purity (99.0 %, Taian Health Chemical Co., Ltd.) were slowly added into the molten Al metal during melt stirring at 600 rpm for 15 min. After slag removal, the molten composite was cast into an iron mold to obtain an in-situ TiB_2 reinforced pure Al composite master alloy. Second, Mg (99.99 %, CHALCO) and Al-Si master (99.99 %, CHALCO) alloys were subsequently added into the re-molten pre-synthesized TiB_2 reinforced Al composite master alloy and homogenized for 10 min. Then the composite powder was produced by an in-house built gas-atomizer. The chemical composition of the powder is 9.81 wt% Si, 0.32 wt% Mg, 7.0 wt% TiB_2 with Al balance, measured through inductively coupled plasma atomic emission analysis (ICP-AES). More details about the composite powder preparation process can be found elsewhere [5]. The gas-atomized pure AlSi10Mg powder produced by LERMPS was used as the feedstock for comparison.

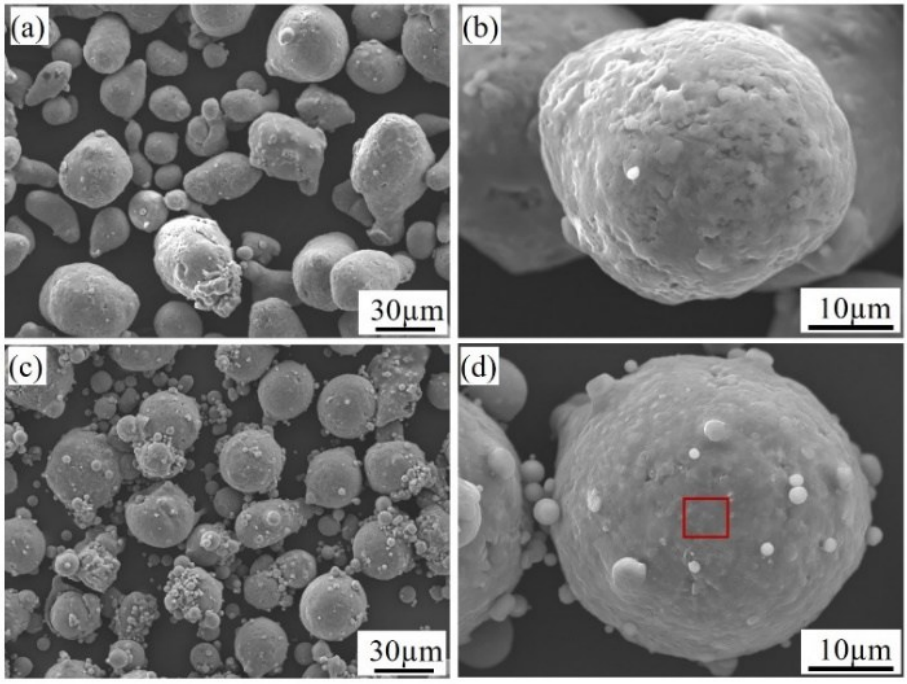

Figure 2-5 Morphologies of the gas atomized powder feedstocks in different magnifications: (a) and (b) AlSi10Mg powder; (c) and (d) TiB_2/AlSi10Mg composite powder.

2.1.2.2 Powder morphology

Figure 2-5 shows the surface morphologies of the gas-atomized pure AlSi10Mg and TiB_2/AlSi10Mg composite powders observed by scanning electron microscope (SEM). Both the pure AlSi10Mg and TiB_2/AlSi10Mg composite powders exhibit a near-spherical shape, while some micro-satellites can be observed, which may be due to smaller melt droplets sticking to the surface of large droplets during gas atomization. According to the laser diffraction sizer (Mastersizer 2000, Malvern Instruments Ltd., UK), the AlSi10Mg powder and TiB_2/AlSi10Mg composite powder possess a similar size range with average particle sizes of 45 μm and 42 μm (see Figure 2-6), respectively. Figure 2-7 shows a magnified view of the composite particle surface within the red boxed area in Figure 2-5d,

where micron-sized grain structure can be clearly observed. According to the energy-dispersive X-ray spectroscopy (EDS) mapping results shown in Figure 2-7 and Figure 2-8, precipitate eutectic Si is in a network-structure, meanwhile, a few accumulations of Mg can also be observed at the grain boundaries (GBs). The Ti element marked by blue color represents the TiB_2 particles. It can be noted that, in addition to the uniformly distributed ultrafine TiB_2 particles, some clusters on the micrometer scale (as marked by red circles) are dispersed inside the composite particle. This inhomogeneous distribution of TiB_2 particles derives from the in-situ reaction and solidification process.

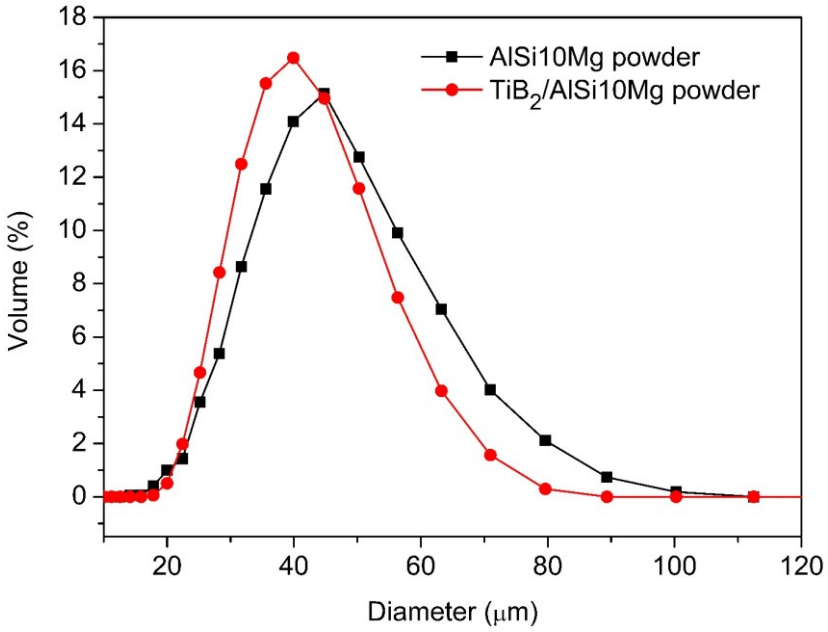

Figure 2-6 Particle size distributions of powder feedstocks.

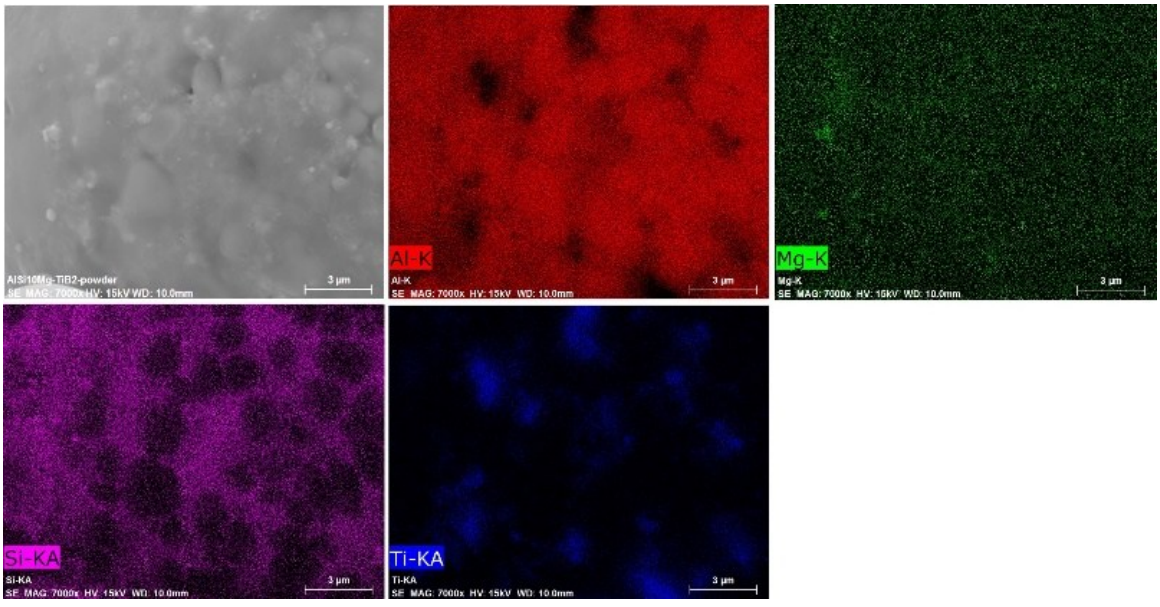

Figure 2-7 SEM image and EDS mapping of the magnified area of a composite particle in Figure 2-5d.

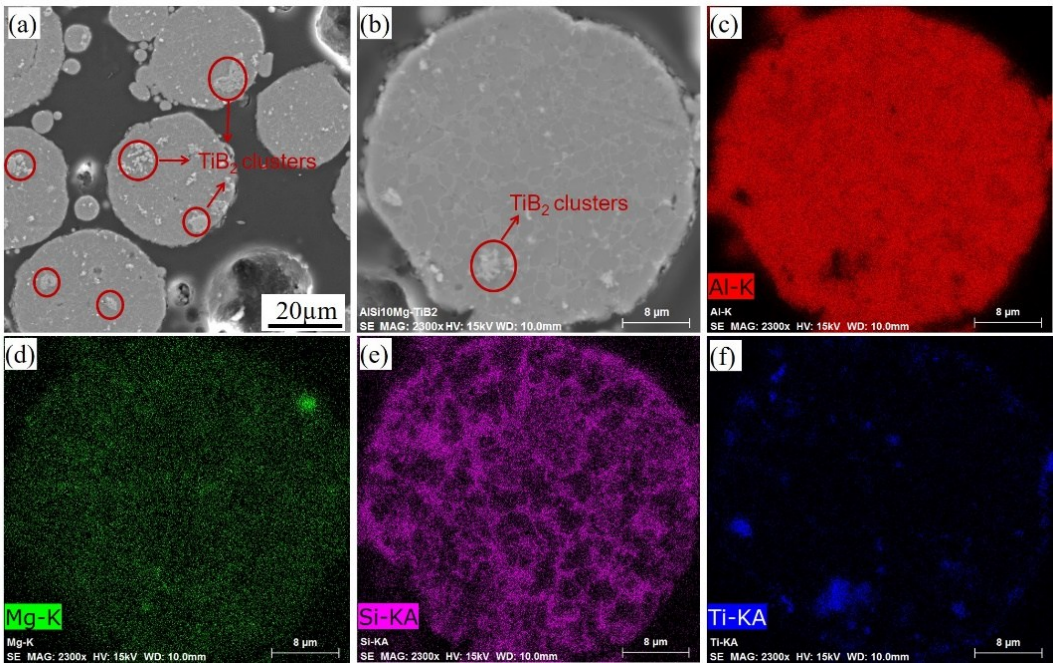

Figure 2-8 Cross-sectional microstructure in (a) low and (b) high magnifications and (c-f) the corresponding EDS mapping of a TiB_2/AlSi10Mg composite particle.

2.1.3 TiB_2/7075Al composite powder

2.1.3.1 In-situ TiB_2/7075Al composite powder fabrication

The TiB_2/7075Al composite powder used in this study was also synthesized via in-situ reaction and followed by gas-atomization process in Shanghai Jiao Tong University. Its production process is similar to that of the TiB_2/AlSi10Mg composite powder, as described in Section 2.1.2. The designed Al-Zn-Mg-Cu (8 wt.% TiB_2) composites were produced by remelting Al/TiB_2 ingots with pure Zn, Mg, and Al-Cu master alloy. Then the composite powders were produced using an in-house built atomization tower. The main chemical composition of the composite powder was 5.4 wt.% Zn, 1.5 wt.% Cu, 2.4 wt.% Mg, 0.15 wt.% Cr, 0.14 wt.% Fe, and 7.0 wt.% TiB_2 (~4.2 vol.%) with Al balance based on ICP-AES analysis. More details about the composite powder production process can be found elsewhere [5, 6]. The composite powder was sieved and the particles in the range of 20–60 μm were selected for CS deposition. The gas-atomized pure 7075Al powder (provided by LERMPS) with a similar size distribution was used as the feedstock for comparison. Table 2-1 gives the chemical composition of the pure 7075Al powder.

Table 2-1 Chemical composition of the 7075Al starting powder.

Element	Zn	Mg	Cu	Cr	Fe	Si	Mn	Ti	Al
wt.%	5.52	2.29	1.41	0.203	0.209	0.12	0.0473	0.0208	Bal.

2.1.3.2 Microstructure of the starting powders

Figure 2-9 (a, b) and (c, d) show the overview and magnified surface morphologies of the pure 7075Al and TiB_2/7075Al composite powders, respectively. Both powders display a spherical shape with some local micro-satellite structure, which may be due to smaller melt droplets sticking to the surface of large ones during gas atomization. According to the laser diffraction sizer, the 7075Al and TiB_2/7075Al composite powders possess the similar particle size ranges with the average sizes of 33

and 37 μm, respectively (Figure 2-9f). Figure 2-9e shows the magnified view of a composite particle within the red boxed area in Figure 2-9d. Clearly, ultrafine TiB_2 particles (as marked by red arrows) are uniformly distributed on the composite particle surface. Furthermore, the cross-sectional backscattered electrons (BSE/SEM) image in Figure 2-9a reveals that these ultrafine TiB_2 particles are also uniformly distributed inside the composite particle. As shown in the magnified BSE image in Figure 2-10b, the TiB_2 nanoparticles and their agglomerations (indicated by red arrows) dispersed not only inside the α - Al grains (grey) but also along the GBs. The evident atomic number contrast of these BSE images suggests a significant composition variation between the GBs and grain interior. The EDS mapping results (Figure 2-10 (c-f)) confirm some degree of solute segregation (Mg, Cu, Zn) at GBs and interdendritic regions within the initial powder. The analysis of the composite powder reveals that the TiB_2 nanoparticles reinforced composite spherical powder was successfully produced by in-situ reaction and gas atomization.

Electron backscatter diffraction (EBSD) characterization was carried out to further identify the microstructure of the gas-atomized pure 7075Al and TiB_2/7075Al composite powders. As it can be seen from Figure 2-11b, the pure 7075Al particle features a cellular-like dendritic structure, which is due to the typical rapid solidification process during gas atomization [7, 8]. In addition to some small grains, several large dendritic grains (over 7 μm in size) can be found inside the pure 7075Al particle. The grain size of pure 7075Al particle is in the range of 400 nm to 9 μm with a mean value of 4.8 μm (Figure 2-11c). Comparatively, the micron-sized equiaxed crystals with random orientations is observed in the TiB_2/7075Al composite particle (Figure 2-11d and e). Figure 2-11f shows that the grain size of the composite powder is in the range of 400 nm to 5 μm with an average size of 2.5 μm, which is much smaller than that of the pure 7075Al powder. The grain structure modification is likely caused by the influence of in-situ nano-TiB_2 particles on the solidification process, during which these TiB_2 nanoparticles serve as good nucleating agents, improving the nucleation rate of α-Al phase and refining the grains [5, 9].

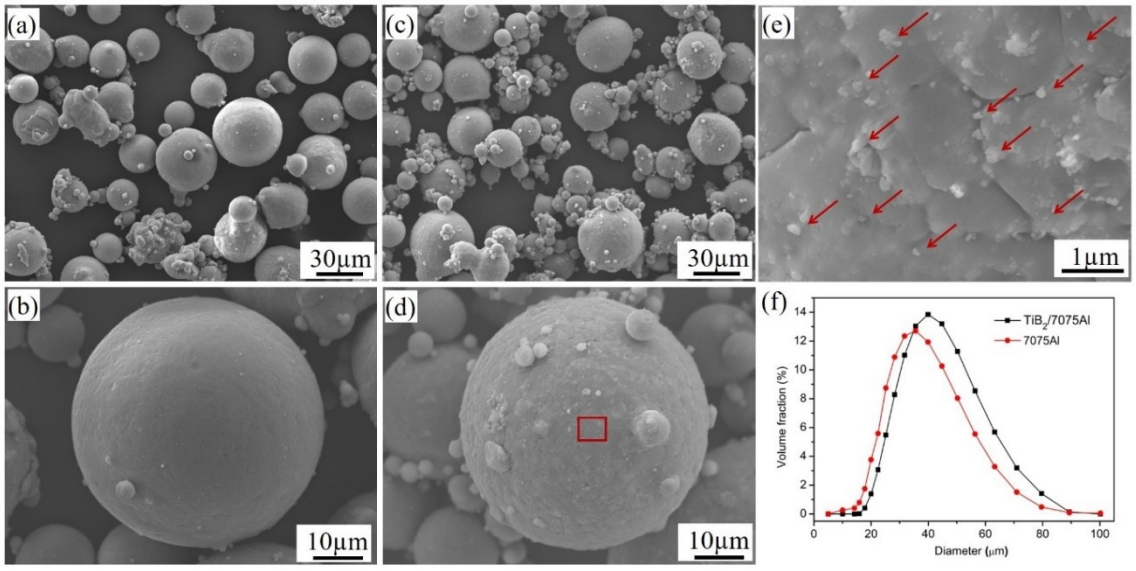

Figure 2-9 Particle morphologies of the (a, b) pure 7075Al powder and (c, d) TiB_2/7075Al composite powder in different magnifications; (e) Magnified view of the composite particle surface area marked in (d), showing uniform distribution of TiB_2 nanoparticles (indicated by red arrows) on the surface of an Al micro-particle; (f) displays the particle size distribution of the initial powder feedstocks.

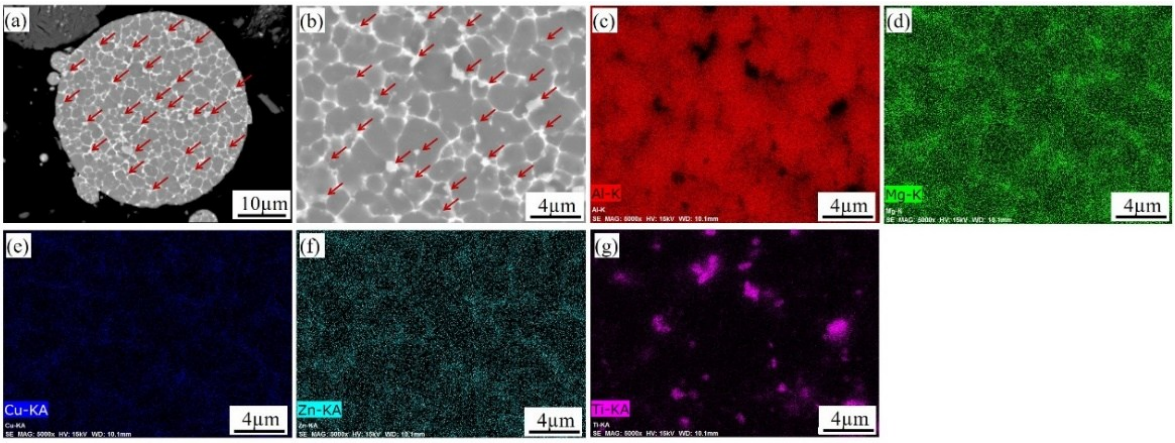

Figure 2-10 BSE/SEM micrographs of the cross-section of (a) a whole TiB_2/7075Al composite particle in the as-received condition and (b) magnified view highlighting the distribution of TiB_2 particles; corresponding EDS element distributions of (c) Al, (d) Mg, (e) Cu, (f) Zn and (g) Ti.

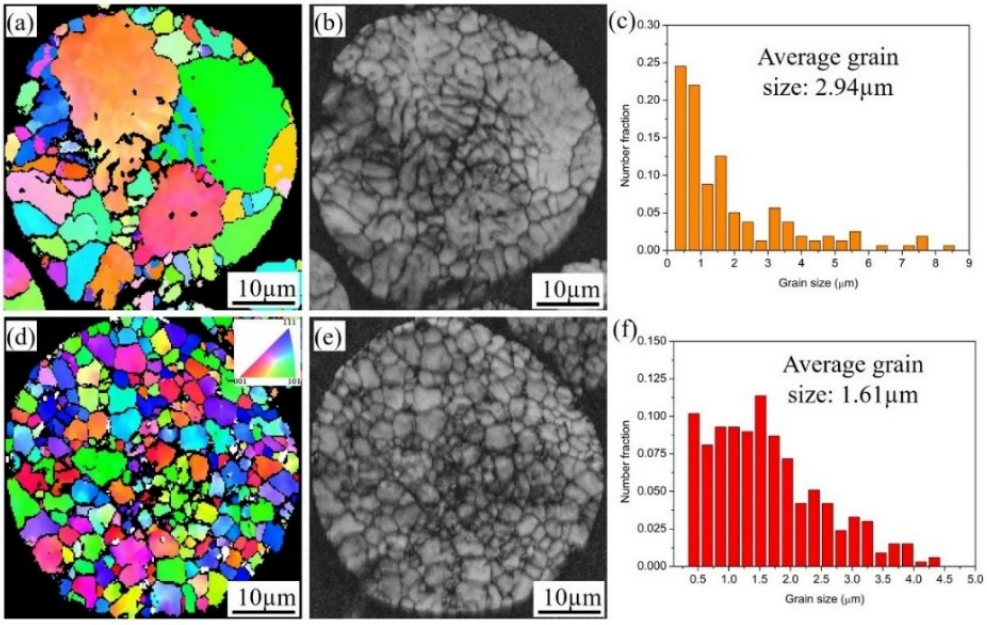

Figure 2-11 SEM/EBSD characterization of the cross-section of the gas-atomized (a-c) 7075Al particle and (d-f) TiB_2/7075Al composite particle: (a) and (d) IPF mapping images, (b) and (e) band contrast images, (c) and (f) Al grain size distributions. The image reveals the grains by cleaning up the nanoparticle TiB_2 phase.

2.2 Cold spray process

2.2.1 Cold spray systems

In this study, in order to investigate the influence of processing parameters on the deposition process, CS deposition was performed on substrates using three different CS systems. Firstly, these three kinds of composite powders were deposited by using a cold spray (CS) system (Kinetic 3000, CGT Gmbh, Germany) installed in LERMPS. The description of this CS system can be found elsewhere [10]. In this system, compressed air or N_2 is used as the principal gas, and Ar is commonly used as the carrier gas for the Al or Al alloy powder feedstocks. The propulsive gas pressure and temperature of this system are adjustable, with a maximum value of 3.2 MPa and 700 ℃, respectively. A Laval nozzle made of SiC

was employed in this CS system. The size dimensions and expansion ratio of this nozzle (named SiC-1) are given in table 2-2. In order to prevent nozzle clogging and improve the reliability of this system, the nozzle was cooled by running water, as shown in Figure 2-12a. The movement of nozzle for coating deposition was controlled by robot manipulator with a variety travel speed in the range of 5 mm to 500 mm/s.

As described in Figure 2-12b, CS deposition was also performed using a commercial Impact 5/8 system, of which compressed N_2 was used as the propellant gas and carrier gas. In this system, the powder particles are fed axially upstream of the nozzle from the back of the gun and the accelerating gas is introduced from the gas inlet into a pre-chamber. The maximum operation gas pressure and temperature of this CS system can reach 5.0 MPa and 800℃, respectively. Another SiC nozzle (named SiC-2) was installed in this CS system, and its size dimensions are given in Table 2-2. The expansion ratio of this nozzle is 6.15, higher than that of nozzle SiC-1.

Moreover, helium (He) was employed to accelerate particles to a higher velocity using a home-made He circulation CS system (LERMPS). The enclosure of this circulation CS system is shown in Figure 2-12c. Prior to the deposition process, the chamber was evacuated and then filled with He. Due to the limited He resources on earth, straight CS deposition with He may not be a sustainable and cost-effective way. Therefore, in order to drastically limit the amount of He necessary to operate the deposition system, a closed loop circulating device, which mainly consists of cooling, filtering and compressing the gas, was implemented. This CS system developed in LERMPs laboratory operates at a chamber pressure close to 950 mbar. The oxygen level in the deposition chamber, as measured with an electrolytic oxygen analyzer (Mecanalyse, France), was always lower than 1000 ppm. In order to prevent nozzle clogging, a polymer nozzle with an expansion ratio of 14.0 was installed in this CS system. The size dimensions of this polymer nozzle (PBI-3) are given in Table 2-2. The maximum operation gas pressure and temperature using this nozzle are 2.0 MPa and 350 ℃, respectively.

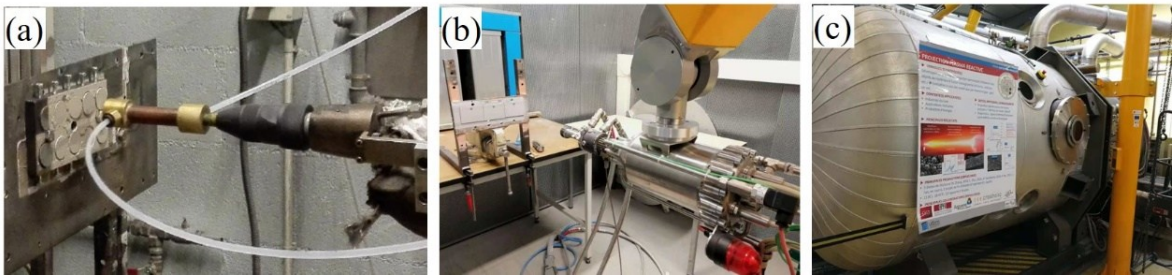

Figure 2-12 Photos of the CS systems: (a) CGT-3000 (LERMPS); (b) Impact 5/8 (INSA-Lyon); (c) Helium circulation CS system (LERMPS).

Table 2-2 Nozzle dimensions and expansion ratios.

Nozzle	Enter diameter (mm)	Throat diameter (mm)	Exit diameter (mm)	Divergent length (mm)	Convergent length (mm)	Expansion ratio
SiC-1	15	2.7	6.4	132.4	30	5.6
SiC-2	12	2.4	6.0	140	20	6.25
PBI-3	18	2.7	10.1	192.4	30	14.0

2.2.2 Processing parameters

2.2.2.1 Deposition of CNT/Al composite powder

The CS deposition of CNT/Al composite powder was performed in different conditions using these three different CS systems. The main processing parameters are given in Table 2-3. First, the influence of gas temperature on the deposition behavior of the CNT/Al composite powders was studied by varying gas temperatures from 300 ℃ to 550 ℃ using the CGT-3000 CS system. Compressed air and Ar were used as the propulsive gas and carrier gas, respectively. Four different gas temperatures (300, 400, 500 and 550 ℃) referring to four different conditions (CC1-CC4) were operated individually while the gas pressure at the nozzle inlet maintained at 3.0 MPa. The nozzle was cooled by running water in order to prevent nozzle clogging and improve the reliability of this system. The standoff distance between the substrate and the nozzle exit was set to 30 mm. The nozzle traverse speeds for individual splat and coating deposition were set to 500 mm/s and 100 mm/s, respectively. For coating deposition, nozzle trajectory was repeated for 20 times. The gas-atomized pure Al powder was also deposited using the same conditions for comparison.

In order to further improve the deposition efficiency (DE) of the SSBM CNT/Al composite powder and obtain thick coatings, this composite powder was deposited using the Impact 5/8 CS system and He circulation CS system, which refers to CC5 and CC6, respectively. In CC5, high-pressure compressed N_2 was used as the powder carrier gas and propelling gas. The propellant gas at the nozzle inlet had a pressure of 5.0 MPa and a temperature of 500 °C. In CC6, the particles were accelerated to high impact velocity using He at a pressure of 1.8 MPa and a temperature of 320 °C. The standoff distance and nozzle traverse speeds in CC5 and CC6 were set to 30 mm and 100 mm/s. Nozzle trajectory (Z-type with a hatch distance of 2 mm) was repeated for more than 40 times to obtain thick coatings.

Table 2-3 Processing parameters used for CS deposition of CNT/Al composite powder feedstocks.

Conditions	Nozzle	Propelling gas	Carrier gas	Gas pressure (MPa)	Gas temperature (°C)	CS system
CC1	SiC-1	Air	Ar	3.0	300	CGT-3000
CC2	SiC-1	Air	Ar	3.0	400	CGT-3000
CC3	SiC-1	Air	Ar	3.0	500	CGT-3000
CC4	SiC-1	Air	Ar	3.0	550	CGT-3000
CC5	SiC-2	N_2	N_2	5.0	500	Impact 5/8
CC6	PBI-3	He	He	1.8	320	LERMPS

2.2.2.2 Deposition of TiB_2/AlSi10Mg composite powder

The TiB_2/AlSi10Mg composite powder as well as the pure AlSi10Mg powder were CSed onto 7075Al-T6 substrates in different processing conditions using two different CS systems. First, the CS deposition was performed using the CGT-3000 CS system, at which compressed air was used as the propellent gas. In CT1, a gas pressure and temperature of 3.0 MPa and 470 °C were used for the deposition. Moreover, CS deposition was also performed using He as the propellent gas at a pressure of 1.8 MPa and a temperature of 320 °C, which refers to CT2. The standoff distance and nozzle traverse speed in both conditions were set to 30 mm and 100 mm/s, respectively. A coating with a thickness of 2 mm was obtained in CT2.

Table 2-4 Processing parameters used for CS deposition of TiB_2/AlSi10Mg composite powder feedstocks.

Conditions	Nozzle	Propelling gas	Carrier gas	Gas pressure (MPa)	Gas temperature (°C)	CS system
CT1	SiC-1	Air	Ar	3.0	470	CGT-3000
CT2	PBI-3	He	He	1.8	320	LERMPS

2.2.2.3 Deposition of TiB_2/7075Al composite powder

CS deposition was performed on 7075Al-T6 plate substrates in different processing conditions using three different CS systems. The main processing parameters used for CS deposition are listed in Table 2-5. In C1, deposition was conducted using compressed air as propellent as at a pressure of 3.0 MPa and a temperature of 550 ℃. In C2, compressed N_2 having a pressure of 5.0 MPa and a temperature of 500 ℃ was employed using the Impact 5/8 CS system. Besides, CS deposition was also carried out by using He as the propellent gas at a pressure of 1.8 MPa and a temperature of 320 °C, which corresponds to C3. All the depositions were conducted using a standoff distance of 30 mm, a traverse speed of 100 mm/s, and deposition angle of 90°. In order to obtain thick deposits (~2 mm), the nozzle trajectory was repeated more than 25 times for each deposition. Single particle deposition was performed at a high gun traverse speed (500 m/s) and a very low powder feed rate.

Table 2-5 Processing parameters used for CS deposition of TiB_2/7075Al composite powder feedstocks.

Conditions	Nozzle	Propelling gas	Carrier gas	Gas pressure (MPa)	Gas temperature (°C)	CS system
C1	SiC-1	Air	Ar	3.0	550	CGT-3000
C2	SiC-2	N_2	N_2	5.0	500	Impact 5/8
C3	PBI-3	He	He	1.8	320	LERMPS

2.3 Heat treatments

In order to release residual stress and heal the defects of the CSed deposits, post heat treatments were performed using a home-made furnace (LERMPS) under Ar protective atmosphere to prevent the samples from oxidation. The furnace temperature can reach 1100 ℃. The heating rate was about 5 °C min^{-1} and the samples can be cooled in different ways, such as with furnace cooling, air cooling, or water quenching, depending on the needs of the experiment.

2.3.1 CNT/Al composites

The as-sprayed CNT/Al composite coatings were annealed at different temperatures (300, 400, 500 and 550 ℃) for a duration of 4 h. Besides, some other samples were annealed at 500 ℃ for a duration of 8 h and 12 h. The samples were cooled to room temperature inside the oven.

2.3.2 TiB_2/AlSi10Mg composites

The as-sprayed AlSi10Mg and TiB_2/AlSi10Mg composite deposits were heat treated at various temperatures ranging from 200 °C to 500 °C for different durations (2-12 h). Microhardness measurements were carried out for all the specimens while the CT2 specimens treated at 300 ℃, 400 ℃ and 500 ℃ for 4 h were selected to study the tensile properties.

2.3.3 TiB_2/7075Al composites

Age-hardenable 7075Al alloy as well as TiB_2/7075Al composite are the material which can be strengthened by precipitation reactions after solution and aging treatments. Therefore, the aim of heat treatment is twofold: on the one hand, heat treatment allows for healing the defects and enhancing the inter-splat bonding via atom diffusion; on the other hand, it provides to form a high density of nano precipitates within the Al matrix to further strengthen the material.

First, solution treatments on the as-sprayed 7075Al and TiB_2/7075Al composite coatings fabricated from different processing conditions (C1, C2, and C3) were performed at 470 ℃ for different durations (70 min, 2 h, and 4 h). The solution treatments were carried out at the furnace under the protective Ar atmosphere followed by water quenching. Then aging treatments were performed by immersing the samples into an oil bath with a constant temperature (121 ℃) for a duration from 2 h to 48 h. Then the samples were taken out from the oil bath and cooled to room temperature every 4 h to study the influence of aging time on the precipitation behavior of the CSed deposits. Moreover, in order to further enhance the inter splats bonding, the samples were pre-annealed at 412 ℃ for 4 h prior T6 treatment (470 ℃/70 min water quenching + 121 ℃/24 h aging).

Additionally, the CSed coatings were annealed at two different conditions to study the influence of annealing treatments on the corrosion behavior: one was performed at 230 ℃ for 6 h, the samples of which refers to HT1; and the other was conducted at 412 ℃ for 4 h, the samples of which refers to HT2.

2.4 Friction stir treatment on the as-sprayed coatings

The post-treatment friction stir processing (FSP) was performed on the CSed TiB_2/AlSi10Mg composite coatings using two different passes (1 and 3 passes). A commercial friction stir welding (FSW) machine (FSW-RL31-010, Beijing FSW Technology Co., Ltd, China) was used in this study. An H13 steel stir-tool with a threaded pin of 3.5 mm in root diameter and 2.0 mm in length, and a concave shoulder of 10 mm in diameter, was installed in this FSW equipment. The tool was set to a 2.5° tilt angle to avoid surface defects. The rotation direction was anticlockwise at a rotation speed of 1500 rpm and a traverse speed of 500 mm/min for each pass. The pin and shoulder movement strategies as well as the coating morphology before and after FSP treatment are present in Figure 2-13.

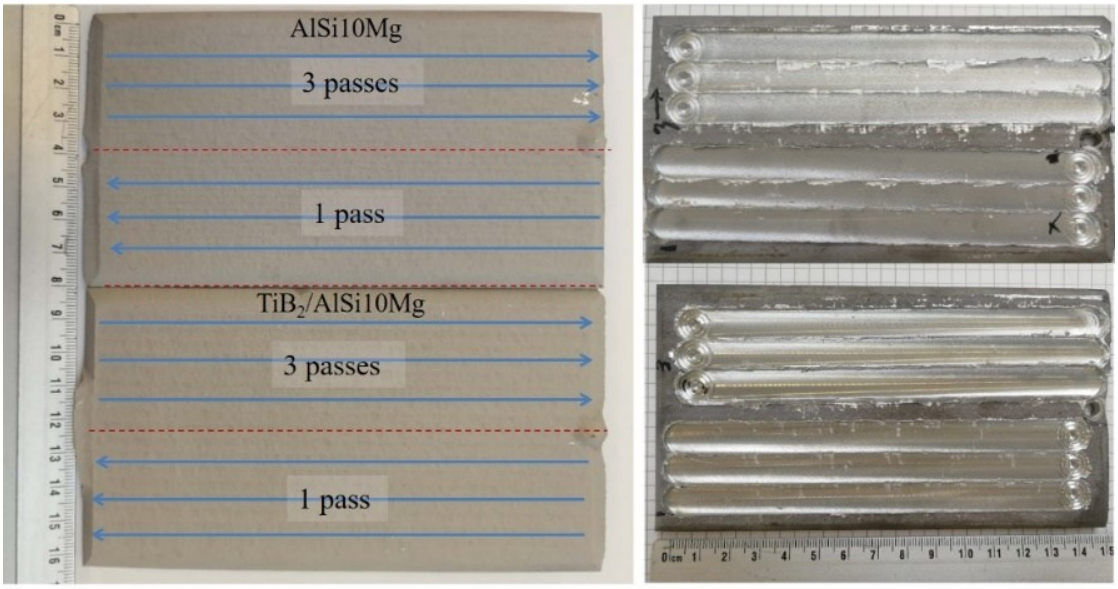

Figure 2-13 Photos of the as-sprayed AlSi10Mg and TiB_2/AlSi10Mg composite coating (a) before and (b) after FSP treatment.

2.5 Material characterization

2.5.1 Deposition efficiency measurement

The DE was determined by measuring the weights of the substrate (W_1), feedstock powder (W_2), substrate with coating (W_3), and the left-over feedstock powder (W_4) according to Eq. (2-1):

$$DE = \frac{W_3 - W_1}{W_2 - W_4} \times 100\% \qquad (2\text{-}1)$$

2.5.2 Phase composition characterization

XRD analyses were performed on an X-Ray diffractometer (XRD-6100, Shimadzu Co. Ltd., Japan), operating at 40 kV/40 mA and using Cu Kα radiation (λ=0.15406 nm). 2θ scans were performed between 20 and 110° with a scan speed of $5°\cdot min^{-1}$.

Raman spectroscopy tests were performed by using SENTERRA R200-L with the 532 nm line of an Ar+ laser as the excitation source to validate the structure of CNT and the formation of Al_4C_3 phase in the spectral range from 200 to 2000 cm^{-1}. For each sample, at least five measurements were conducted on the cross-section of the depositions at different positions. Raman mapping of the cross-section of CNT/Al composite coatings was carried out to determine the CNT distribution at a step of 0.7 μm within an area of 30×30 μm^2.

2.5.3 Microstructure characterization

Optical microscope (OM) (Nikon, Japan) was used to observe the microstructures of the powder and the coatings. The coating porosity was estimated by software Image J. To clearly observe the microstructure of the coating cross-section, specimens were polished and etched at room temperature using Kroll's reagent (3ml HF+6ml HNO_3 +100ml H_2O).

The polished samples as well as the surface morphologies were observed by SEM instrument (JSM5800LV, JEOL, Japan), equipped with an EDS unit. The TiB_2 particle size distribution and its volume fraction in the as-sprayed deposits were also examined using ImageJ software based on SEM images. The flattening ratio measurements on the initial powders and the deposits were performed using at least 35 particles per sample.

Another SEM instrument (JSM7800F, JEOL, Japan) equipped with an EBSD detector from Oxford instruments was employed to obtain information about grain structure. Samples for SEM/EBSD characterization were prepared by mechanical polishing and final surface iron milling using a Fischione instruments model 1060 miller. EBSD measurements were conducted on the cross-sections of the feedstock particles and deposits at an electron energy of 25 KeV and with a step size of 100 nm.

An FEI Tecnai G2 microscope, operating at 200 kV, equipped with a Nanomegas ASTAR unit was used for transmission electron microscopy (TEM) associated with automated crystal orientation mapping. Cross-sectional TEM samples were prepared by mechanical polishing followed by final ion milling using a Gatan Model 691 precision ion polishing system.

2.6 Properties characterization

2.6.1 Microhardness and nanoindentation test

Microhardness was measured by a Vickers hardness indenter (Leitz, Germany) with different loads depending on the hardness of the material. The microhardness measurement of the powder was conducted on the polished cross-section of large particles using a load of 15 gf. A load of 100 gf was used for CNT/Al and TiB_2/AlSi10Mg composite coatings, while a load of 300 gf was used for the TiB_2/7075Al composite coatings. 10 positions were randomly tested on the polished cross-sections to have an average value for each sample. Besides, to obtain the distribution of microhardness value in the FSP treated (FSPed) AlSi10Mg and TiB_2/AlSi10Mg samples, tests were conducted at an interval of 500 μm between indentation points.

Nanoindentation tests were conducted using a commercial nanoindenter (MTS Nanoindenter XP; Keysight Technologies, Santa Rosa, CA) in load control model with a Berkovich indenter. The load function comprised a linear increase in load up to 10 mN at a rate of 3.6 $mN \cdot min^{-1}$ followed by a 5 s held at maximum load and then decrease to zero with an upload rate of 3.6 $mN \cdot min^{-1}$. 12 points were tested in each specimen, and the measurements for the points with extreme values (maximum and minimum values) were discarded. 10 measurements were selected to obtain the average values. The Oliver and Pharr method [11] was used to determine hardness and the elastic modulus of the corresponding deposition.

2.6.2 Adhesion test

Adhesion strength of the deposits was evaluated based on the ASTM C-633 standard [11]. The composite coatings with a thickness between approximately 300 μm were deposited on cylindric substrates with a diameter of 25.4 mm and a thickness of 10 mm. A tensile tester (IC ESCOFFIER, Estotest 50, France) was used to pull-out the adhesion samples at a speed of 1.26 mm/min. For each deposition condition, four adhesion samples were tested to obtain an average value. All substrates were grit blasted, cleaned in an ultrasonic bath of ethanol and were dried using compressed air prior to the CS. The roughness of the Al alloy substrates after grit blasting was measured to be about ~28 μm, while the 316 stainless steel after grit blasting has an average value of 19 μm.

2.6.3 Tribological test

Dry sliding wear tests were conducted at ambient temperature with a CSEM tribometer implement (Switzerland). Before the wear test, the surface roughness of samples was kept less than 0.05 μm by standard preparation procedure with final polishing by 0.05 μm Al_2O_3 solution. A cleaned Al_2O_3 ball with a diameter of 6 mm was chosen as the counterpart material under a load of 2 N. A linear rotation speed of 10 cm/min and a rotation radius of 4 mm were set for the friction test. The friction coefficient was recorded for a sliding distance of 300 m. After the friction test, the surface of worn samples was observed and analyzed by SEM and EDS. The wear rates of the samples were calculated according to the cross-sectional profiles of worn track measured by an Altisurf 500 profilometer (France). The worn volumes of the samples were calculated via the product between the cross-sectional areas and length of worn tracks. To evaluate the wear resistance performance, the wear rate of friction test is defined as the worn volume per unit of normal load and sliding distance, where the formula is given as following [12]:

$$\omega = \frac{2\pi r S}{pl} \qquad (2\text{-}2)$$

where ω is the wear rate in $mm^3/(N \cdot m)$, r is the wear radius in mm, S is the cross-sectional area in mm^2, p is the normal load in N, l is the sliding distance in m.

2.6.4 Electrochemical corrosion test

Corrosion characteristics were determined utilizing electrochemical and immersion experiments. Before each corrosion experiment, samples were ground up to 2000 grit with abrasive papers and mounted in epoxy resin with only a square area about 1 cm^2 exposed to the test solution.

All electrochemical measurements were conducted in a conventional three-electrode electrolyte cell with a sample as the working electrode, a platinum plate as the auxiliary electrode and a saturated calomel electrode (SCE) as the reference. All experiments were carried out in a 0.1 M or 0.6 M NaCl solutions at room temperature. Prior electrochemical testing, the solution was purged with Ar for 15 min and it continued to be purged with Ar through the test. After the samples were kept in the corrosion cell (with NaCl solution) for 5 min, potentiodynamic polarization experiments were carried out at a scan rate of 0.167 mV/s, from -150 mV to +100 mV versus the open-circuit potential (OCP). Electrochemical impedance spectroscopy (EIS) measurements were performed in the potentiostatic mode at the OCP. A sinusoidal AC perturbation was amplitude of 10 mv (rms) and the frequency range was from 100 kHz to 10 Hz.

Immersion experiments were conducted in a 0.1M or a 0.6 M NaCl solution, at open circuit conditions, for 7 days at room temperature. After the immersion test, the samples were characterized by SEM.

2.6.5 Tensile tests

The as-sprayed CNT/Al, TiB_2/AlSi10Mg, and TiB_2/7075Al composite deposits fabricated using different processing parameters are shown in Figure 2-14, Figure 2-15 and Figure 2-16, respectively. As can be seen from these photos, the 7075Al-T6 substrates with different sizes were used deposition, whereas the specimens for tensile tests have different sizes. The size dimensions of these tensile test specimens are presented in Figure 2-17 and Figure 2-18. Before tensile tests, substrates were removed, and the deposits for tensile test were cut in the direction being parallel or vertical to the nozzle moving direction. The tensile tests were performed on three different machines based on the specimen's size. For the micro tensile test samples, they were conducted using a commercial machine (INSTRON-3382, USA). A specially designed fixture (Figure 2-17) was used for these specimens to ensure the correct

application of the load and prevent secondary bending or any other unwanted movement of the specimens. In addition, a medium-sized tensile specimen with the width in the gauge section and total length of 2 and 37 mm was tested using a Zwick/Roell Z100 machine at a strain rate of 1 mm/min. Moreover, as for the standard tensile samples (see Figure 2-18), tensile tests were conducted at a strain rate of 1 mm/min by a universal testing system (INSTRON 5982, USA) based on the ASTM E8/E8M-16a standard [13]. At least 3 samples were tested at each condition.

As for the FSPed samples, as shown in Figure 2-19, the tensile test sample was cut in the direction parallel with the pin movement direction. A 2 mm thick tensile specimen with the width in the gauge section and total length of 2 and 37 mm was used. The fractured surfaces of tensile specimens were analysed using SEM.

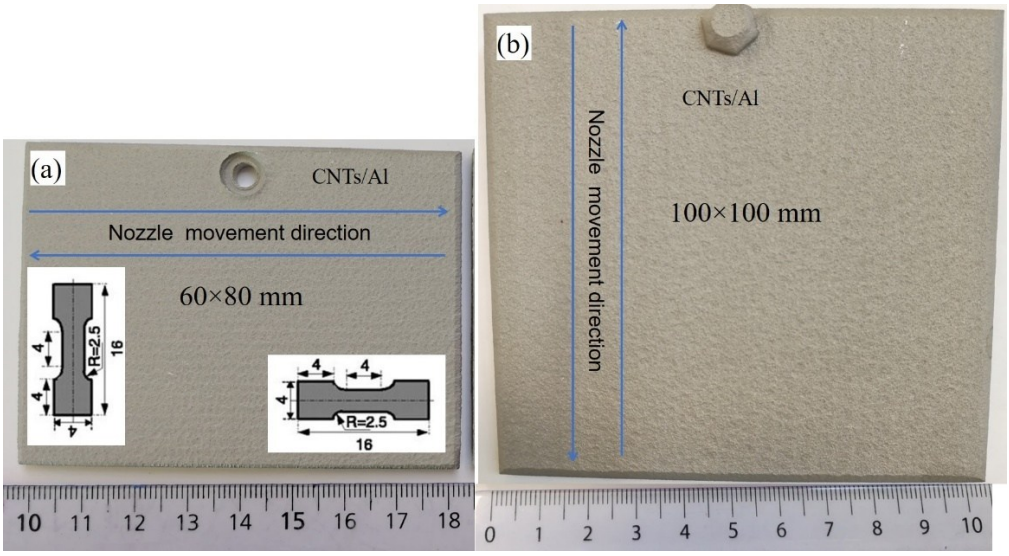

Figure 2-14 Photos of the CSed CNT/Al composite coatings onto Al substrates using different processing parameters: (a) CC5; (b) CC6.

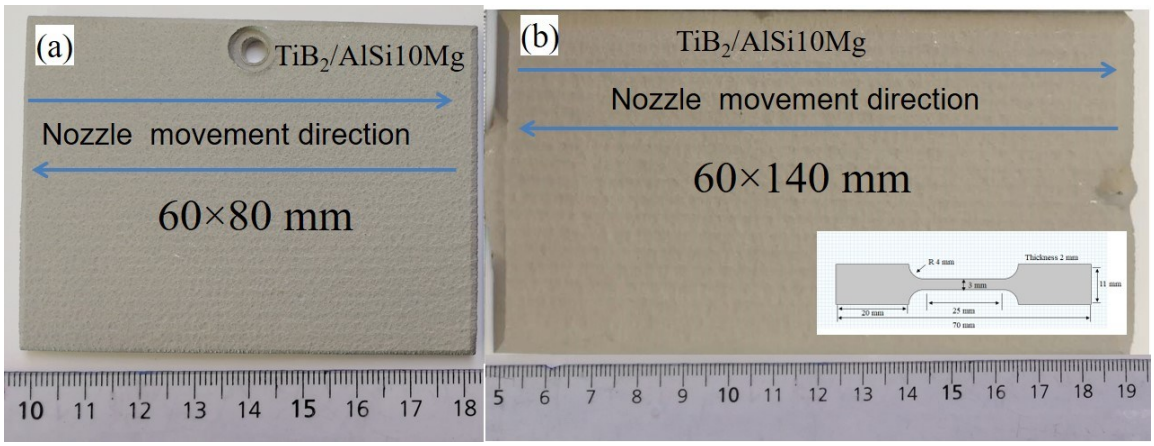

Figure 2-15 Photos of the CSed TiB_2/AlSi10Mg composite coatings onto Al substrates using different processing parameters: (a) CT1; (b) CT2.

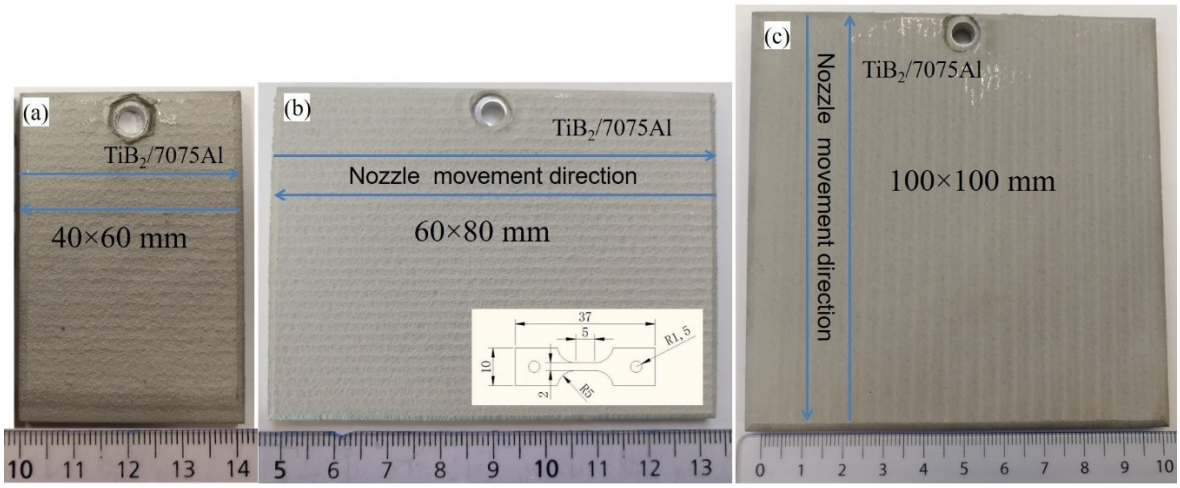

Figure 2-16 Photos of the CSed TiB_2/7075Al composite coatings onto Al substrates using different processing parameters: (a) C1; (b) C2; (c) C3.

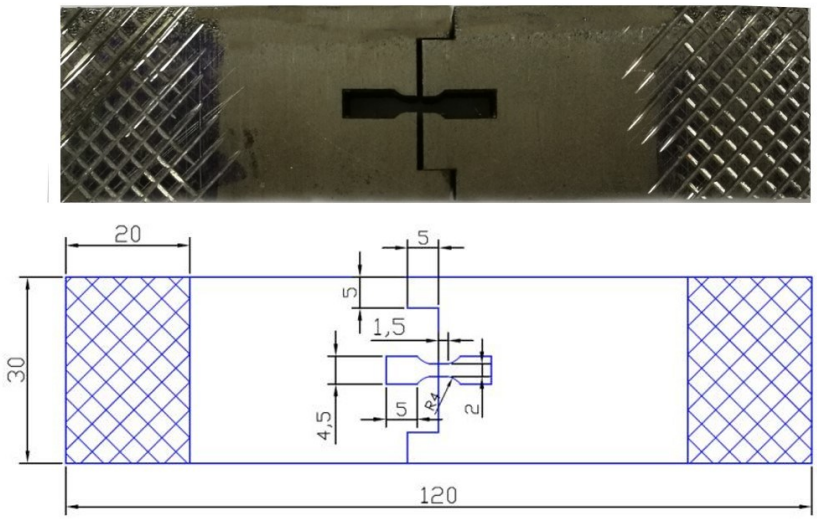

Figure 2-17 Specially designed fixture for tensile tests.

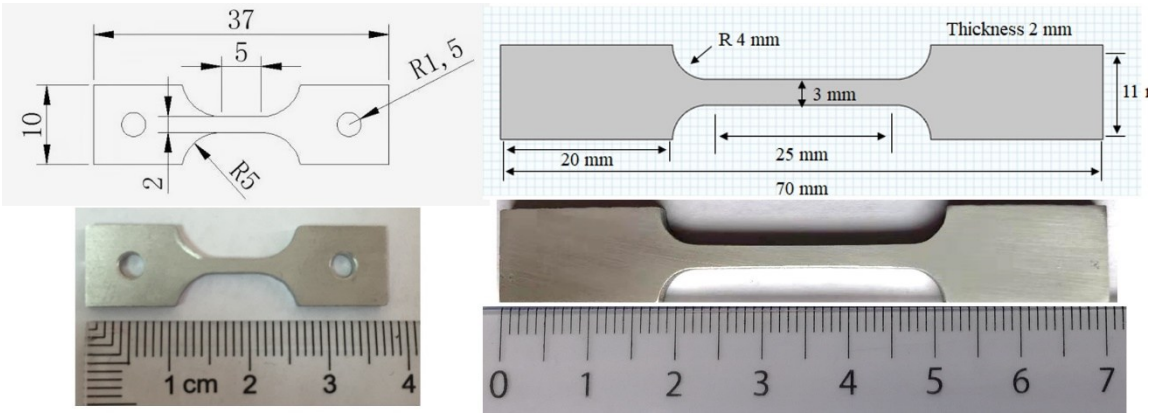

Figure 2-18 The size dimensions of the tensile test samples.

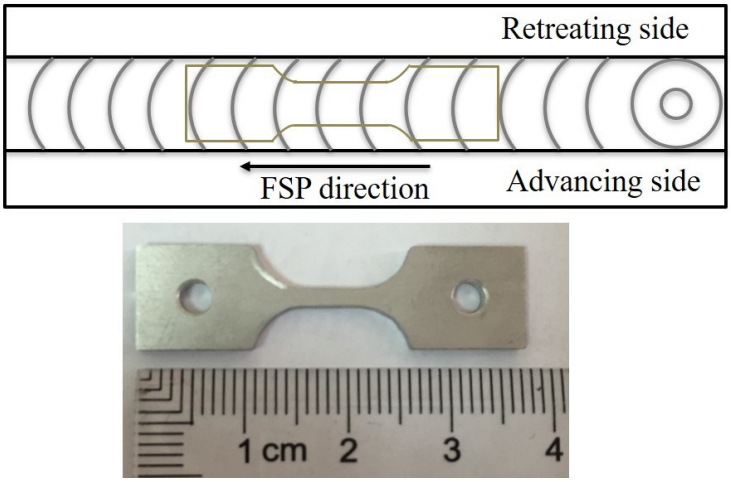

Figure 2-19 Schematic diagram of FSP and the dimension size of tensile test samples.

2.7 Single particle compression test

Single particle compression tests of the gas atomized pure 7075Al and TiB_2/7075Al composite powders were carried out by our partner Dr. Frank GARTNER from Helmut Schmidt University to obtain their mechanical properties, such as ultimate tensile strength (UTS), and Johnson-Cook (JC) parameters. This test was performed under quasi-static conditions using a nanoindentation tester (NHT^2 from CSM Instruments, Switzerland) with a flat diamond head of 200 μm diameter. A schematic of the method is shown in Figure 2-20. First, 12 particles in a near-spherical shape with a particle diameter in the range of 40-55 μm were selected for each powder. Then, they were placed individually on a 'hard metal' substrate (WC-Co composite, hardness 1780 HV_2) and compressed under a constantly increasing load from zero up to a maximum value of 2 N within 120 s. The pure 7075Al and TiB_2/7075Al composite particles were investigated before and after deformation using confocal 3D Laser Scanning Microscope (VK-X200 KEYENCE GmbH, Germany) to reveal the geometry, as illustrated in Figure 2-21. Therefore, it provides additional information for cross checking with the force–displacement data obtained from the nanoindenter. More detailed information about this compression test can be found in the literature [14].

JC model is commonly used in finite element analysis (FEA) simulation of the particle impact during CS deposition. In this model, the flow stress of material (σ) was taken to vary with plastic strain according to the following relationship:

$$\sigma = A + B\varepsilon^n \qquad (2\text{-}3)$$

where A, B and n are constants, referred to rate independent JC parameters. The steps to determine plastic constitutive properties, i.e. JC parameters A, B and n, from the measured force–displacement data are summarized below:

First, force–displacement data were translated into nominal stress (σ_{nom}) and nominal strain (ε_{nom}) as defined by the equation described below [14]:

$$\sigma_{nom} = \frac{4F}{\pi d_o^2}\frac{h_o-\delta}{h_o},\ \varepsilon_{nom} = -ln(1-\frac{\delta}{h_o}) \qquad (2\text{-}4)$$

Where d_o is the mean particle diameter on the horizontal cross-section, h_o is the initial height of the particle as shown Figure 2-20. Obviously, h_o would be identical to d_o for a perfectly spherical particle.

Then the experimental data were then fitted by the following expression:

$$\sigma_{nom} = \alpha\varepsilon_{nom} + b\ln(1 + c\varepsilon_{nom}) \quad (2\text{-}5)$$

Where a, b and c are fitting parameters. In order to fit the experimental data, set initial values for A, B and n given in Eq. (2-3), and then calculate a, b and c for the respective n and A.

Then calculate nominal stress from Eq. (2-5) using the obtained fitting parameters a, b and c. By varying the JC parameters (A, B and n), a best match can be obtained between the experimental and the modeled nominal stresses. A more detailed description of this fitting process can be found elsewhere [14].

The final values of A, B and n obtained are taken as representing the relevant plastic constitutive properties of the examined particle. Moreover, the UTS of the tested particle can be calculated since it can be linked to σ_{nom}, as obtained for a given set of JC parameters [14]:

$$UTS \approx (1.4 \pm 0.2) \times \sigma^*_{nom} = (0.9 \pm 0.1)\frac{F^*}{d_o^2} \quad (2\text{-}6)$$

Where σ^*_{nom} and F^* are the normal stress and the force at $\delta h = 0.5\ h_o$, respectively.

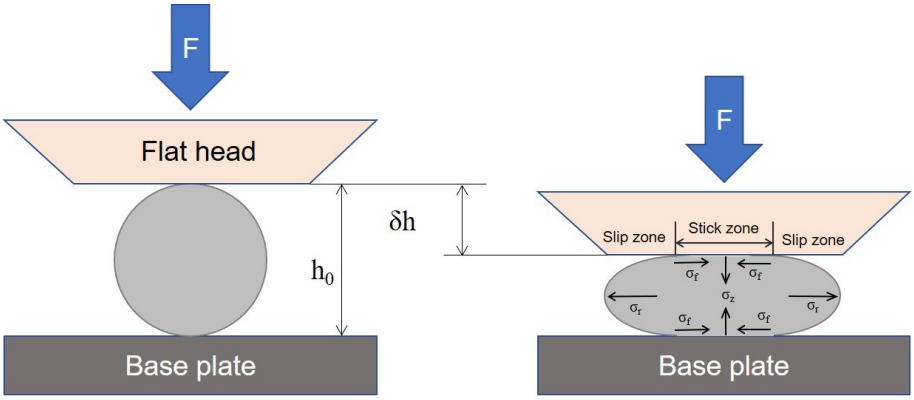

Figure 2-20 Schematic diagram of single particle compression test [14].

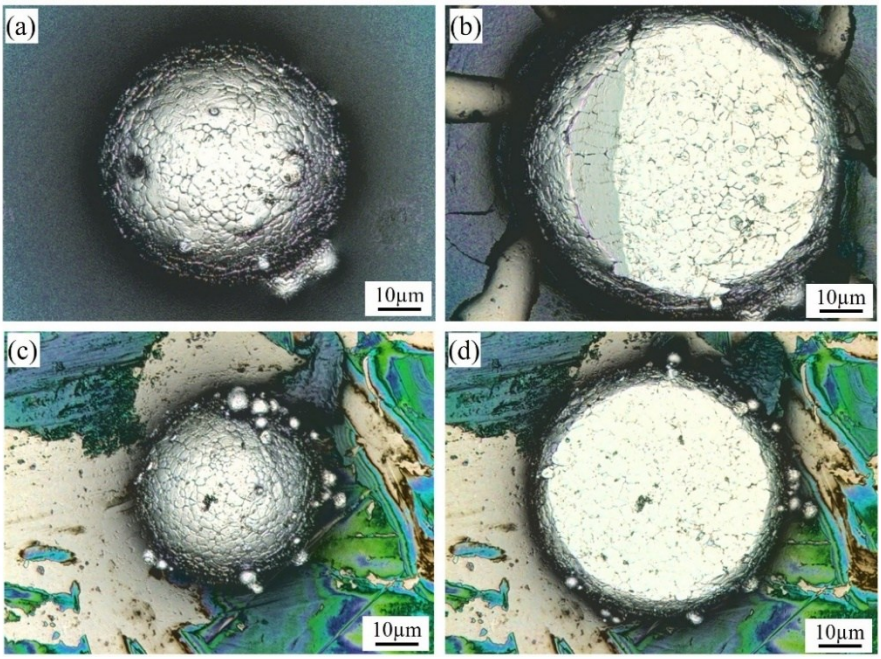

Figure 2-21 The particle morphologies before and after compression tests: (a, b) a 7075Al particle with a size of 51 μm before and after compression tests; (c, d) a TiB_2/7075Al composite particle with a size of 44 μm before and after compression tests.

2.8 Numerical simulation methods

2.8.1 Simulation of the particle impact velocity and temperature

A computational fluid dynamics (CFD) model by the commercial code of Fluent (CFD; ANSYS Fluent Version 17.1) was developed to predict the velocity and the temperature of the particle prior to impact [15]. In order to save computational time, two-dimensional axisymmetric models were used for these three CS systems. A schematic diagram of the computational domain and boundary conditions is shown in Figure 2-22a. The computational domain is meshed using a regular and structured grid of quadrilateral elements. In this model, particles were presented at the nozzle inlet. The initial particle velocity and temperature were set as 25 $m \cdot s^{-1}$ and 298 K, respectively. The densities of pure Al, 7075Al powder, and 7 wt.% TiB_2/7075Al composite powder for the simulations were set to be 2.7, 2.81, and 2.88 g/cm^3, respectively. The gas velocity and temperature fields obtained by CFD simulations of the gas are given in Figure 2-22b and c.

The particle velocities were calculated with an equation of motion such that

$$m_p \cdot \frac{d\vec{u}_p}{dt} = \vec{F}D \qquad (2\text{-}7)$$

Where $\vec{u}_p$ and m_p are the velocity vector and mass of the particle, respectively; and the drag force F_D is calculated using the approach proposed by Haider and Levenspiel that considers the shape factor of the particles according to the Wadell factor ψ_{wa}. The shape factor ψ_{wa} is defined as the surface of a sphere, A_s, with the same volume as a real particle divided by the real particle surface area, A_P, given as

$$\psi_{wa} = \frac{A_s}{A_p} \qquad (2\text{-}8)$$

In this study, a parametric study was conducted to evaluate the influence of particle size distribution, particle morphology and processing parameters on the impact velocities and temperatures.

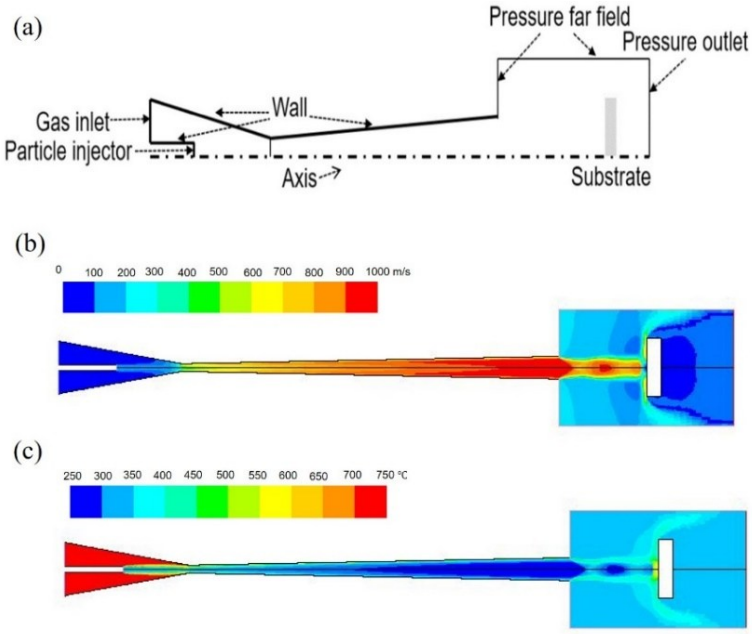

Figure 2-22 (a) Schematic diagram of the computational domain and boundaries [15]. (b) and (c) display the gas velocity and gas temperature contours during CS deposition.

2.8.2 FEA simulation of the particle deformation

2.8.2.1 Description of Lagrangian model

The impacting behavior of a particle on a substrate was modeled by using an explicit FEA program ABAQUS/Explicit with the Lagrangian formulation [16]. In order to reduce the computational resource, the simulation model was simplified into a one-half symmetric computational domain. Particle with a diameter of 35 μm was used in the model for pure 7075Al and TiB_2/7075Al powders based on the particle size distribution in experiments. The radius and height of the substrate were defined as six and eight times larger than the particle diameter to avoid the effect of computational domain boundary on the simulation results. Pure Al and 7075Al-T6 alloy were used as the substrate material. The space surrounding the particle and substrate was considered as void. The mesh at the region where the particle and substrate experience intensive deformation was refined to 0.2 μm for accurately capturing the deformation features. The computation domain, meshing, and boundary conditions are given in Figure 2-23. The particle initial velocity and temperature were calculated using a CFD model in which the nozzle geometry and working parameters were the same as those used in the experiments. The substrate temperature was set to 25 ℃.

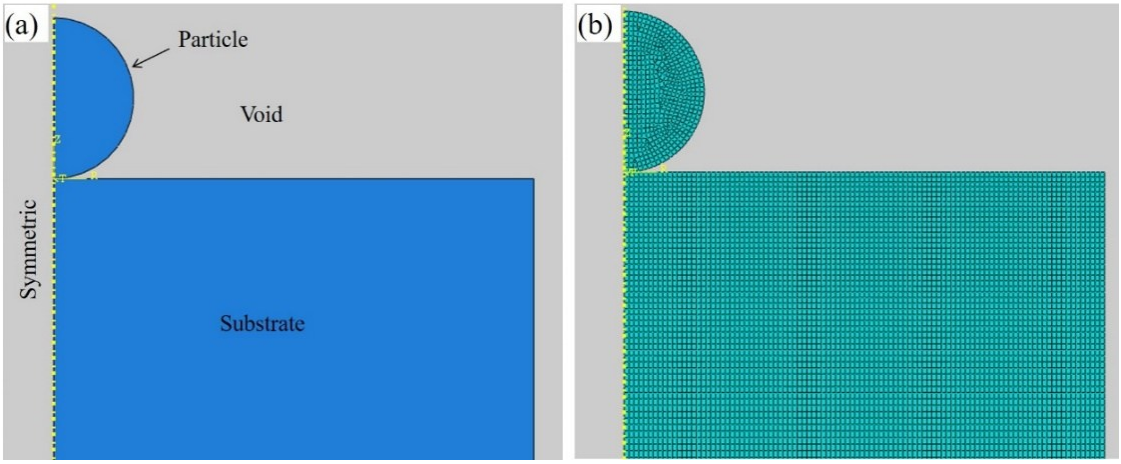

Figure 2-23 Geometric model and computational domain of spherical 7075Al particle impinging on Al or 7075Al-T6 substrate.

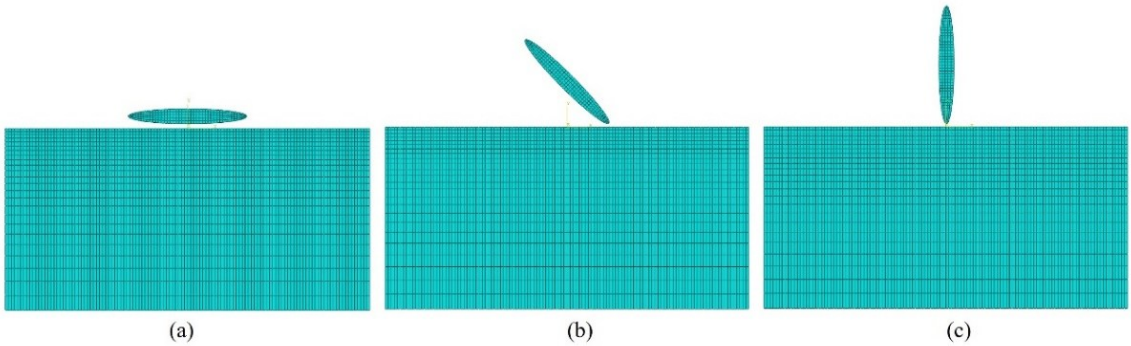

Figure 2-24 Geometric and meshing of flaky Al particle placed in three different posture angles: (a) 0°; (b) 45°; (c) 90°.

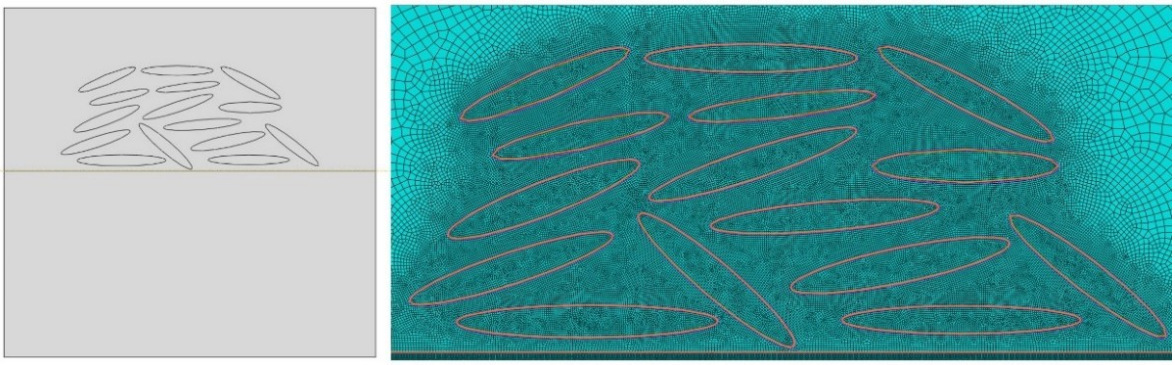

Figure 2-25 Geometric model and computational domain of flaky Al particle impinging on Al substrate under the Eulerian frame and (b) the enlarged view of elements around the particle.

The deformation behavior of the flaky Al particles was also simulated using an explicit FEA code, ABAQUS with Lagrangian formulation. Based on the morphology observation (Figure 2-2c), the particle was modelled with a flattening ratio of 8 (particle diameter over thickness). As shown in Figure 2-24, three possible postures were modeled to represent the irregular impact behavior of a flaky particle. The particle velocity and temperature prior to impact on a substrate were predicted from CFD simulation. In this case, inox 316L was used as the substrate material, and its initial temperature was set to 25℃. For multi-particle impact, the meshing is partitioned in a similar way, as given in Figure 2-25. Several flaky particles having a similar flattening ratio were randomly arranged above the substrate surface. The temperature and velocity of these particles were set the same values as in the case of single particle impact.

2.8.2.2 Description of material model

The material flow behavior of the pure Al and composite particle impacting onto substrate was described by the JC plasticity model [17]:

$$\sigma = (A + B\varepsilon_p^n)\left[1 + C\ln(1 + \frac{\varepsilon}{\varepsilon_0}\right]\left[1 - (\frac{T-T_r}{T_m-T_r})^m\right] \quad (2\text{-}9)$$

Here the flow stress, σ, is the product of three bracketed terms. The first bracketed term represents strain hardening, with $\varepsilon_p$being the plastic strain, and A, B and n being material constants. The second bracketed term represents strain rate hardening, with ε being the strain rate, C being a material constant and ε_0 being a reference strain rate. The third bracketed term represents thermal softening with T being the temperature, T_m being melting temperature, m being a material constant, and T_r being a reference temperature.

A linear Mie-Gruneisen equation of state (EOS) was employed for the elastic behavior of the particles. The linear Us-Up Hugoniot form is defined as [18]:

$$p = \frac{\rho_o C_o^2 \eta}{(1-S\eta)^2}\left(1 - \frac{\Gamma_o}{2}\eta\right) + \Gamma_o \rho_o E_m \quad (2\text{-}10)$$

where $\eta = 1 - \rho/\rho_o$ is the nominal volumetric compressive strain, ρ_o the initial density, ρ the current density, C_o the bulk speed of sound, Γ_o the material constant named Gunrisen's gamma, S the linear Hugoniot slope coefficient, E_m the internal energy per unit reference specific volume.

The material parameters of Al and 7075Al-T6 bulk to define the Mie–Grüneisen EOS and JC plasticity model are given in

Table 2-6. These parameters were taken from existing literature [19, 20]. The A, B and n parameters of JC model obtained from single particle compression tests were used for 7075Al and TiB_2/7075Al particles

Table 2-6 Material parameters for Al, 7075Al-T6 bulk, 7075Al and TiB_2/7075Al composite.

Material properties	Symbol	Al	7075Al-T6	7075Al	TiB_2/7075Al
Density	ρ (kg/m^3)	2700	2810	2810	2880
Shear modulus	G (GPa)	26200	26900	26900	26900
J-C yield strength	A (MPa)	148	546	167	359
J-C hardening coefficient	B (MPa)	346	678	439	384
J-C strain hardening exponent	n	0.31	0.71	0.71	0.71
J-C strain rate constant	C	0.025	0.024	0.024	0.024
J-C softening exponent	M	0.86	1.56	1.56	1.56
Melting temperature	T_m (K)	620	604	604	604
Elastic bulk wave velocity	C_o (km/s)	5328	5288	5288	5288
Slope in u_s vs.u_p diagram	S	1.336	1.3756	1.3756	1.3756
Grüneisen coefficient	γ_o	2	2.14	2.14	2.14
Specific heat	c (J/kg ºC)	892	960	960	960

References of Chapter II

[1] Ziyun Yu, Zhanqiu Tan, Run Xu, Gang Ji, Genlian Fan, Ding-Bang Xiong, Qiang Guo, Zhiqiang Li, Di Zhang, Enhanced load transfer by designing mechanical interfacial bonding in carbon nanotube reinforced aluminum composites, Carbon, (2019),
[2] Run Xu, Zhanqiu Tan, Dingbang Xiong, Genlian Fan, Qiang Guo, Jie Zhang, Yishi Su, Zhiqiang Li, Di Zhang, Balanced strength and ductility in CNT/Al composites achieved by flake powder metallurgy via shift-speed ball milling, Composites Part A, 96 (2017), 57-66.
[3] Malin Chen, Genlian Fan, Zhanqiu Tan, Dingbang Xiong, Qiang Guo, Yishi Su, Jie Zhang, Zhiqiang Li, Makio Naito, Di Zhang, Design of an efficient flake powder metallurgy route to fabricate CNT/6061Al composites, Mater. Des., 142 (2018), 288-296.
[4] Makio Naito, Hiroya Abe, Akira Kondo, Toyokazu Yokoyama, Huang CC, Smart powder processing for advanced materials, KONA Powder and Particle Journal, 27 (2009), 130-143.
[5] Mengxing Chen, Xiaopeng Li, Gang Ji, Yi Wu, Zhe Chen, Wouter Baekelant, Kim Vanmeensel, Haowei Wang, Jean-Pierre Kruth, Novel composite powders with uniform TiB2 nano-particle distribution for 3D printing, Applied Sciences, 7 (2017), 250.
[6] Q Yang, YT Liu, J Liu, L Wang, Z Chen, ML Wang, SY Zhong, Y Wu, HW Wang, Microstructure evolution of the rapidly solidified alloy powders and composite powders, Mater. Des., 182 (2019), 108045.
[7] MR Rokni, CA Widener, GA Crawford, Microstructural evolution of 7075 Al gas atomized powder and high-pressure cold sprayed deposition, Surf. Coat. Technol., 251 (2014), 254-263.
[8] Tian Liu, Jeremy D Leazer, Luke N Brewer, Particle deformation and microstructure evolution during cold spray of individual Al-Cu alloy powder particles, Acta Mater., (2019), 13-23.
[9] Z Fan, Y Wang, Y Zhang, T Qin, XR Zhou, GE Thompson, T Pennycook, T Hashimoto, Grain refining mechanism in the Al/Al–Ti–B system, Acta Mater., 84 (2015), 292-304.
[10] Min Yu, Belfort-Montbéliard, 2013.
[11] American Society for Testing, Materials, ASTM West Conshohocken (PA, 2001.
[12] SA Alidokht, P Manimunda, P Vo, S Yue, RR Chromik, Cold spray deposition of a Ni-WC composite coating and its dry sliding wear behavior, Surf. Coat. Technol., 308 (2016), 424-434.
[13] I ASTM, ASTM E8/E8M-16a: Standard Test Methods for Tension Testing of Metallic Materials, West Conshohocken, PA, USA: ASTM International, (2016),
[14] H Assadi, I Irkhin, H Gutzmann, F Gärtner, M Schulze, M Villa Vidaller, T Klassen, Determination of plastic constitutive properties of microparticles through single particle compression, Advanced Powder Technology, 26 (2015), 1544-1554.
[15] Yingchun Xie, Marie-Pierre Planche, Rija Raoelison, Philippe Hervé, Xinkun Suo, Pengjiang He, Hanlin Liao, Investigation on the influence of particle preheating temperature on bonding of cold-sprayed nickel coatings, Surf. Coat. Technol., 318 (2017), 99-105.
[16] HD Hibbitt, BI Karlsson, EP Sorensen, ABAQUS-Standard, User Manual, Version 10.1, Inc., Pawtucket RI, USA, (2011),
[17] Gordon R Johnson, William H Cook, Proceedings of the 7th International Symposium on Ballistics, The Hague, The Netherlands, 1983, pp. 541-547.
[18] D Simulia, ABAQUS 6.11 analysis user's manual, Abaqus, 6 (2011), 22.22.
[19] Marco Sasso, Archimede Forcellese, Michela Simoncini, Dario Amodio, Edoardo Mancini, Key Engineering Materials, Trans Tech Publ, 2015, pp. 114-119.
[20] Gyuyeol Bae, Yuming Xiong, S Kumar, Kicheol Kang, Changhee Lee, General aspects of interface bonding in kinetic sprayed coatings, Acta Mater., 56 (2008), 4858-4868.

Chapter III Cold spraying of CNT/Al composites

3.1 Introduction

Uniform dispersion of CNTs into the Al matrix and high interfacial bonding between CNT/Al are the two key factors achieving high performance for CNT/Al composite. In this chapter, first, two distinct methods, namely high shear dispersion (HSD) and shift-speed ball milling (SSBM), were employed to prepare CNT/Al composite powder for cold spraying (CS). The influence of processing parameters, including gas temperature and pressure on the deposition efficiency (DE), microstructure evolution as well as the mechanical properties, were investigated in detail. The distribution and structural integrity of CNTs within the as-sprayed composites were characterized by using the Raman spectra and TEM analysis. FEA simulation was applied to study the plastic deformation behavior of the spherical and flaky pure Al particles during CS deposition. Afterwards, the annealing treatments were performed at different temperatures and for different durations, to study their effects on microstructure evolution, phase stability, as well as the mechanical performance of the composite. Finally, a fracture model based on micro-scale and submicron-scale observation was put forward in order to illuminate the fracture mechanisms of the CSed CNT/Al composite.

3.2 Effect of propelling gas temperature

3.2.1 Particle impact velocity and temperature

In this study, a computational fluid dynamics (CFD) model by the commercial code of Fluent (CFD; ANSYS Fluent Version 17.1) was used to predict the velocity and the temperature of the particle prior to impact. The particle velocity and particle temperature along the nozzle central line are given in Figure 3-1. The simulation was performed for the pure Al particle with an average particle size of 25 μm. Figure 3-2 presents the particle impact velocity and temperature as a function of propelling gas temperature (300-550 ℃). Clearly, both the particle impact velocity and temperature increase with the increase in propelling gas temperature. A particle impact velocity of 642 m/s and a particle impact temperature of 355 ℃ were obtained at a propulsive gas (compressed air) pressure of 3.0 MPa and a temperature of 550 ℃. It should be noticed that the HSD CNT/Al composite powder could have similar particle impact velocity and temperature compared to the pure Al powder as they them have similar particle size, morphology and other physical properties, including density and specific heat.

In addition, the SSBM CNT/Al composite powder after ball milling displayed a non-spherical morphology. This can also affect the acceleration behaviour of the particle within the nozzle. Therefore, a variation of shape factor from 0.3 to 1 was considered for the Al particles. The particles with an equivalent diameter of 25, 45 and 62 μm were used for simulation, and the results are given in Figure 3-3. A smaller shape factor (i.e., $\Psi_{Wa} = 0.6$) exhibits greater particle velocities. Further, it was found that smaller equivalent diameters reduced the effect of the shape on the velocity. In addition, the temperature of the non-spherical particles was slightly greater over the complete distance up to impact than that of the spherical particles.

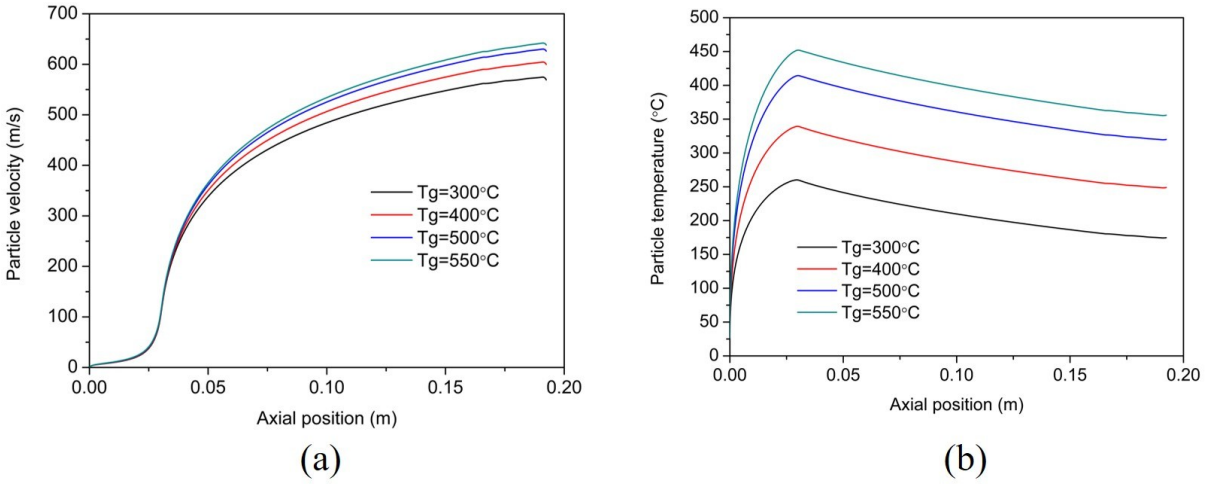

Figure 3-1 (a) Particle velocity and (b) particle temperature along the nozzle central line.

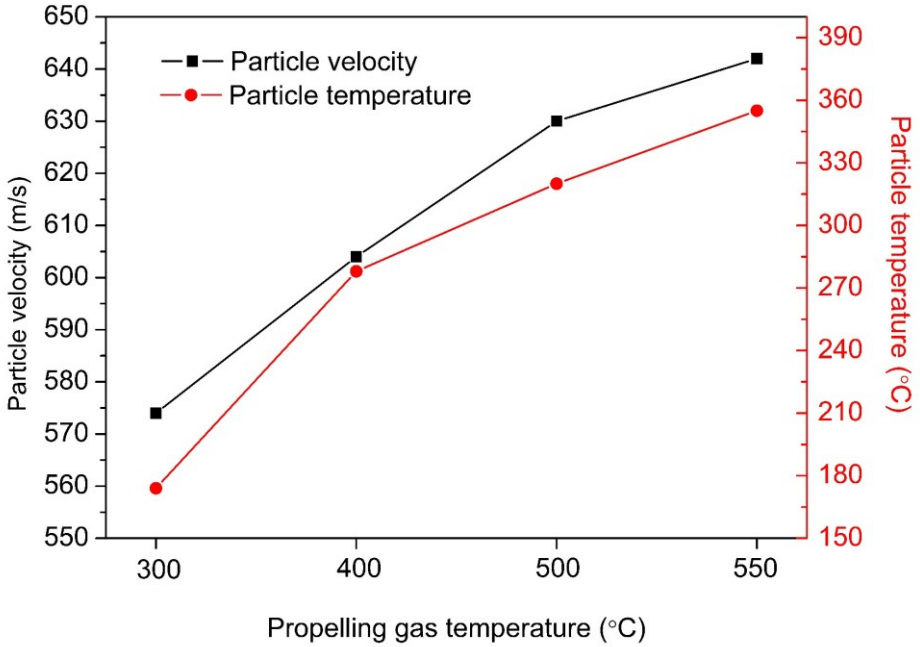

Figure 3-2 Particle impact velocity and temperature as a function of propelling gas temperature.

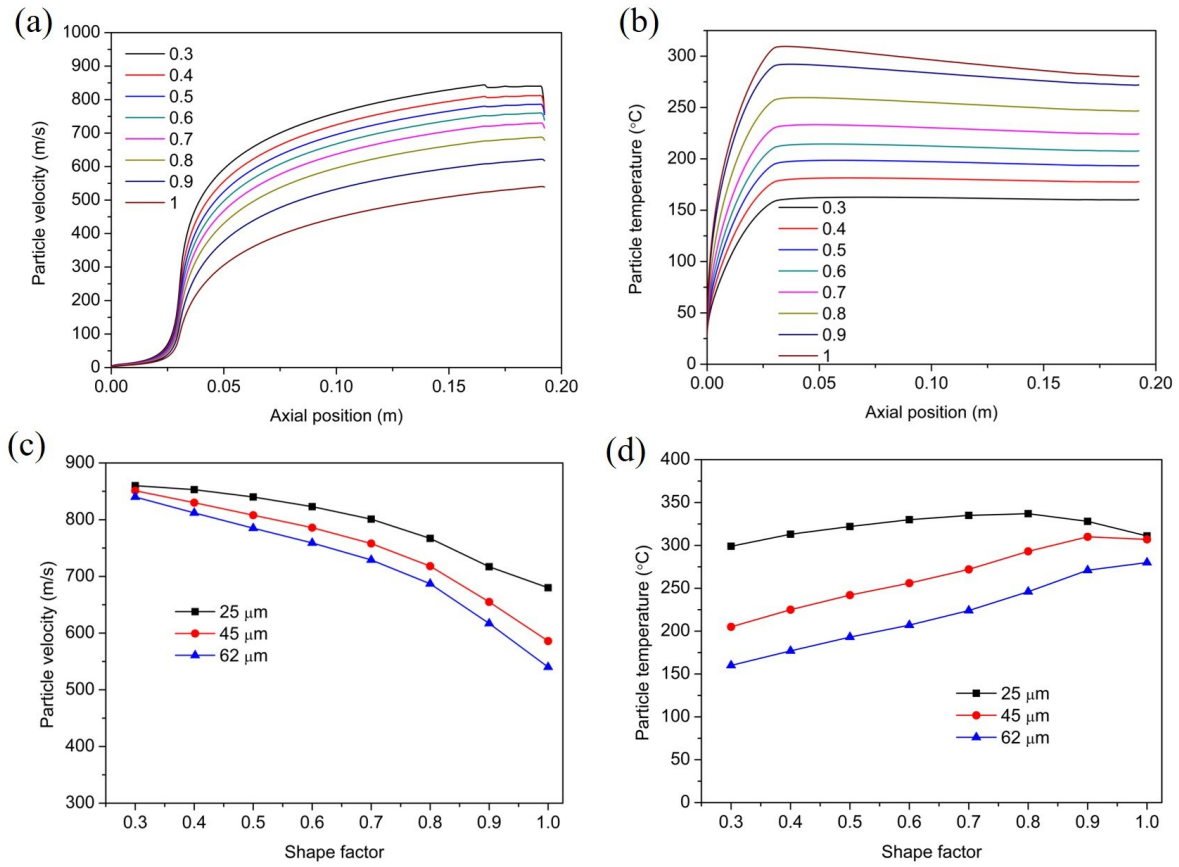

Figure 3-3 (a) Particle velocity and (b) particle temperature along the nozzle central line for the particles with the shape factor (Ψ_{Wa}) from 0.3 to 1; (c) and (d) show particle impact velocity and particle impact temperature as a function of shape factor, respectively. An equivalent average particle size of 25 μm and 45 μm and 62 μm were used for this simulation.

3.2.2 Deposition efficiency

Figure 3-4 shows the DE values of the pure Al and CNT/Al composite feedstocks under different processing conditions. As the propelling gas temperature increases from 300 ℃ to 550 ℃, the DE of each feedstock increases. The DE values of both the CNT/Al composite powders are much lower than those of pure Al powder under the same processing conditions. Besides, the DE of the SSBM composite powder is slightly lower than that of the HSD composite powder. The evolution of DE values is the result of the gap between the mean particle velocity and the critical velocity. In terms of process conditions, the enhanced DE with the propelling gas temperature increased from 300 ℃ to 550 ℃ is due to the improved mean particle velocity relative to the critical velocity. Besides, as shown in Figure 3-2, an increase in the inlet gas temperature also increases the particle impact temperature and thus the DE.

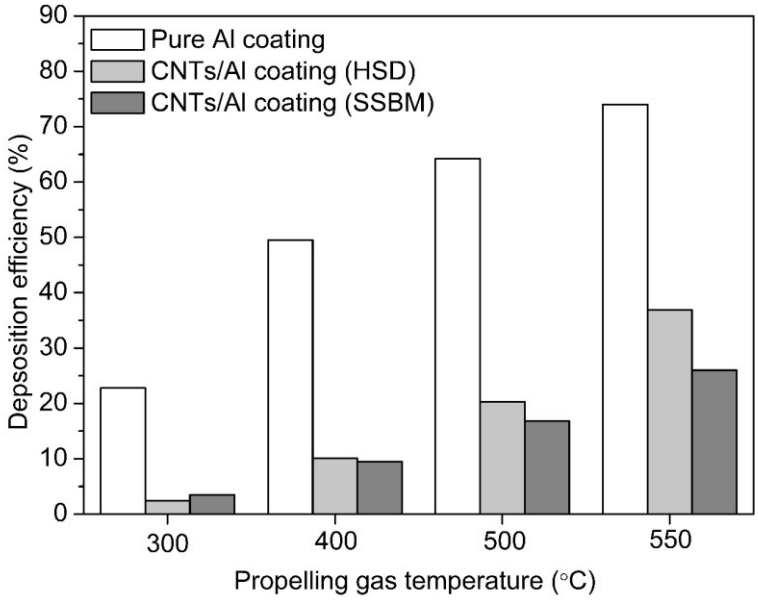

Figure 3-4 DE as a function of propelling gas temperatures.

Due to the similar particle size distribution and morphology, the HSD composite powder and pure Al powder should have similar impact velocities and resultant DE values under the same processing parameters. The microhardness tests on the cross-section of the HSD composite powders revealed an average value of 32 $HV_{0.015}$, which is equal to that of the pure Al powder. Therefore, in terms of the HSD composite powder, the primary cause of the decrease in DE should not be the strengthening effect by embedded CNTs onto the Al particles. Indeed, the critical velocity and DE were found to be relative to the particle surface contamination level [1, 2]. It has been determined that a contamination-free interface is of great importance for the true metal-to-metal contact and the successful particle–substrate or interparticle metallic bonding [3, 4]. Therefore, dispersion of CNTs on the surface of particles may act in a role equivalent to that of oxide films that can prevent the impact particles from metallic bonding. As the surface morphology of pure Al coating fabricated at a gas temperature of 550 ℃ is given in Figure 3-5a and b, the severely deformed particles, and only a few traces of rebounded particles, can be observed. In the case of the HSD composite coating (Figure 3-5c and d), obvious traces of rebounded particles can be noticed on the surface, indicating unsuccessful bonding, and rebounding of the particles due to the limited plastic deformation. Consequently, the HSD composite powders decorated with CNTs show a much lower DE compared to that of the pure Al.

In terms of SSBM composite powders, the microhardness tests revealed an average value of 84 $HV_{0.015}$, much higher than those of the pure Al particle and the HSD composite particle. The enhanced microhardness of the SSBM composite powder is mainly attributed to the uniform distribution of CNTs, work hardening effect, and the grain refinement during the ball milling process, which in turn lead to the decreased DE. It is known that the critical velocity of a feedstock material can be affected by its mechanical properties (i.e. deformability of material) [5, 6]. The increased hardness of the composite powder particles after ball milling may be unfavorable for CS deposition, as the harder particles require a higher critical velocity [7]. As shown in Figure 3-5e and f, many traces of rebounded particles can be observed on the composite coating surface. These rebounded particles were acting as in-situ shot peening particles, inducing a hammering effect on the previous deposited layers [8, 9].

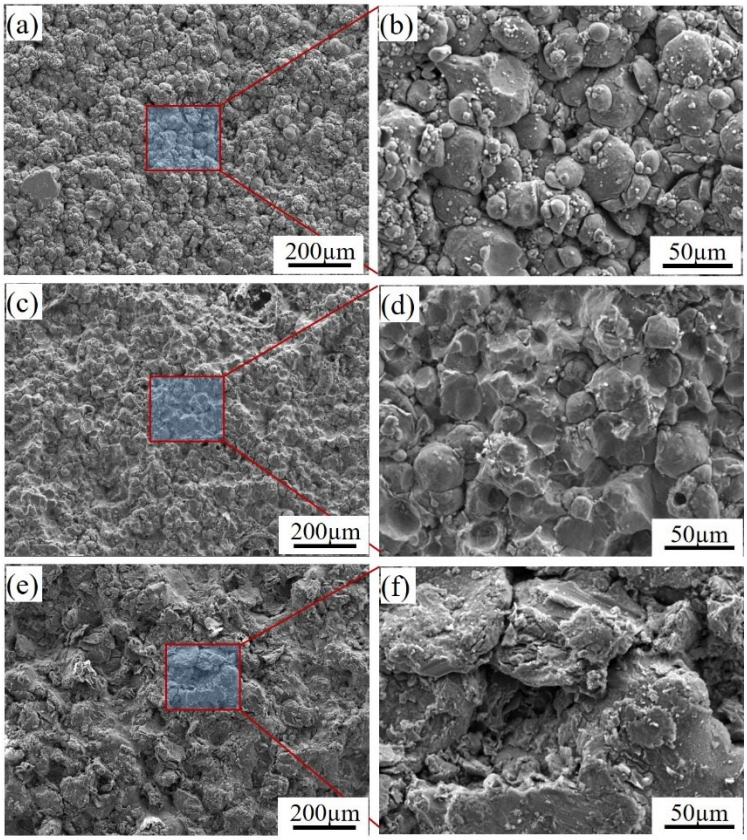

Figure 3-5 Surface morphologies of the pure Al and CNT/Al composite coatings produced at a gas pressure of 3.0 MPa and a temperature of 550 ℃: (a) pure Al coating; (c) HSD composite coating; (e) SSBM composite coatings. (b), (d) and (f) are the corresponding magnified views of (a), (b) and (c), respectively.

3.2.2 Microstructure

Figure 3-6 shows the optical micrograph of the CSed pure Al and CNT/Al composite coatings at different propelling gas temperatures. It can be seen that the coating thickness increases with the increase in propelling gas temperature. For each feedstock, thick and dense coatings were formed at higher gas temperatures, indicating increased DE values. Compared with the pure Al coating, much lower thickness values were obtained in both HSD and SSBM composite coatings (Figure 3-7). Etched cross-sectional images of coatings deposited at 550 ℃ are shown in Figure 3-8. As can be seen from Figure 3-8a and d, the deposited pure Al particles were severely deformed, forming a parachute shape and intimate interparticle bonding. The grains at interparticle boundaries were severely elongated due to strain localization during CS. The HSD composite coating, however, contained voids as indicated by the arrows in images (Figure 3-8b and e). These voids appeared to be gaps along the interfaces of the particles. This result suggests that the dispersion of CNTs onto the particle surface can affect the metallic bonding of the particles during coating build-up. As the processing gas temperature decreases from 550 ℃ to 500 ℃, interestingly, the CNT/Al particles experience greater plastic deformation (Figure 3-9a and c). As the propelling gas temperature decreases further to 400 ℃, a ‘curly’ structure with enhanced bonding between largely deformed particles is formed (Figure 3-9b and d). This observed microstructure evolution is not consistent with the existing concept that a higher particle impact velocity results in a greater particle deformation. The peening effect could be responsible for the enhanced particle deformation at lower processing parameters. A lower DE at a relatively lower propelling gas temperature,

due to the enhanced rebounding particles, leads to a stronger in-situ particle peening effect. As a result, the previously deposited layers undergo greater deformation with the aid of such an enhanced in-situ hammering effect [10]. It should be noticed that this phenomenon is not obviously observed in the case of pure Al coating due to a much higher DE and thus a much lower peening effect.

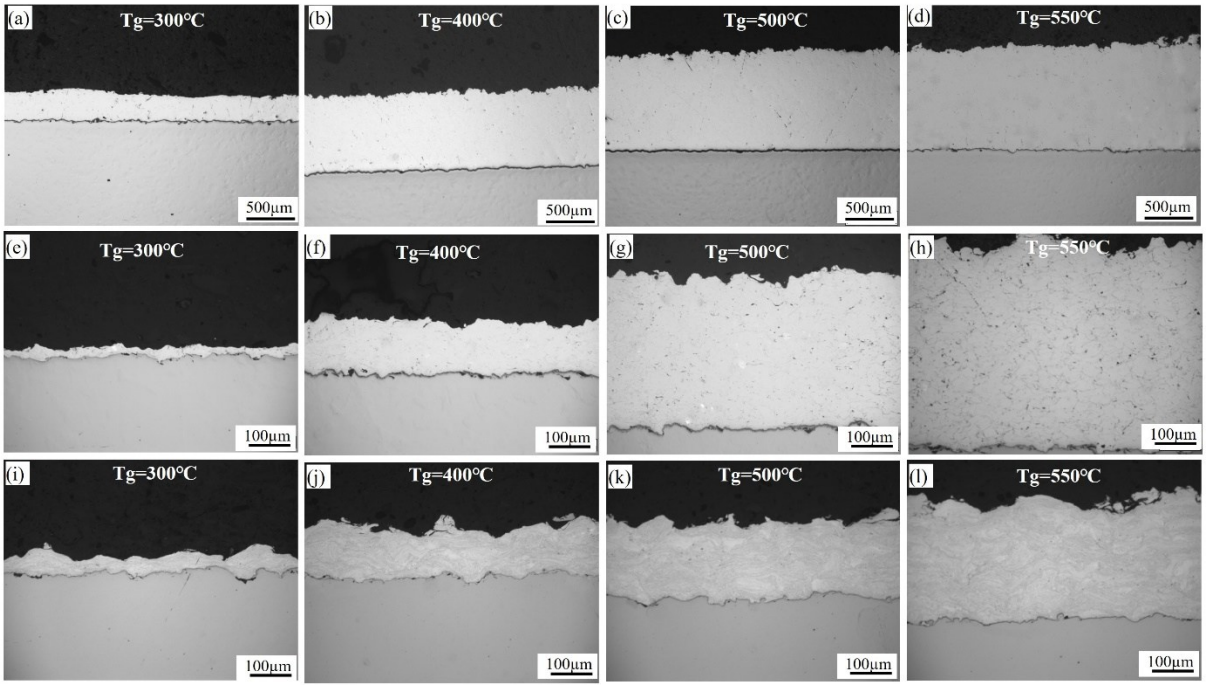

Figure 3-6 Optical micrograph of the coatings produced at different propelling gas temperatures: (a-d) pure Al coatings; (e-h) HSD composite coatings; (i-l) SSBM composite coatings.

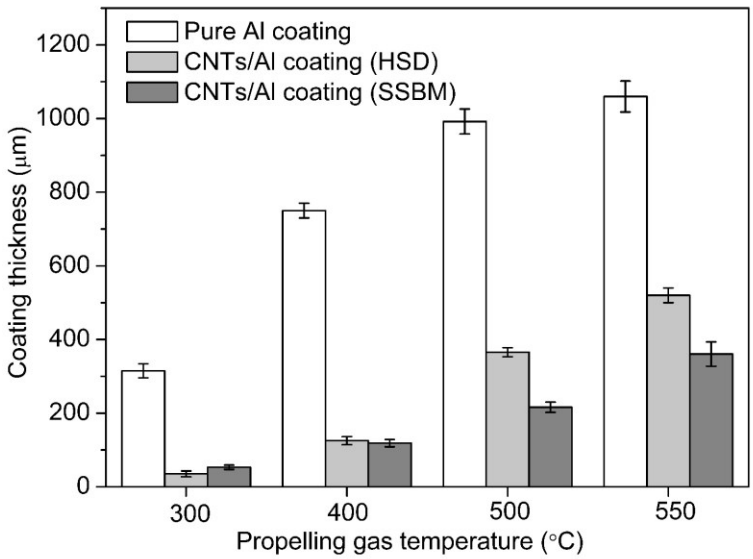

Figure 3-7 Coating thickness as a function of propelling gas temperature.

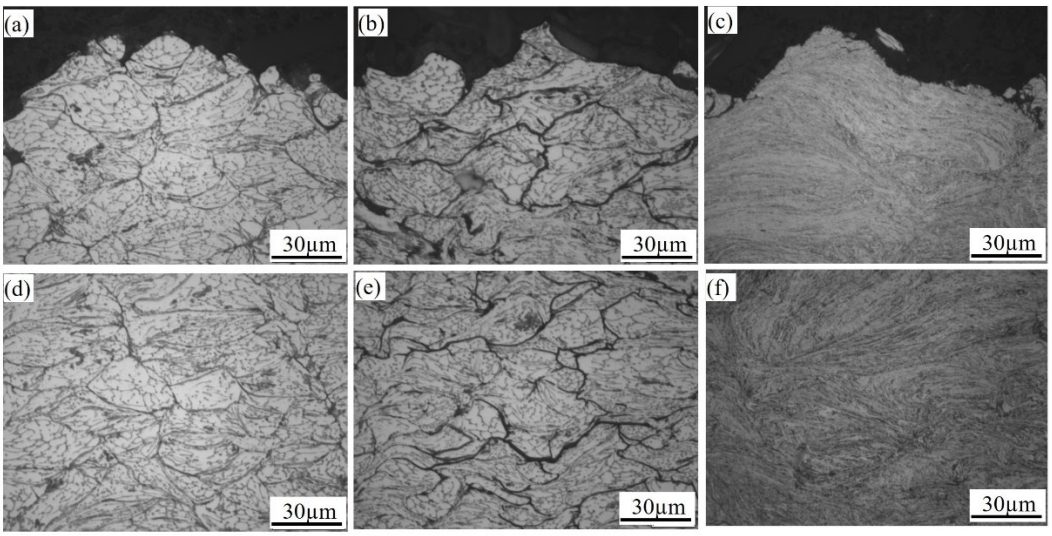

Figure 3-8 Etched cross-sectional microstructures of the coatings deposited at a processing gas temperature of 550 ℃: (a, d) pure Al; (b, e) HSD composite; (c, f) SSBM composite. (a-c) are the top areas and (d-f) are the center areas of the corresponding coatings.

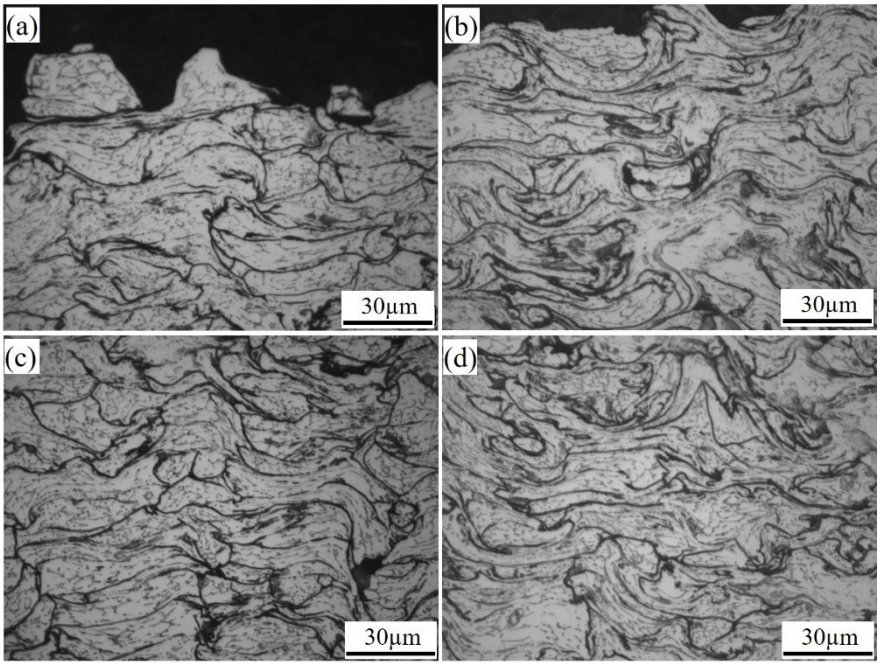

Figure 3-9 Etched cross-sectional microstructures of the CNT/Al HSD coatings fabricated at processing gas temperature of (a, c) 500 ℃ and (b, d) 400 ℃. (a, b) top areas and (c, d) center areas of the corresponding coatings.

Different greatly from pure Al coating and HSD composite coating, the microstructure of SSBM composite coating exhibits a wavy shape with intimate interparticle bonding states (Figure 3-8c and f). This is influenced by the flake-like shape of the initial composite particle. The lamellar structure of the initial composite powder was well retained in the SSBM composite coating. Since the grains of the initial composite particle are sub-micron or even smaller, grain boundaries are not revealed even after chemical etching. Besides this, interparticle boundaries are also difficult to identify.

SEM/EBSD characterization was applied to further investigate the particle deformation behavior and microstructure evolution of the CSed CNT/Al composite coatings produced from two different

feedstocks. As shown in the inverse pole figure (IPF) mappings (see Figure 3-10a and b), significant difference in microstructure can be observed for these two composite coatings. As for the HSD composite coating (Figure 3-10a), the particle deformation is clearly inhomogeneous, as shown by the mixture of large grains and equiaxed small grains. The particle-particle boundaries, which experienced severe deformation during deposition, are characterized by ultrafine grains. Particle interiors are featured by a high density of large angle grain boundary due to a significant plastic strain, but limited recrystallization. According to the grain size distribution (Figure 3-10c), HSD composite coating has an average grain size of about 1.2 μm. The SSBM coating was characterized by uniformly distributed ultrafine grains with an average size of 215 nm (Figure 3-10b and d). The SSBM composite coating demonstrates a much lower pattern quality compared to that of the HSD composite coating, indicating a higher defect density and/or lattice strain inside the ultrafine grains. These defects and the residual stress are mainly produced from the SSBM process, during which the soft Al powder particles are subjected to high energetic impact, and experience extreme deformation. Therefore, the powder preparation approach has significant influence on the microstructure of composite coating.

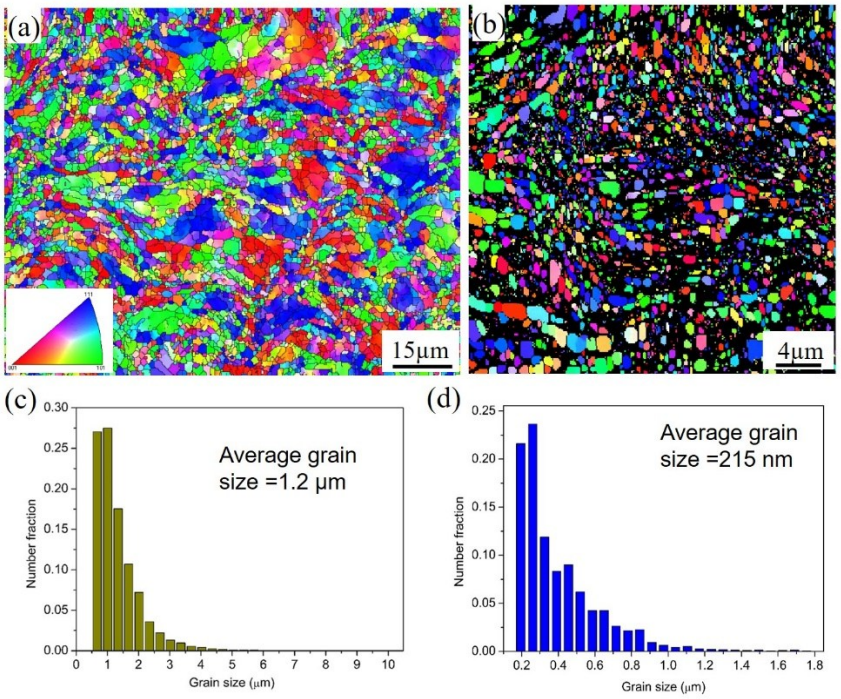

Figure 3-10 EBSD characterization of the cross-section of the as-sprayed composite coatings at a propelling gas temperature of 550 ℃: (a) IPF mapping and (c) grain size distribution of the HSD composite coating; (b) IPF mapping and (d) grain size distribution of SSBM coating.

As shown in Figure 3-11a, thick and fully dense SSBM CNT/Al composite deposits were obtained by using a higher gas pressure in CC5 (P_g=5.0 MPa, T_g=550). Significant improvement in DE is obtained when He was used as the propellent gas in CC6. The etched cross-sectional views in both Figure 3-11b and e present a laminated structure, being similar to that of the composite powder. The SEM images in Figure 3-11c and f also show a dense microstructure with almost no porosity. Besides this, interlocking of wavy-shaped particles can be observed in the CNT/Al composite, which is similar to that obtained from other conditions.

As further shown in the TEM/EBSD image (Figure 3-12a), the SSBM CNT/Al composite is characterized by elongated and ultrafine Al grains, representing the nano-laminated structure. The embedded CNTs show tight contact between the two adjacent Al lamellas, without any gaps. The ‘brick-

and-mortar' structure similar to the natural nacre is thus preserved. The HRTEM image, shown in Figure 3-12d, indicates that the CNT structure is largely retained with the interlayer spacing distance of around 0.34 nm, and no chemical reaction products (e.g. Al_4C_3) are observed at the CNT/Al interface. This is in agreement with the Raman analysis (Figure 3-15). This result confirms that the robust physical and diffusion-assisted bonding state (without any interfacial defects such as porosity) is ideal for enhancing properties. Post-treatment using annealing enables to the further tailoring of the interface structure, which will be studied in the following section. As revealed by the TEM/EBSD analysis (Figure 3-12b), the average size of the elongated Al grains is around 196 nm, which is slightly lower than that determined by SEM/EBSD (Figure 3-10d).

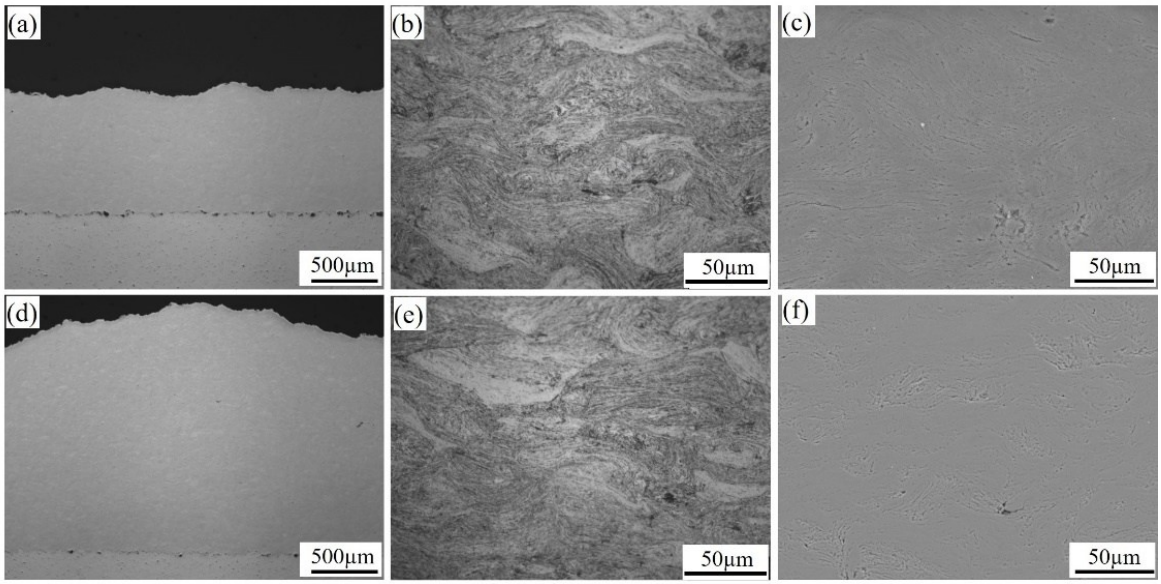

Figure 3-11 Optical micrograph and SEM images of the CSed SSBM CNT/Al composite coating in（a-c）CC5 and (d-f) CC6.

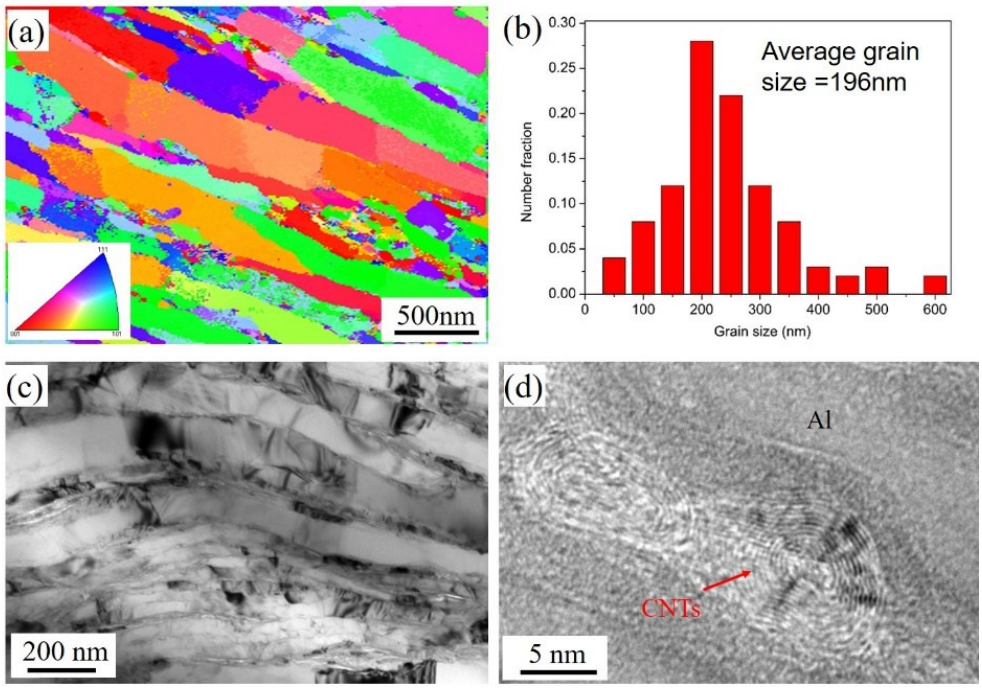

Figure 3-12 (a)TEM/EBSD orientation mapping of the SSBM CNT/Al composite (b) grain size distribution; (c) BF TEM images show the laminar structure; (d) magnified TEM image displays the CNTs embedded into the Al matrix.

3.2.3 Phase composition

XRD and Raman spectra of the CSed coatings and feedstock powders are shown in Figure 3-13 and Figure 3-15, respectively. No obvious peaks corresponding to the Al_4C_3 phase are observed from the XRD patterns (the main Al_4C_3 peak is at ~55° [11]) and Raman analysis (main peak is at ~850 cm^{-1} [12]), which is frequently observed in CNT/Al composites made by powder metallurgy (PM) method [13]. This should be attributed to the low particle temperature feature of CS process.

Due to the relatively low CNT content (1.5 wt.%) within the Al matrix, EDS/SEM is incapable of determining their distributions in the composite coatings. According to previous studies [14-16], the Raman spectra provides an exceedingly powerful tool for the characterization of CNTs, as it can reveal the characteristic G-band, which are high crystalline graphite layers of CNTs. Therefore, Raman mapping of the cross-section of the composite coatings was carried out to determine the distribution of the CNTs. The corresponding confocal Raman mapping images of the representative G-band (1520~1650 cm^{-1}) of the HSD and SSBM composite coatings are shown in Figure 3-14b and e, respectively. The green color indicates the presence of CNTs. In the case of the HSD composite coating (Figure 3-14b), one can notice that CNTs are mainly concentrated around the particle boundaries while CNTs can be rarely observed within Al particles. In the case of the SSBM coating (Figure 3-14e), the CNTs are uniformly distributed over the tested region (30×30 μm^2) without any appreciable agglomeration. These results suggest uniform distribution of CNTs were achieved by SSBM processing, while the HSD process failed in the dispersion of CNTs inside Al particles.

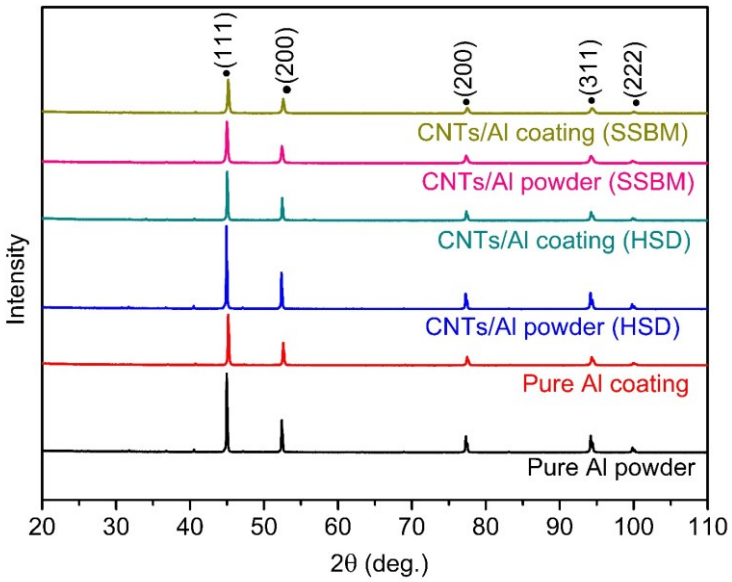

Figure 3-13 X-ray diffraction patterns of CSed coatings and feedstock powders.

In addition, Raman spectroscopy was used to characterize the structural integrity of CNTs. As shown in Figure 3-15, the peaks at~1350 cm^{-1} and ~1570 cm^{-1} correspond to a typical D-band and G-band, respectively [14]. Generally, the G-band reveals highly crystalline graphite layers, and the D-band reveals the presence of defects in the graphite layer [14]. Therefore, intensity ratio (I_D/I_G) is capable of providing information on the crystal structure of CNTs [17, 18]. A higher value of intensity ratio (I_D/I_G) indicates greater damage of the CNT structure. The average I_D/I_G value of HSD powder was measured

to be ~1.26, showing a slight increment compared with the raw CNT powder (1.22). This result suggests that the structural integrity of the CNTs was well retained during the HSD process. Besides, the I_D/I_G value of HSD coating increases to 1.44 from 1.26, indicating some structural damages of CNTs during CS process. Figure 3-14c shows the map of I_D/I_G values in the HSD composite coating. High I_D/I_G values can be found in inter-splat regions. Also, the I_D/I_G value of the SSBM powders increased to 1.35, indicating that the CNTs were slightly damaged during SSBM processing. Compared with the popularly used high-speed ball milling process, the dispersion method used in this study (SSBM) showed less structural damage of CNTs because of the relative low energy input [13]. After CS deposition, the I_D/I_G value slightly increases to 1.40 from 1.35. Therefore, less structural damage of the CNTs was found during the deposition of ball-milled composite powder compared with the CNT coated composite powder. Besides this, a peak shift of G-band from ~1570 to ~1590 cm^{-1} was observed in the CNT/Al composites. The peak shift might originate from the infiltration of Al atoms in the CNTs, causing slight distortion of sp^2 bonding structure of CNTs [19, 20].

In the case of HSD composite coating, since the CNTs were distributed on the surface of the Al particles, they could be shortened in length and fractured due to the impact and shearing between composite particles during the deposition process. In the case of the SSBM composite coating, some structural damage of CNTs was found during the SSBM process, while less damage occurred during the CS deposition process. This is because the SSBM process allows uniform distribution of CNTs inside the Al particles, preventing most of the CNTs from being fractured during the deposition process, due to the fact that severe plastic deformation mainly occurs at the rim of the composite particles. The structural integrity of CNTs could have significant influence on the mechanical properties of the CNT/Al composites.

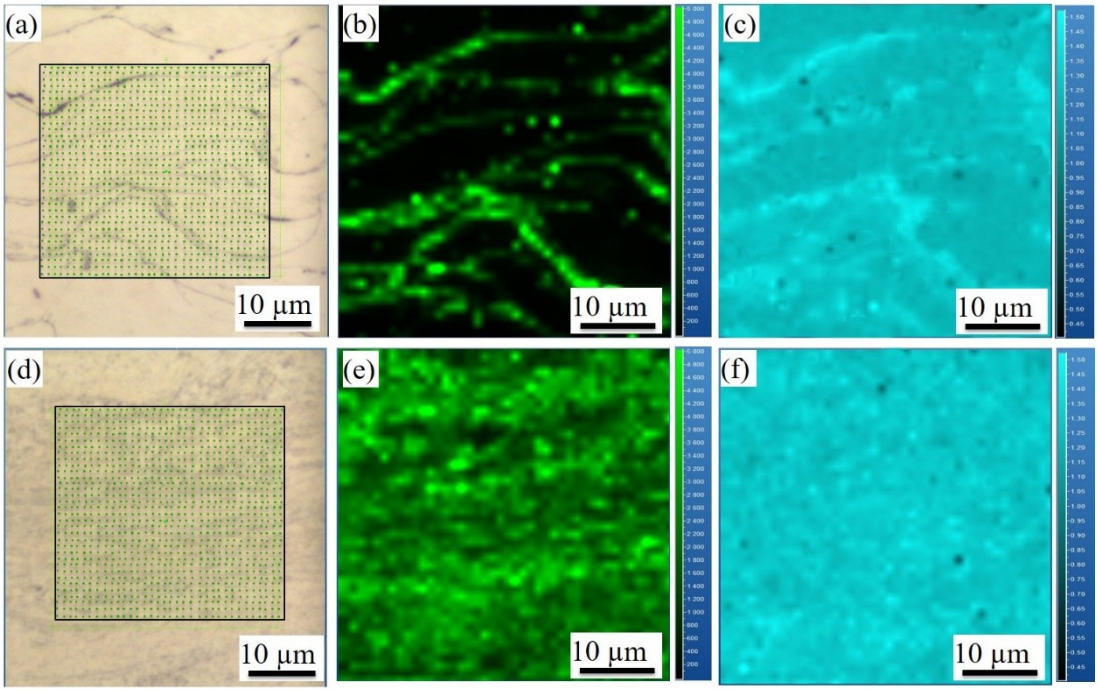

Figure 3-14 Raman spectra mapping of the (a-c) HSD coating and (d-f) SSBM coating fabricated at P_g=550 ℃: (a) and (d) Optical micrographs; (b) and (e) Corresponding confocal Raman maps of G-band intensity (1520~1650 cm^{-1}); (c) and (f) Maps of I_D/I_G ratio value.

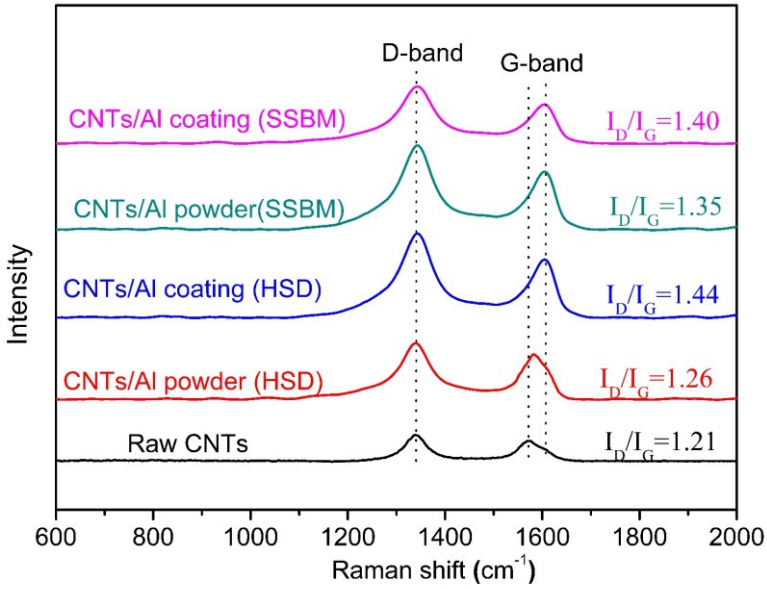

Figure 3-15 Raman spectra of the feedstocks and composite coatings.

3.2.4 Adhesion strength

Tensile pull-off adhesion testing was conducted to investigate the influence of powder type and CS processing conditions on the resulting coating adhesion strength. Figure 3-16 provides the adhesion strength values of the pure Al, HSD and SSBM composite coatings deposited on the stainless steel (SS) substrates using different gas temperatures. The values of HSD and SSBM coatings obtained at 300 ℃ are absent because they were too thin to perform this test on. It is evident that pure Al coatings have much higher adhesion strength values compared to both HSD and SSBM composite coatings. Besides, the adhesion strength of the pure Al coating increases with the increase of the propelling gas temperature, and the highest value of ~37 MPa is obtained at 550 ℃. However, the adhesion strength of HSD composite coating experiences a small decrease when adjusting the gas temperature from 400 to 550 ℃. The adhesion strength of SSBM composite coating shows little variation at different propelling gas temperatures.

The adhesion strength is mainly determined by mechanical (including plastic deformation of particle and substrate) and thermal interaction between particle and substrate when the particles impact onto the substrate with a high velocity. Previous studies found that the particle impact velocity, particle or substrate temperature, substrate roughness and the particle morphology play important roles in improving the adhesion strength based on plastic deformation [21-24]. A higher particle impact velocity at higher gas temperatures benefits the mechanical interlock effect resulting in excellent bonding between the coating and the substrate. In addition, particles sprayed with a higher gas preheat temperature are expected to retain some thermal energy and arrive at the substrate at a higher temperature than those with lower gas preheat temperatures. Such an increase in the gas temperature can reduce the shear stress of Al and can affect the deformation and adhesion mechanisms of the material. Therefore, a higher adhesion strength was achieved for the pure Al coating obtained with higher gas temperatures.

The HSD composite coatings showed much lower adhesion strength values. The presence of CNTs around the Al particles, on one hand, can act as impurities which can prevent the exposure of fresh metal and metallic bonding of the composite particle and substrate; on the other hand, the enhanced work

hardening of the CNTs can prevent the particle from plastic deformation and the formation of adiabatic shear instability (ASI) between the particle and the substrate. In the case of the SSBM composite coating, even though the flaky shape particle may possess a higher particle impact velocity due to its better acceleration effect in the gas flow (Figure 3-3), the enhanced work hardening effect originated from ball-milling and CNTs addition, can lead to a higher critical velocity for successful bonding. Further, as suggested by the FEA simulation result from S.Yin et al. [25], quite a small fraction of interface can realize the true metallic bonding for the irregular particle.

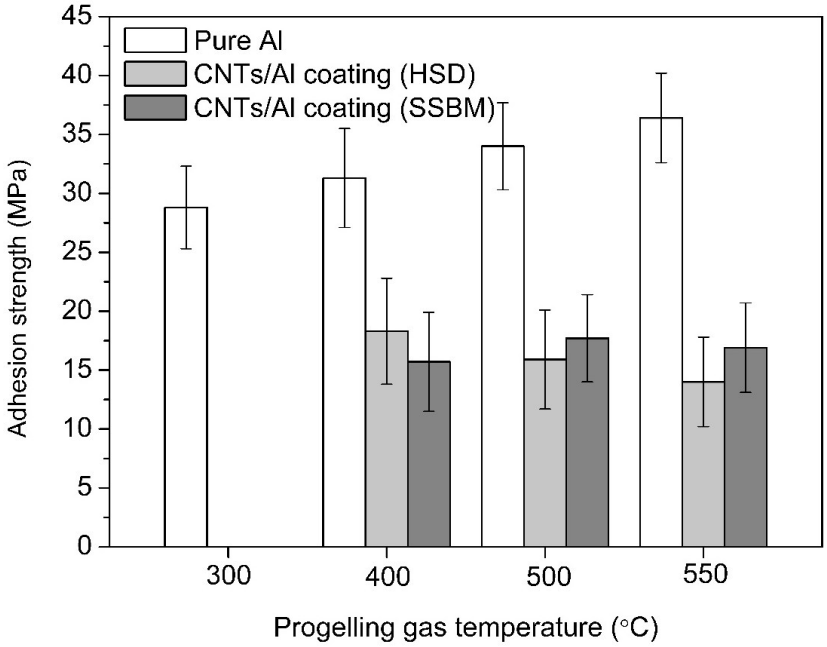

Figure 3-16 Adhesion strength of CSed pure Al, HSD composite and BBSM composite coatings deposited on SS substrates using different propelling gas temperatures.

3.2.5 Microhardness

The measured microhardness values of pure Al and composite coatings as a function of processing gas temperatures are shown in Figure 3-17. Microhardness of the as-sprayed pure Al coating gradually increased from 36 to 50 $HV_{0.1}$, as the processing gas temperature increased from 300 to 550 ℃. This is because the higher particle impact velocity achieved at a higher gas temperature leads to enhanced particle deformation and fully dense coatings. The 1.5 wt.% CNT/Al composite coating produced from the HSD powder showed a slight increment in microhardness at low propelling gas temperatures compared with the pure Al coating. As the propelling gas temperature increases, its microhardness decreases slightly, even being much lower than that of pure Al coating. These results demonstrate that the dispersion of CNTs by the HSD approach did not achieve a significant strengthening effect on the composite coatings, but adversely affected the metallic bonding of the particles, resulting in decreased strength. The CNT/Al composite coating produced from the SSBM powder had a value of 115 $HV_{0.1}$, which was more than twice that of pure Al coating. Nevertheless, the CNT/Al composite coatings obtained at different propelling gas temperatures, exhibited similar values. However, higher values of 125 $HV_{0.1}$ and 132 $HV_{0.1}$ are obtained when further increasing the propelling gas pressure to 5.0 MPa (CC5) or using high pressured He as the propelling gas (CC6). One important reason for such significant improvement in microhardness is that fully dense and ultrafine microstructure was achieved in these

SSBM composite coatings. Besides, the uniformly distributed CNTs also play an important role in strengthening the mechanical properties of the composite.

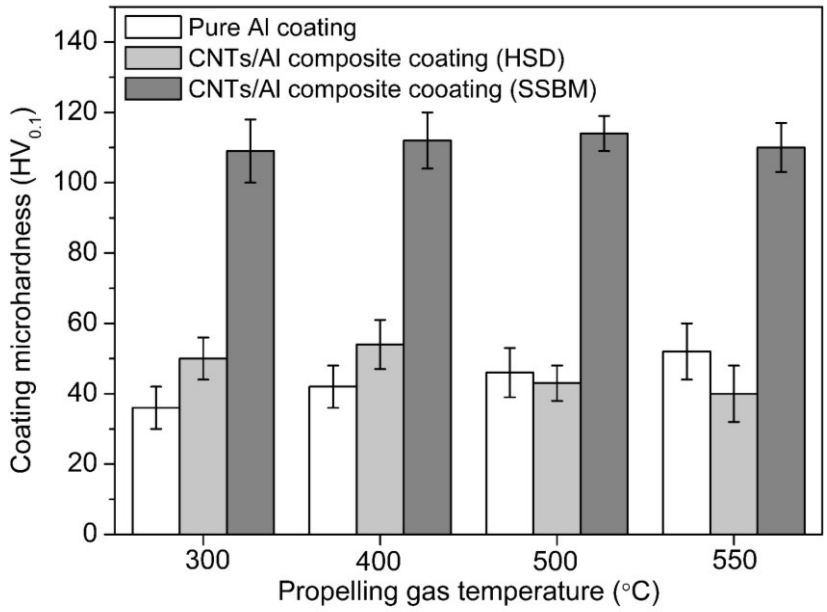

Figure 3-17 Microhardness of the as-sprayed coatings.

The strengthening mechanisms of the CSed CNT/Al composite coatings are related to the microstructure. The microhardness of the CSed composites can be expressed as follows [26]:

$$\mathrm{H} = H_0 + \Delta H_{WH} + \Delta H_{GB} + \Delta H_{CNTs} \qquad (3\text{-}1)$$

where H_0 is the microhardness of annealed Al with coarse grains (15.0 $HV_{0.1}$), ΔH_{WH} is the strengthening due to work hardening, ΔH_{GB} the strength contribution of the grain boundary (Hall-Petch relation), and ΔH_{CNTs} hardening by the dispersion of CNTs into Al matrix. The work hardening is express as follows [27]:

$$\Delta H_{WH} = k_w \rho_{dis}^{1/2} = \alpha G b \rho_{dis}^{1/2} \qquad (3\text{-}2)$$

Here, G is the shear modulus of Al, b is the Burgers vector, α is a constant (0.3), and $\rho_{dis}^{1/2}$ is the dislocation density of the grain interior. The dislocation density of a kinetic sprayed Al coating was reported to be ~$10^{11}$$cm^{-2}$ [28]. Since the plastic deformation of the HSD composite powder was similar with the pure Al powder, the dislocation density in the HSD composite coating should have had a magnitude equal to that of pure Al coating. Therefore, the calculated work hardening effect of the CSed HSD composite coating was 27.9 HV, which was consistent with the value of pure Al coating in Ref [29]. As for the SSBM composite coating, the work hardening effect resulting from the SSBM powder preparation process was more pronounced than that from the CS process. This is because a large grain boundary area of the nanosized Al matrix accommodated the dislocations during the CS deposition [27, 29]

The grain boundary hardening (Hall-Petch relation) can be expressed as follows:

$$\Delta H_{HP} = k_H d^{-1/2} \qquad (3\text{-}3)$$

Where k_H is constant (0.14 MPa $m^{1/2}$), and d is the grain diameter. In this work, the grain size of the CSed HSD composite coating was similar with that of the pure Al coating, which was measured to be 1.2 μm (Figure 3-10c). The calculated grain boundary hardening of the HSD coating was 13.9 HV. Since

the average grain size of the CSed SSBM composite was measured to be 215 nm (Figure 3-10d), the grain boundary hardening of the SSBM composite coating was 32.8 HV. These results indicate that greater grain boundary hardening effect was achieved in the SSBM composite coating due to its ultra-fine microstructure.

The hardening by CNTs embedded in the Al matrix was attributed to Orowan looping by CNTs [17]. The stiff CNTs in the ductile Al matrix act as barriers to dislocation movement. As a result, pile-ups of the dislocations occurred, enhancing hardening of the Al matrix around the CNTs. Hardening by CNTs can be expressed as follows [17, 26]:

$$\Delta H_{CNTs} = \frac{0.13Gb}{\lambda}\ln(2r/r_0) \qquad (3\text{-}4)$$

Where r is the volume equivalent radius of a CNT (1.593×10^{-7}m), r_0 is the core radius of a dislocation (3.5×10^{-9}m) and λ is the distance between CNTs. In the case of HSD composite coating, since the CNTs were mainly distributed in the interparticle boundaries, and obvious gaps between CNTs and Al matrix can be observed (see Figure 3-14b), the strengthening effect by CNTs was largely weakened. In the case of the SSBM composite, the CNTs were uniformly distributed into the Al matrix, resulting in the significant improvement in microhardness because of the Orowan looping by the CNTs in the composite.

3.4 Single particle deposition and FEA simulation

The deposition behavior of a single particle was studied to provide direct insight into the bonding mechanism of full-coating deposition. Figure 3-18 shows the overviews of different surface morphologies at SS substrates surface after impact of several pure Al, HSD and SSBM composite particles. It can be observed that both the pure Al and HSD composite particles deform extensively, generating metal jet at the rim of the deformed splats. Some cracks or even fragments resulting from intense impact can be observed on the HSD composite splats, which are not, or rarely apparent for the pure Al particles. This phenomenon suggests that the CNT reinforced Al composite particle seems to be much more brittle than the pure Al powder. Nevertheless, the SSBM composite splat presents a distinct morphology. Different from the traditionally-employed spherical particle, the in-flight and impact behavior of the flaky one is more complex in the supersonic turbulent flow. Therefore, FEA simulation combined with the individual splat deposition experiment using the Al flaky powder was carried out to better understand the formation mechanisms.

As shown in Figure 3-19, three possible postures were modelled to represent the irregular impact behavior of a flaky particle. In the case of horizontal impact (see Figure 3-19a), the flaky particle undergoes limited deformation within 10 ns due to the large interfacial contact area. Similar to the morphology of individual splat (see Figure 3-19a), the metal jet (marked by red arrows) is observed at the rim of the deformed cake-like particle. This indicates the possible occurrence of metallurgy bonding between the particle and the substrate after deposition. More usually, the flaky particle impacts upon the substrate surface with a certain incidence angle (here an example of a particle with an angle of 45°). As shown in Figure 3-19b, as the initial contact takes place on only one side, the severe deformation gradually spreads across the entire flaky particle. To the end, the particle is aligned on the substrate surface with a prominent metal jet formed in the initial contact side, which is consistent with the single splat morphology in Figure 3-19b. In this case, it should be noticed that a torque is generated at the other side away from the initial contact area as a result of the inertia force [25]. This additional torque tends to bend the last deformed side to the substrate surface, thereby forming a perfect cake-like morphology. In the case of vertical impact, as shown in Figure 3-19c, the lower part of the particle with a small area undergoes significant deformation, and metal jet is formed at the rim of the particle. However, the top of the particle still retains undeformed, which is consistent with the single splat morphology (Figure

3-19c). It should be noticed that such a vertical impact held a very low fraction in the single particle experiment.

A model with multi flaky particles randomly aligned above the substrate surface was used to simulate the coating build-up process. Figure 3-20 shows the contours of equivalent plastic strain and temperature evolution at different time. After impacting on the surface of previously deposited layers, the flaky particles deform severely, realizing metallic bonding with each other. Consequently, a laminar structure is formed by combing of the severe plastic deformation of the deposited particles themselves and the in-situ peening effect produced by subsequent particles during coating build-up in spite of the different impact postures. Such an effect is more prominent for the CNT reinforced composite powder with a relative low DE. The resultant tamping effect of rebounding particles can promote the metallic bonding between the deposited flaky particles, which is beneficial for the mechanical properties [8, 30].

As shown in Figure 3-21, a model with several spherical particles was also used to compare with the simulation results of flaky particles. The same particle impact velocity (600 m/s) and temperature (200 ℃) were used for the FEA simulation in both cases. It can be noticed that the spherical particles exhibited greater deformation and higher plastic strain at the particle-particle regions compared to the case of flaky particles. Therefore, it is speculated that the flaky particles may result in a worse metallic bonding and adhesion in comparison with the spherical particles. Similar results were also reported by S.Yin et al.[25].

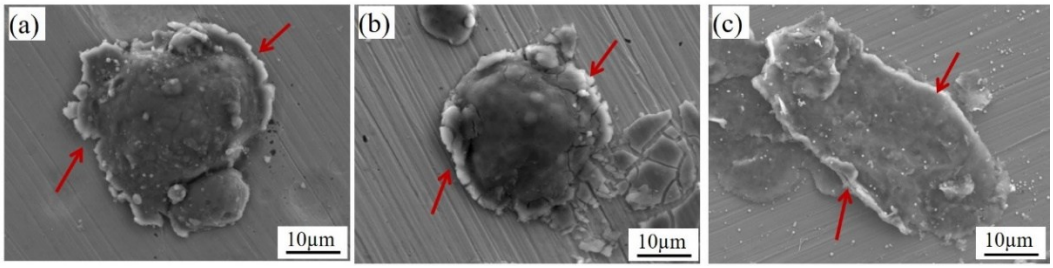

Figure 3-18 Single splat morphologies of (a) pure Al, (b) HSD and (c) SSBM composite deposited on SS substrate at P_g=3.0 MPa, T_g=550 ℃.

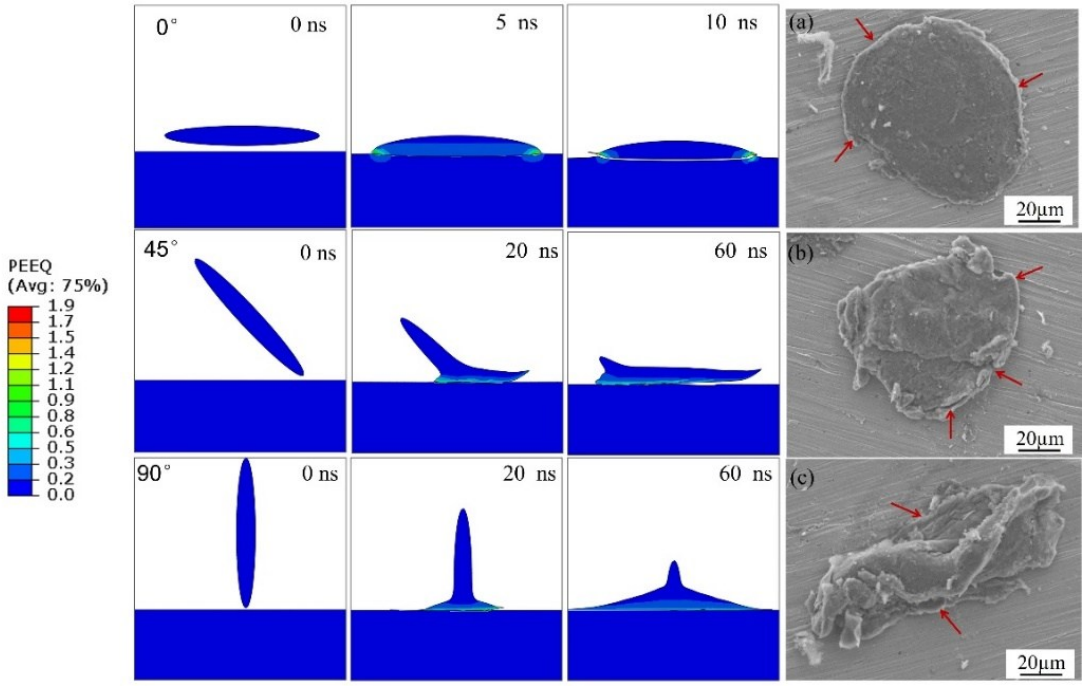

Figure 3-19 Evaluation of effective plastic strain contours and corresponding morphologies of the deposited single Al splat observed by SEM in the cases of the different posture angles: (a) 0°; (b) 45°; (c) 90°.

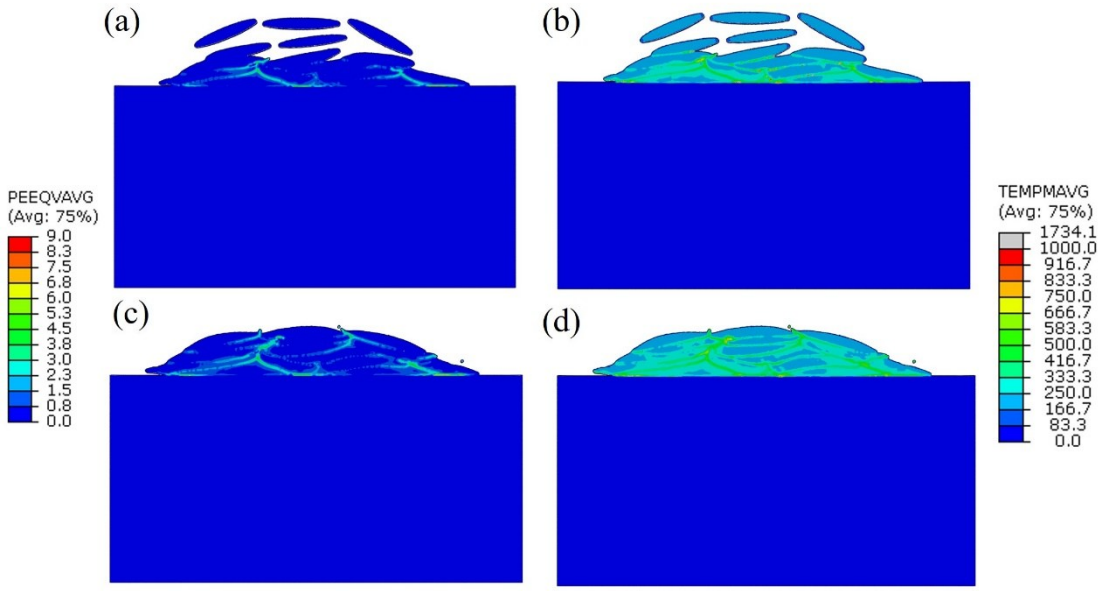

Figure 3-20 Contours of (a, c) effective plastic strain and (b, d) temperature of several flaky Al particles depositing on a SS substrate at different time: (a) and (b) 15 ns; (c) and (d) 25 ns.

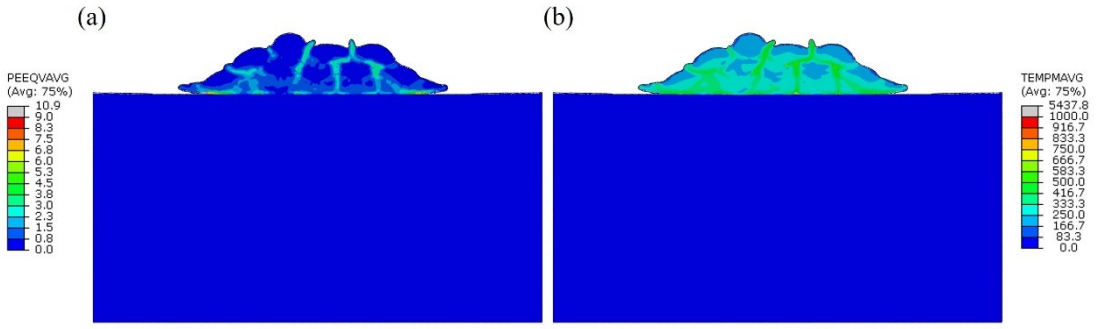

Figure 3-21 Contours of (a, c) effective plastic strain and (b, d) temperature of several spherical Al particles depositing on a SS substrate at 25 ns.

3.5 Effect of annealing treatment

The SSBM CNT/Al composite deposits obtained from CC5 and CC6 were annealed at different temperatures (300-550 ℃) and for different durations (2-12 h).

3.5.1 Phase composition

The XRD patterns and Raman spectra of the SSBM CNT/Al composite deposits (CC5) annealed at different conditions are shown in Figure 3-22 and Figure 3-23. In the as-sprayed state, no obvious diffraction peaks corresponding to the Al_4C_3 phase are observed from the XRD patterns and Raman spectra, which is consistent well with our previous results (Figure 3-13). Besides, the XRD patterns in Figure 3-13 show the trace of oxides (e.g. Al_2O_3) in all the samples. These oxides are initially formed during the ball-milling process and are conserved in the CS deposit. Further, no evident difference can be observed in the XRD patterns of the annealed samples. However, according to the Raman analysis,

it can be noticed that the Al_4C_3 phase starts to form at 500 ℃, and its amount increases at a higher annealing temperature and a longer annealing time. It was reported that Al_4C_3 can be formed by the solid-state reaction between CNTs and Al during hot-press sintering (600 °C) of the CNT/Al composite [31, 32]. Besides this, according to Z.Y. Yu et al. [33], interfacial reaction between CNTs and Al matrix and the formation of Al_4C_3 occurred at an annealing temperature of 500 ℃ for 4 h. This phenomenon was also confirmed in this study. The innate defects, such as disconnection of C-C bonding of the CNTs and disconnections/fracture of the CNTs produced by severe deformation, can play a role as precursors to the chemical reaction and destruction of the CNTs [34]. As presented from the TEM images and Raman analysis in Figure 3-12d and Figure 3-14, the milling process, as well as the CS deposition process may introduce extra structural defects to the CNT , which makes them more susceptible to reaction with the Al matrix and leads to a low activation energy [35]. Ci et al. [36] have revealed that CNT/Al interfacial reaction occurs stage by stage due to the special structure of CNTs. In the first stage, the C atoms at the cap or defect sites preferentially react with Al, and the Al_4C_3 can nucleate at these defect places even at a temperature even lower than 500 °C. In the second stage, following the consumption of C atoms at the cap or defect sites, the C atoms elsewhere will diffuse through the Al matrix toward the nucleus, and then Al_4C_3 begins to grow and coarsen. The quantity of this phase increases as a function of the annealing temperature and duration of time.

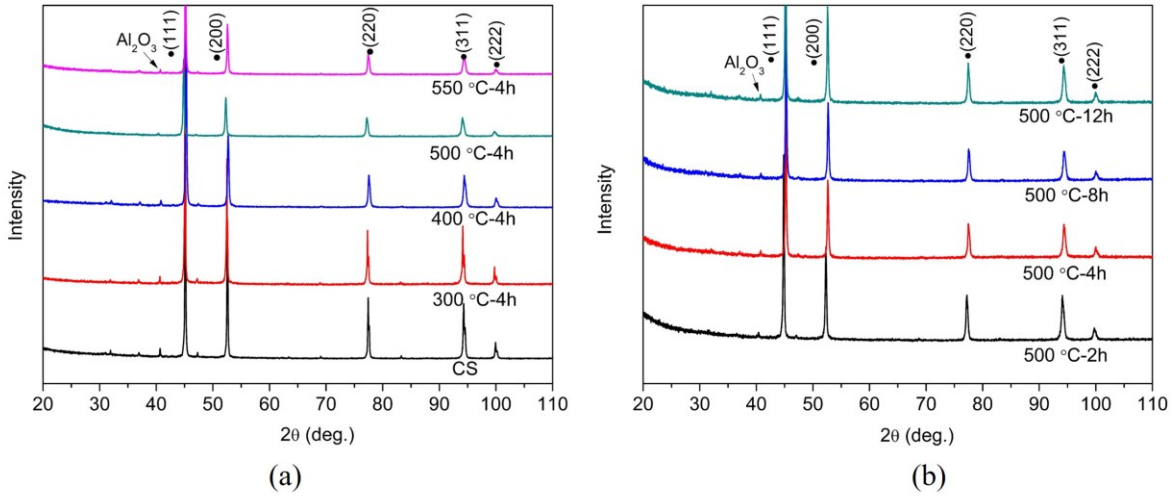

Figure 3-22 XRD patterns of the SSBM CNT/Al composite deposits (obtained from CC5) annealed at different (a) temperatures and (b) duration (annealing temperature kept at 500 ℃).

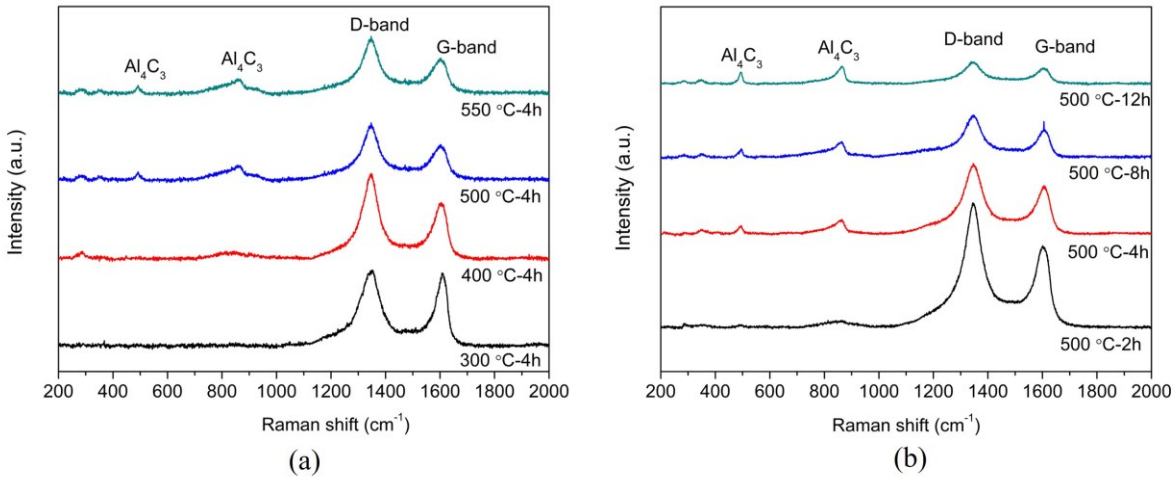

Figure 3-23 Raman shifts of the SSBM CNT/Al composite coatings annealed under different temperatures (a) and for different durations at a constant temperature of 500 ℃ (b).

3.5.2 Microstructure

Microstructures of the heat-treated SSBM CNT/Al composites at different temperatures are shown in Figure 3-24. No significant changes in microstructure can be found compared to the as-sprayed state (Figure 3-11c). When the composites were annealed at a higher temperature or for a longer duration, the interparticle boundaries become more and more obscure. However, a few small pores can be still observed on the etched cross-section of the annealed samples.

Figure 3-25 shows BF TEM images of the cross-section of CNT/Al composite sample annealed at 500 ℃ for 4 h. A similar laminated structure was well-preserved in the annealed sample in comparison to that of the as-sprayed sample. Besides, the annealed composite sample has a mean grain size of 230 nm, which was similar to that of the as-sprayed composite coating. This indicates that grain growth of the composite coating did not occur during the heat-treatment process. The thermal stability of the this SSBM CNT/Al composite may be attributed to Zener drag and solute drag phenomena [37]. Similar results have been reported by K. Kang et al. [29] and Zhou et al. [37], who investigated the heat-treatment effect on pure nanocrystalline Al and CNT/Al composite with various temperatures and duration of time.

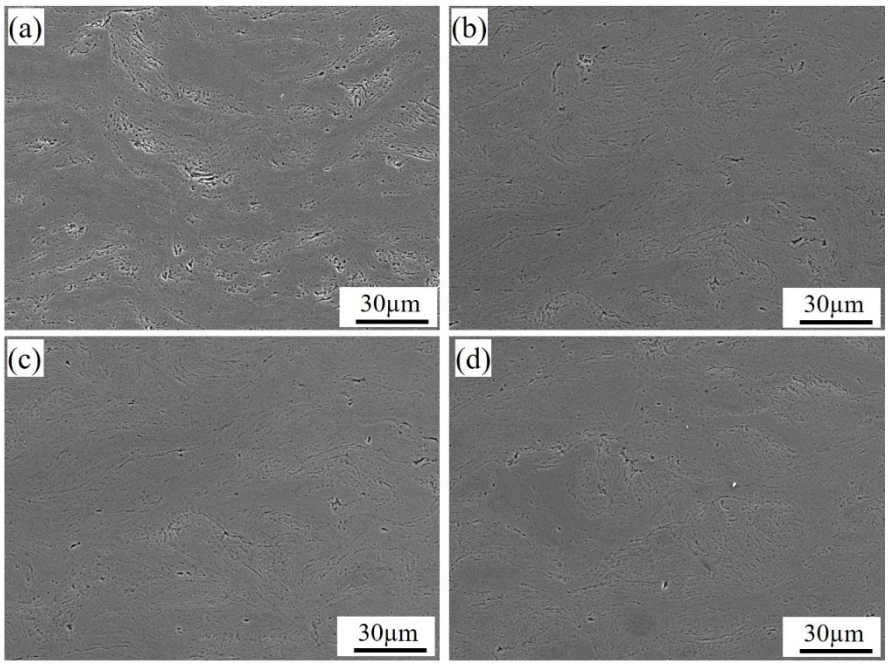

Figure 3-24 SEM images of SSBM CNT/Al composite annealed at different temperatures: (a) 300 ℃; (b) 400 ℃; (c) 500 ℃; (d) 550 ℃.

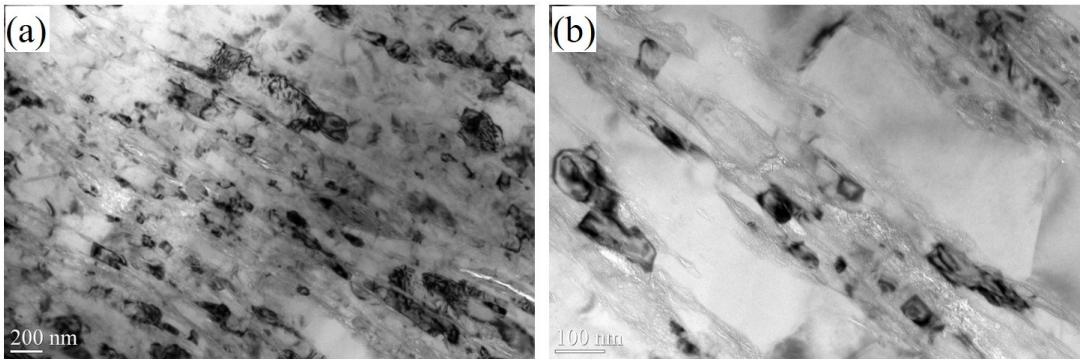

Figure 3-25 TEM images of the CNT/Al composite deposit (CC5) annealed at 500 ℃ for 4 h.

3.5.3 Microhardness

The measured microhardness values of the SSBM CNT/Al composite as a function of annealing temperature and duration are shown in Figure 3-26a and b, respectively. It can be found that the as-sprayed composite obtained from CC6 had a higher value than that obtained from CC5. The microhardness of CC5 composite decreases slightly as the annealing temperature increases from 300 ℃ to 550 ℃. Moreover, a slight decrease in microhardness can also observed with the increase of annealing duration when the annealing temperature was kept at 500 ℃. The CC6 composite showed a sharper decrease in microhardness within the first 4 h compared to that of the CC5 composite. Further increase in annealing temperature and extending of annealing duration did not lead to much change in microhardness. The slight decrease in microhardness in the initial annealing state should be attributed to the relief of strain stress, which was produced from the ball-milling and CS process. However, because of the limited grain growth during heat treatment, no significant changes in microhardness could be found at a higher temperature or a longer duration.

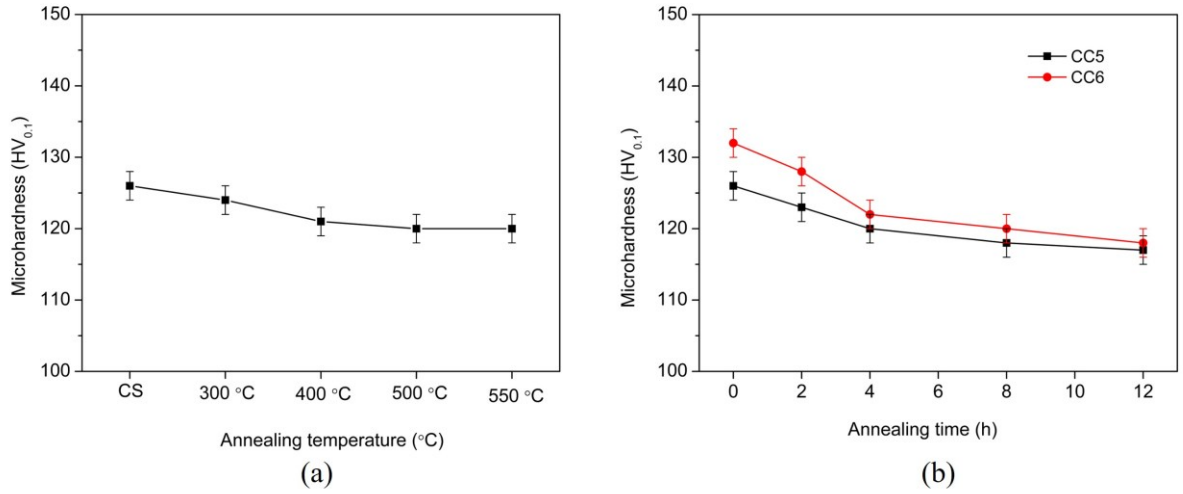

Figure 3-26 Microhardness evolution as a function of (a) annealing temperature and (b) annealing duration (the annealing temperature kept at 500 ℃).

3.5.4 Tensile property

Figure 3-27a shows the typical tensile stress vs strain curves of the as-sprayed and annealed SSBM CNT/Al composite samples (CC5) at different temperatures for 4 h. The values of ultimate tensile strength (UTS) and elongation with error bars are shown in Figure 3-27b and c, respectively. It is

revealed that the as-sprayed composite samples were fractured at an earlier stage, having an average UTS value of 168 MPa, but almost no elongation. A lower annealing temperature seemed to have no positive affect on the tensile property of these composite samples. However, a slight improvement in both tensile strength and elongation was achieved when using higher annealing temperatures (500 ℃ and 550 ℃). As shown in Figure 3-28, when the annealing temperature was kept at 500 ℃, increase of the duration of time (from 2 h to 12 h) could also slightly improve both the UTS and elongation of the composite. The highest UTS value of 205 MPa and elongation of 1.8% were obtained when the samples were annealed at 500 ℃ for 12 h. However, their tensile properties have not been improved as much as expected, being still very poor compared to the samples fabricated by PM process (higher than 400 MPa).

Moreover, tensile anisotropy was also investigated by using tensile samples cut in the direction parallel or vertical to nozzle traverse direction. As shown in Figure 3-29, it can be seen that an small inherent tensile anisotropy exists in both the as-sprayed and annealed composite deposits, with a slightly higher values measured at the parallel direction. A similar phenomenon was also reported on the CSed copper deposits by a previous study [38]. The authors attributed the tensile anisotropy to the parallel multiple passes during CS deposition [38].

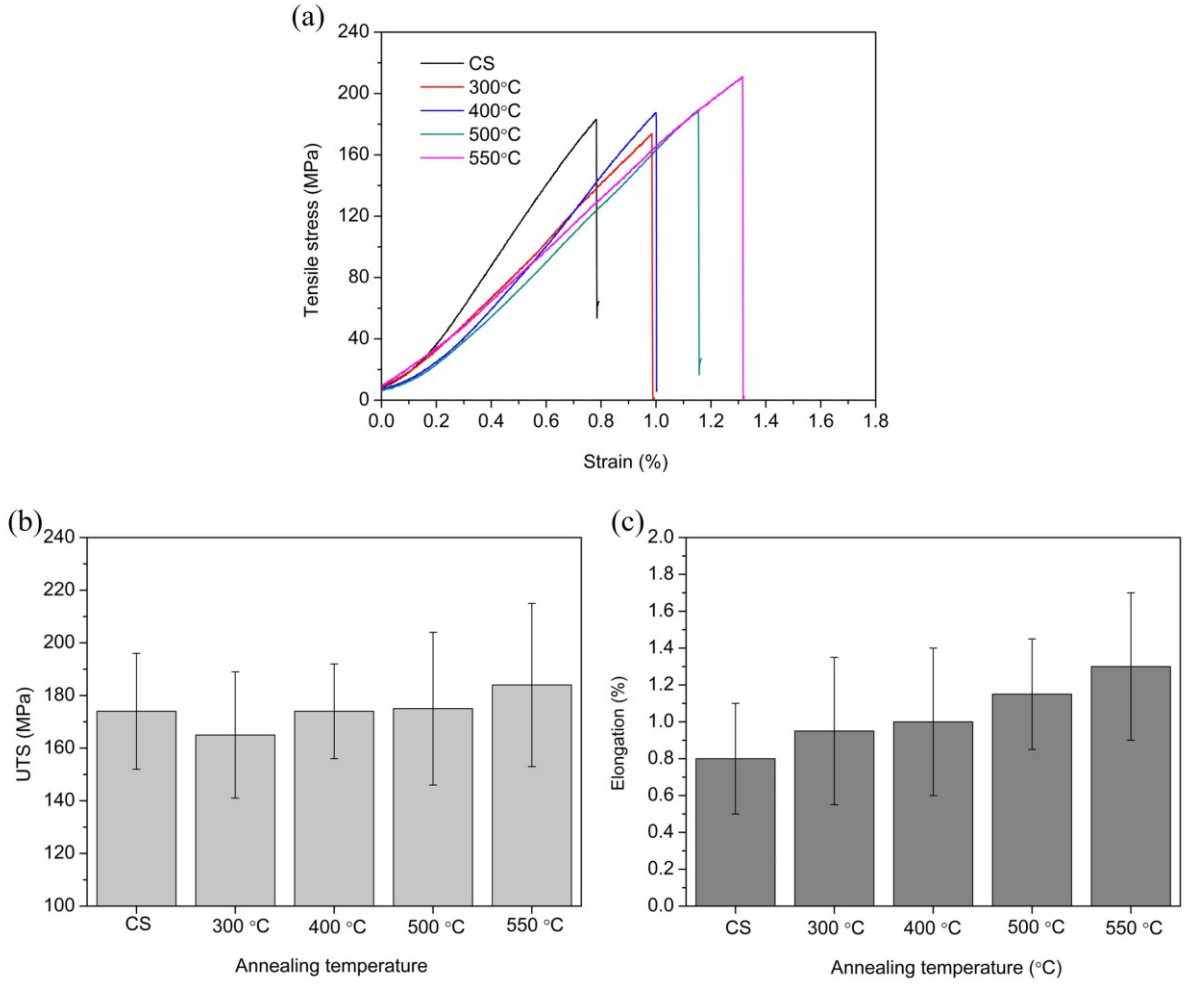

Figure 3-27 (a) Tensile stress-strain curves for SSBM CNT/Al composites annealing treated at different temperatures for 4 h. (b) and (c) summarize the UTS values and elongation of the specimens, respectively.

The fracture surface morphologies were examined by using SEM to further study the fracture mechanisms of the SSBM CNT/Al composite deposits. As shown in Figure 3-30 (a-c), fracture surface of the as-sprayed deposit exhibits multi-scale laminar microstructure, with micro-level deformed splats and a few porosity morphologies. It can be noticed that fracture takes place not only along the weak inter-splat boundaries, but also through the intergranular. The fracture model in the micro-level is schematically described in Figure 3-32a. The presence of pores and weak inter-splat bonding due to insufficient plastic deformation could facilitate the fracture behavior of the composite deposits. As presented in the FEA simulation result (see Figure 3-20), flaky-shaped particles experienced less plastic deformation after impact with the substrate or with the previously deposited layer compared to the spherical one, even though the rebounding particles due to unsuccessful deposition can further deform these splats and enhance metallic bonding. However, it can be speculated that there are still some weak interfacial bonding regions within the deposits. Therefore, heat treatments were performed to enhance the inter-splat bonding and heal some defects, such as small pores, by atom diffusion at high annealing temperature. As can be seen from the overview of the fracture surface in Figure 3-30e and h, the annealed samples present a similar fracture morphology compared to the as-sprayed state. However, the magnified views reveal that fracture primary occurs through the intergranular, rather than along inter-splat boundaries, especially for samples treated for a longer duration. The change of fracture morphology after annealing treatment can be attributed to the improved inter-splat bonding. Nevertheless, ductile characteristics with numbers of dimples are absent on the fracture surface of the annealed samples. As a result, tensile properties of the annealed samples were slightly improved.

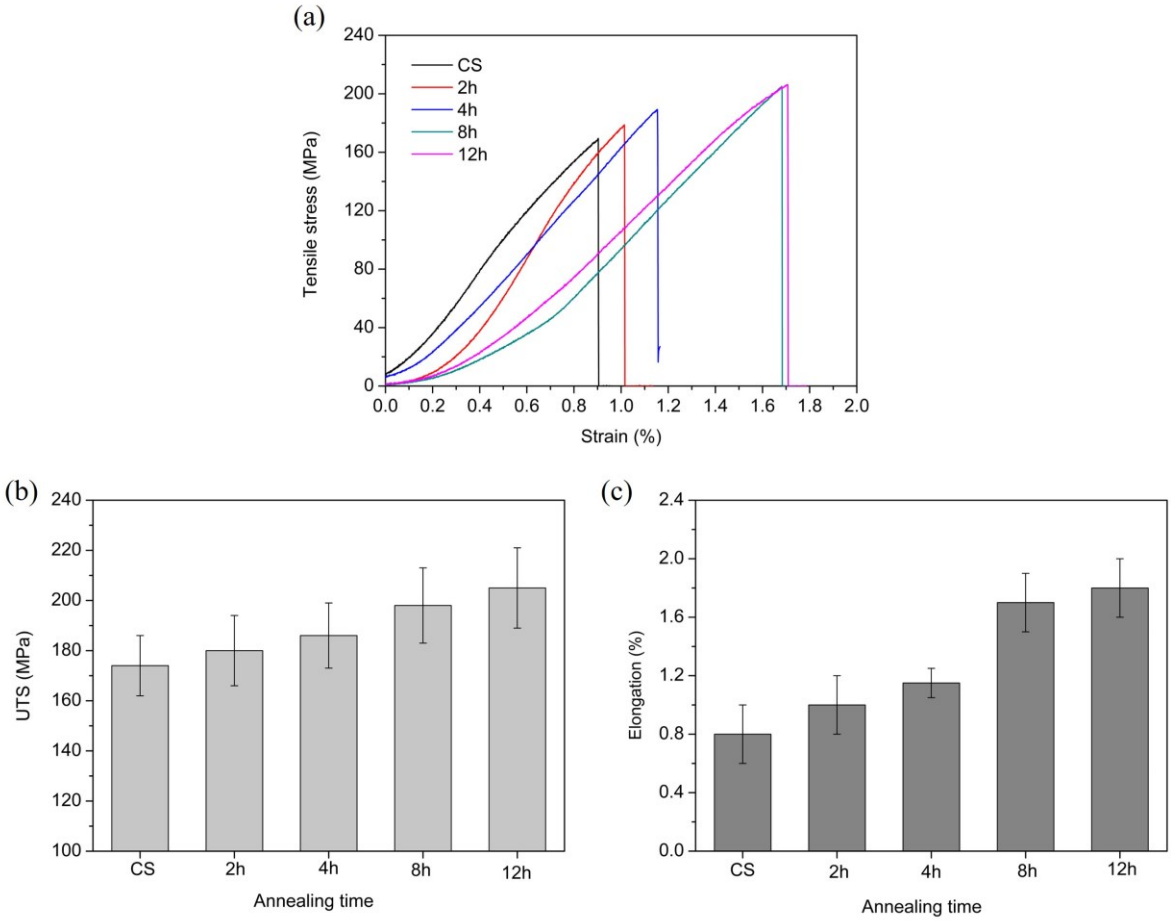

Figure 3-28 (a) Tensile stress-strain curves for SSBM CNT/Al composites annealing treated at different duration of time. (b) and (c) summarize the UTS values and elongation of the specimens, respectively.

In addition to micro-level fracture characteristics, nanocomposite had different fracture characteristics at the submicron or nano-level that involved ultrafine Al grains within a single splat and CNT distributed within a splat. The magnified fracture surface morphologies of the nanocomposite are shown in Figure 3-31. In addition to intergranular fracture, pull out of the CNTs can be also observed on the fracture surface. As schematically described in Figure 3-32b, well aligned CNTs have straightened out from fracture plane in the loading direction, demonstrating a load transfer model. Besides, according to previous studies [39, 40], the formation of Al_4C_3 at the interface between the CNTs and the Al matrix in the annealed samples can assist such a load transfer due to the enhanced metallurgical bonding. However, its quantity is too small, and it may contribute less to the improvement of bonding strength.

From above analysis, two main reasons should be responsible for the unobvious improved tensile properties after a series of heat treatments: first of all, in the micro-scale level, the enhancement of inter-splat bonding to heal all defects by atomic diffusion is still very limited, especially in the regions that experienced insufficient plastic deformation. The TEM images in Figure 3-25 revealed that no obvious recrystallization or grain growth occurred after annealing treatment, which indicates the difficulty in realizing metallic bonding between inter-splats. Additionally, the presence of CNTs or contamination layers, such as oxides at the inter-splat surface, is likely to prevent the inter-splat boundary from metallic bonding even at a higher annealing temperature. Furthermore, in the submicron and nano-level, the interfacial bonding between Al grains and CNT/Al matrix is dominated by a physical bonding mechanism, which is not strong enough to transfer high load. However, the bonding quality in micro-scale level is more critical in achieving good tensile properties of the SSBM CNT/Al composites.

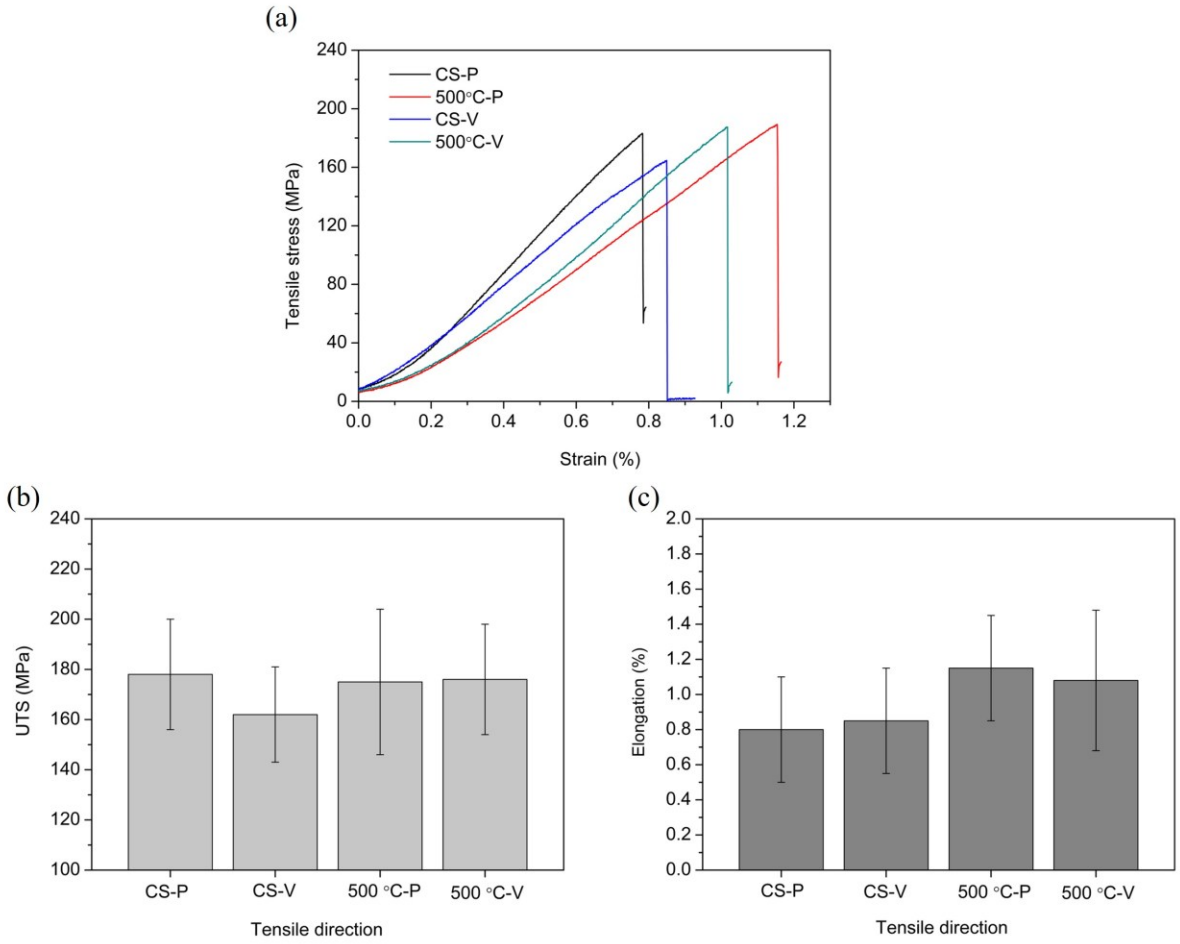

Figure 3-29 (a) Tensile stress-strain curves for SSBM CNT/Al composites in different tensile directions. (b) and (c) summarize the UTS values and elongation of the specimens, respectively.

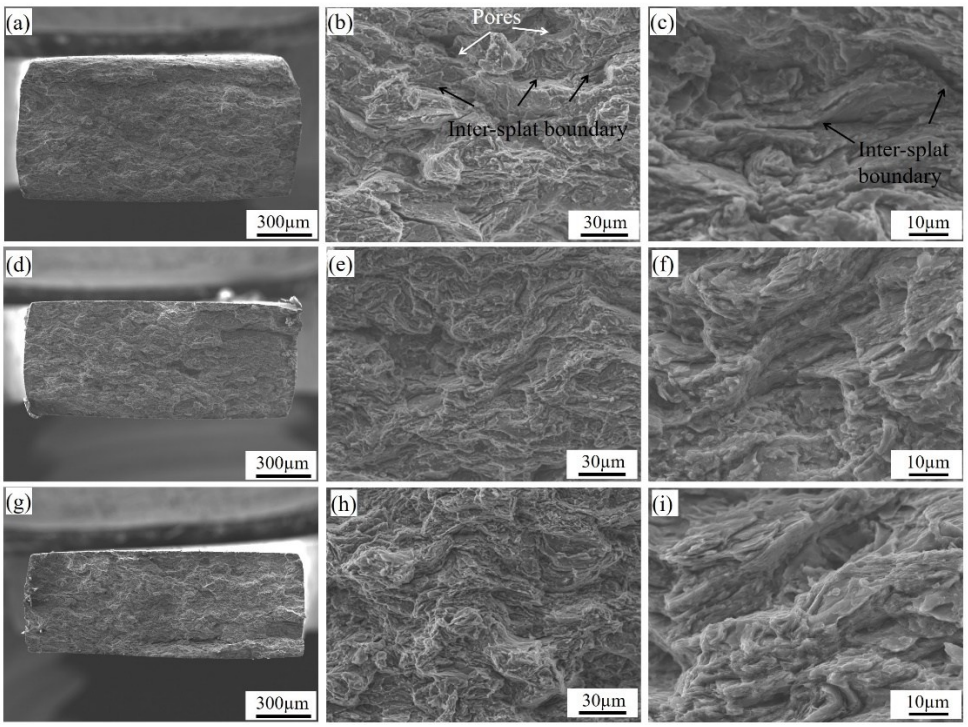

Figure 3-30 Fracture morphologies of the as-sprayed and annealed CNT/Al composite samples at different conditions (a-c) as-sprayed state; (d-f) 500 ℃/4 h; (g-i) 500 ℃/12 h.

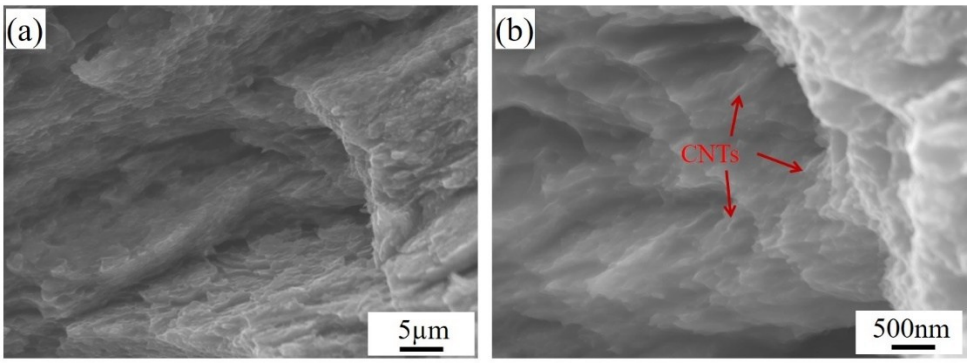

Figure 3-31 Magnified SEM image of the fractured surface: (a) intergranular fracture and (b) pull out of CNTs.

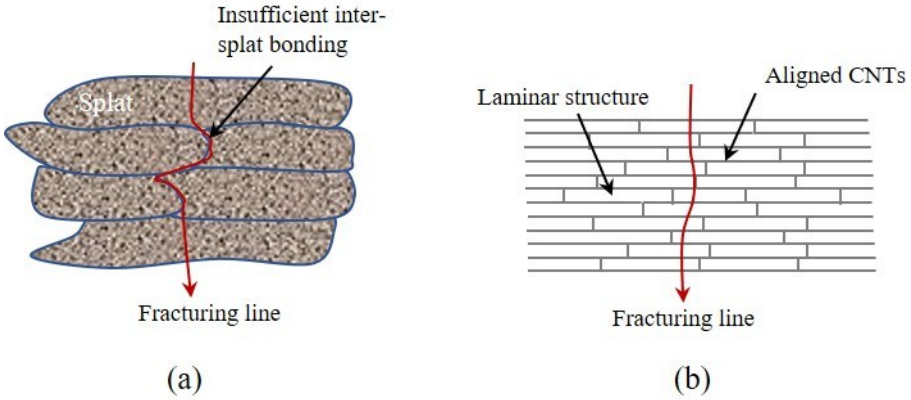

Figure 3-32 Fracture model for the as-sprayed SSBM CNT/Al composite deposit: (a) Fracture through weak inter-splat boundary and intergranular; (b) intergranular fracture by CNT pull out.

3.7 Summary

In this chapter, two distinct approaches, namely HSD and SSBM processes, were applied to prepare the CNT/Al composite powders for CS. The influence of CS processing parameters and post annealing treatments on the microstructure evolution, phase composition and structural integrity of CNTs were examined in terms of SEM, EBSD, TEM, XRD and Raman analysis. The main conclusions can be drawn and are described in the following:

(1) In the case of CNT/Al composite powder produced by HSD process, CNTs were uniformly coated on the surface of Al particles without serious damage to the CNTs during composite powder preparation. However, the dispersion of the CNTs onto the Al particle surface could prevent the particles from metallic bonding during CS deposition, resulting in a dramatic decrease of DE and a low strength of the composite coating.

(2) In the case of the CNT/Al composite powder produced by SSBM process, uniform distribution of the CNTs into the Al matrix was achieved, but the CNTs were slightly damaged during processing. The microhardness of CNT/Al composite coating produced from SSBM powders reached as high as 133 $HV_{0.1}$, showing a significant improvement compared with the pure Al coating.

(3) The strengthening mainly resulted from grain boundary hardening due to nanocrystalline

structure and hardening by CNTs. In addition, according to the XRD and Raman analysis, the brittle Al_4C_3 phase was not formed in both CNT/Al composite coatings.

(4) The combination of FEA simulation and experimental results demonstrates that the dense lamellar structure at microscale results from the self-alignment of flaky particles and the enhanced peening effect during deposition. The flaky shaped particle experienced less plastic deformation and thus weaker interfacial bonding and lower adhesion strength compared to the spherical particle.

(5) The phase composition, as well as the structural integrity of the CNTs, were well preserved in the composite samples annealed at lower temperatures. Al_4C_3 phase started to form in the highly fractured CNTs regions as the annealing temperature rose up to 500℃. Extending annealing duration can also facilitate the nucleation and growth of the Al_4C_3 phase.

(6) A slight decrease of microhardness was observed on the annealed SSBM CNT/Al composites. This could be explained by the limited grain growth due to Zener drag and solute drag phenomena during heat treatment.

(7) The tensile tests on the as-sprayed SSBM CNT/Al composite presents a brittle feature, with fracture primarily occurred along the weak inter-splat interface. A slight improvement in both the UTS and elongation was obtained after annealing treatment as a result of enhanced interfacial bonding and defect-healing effect.

References of Chapter III

[1] Shuo Yin, Xiaofang Wang, Wenya Li, Hanlin Liao, Hongen Jie, Deformation behavior of the oxide film on the surface of cold sprayed powder particle, Appl. Surf. Sci., 259 (2012), 294-300.

[2] Wen-Ya Li, Hanlin Liao, Chang-Jiu Li, Hee-Seon Bang, C Coddet, Numerical simulation of deformation behavior of Al particles impacting on Al substrate and effect of surface oxide films on interfacial bonding in cold spraying, Appl. Surf. Sci., 253 (2007), 5084-5091.

[3] W. Y. Li, C. J. Li, H. L. Liao, Significant influence of particle surface oxidation on deposition efficiency, interface microstructure and adhesive strength of cold-sprayed copper coatings, Appl. Surf. Sci., 256 (2010), 4953-4958.

[4] Chaoyue Chen, Yingchun Xie, Renzhong Huang, Sihao Deng, Zhongming Ren, Hanlin Liao, On the role of oxide film's cleaning effect into the metallurgical bonding during cold spray, Mater. Lett., 210 (2018), 199-202.

[5] Hamid Assadi, Frank Gärtner, Thorsten Stoltenhoff, Heinrich Kreye, Bonding mechanism in cold gas spraying, Acta Mater., 51 (2003), 4379-4394.

[6] Shuo Yin, Xiaofang Wang, Xinkun Suo, Hanlin Liao, Zhiwei Guo, Wenya Li, Christian Coddet, Deposition behavior of thermally softened copper particles in cold spraying, Acta Mater., 61 (2013), 5105-5118.

[7] DJ Woo, FC Heer, LN Brewer, JP Hooper, S Osswald, Synthesis of nanodiamond-reinforced aluminum metal matrix composites using cold-spray deposition, Carbon, 86 (2015), 15-25.
[8] Xiao-Tao Luo, Ying-Kang Wei, Yan Wang, Chang-Jiu Li, Microstructure and mechanical property of Ti and Ti6Al4V prepared by an in-situ shot peening assisted cold spraying, Mater. Des., 85 (2015), 527-533.
[9] Xinliang Xie, Chaoyue Chen, Yingchun Xie, Zhongming Ren, Eric Aubry, Gang Ji, Hanlin Liao, A novel approach for fabricating Ni-coated FeSiAl soft magnetic composite via cold spraying, J. Alloys Compd., 749 (2018), 523-533.
[10] Richard Jenkins, Shuo Yin, Barry Aldwell, Morten Meyer, Rocco Lupoi, New insights into the in-process densification mechanism of cold spray Al coatings: low deposition efficiency induced densification, J. Mater. Sci. Technol., (2018),
[11] Biao Chen, Lei Jia, Shufeng Li, Hisashi Imai, Makoto Takahashi, Katsuyoshi Kondoh, In situ synthesized Al4C3 nanorods with excellent strengthening effect in aluminum matrix composites, Adv. Eng. Mater., 16 (2014), 972-975.
[12] Laipeng Yan, Zhanqiu Tan, Gang Ji, Zhiqiang Li, Genlian Fan, Dominique Schryvers, Aidang Shan, Di Zhang, A quantitative method to characterize the Al 4 C 3-formed interfacial reaction: The case study of MWCNT/Al composites, Mater. Charact., 112 (2016), 213-218.
[13] Run Xu, Zhanqiu Tan, Dingbang Xiong, Genlian Fan, Qiang Guo, Jie Zhang, Yishi Su, Zhiqiang Li, Di Zhang, Balanced strength and ductility in CNT/Al composites achieved by flake powder metallurgy via shift-speed ball milling, Composites Part A, 96 (2017), 57-66.
[14] Mildred S Dresselhaus, G Dresselhaus, R Saito, A Jorio, Raman spectroscopy of carbon nanotubes, Physics reports, 409 (2005), 47-99.
[15] Mildred S Dresselhaus, Ado Jorio, Mario Hofmann, Gene Dresselhaus, Riichiro Saito, Perspectives on carbon nanotubes and graphene Raman spectroscopy, Nano Lett., 10 (2010), 751-758.
[16] R Saito, M Hofmann, G Dresselhaus, A Jorio, MS Dresselhaus, Raman spectroscopy of graphene and carbon nanotubes, Advances in Physics, 60 (2011), 413-550.
[17] R George, KT Kashyap, R Rahul, S Yamdagni, Strengthening in carbon nanotube/aluminium (CNT/Al) composites, Scripta Mater., 53 (2005), 1159-1163.
[18] Chunnian He, Naiqin Zhao, Chunsheng Shi, Xiwen Du, Jiajun Li, Haipeng Li, Qingran Cui, An approach to obtaining homogeneously dispersed carbon nanotubes in Al Powders for preparing reinforced Al‐matrix composites, Adv. Mater., 19 (2007), 1128-1132.
[19] Hyunjoo Choi, Jaehyuck Shin, Byungho Min, Junsik Park, Donghyun Bae, Reinforcing effects of carbon nanotubes in structural aluminum matrix nanocomposites, J. Mater. Res., 24 (2009), 2610-2616.
[20] B Chen, K Kondoh, H Imai, J Umeda, M Takahashi, Simultaneously enhancing strength and ductility of carbon nanotube/aluminum composites by improving bonding conditions, Scripta Mater., 113 (2016), 158-162.
[21] Dina Goldbaum, J Michael Shockley, Richard R Chromik, Ahmad Rezaeian, Stephen Yue, Jean-Gabriel Legoux, Eric Irissou, The effect of deposition conditions on adhesion strength of Ti and Ti6Al4V cold spray splats, J. Therm. Spray Technol., 21 (2012), 288-303.
[22] R Huang, H Fukanuma, Study of the influence of particle velocity on adhesive strength of cold spray deposits, J. Therm. Spray Technol., 21 (2012), 541-549.
[23] Wen-Ya Li, Chang-Jiu Li, Hanlin Liao, Significant influence of particle surface oxidation on deposition efficiency, interface microstructure and adhesive strength of cold-sprayed copper coatings, Appl. Surf. Sci., 256 (2010), 4953-4958.
[24] Yuta Watanabe, Chisato Yoshida, Keisuke Atsumi, Motohiro Yamada, Masahiro Fukumoto, Influence of substrate temperature on adhesion strength of cold-sprayed coatings, J. Therm. Spray Technol., 24 (2015), 86-91.

[25] Shuo Yin, Pengjiang He, Hanlin Liao, Xiaofang Wang, Deposition features of Ti coating using irregular powders in cold spray, J. Therm. Spray Technol., 23 (2014), 984-990.
[26] Kicheol Kang, Gyuyeol Bae, Juyeon Won, Changhee Lee, Mechanical property enhancement of kinetic sprayed Al coatings reinforced by multi-walled carbon nanotubes, Acta Mater., 60 (2012), 5031-5039.
[27] Niels Hansen, Hall–Petch relation and boundary strengthening, Scripta Mater., 51 (2004), 801-806.
[28] C Borchers, F Gärtner, T Stoltenhoff, H Kreye, Microstructural bonding features of cold sprayed face centered cubic metals, J. Appl. Phys., 96 (2004), 4288-4292.
[29] Kicheol Kang, Jaeick Kim, Hyungkwon Park, Changhee Lee, Formation and heat treatment of kinetic sprayed nanocrystalline Al coatings reinforced with multi-walled carbon nanotubes: The relationship between microstructural features and physical properties, Surf. Coat. Technol., 289 (2016), 124-135.
[30] Ying-Kang Wei, Xiao-Tao Luo, Cheng-Xin Li, Chang-Jiu Li, Optimization of in-situ shot-peening-assisted cold spraying parameters for full corrosion protection of Mg alloy by fully dense Al-based alloy coating, J. Therm. Spray Technol., 26 (2017), 173-183.
[31] Toru Kuzumaki, K Miyazawa, Hideki Ichinose, Kunio Ito, Processing of carbon nanotube reinforced aluminum composite, J. Mater. Res., 13 (1998), 2445-2449.
[32] Hansang Kwon, Mehdi Estili, Kenta Takagi, Takamichi Miyazaki, Akira Kawasaki, Combination of hot extrusion and spark plasma sintering for producing carbon nanotube reinforced aluminum matrix composites, Carbon, 47 (2009), 570-577.
[33] Ziyun Yu, Zhanqiu Tan, Genlian Fan, Ding-Bang Xiong, Qiang Guo, Renbang Lin, Li Hu, Zhiqiang Li, Di Zhang, Effect of interfacial reaction on Young's modulus in CNT/Al nanocomposite: A quantitative analysis, Mater. Charact., 137 (2018), 84-90.
[34] T Laha, S Kuchibhatla, S Seal, W Li, A Agarwal, Interfacial phenomena in thermally sprayed multiwalled carbon nanotube reinforced aluminum nanocomposite, Acta Mater., 55 (2007), 1059-1066.
[35] Laipeng Yan, Zhanqiu Tan, Gang Ji, Zhiqiang Li, Genlian Fan, Dominique Schryvers, Aidang Shan, Di Zhang, A quantitative method to characterize the Al4C3-formed interfacial reaction: The case study of MWCNT/Al composites, Mater. Charact., 112 (2016), 213-218.
[36] Lijie Ci, Zhenyu Ryu, Neng Yun Jin-Phillipp, Manfred Rühle, Investigation of the interfacial reaction between multi-walled carbon nanotubes and aluminum, Acta Mater., 54 (2006), 5367-5375.
[37] F Zhou, J Lee, S Dallek, EJ Lavernia, High grain size stability of nanocrystalline Al prepared by mechanical attrition, J. Mater. Res., 16 (2001), 3451-3458.
[38] Kang Yang, Wenya Li, Xiawei Yang, Yaxin Xu, Achilles Vairis, Effect of heat treatment on the inherent anisotropy of cold sprayed copper deposits, Surf. Coat. Technol., 350 (2018), 519-530.
[39] Malin Chen, Genlian Fan, Zhanqiu Tan, Dingbang Xiong, Qiang Guo, Yishi Su, Jie Zhang, Zhiqiang Li, Makio Naito, Di Zhang, Design of an efficient flake powder metallurgy route to fabricate CNT/6061Al composites, Mater. Des., 142 (2018), 288-296.
[40] Genlian Fan, Yue Jiang, Zhanqiu Tan, Qiang Guo, Ding-bang Xiong, Yishi Su, Renbang Lin, Li Hu, Zhiqiang Li, Di Zhang, Enhanced interfacial bonding and mechanical properties in CNT/Al composites fabricated by flake powder metallurgy, Carbon, 130 (2018), 333-339.

Chapter IV Cold spraying of TiB_2/AlSi10Mg composites

4.1 Introduction

In this chapter, an in-situ TiB_2 particle reinforced AlSi10Mg composite powder was used as the novel feedstock to fabricate composite components by cold spraying (CS). First, the effect of the processing parameters on the microstructure evolution and mechanical properties of the TiB_2/AlSi10Mg composite was investigated. In order to further improve the mechanical properties of the as-sprayed deposits, post-treatments including annealing treatments and friction stir processing (FSP) were performed in different conditions. The phase composition and microstructure evolution were examined in terms of by X-ray diffraction (XRD), scanning electron microscopy (SEM), and transmission electron microscopy (TEM) The mechanical properties of the as-sprayed and post-treated samples were evaluated by Vickers hardness, tribological, and tensile tests. The fracture mechanisms of the as-sprayed and post-treated deposits were proposed based on morphology observation. Last, the reinforcing mechanisms of the TiB_2/AlSi10Mg composites are discussed in detail.

4.2 Microstructure characterization of as-sprayed deposits

Figure 4-1 shows the surface morphologies of the CSed AlSi10Mg and TiB_2/AlSi10Mg composite deposits using different processing conditions. The morphologies exhibit different deposition features for different processing conditions. Here, the deposits prepared under the CT1 (P_g=3.0 MPa, T_g=470 ℃, compressed air) and CT2 (P_g=1.8 MPa, T_g=320 ℃, helium) conditions were denoted as AlSi10Mg-CT1, TiB_2/AlSi10Mg-CT1, AlSi10Mg-CT2, and TiB_2/AlSi10Mg-CT2. Regarding the CT1 deposits, as shown in Figure 4-1a and b, the particle morphology at the top layer remains spherical or quasi-spherical, indicating that relatively little plastic deformation occurred during deposition. However, in the case of CT2 deposits, when He was used as the propellant gas, both the pure AlSi10Mg and TiB_2/AlSi10Mg composite particles experienced greater plastic deformation and prominent metal jet can be observed at the rim of the deformed splats (Figure 4-1c and d). CFD modelling of particle velocity and temperature during the CS process was conducted by using Fluent/Ansys software. The simulation results reveal that the average particle velocities for pure AlSi10Mg powder and TiB_2/AlSi10Mg composite powder in CT2 are about 820 m/s, and 816 m/s, respectively, which are much higher than those obtained from CT1 (654 m/s and 646 m/s for the pure AlSi10Mg powder and TiB_2/AlSi10Mg composite powder, respectively). Therefore, a much higher particle impact velocity using He as the propellant gas leads to intensive plastic deformation of the particle, which is beneficial for metallic bonding between the deformed splats.

Figure 4-2 shows the cross-sectional micrographs of the pure AlSi10Mg and TiB_2/AlSi10Mg composite deposits. Thick and dense deposits were successfully fabricated by CS. Besides, Figure 4-2c and d reveal that the deposits are well bonded with Al substrates without any cracks or gaps. The magnified views of the deposits are shown in Figure 4-3. A few small pores with a size less than 2 μm can be observed on the polished surface of the CT1 deposits. The porosity measurements based on five SEM images using the Image J software show that the porosity values of the pure AlSi10Mg and TiB_2/AlSi10Mg composite deposits in CT1 are about 0.68 and 0.45, respectively; the CT2 deposits have much lower values of approximately 0.35 and 0.24 for the pure AlSi10Mg and TiB_2/AlSi10Mg composite deposits, respectively. It is well understood that a much higher particle velocity in CT2 can result in greater plastic deformation of the particles and thus denser structures. It is also interesting to note that the composite deposits possess lower porosities compared to the pure AlSi10Mg deposits in both CT1 and CT2 conditions. The increased density of the composite deposit can be explained by the

enhanced in-situ hammering effect of the rebounding particles during CS deposition. On the one hand, the dispersion of TiB_2 particles in AlSi10Mg matrix can strengthen the particles. The microhardness measurements on the cross-section of the TiB_2/AlSi10Mg composite powder revealed an average value of 68 $HV_{0.015}$, which is higher than that of the pure AlSi10Mg powder (52 $HV_{0.015}$). As a result, higher critical velocity is required for successful deposition of these composite particles. That is to say, more particles with a velocity lower than the critical value cannot be deposited successfully but rebound away from the surface. On the other hand, the presence of TiB_2 particles on the composite particle surface may act as contaminants like oxides, which can hinder the metallic bonding between splats during deposition. These two factors together can lead to more particles rebounding away from the deposit surface due to unsuccessful deposition. These rebounded particles work as in-situ peening particles, which can further deform the previously deposited layers [1, 2]. Consequently, a slightly denser structure was obtained for the composite deposits. As indicated by the EDS mapping (see Figure 4-5), these white ultrafine particles marked by red arrows are TiB_2 phase. It can be observed in Figure 4-3b and d that the ultrafine TiB_2 particles are uniformly dispersed across the composite deposits. Meanwhile, some micron-sized TiB_2 clusters can also be observed. The TiB_2 particle size is in the range of 100 nm to 8 µm, while most of them are smaller than 700 nm. By analyzing five SEM images, the volume content of TiB_2 particles in the composite deposits yields about 4.4 vol.%. The structure and content of TiB_2 particles in the initial composite powder are well preserved in the CSed composite deposits.

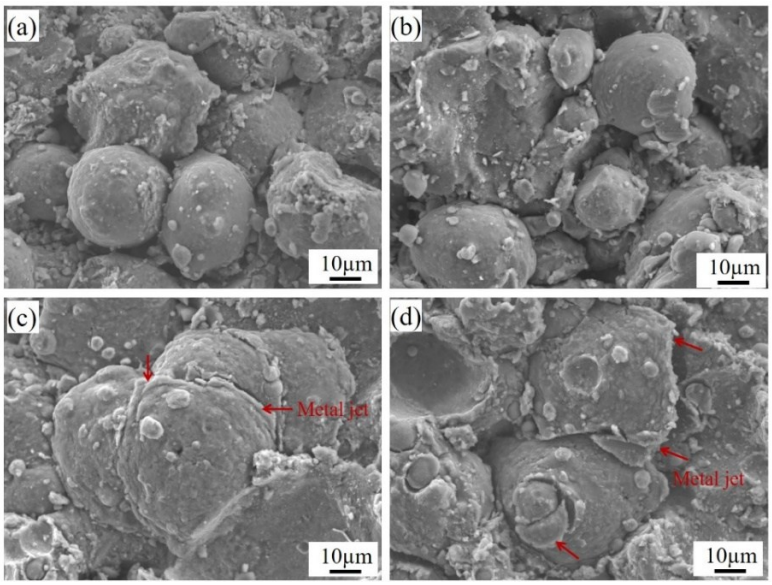

Figure 4-1 Surface morphologies of the as-sprayed AlSi10Mg and TiB_2/AlSi10Mg deposits obtained from different conditions: (a) AlSi10Mg-CT1; (b) TiB_2/AlSi10Mg-CT1; (c) AlSi10Mg-CT2; (d) TiB_2/AlSi10Mg-CT2.

SEM micrographs of the etched cross-sections of the as-sprayed deposits are presented in Figure 4-4. From the lower magnified views of Figure 4-4a and b, the AlSi10Mg particles are largely deformed during deposition, forming a very dense structure. Nevertheless, some poorly bonded inter-splat boundaries together with some small pores located at inter-splat boundaries can still be observed. Comparatively, the particles within the CT2 deposits experienced much greater deformation, resulting in a larger flattening ratio compared to those in the CT1 deposits. However, there are still some poor bonding inter-splat interfaces that can be observed within the CT2 deposits. The higher magnified SEM views and the EDS mapping of the CT2 deposits are shown in Figure 4-4 (e, f) and Figure 4-5. Grey primary α-Al matrix decorated with a white fibrous Si network can be observed in both the as-sprayed pure AlSi10Mg and TiB_2/AlSi10Mg composite deposits, which is similar to the structure of the initial

powder. Some fibrous Si network was heavily deformed in some regions, resulting in the formation of linear arrayed ultrafine Si particles, especially near the inter-splat boundaries. The fine dispersion of these ultrafine Si particles in Al the matrix has a positive impact on the mechanical properties of the as-sprayed samples.

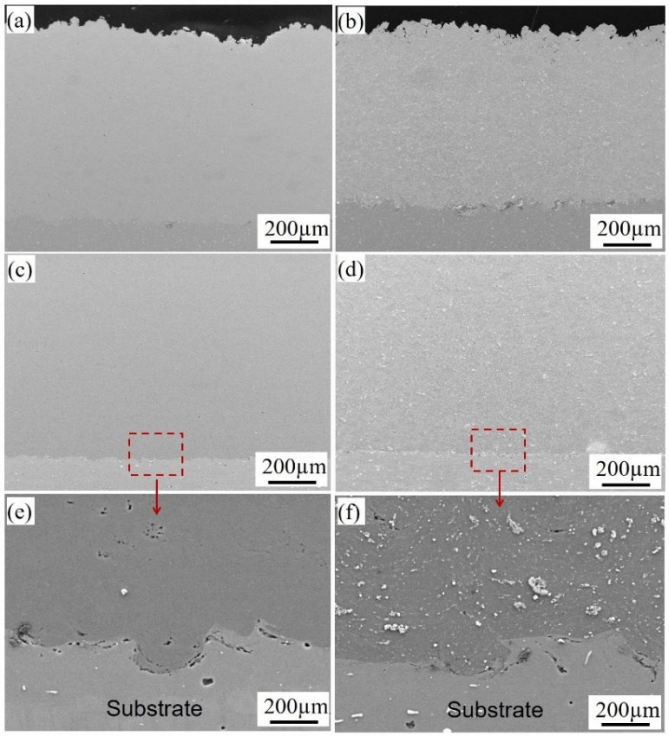

Figure 4-2 Cross-sectional morphologies of the CSed AlSi10Mg and TiB_2/AlSi10Mg composite deposits at lower magnification: (a) AlSi10Mg-CT1; (b) TiB_2/AlSi10Mg-CT1; (c) AlSi10Mg-CT2; (b) TiB_2/AlSi10Mg-CT2. (e) and (f) are the magnified views near the substrate/deposit interface showing well bonding state of the deposit and substrate.

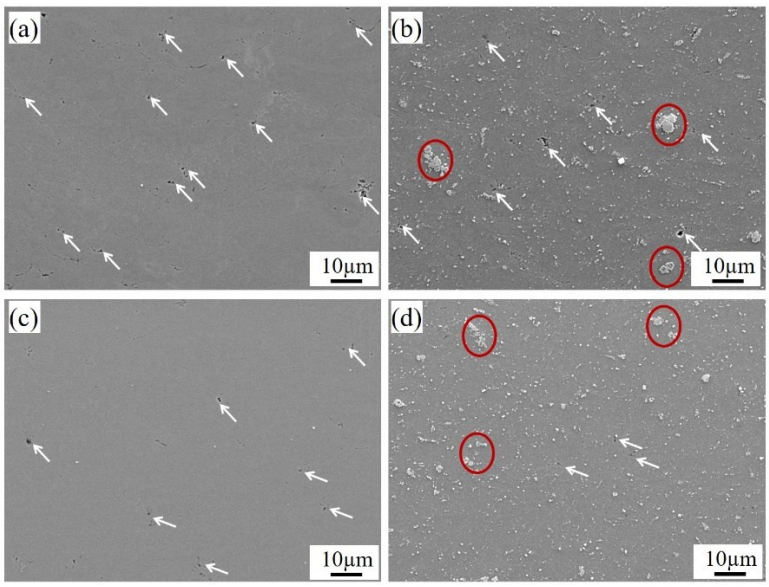

Figure 4-3 Cross-sectional morphologies of the CSed AlSi10Mg and TiB_2/AlSi10Mg composite deposits at higher magnification: (a) AlSi10Mg-CT1; (b) TiB_2/AlSi10Mg-CT1; (c) AlSi10Mg-CT2; (b) TiB_2/AlSi10Mg-CT2.

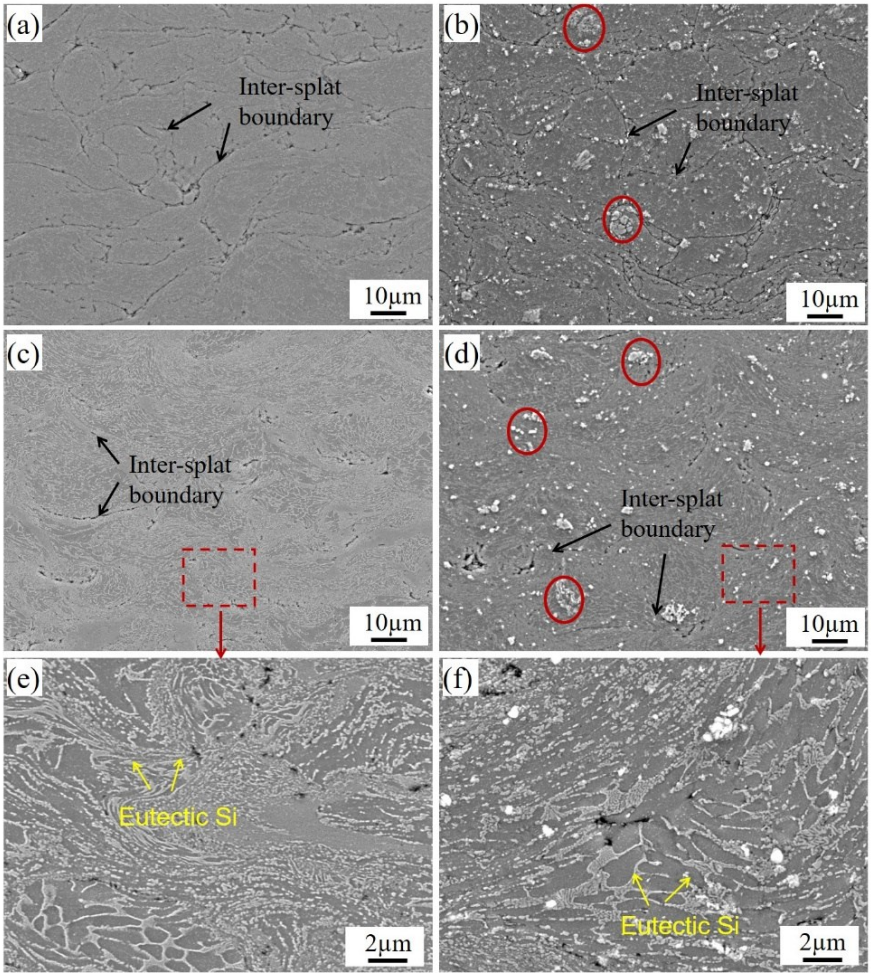

Figure 4-4 SEM micrographs of the etched cross-sections of the as-sprayed AlSi10Mg and TiB_2/AlSi10Mg composite deposits: (a) AlSi10Mg-CT1; (b) TiB_2/AlSi10Mg-CT1; (c) AlSi10Mg-CT2; (b) TiB_2/AlSi10Mg-CT2. (e) and (f) are the magnified regions marked in (c) and (d), respectively.

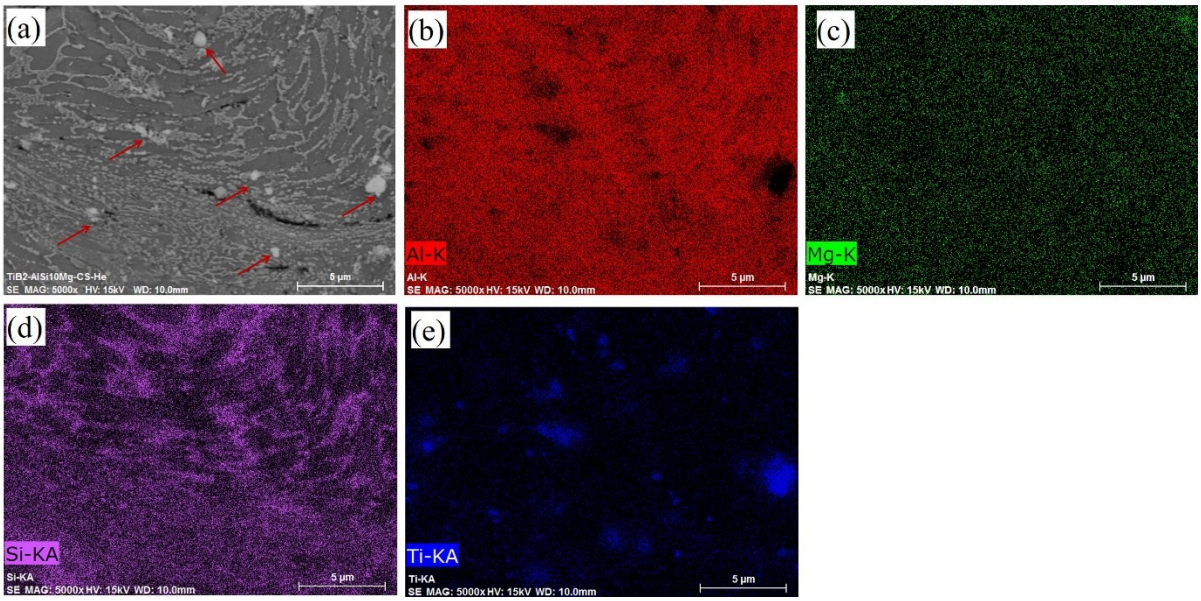

Figure 4-5 EDS mapping of CSed TiB_2/AlSi10Mg-CT2 deposit.

4.3 The effect of annealing treatment

4.3.1 Phase composition

The XRD patterns of the pure AlSi10Mg and TiB_2/AlSi10Mg composite in the as-sprayed and annealed states, as well as their initial powders, are shown in Figure 4-6. The pure AlSi10Mg samples show the Al, Si, and Mg_2Si phases. In addition to these three phases, peaks corresponding to the hexagonal TiB_2 phase appear in XRD patterns of the composite powder and deposits. There was no obvious difference in the XRD patterns between the powder and the fabricated coatings within the limitation of the XRD detection, implying that no formation of new phases occurred during CS and heat treatments. Moreover, the XRD patterns reveal that the intensity of the Si peaks increases with the increase in the annealing temperature. This observation suggests a reduction of Si solid solubility in the Al matrix after the high-temperature annealing treatments. This could be attributed to the fact that Si precipitates out from Al matrix after heat treatment.

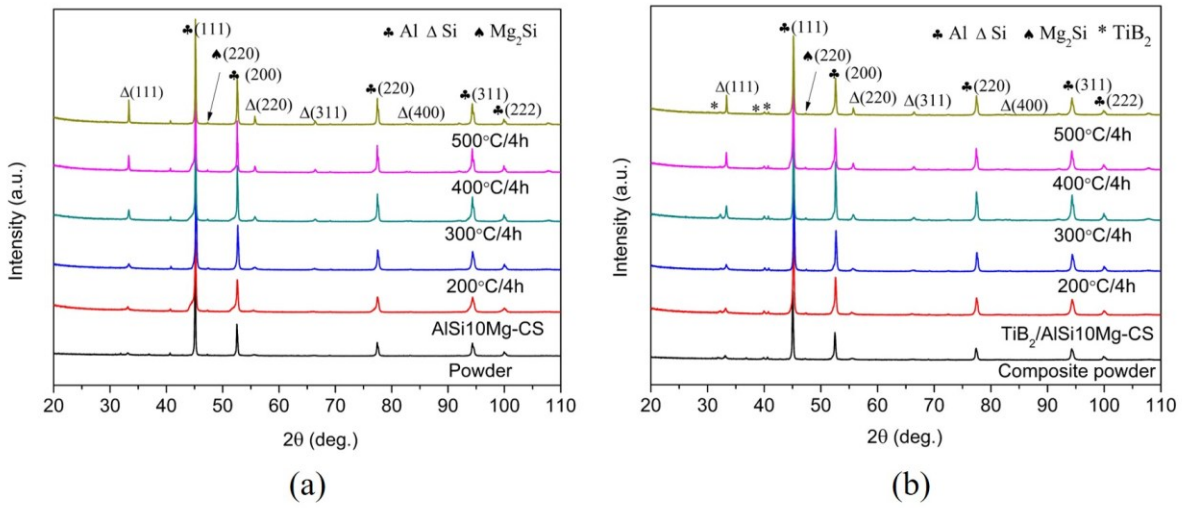

Figure 4-6 XRD patterns of the (a) pure AlSi10Mg-CT2 and (b) TiB_2/AlSi10Mg-CT2 composite at as-sprayed and annealed states as well as the initial feedstocks.

4.3.2 Microstructure evolution

As shown in Figure 4-7, pores (marked by white arrows) become less visible as the annealing temperature increases to 300 °C. However, increased pores of a large size are presented on the cross-section of the samples annealed at high temperatures, especially in the case of 500 °C. The measured porosity evolution of the CT1 and CT2 deposits as a function of annealing temperature is illustrated in Figure 4-8. The porosity values of both deposits decrease as the annealing temperature increases from 200 °C to 300 °C, and then increase when the annealing temperature is further increased up to 500 °C. For each annealing temperature, the TiB_2/AlSi10Mg composite sample exhibits a lower porosity level compared to the pure AlSi10Mg sample. According to previous studies [3, 4], micro-voids between the CS deposited particles could accumulate to form visible pores during heat treatment.

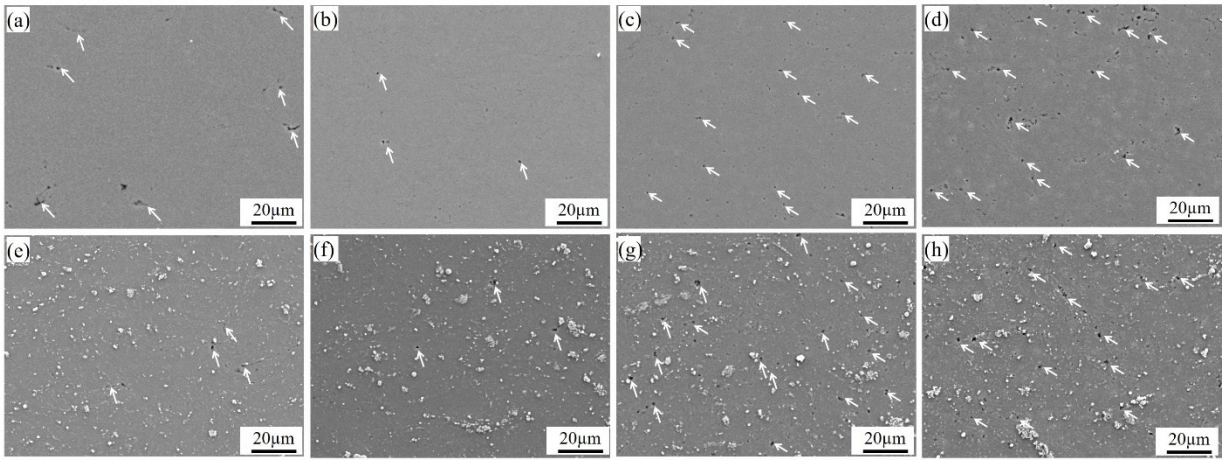

Figure 4-7 Cross-sectional morphologies of annealed (a-d) AlSi10Mg-CT2 and (e-h) TiB_2/AlSi10Mg-CT2 composite coatings at different temperatures: (a) and (e) 200 °C; (b) and (f) 300 °C; (c) and (g) 400 °C; (d) and (h) 500 °C.

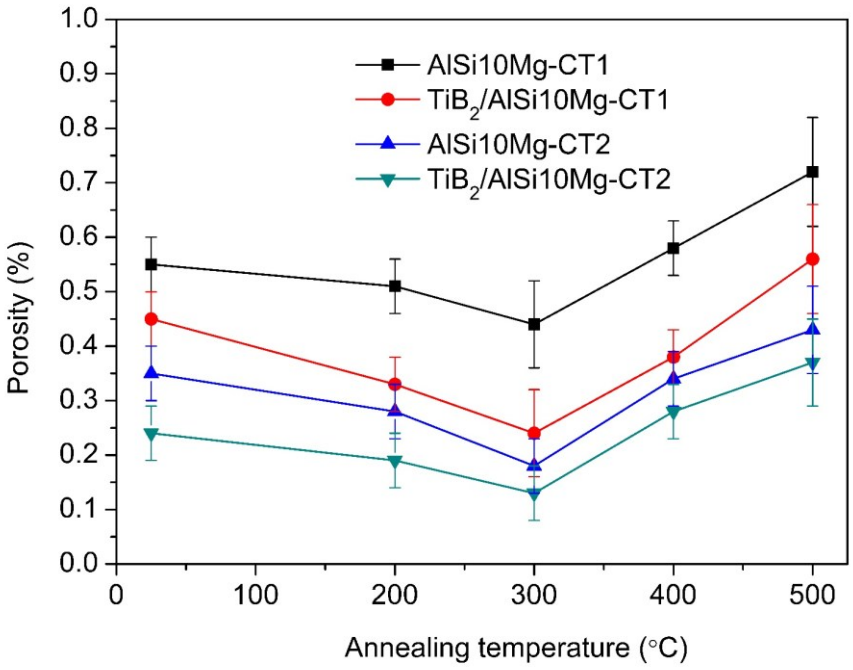

Figure 4-8 Porosity evolution of the AlSi10Mg and TiB_2/AlSi10Mg composite coatings as a function of annealing temperature.

The microstructure evolution of the CT2 deposits after annealing at different temperatures is presented in Figure 4-9. When the samples were annealed at 200 °C for 4 h, inter-splat boundaries could be clearly observed on the cross-section micrographs of both the pure AlSi10Mg and TiB_2/AlSi10Mg composite deposits, as illustrated in Figure 4-9a and e. Few structural changes were found compared to the as-sprayed states. When increasing the annealing temperature to 300 °C, as shown in Figure 4-9b and f, a few well-bonded inter-splat boundaries disappeared, but some poorly bonded regions can still be observed. It seems that effective diffusion between the particle interface only happens with the close cohesion of particles. As the annealing temperature increases to 400 °C, inter-splat boundaries become obscure and discontinuous with only a few poorly bonded interfaces left. When the heat treatment temperature is increase to 500 °C, the inter-splat boundaries mostly disappear, but the apparent porosity

increases. This proves that a significant atom diffusion between the particle interfaces occurs at higher temperatures.

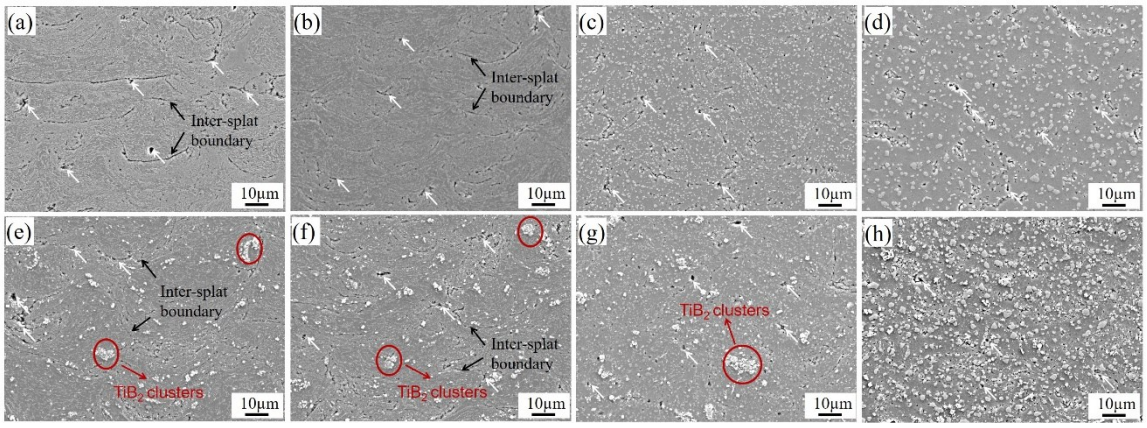

Figure 4-9 SEM micrographs of the etched cross-sections of the annealed (a-d) AlSi10M-CT2 and TiB_2/AlSi10Mg-CT2 composite samples at a lower magnification: (a) and (e) 200 °C; (b) and (f) 300 °C; (c) and (g) 400 °C; (d) and (h) 500 °C.

Highly magnified views of the annealed deposits are shown in Figure 4-10. Similar to the microstructure of the as-sprayed deposit, the samples annealed at 200 °C are characterized by ultrafine Si networks inside the less deformed internal particle and linear alignment of Si particles in highly deformed regions. After heat treatment at 300 °C for 4 h, the eutectic network structure is broken into inconsecutive small Si particles. The microstructure becomes coarser when increasing the annealing temperature from 400 °C to 500 °C. It is possible to schematically describe the microstructure evolution of the as-sprayed AlSi10Mg or TiB_2/AlSi10Mg composite specimens during heat treatment, as shown in Figure 4-11. The as-sprayed samples inherit a microstructure of initial powder, consisting of a supersaturated Al matrix decorated with fibrous eutectic Si particles. After the annealing treatment, the eutectic Si is rejected from the supersaturated Al to form small Si particles. With the increase in the annealing temperature, the Si particles generally precipitate on Al the matrix and grow up with their number decreased remarkably.

Detailed image analysis was conducted based on several SEM images from different annealing temperatures to investigate the change in size and quantity of the eutectic Si particles upon heat treatment. The results, summarized in Figure 4-12, illustrate that when the as-sprayed samples were annealed at 300 °C for 4 h, most of the Si particles were less than 0.5 μm and most of them dispersed along the GBs of the Al matrix. When the annealing temperature increased from 400 °C to 500 °C, some of the Si particles coarsened with their diameter increased from 0.9 μm to 1.6 μm. Also, these coarsened Si particles were uniformly distributed in Al matrix. A decrease in particle number accompanied the increase in the size of Si particles. As can be seen from Figure 4-12, Si particle density decreased from 14.4 particles/μm^2 to 0.23 particles/μm^2. A similar tend on Si particle size and particle density can also be observed in the TiB_2/AlSi10Mg composite deposits.

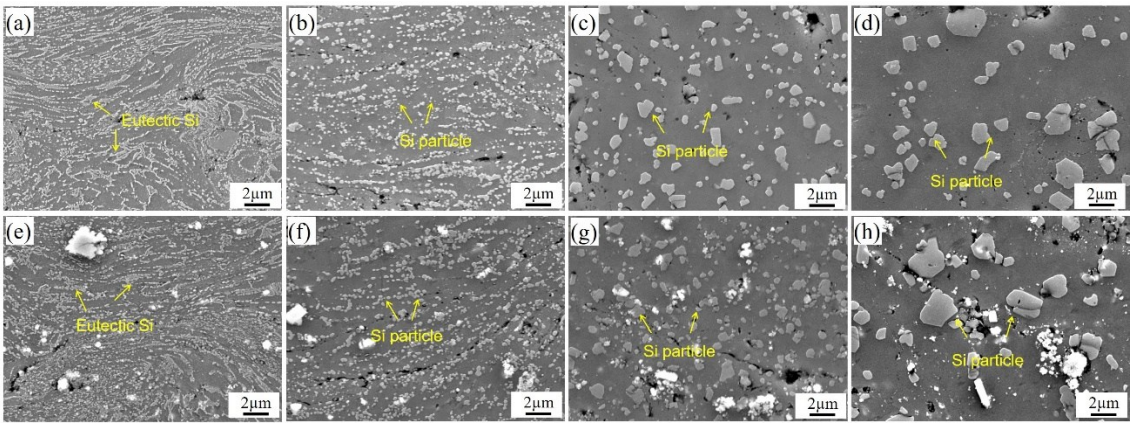

Figure 4-10 Cross-sectional morphologies (higher magnification) of the annealed (a-d) AlSi10Mg-CT2 and TiB_2/AlSi10Mg-CT2 composite coatings: (a) and (e) 200 °C; (b) and (f) 300 °C; (c) and (g) 400 °C; (d) and (h) 500 °C.

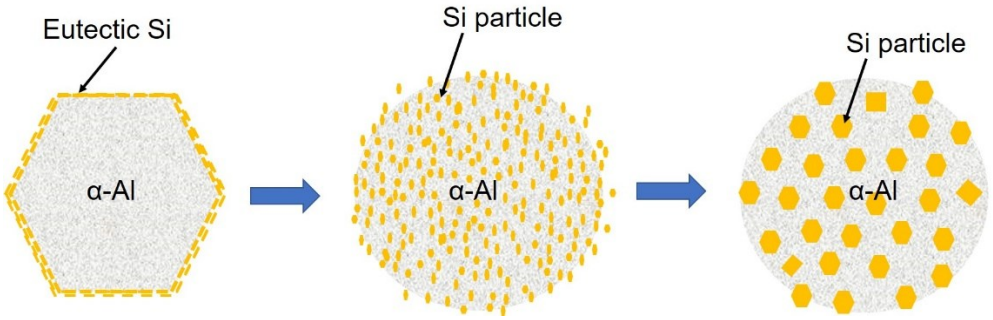

Figure 4-11 Schematic of Si particle evolution in morphology and size during annealing treatment.

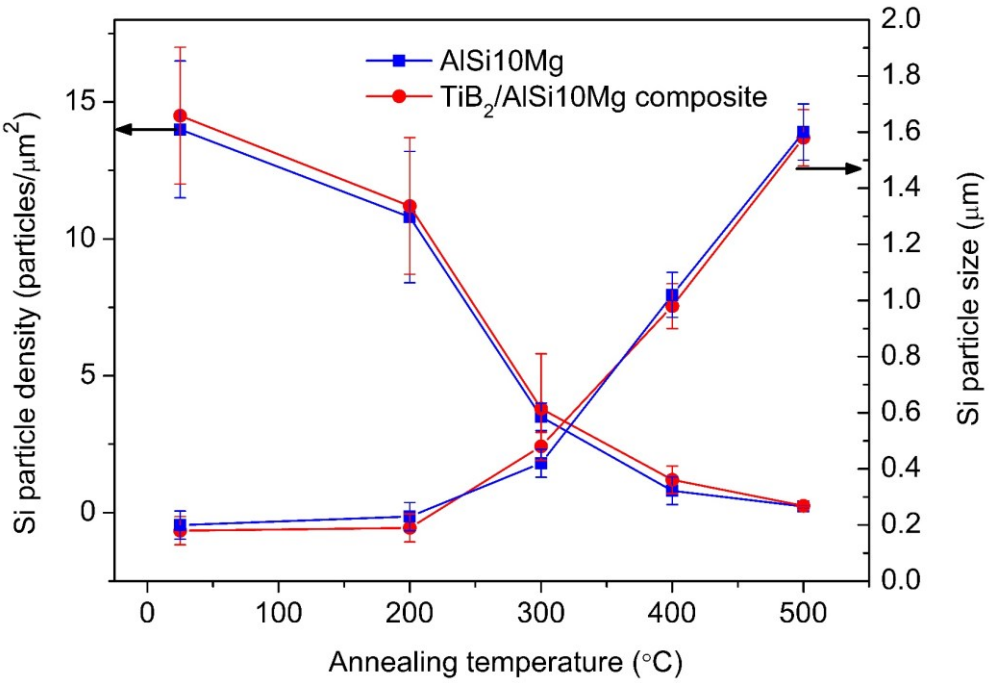

Figure 4-12 Si particle density and particle size evolution as a function of annealing temperatures.

EDS mapping was conducted to examine the Al, Si and Mg distributions of CT2 deposits after annealing treatment in detail. The results of the AlSi10Mg and TiB_2/AlSi10Mg deposits are shown in

Figure 4-13 and Figure 4-14, respectively. From the EDS analysis, besides the remarkable change in the network eutectic Si structure to separated Si particles, some aggregation of Mg can be observed in the deposits after annealing at 500 °C for 4 h. This may be because Mg can react with Si to form the Mg_2Si phase, which is consistent with the XRD results. However, the size of this formed Mg_2Si phase in the Al matrix after the annealing treatment is on a micrometer scale, which may negatively affect the mechanical properties of the Al matrix.

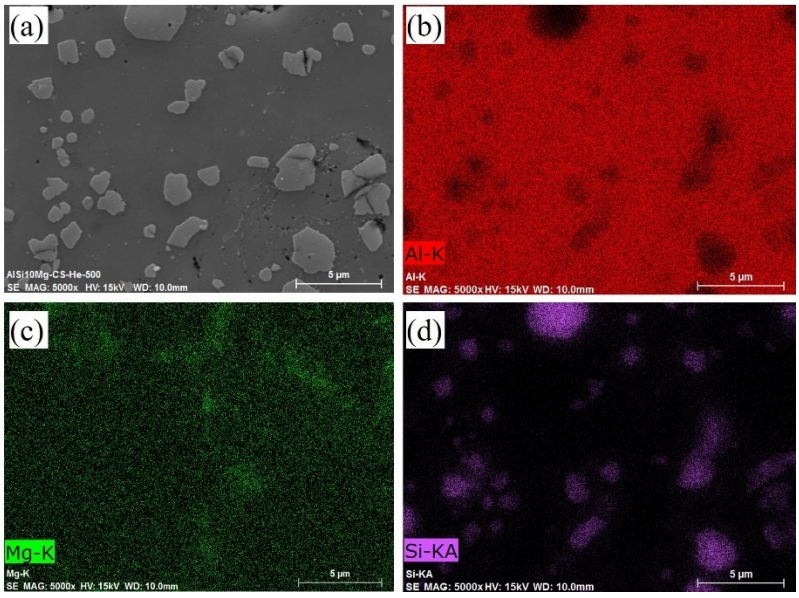

Figure 4-13 SEM microstructure and EDS mapping of AlSi10M-CT2 deposits annealed at 500 °C for 4 h.

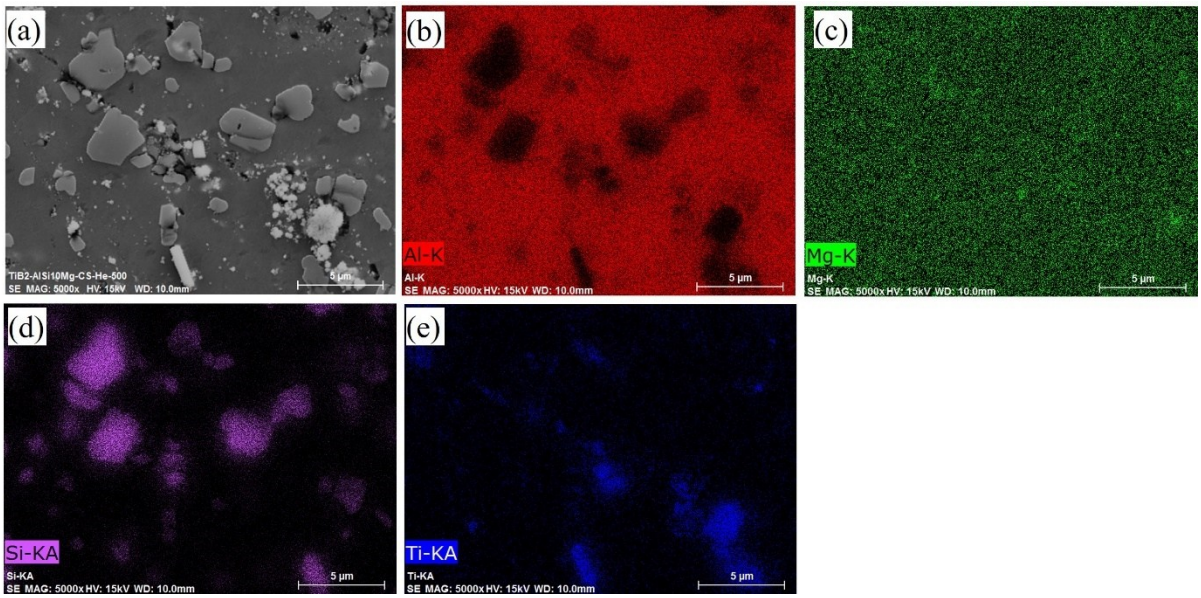

Figure 4-14 SEM microstructure and EDS mapping of TiB_2/AlSi10Mg-CT2 composite deposits annealed at 500 °C for 4 h.

4.3.3 Microhardness

Figure 4-15 displays the microhardness evolution of the pure AlSi10Mg and TiB_2/AlSi10Mg composite samples as a function of the annealing temperatures. The microhardness of the as-sprayed AlSi10Mg-CT1 deposit is about 105 ± 4 $HV_{0.1,}$ much higher than that of the as-casted samples (67 $HV_{0.1}$)

[5]. Moreover, the AlSi10Mg-CT2 deposit possesses a value of 140 ± 4 $HV_{0.1}$, showing an increment of 33.3 % and 109.0 % in comparison with that of the AlSi10Mg-CT1 and as-cast bulk, respectively. Meanwhile, a significant increase in microhardness (about 50 % increment) was also obtained for the TiB_2/AlSi10Mg-CT2 (176 ± 4 $HV_{0.1}$) deposit compared to the TiB_2/AlSi10Mg-CT1(120 ± 4 $HV_{0.1}$). Such a significant increment in microhardness is likely related to the enhanced work hardening and grain refinement effect during CS deposition, as well as the nanosized Si particles as a consequence of the fast cooling during gas atomization. The composite deposits show an increment of 14.3 % and 28.5 % compared to the pure AlSi10Mg-CT1 and AlSi10Mg-CT2 deposits, respectively. The increased microhardness of the composite deposits should be attributed to the uniformly distributed TiB_2 nanoparticles in the Al matrix and the grain refinement effect.

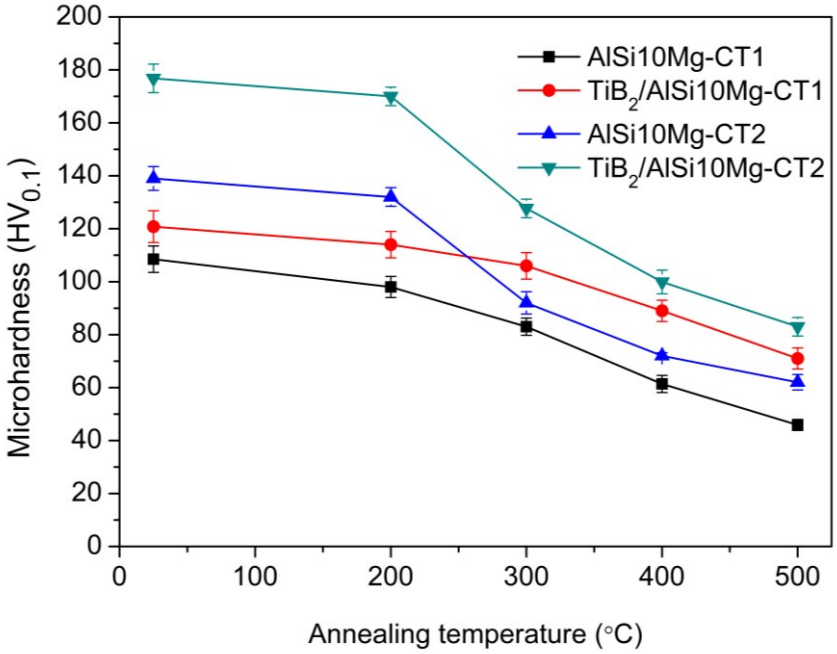

Figure 4-15 Microhardness evolution as a function of annealing temperatures.

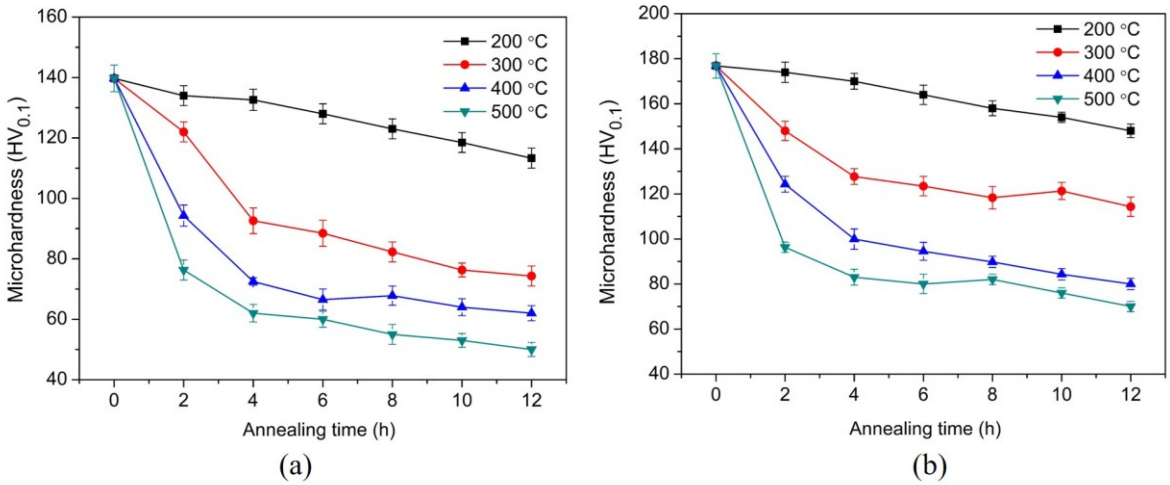

Figure 4-16 Microhardness evolution of the as-sprayed (a) AlSi10Mg-CT2 and (b) TiB_2/AlSi10Mg-CT2 composite as a function of annealing duration and temperatures: 200 ℃; 300 ℃; 400 ℃; 500 ℃.

After the annealing treatment, a varying degree of decrease in microhardness can be observed in both the pure AlSi10Mg and TiB_2/AlSi10Mg composite deposits. In general, the microhardness decreased as the annealing temperature increased when the same treatment duration was applied (Figure 4-15). It clearly shows that the microhardness of the CT2 deposits decreased more sharply than that of the CT1 deposits when the annealing temperature increased. Meanwhile, the microhardness decreased with the duration of time at a fixed heat treatment temperature (Figure 4-16). It can be observed that when annealing at 200 ºC, the microhardness values of both the pure AlSi10Mg and TiB_2/AlSi10Mg composite samples did not change significantly because this lower annealing temperature could not completely remove the work hardening generated during the CS process. As the annealing temperature further increases to 300 °C, the values for both deposits decrease sharply in the first 4 h, and then there is a gentle decrement until 12 h has passed. However, the value of the composite deposit drops more slowly in the second stage compared to the pure AlSi10Mg deposit, resulting in a higher final value. A similar evolution was found when increasing the annealing temperature to 400 °C. In the first stage (0-4 h), the work hardening effect, as well as the dislocations generated in the CS process, were gradually removed over time. This recovery process leads to a decrease in microhardness. Further extension of the annealing duration leads to a coarsening of the Si particles and grain growth, resulting in a decrease in microhardness. However, when the annealing temperature further increases to 500 °C, the hardness values decrease sharply in the first 4 h, while slight changes take place from 4 h to 12 h. This indicates that the coarsening process of the Si phase and Al grains may be completed within 4 h at a high annealing temperature and further extension of the heat treatment duration has little or no effect on hardness [6, 7]. The composite deposit always possesses a higher value compared to the pure AlSi10Mg samples, which can be related to the reinforcement of TiB_2 particles and the finer grain size. The increase of annealing temperature can also result in the precipitation and growth of Si particles, as well as the formation of Mg_2Si phase. As a result, the solid solution strengthening effect of Si and Mg in the Al matrix can be reduced and thus decrease microhardness.

4.3.4 Tribological property

Figure 4-17a and b display the plotted coefficient of friction (COF) versus the wear distance for the pure AlSi10Mg-CT1 and TiB_2/AlSi10Mg-CT1 composite deposits at different annealing temperatures, respectively. In the beginning, the COFs for both deposits show an unstable initial state (run-in) and then become steady after about 80 m and 50 m sliding distance for the pure AlSi10Mg and TiB_2 reinforced composite deposits, respectively. This observation suggests that the TiB_2/Al10Mg composite deposits can reach a relatively steady wear state much earlier than that of the pure AlSi10Mg deposit. However, the COFs of the as-sprayed and annealed (300 °C) pure AlSi10Mg deposits exhibit a sharp increase after sliding for about 200 m and then end in a steady state with high COF values. This is indicative of wear mechanism transformation and cracks on the worn track surface in the final stages, which can accelerate the coating wear rate. A comparative analysis of COFs for deposits without heat treatment demonstrates that the composite deposit is characterized by a higher value (μ= 0.56) compared to the matrix deposit (μ=0.48). After annealing at 300 °C for 4h, the pure AlSi10Mg deposit possesses an average COF value of 0.65. Higher COF values in these cases are associated with the unstable wear mechanisms of the final stages. It can be noticed that the annealing treatments increase the COFs of the composite deposits slightly. The wear rates of the deposits as a function of annealing temperatures are given in Figure 4-17d. As for the deposits in the as-sprayed state, the TiB_2 reinforced composite has a wear rate of 1.5×10^{-3} $mm^3/N\cdot m$, much lower than that of the pure AlSi10Mg deposit. It indicates a better wear performance of the composite deposit due to the enhanced microhardness with the addition of in-situ TiB_2 particles. In the case of the composite deposits, as the annealing temperature increases from 300 °C to 500 °C, the wear rates increase. The decreased microhardness could explain the increased wear rates due to grain growth and a weakened strain hardening effect in the higher temperature

annealing state. However, in the case of the pure AlSi10Mg deposit, the highest wear rate is found in the deposit annealed at 300 °C, and the samples annealed at higher temperatures seem to have better wear performance. Therefore, in addition to the microhardness factor, the interparticle bonding may also be a key feature in determining the wear rate of the deposits.

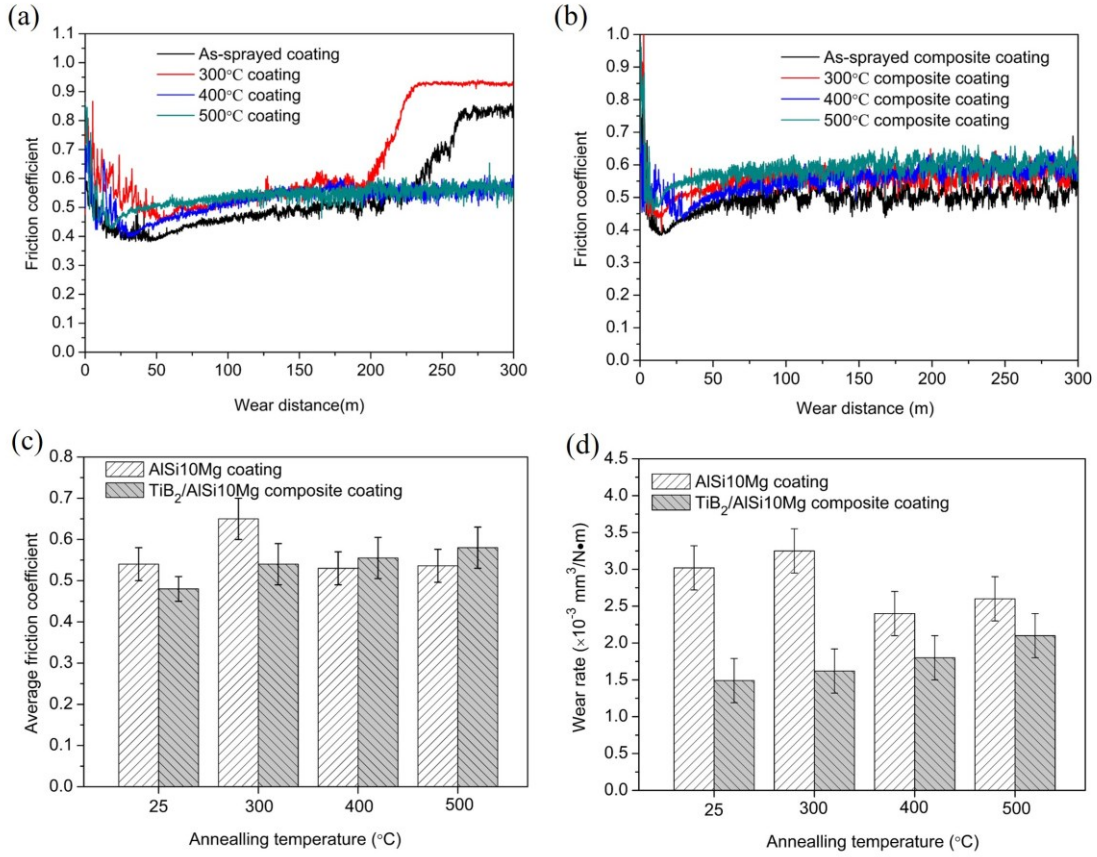

Figure 4-17 Friction coefficient vs. sliding wear distance for (a) AlSi10Mg-CT1 and (b) TiB_2/AlSi10Mg-CT1 composite coatings. (c) and (d) display the average friction coefficient and wear rate as a function of annealing temperatures, respectively.

An examination of the wear surfaces was carried out using SEM to reveal the wear mechanism of the CSed coatings. Typically worn surfaces of the as-sprayed and annealed deposits are shown in Figure 4-19. The worn surface of the as-sprayed AlSi10Mg deposit (Figure 4-19a) reveals a typical feature of adhesive wear, and the wear track profiles show evidence of ploughing and extrusion of the worn material outside the wear track; meanwhile, some loose wear debris and delamination can be observed on the worn surface. The observation of breaks in the smeared wear track can also explain the variation of its COF value at the final stage, which in turn accelerates its wear rate. The pure deposit annealed at 300 °C exhibits similar worn morphologies (not provided at present). Due to the lower microhardness values and relatively weak interparticle bonding in the cases of the as-sprayed and annealed samples at 300 °C, cracks formed on the worn track surface because of localized weakening under normal and tangential loading. These initiated cracks will propagate at the surface along the sliding direction, which leads directly to the observed wear flakes and delamination.

Figure 4-19c shows the wear track of the TiB_2/AlSi10Mg-CT1 composite deposit. The appearance of track shows signs of smearing and adhesive wear as in the pure AlSi10Mg coatings. However, the wear track on the composite deposit surface had a relatively narrow width, shallow ploughing grooves and less debris compared to the pure AlSi10Mg deposits. It is difficult to plough the wear debris from

the matrix because the attachment of TiB_2 particles in the matrix is improved with the in-situ reaction process. Additionally, TiB_2 particles carry a portion of the applied load and prevent plastic deformation of the surface. After annealing treatment at 500 °C for 2 h, both the pure AlSi10Mg and TiB_2/AlSi10Mg composite deposits showed a smooth wear track surrounded by regions of adhesive smearing and small loose wear debris. The EDS results (Figure 4-19) demonstrate a high content of oxygen on the worn surfaces during the sliding process. The annealed deposit showed a uniform distribution of micron-sized Si particles on the worn surface. Annealing at higher temperatures decreases the microhardness of the coating but enhances the interparticle bonding. As a result, the pure AlSi10Mg deposits annealed at 400 °C and 500 °C show better wear performance than the as-sprayed deposit and the deposit annealed at 300 °C. Therefore, we may conclude that both bonding conditions and microhardness are detrimental to the wear performance of the CSed deposits.

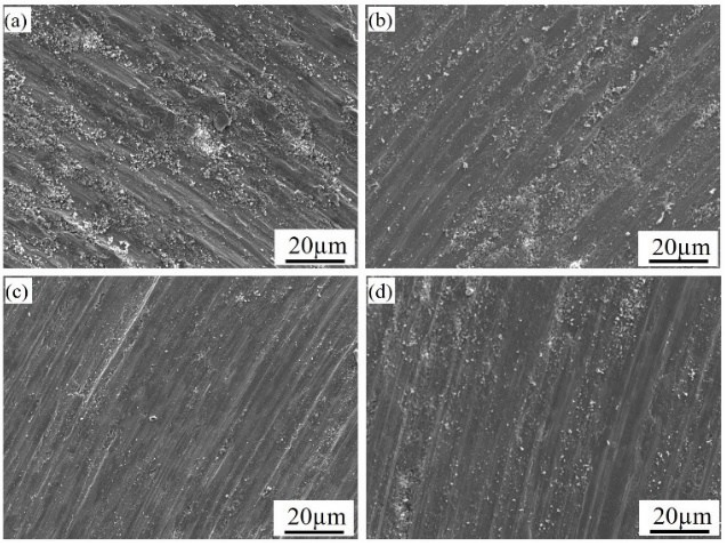

Figure 4-18 The worn morphologies of (a, b) AlSi10Mg-CT1 and (c, d) TiB_2/AlSi10Mg-CT1 deposits at (a, c) as-sprayed state and (b, d) annealed at 500 °C for 4 h.

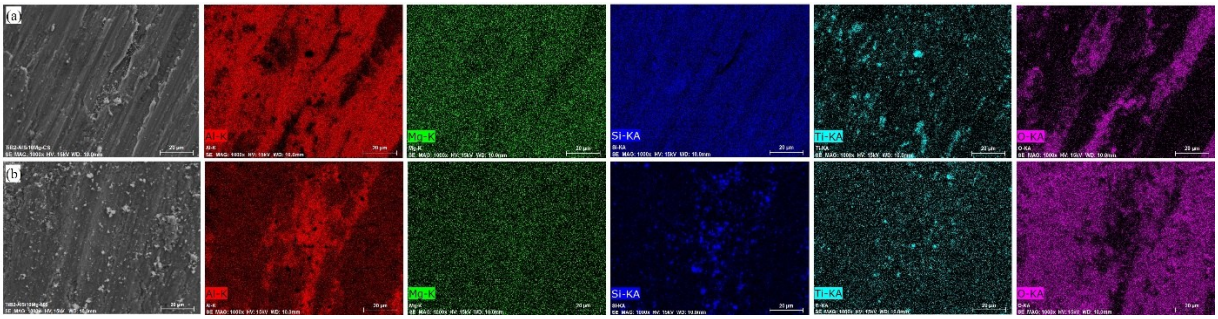

Figure 4-19 EDS mapping of the worn surface of the (a) as-sprayed and (b) annealed (500 °C) TiB_2/AlSi10Mg-CT1 composite deposits.

4.3.5 Tensile property

Figure 4-20 shows representative stress-strain curves of the pure AlSi10Mg and TiB_2/AlSi10Mg composite deposits before and after heat treatment under different conditions. The ultimate tensile strength (UTS) and elongation values are summarized in Figure 4-21a and b, respectively. Both the pure AlSi10Mg and TiB_2/AlSi10Mg composite deposits exhibit high UTS values but almost no elongations in the as-sprayed state, which implies the typical brittle behavior of the CSed deposits [3, 8-10]. However, it can be noted that the as-fabricated composite sample fractured at an earlier stage and has lower strength compared to the pure AlSi10Mg deposit, even though the composite deposit possesses a

denser structure and a much higher microhardness. The brittleness of CS samples in the as-fabricated state was notably improved by introducing annealing treatments. After heat treatment at 300 ℃ for 4h, the UTS values of the pure AlSi10Mg and TiB_2/AlSi10Mg composite deposits decreased from 410 MPa and 354 MPa to 276 MPa and 337 MPa, respectively, while the elongation value increased from 0.4% and 0.7% to 4.3% and 3.2%, respectively. As the annealing temperature increase to 400 ℃, further improvement in ductility but significant decrease in UTS values for both deposits can be observed. The elongation of the pure AlSi10Mg deposit reaches 12.0 ± 0.4%, while the composite has an elongation value of 7.6 ± 0.4%. The trade-off phenomenon between strength and elongation also exists in these heat-treated samples. As the annealing temperature further increases to 500 ℃, the UTS values further decrease to lower values, however, the specimens, especially the pure AlSi10Mg deposits were fractured much earlier with lower elongation values compared to the samples annealed at 400 ℃. This may be due to the formation of defects (large pores) in the deposits after the high-temperature heat treatment, which caused their fracture.

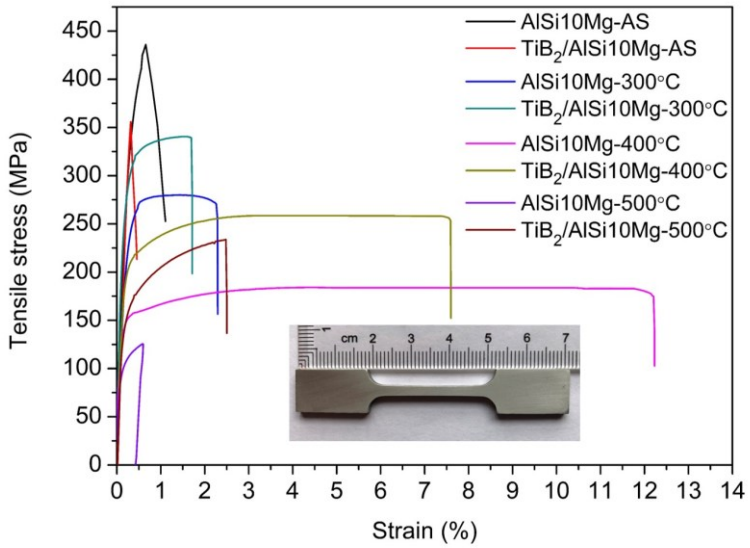

Figure 4-20 Tensile stress-strain curves for pure AlSi10Mg-CT2 and TiB_2/ AlSi10Mg-CT2 composites in as-sprayed state and annealing treated at different temperatures.

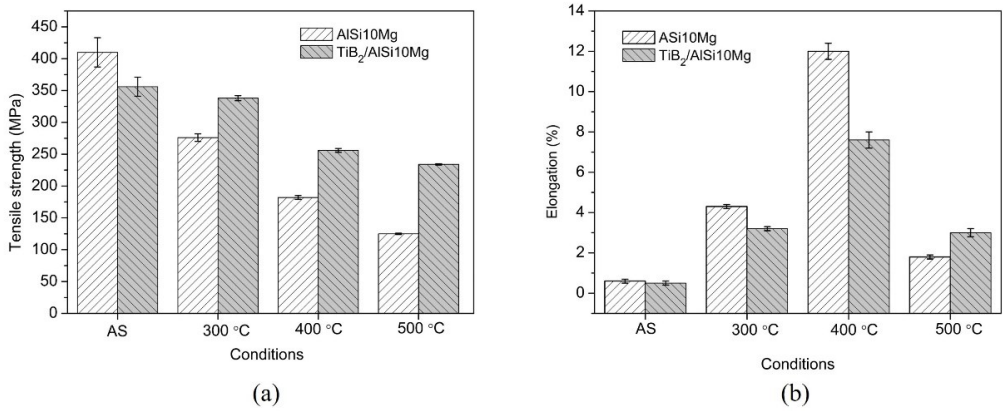

Figure 4-21 (a) and (b) summarize the UTS values and elongation of the tested specimens, respectively.

SEM observation of the fracture morphologies of the AlSi10Mg and TiB_2/AlSi10Mg composite samples after the tensile test were given in Figure 4-22, to further study the fracture mechanisms of the CSed and annealed samples. As can be seen from Figure 4-22a and Figure 4-23a, both the as-sprayed pure AlSi10Mg and TiB_2/AlSi10Mg composite samples were fractured not only along interparticle interfaces but also through the intergranular, which indicates a good cohesive bond between these deformed splats. The entire morphology of the as-sprayed samples demonstrates a brittle feature, even though a few fine dimples can be observed in some highly deformed regions. Moreover, the fracture surface presents some craters, which are formed by plucking out the entire particles. There are some small spherical particles (5-10 μm) at the bottom of these craters. These particles were embedded between two successive bigger splats, without any metallic bonding with the surrounding splats. Although the powders used for spraying were in the range of 20–87 μm, invariably some fine powders (5-10 μm) always remain in the powder mixture. As illustrated in Figure 4-25a, these embedded fine powders act as points of asperity during fracture and thus have a detrimental effect on the tensile strength of deposit [11]. Besides, the work hardening effect, as well as the limited metallurgical bonding between deformed splats, can also result in such a brittle feature. As presented in Figure 4-23a, it can be noted that more large craters (traces of detached particles) were formed on the fracture surface of the composite deposit. In addition to the above-mentioned fine powders, the presence of TiB_2 clusters on the deformed splats surface may also give rise to the formation of these craters. As revealed by EDS mapping of the fracture surface (Figure 4-24a), these TiB_2 clutters act as contaminants, preventing the metallic bonding in these areas. As a result, fracture occurred easily in these weakly bonded regions. This phenomenon can explain the lower strength of the as-sprayed composite samples in comparison to the pure AlSi10Mg samples.

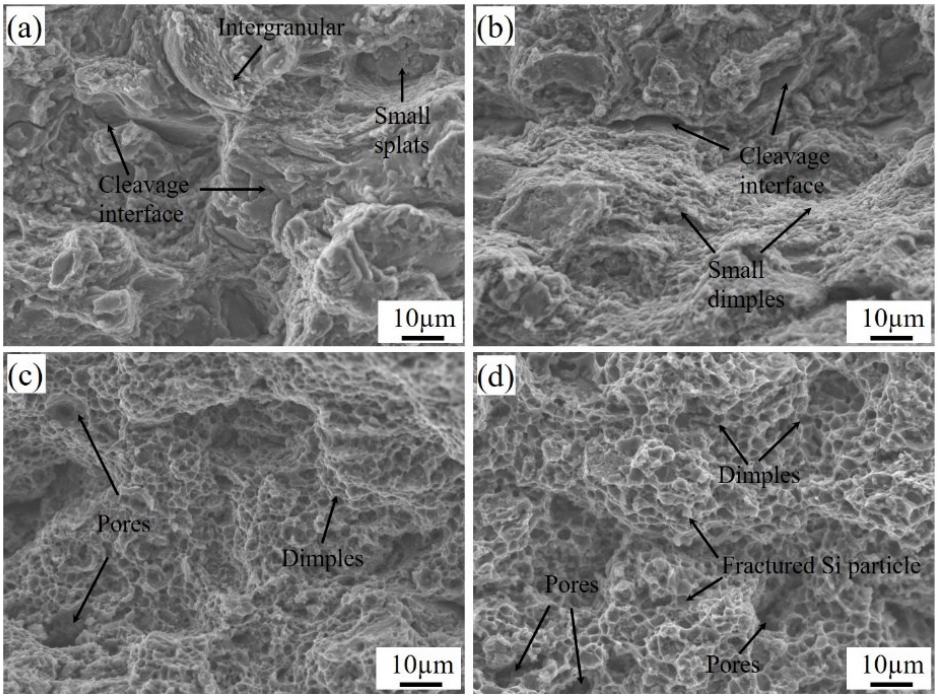

Figure 4-22 Fracture morphologies of the as-sprayed and annealed AlSi10Mg-CT2 deposits after the tensile test: (a) as-sprayed state; (b) 300 ℃; (c) 400 ℃; (d) 500 ℃.

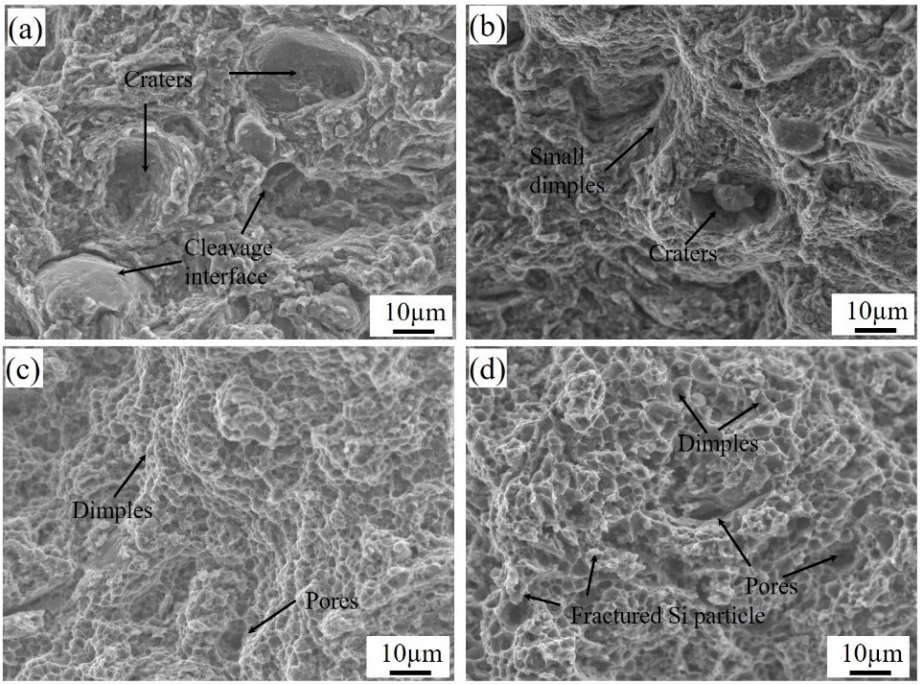

Figure 4-23 Fracture morphologies of the as-sprayed and annealed TiB_2/AlSi10Mg-CT2 composite samples at different temperatures after the tensile test: (a) as-sprayed state; (b) 300 ℃; (c) 400 ℃; (d) 500 ℃.

In addition to the micro-scale fracture characteristic, the TiB_2/AlSi10Mg composite deposit has different fracture characteristics at the submicron and nano-level that involves ultrafine primary Si particles within a single splat and TiB_2 particles distributed within a splat and inter-splat region. Figure 4-24a shows the magnified view of the fracture surface of the as-sprayed composite deposit, which features a cleavage fracture through the interparticle boundaries. According to B. Yu et al. [12], the formation of nanocrystalline grains in the intensively deformed inter-splat regions as a result of recovery or dynamic recrystallization has limited ductility. Once the crack starts from the pores or poor bonding regions, it can propagate along these nanocrystalline grains, resulting in a cleavage fracture. Moreover, it was reported that the size and morphology of the eutectic Si particles and reinforced particles have an important impact on mechanical properties of the Al-Si alloys [13] [14]. According to Li et al. [14], the presence of TiB_2 clusters and Si networks at the GBs can cause localized shearing to occur and hence lead to the crack initiation and propagation.

Figure 4-22b and Figure 4-23b show the fracture morphologies of the samples annealed at 300 ℃ for 4 h. There are two main morphologies on the fracture surfaces in the forms of small dimples and regular cleavage interfaces. The dimples have a size of approximately 1 μm, which is indicative of a ductile fracture. However, some defects, such as pores and craters, can still be observed on the fracture surface, indicating insufficient healing of splat boundaries, triple junctions, and other defects in this condition. Nevertheless, the enhanced metallurgical bonding through diffusion leads to improved ductility but lower UTS by eliminating the work hardening effect. As the annealing temperature increase to 400 ℃, the dominant dimples structure on the fracture surface indicates a significant improvement in ductility. Moreover, fractures occurred in the interior of the particles instead of along the weakly bonded interface, indicating that the diffusion between particles was more completed. Further increasing the annealing temperature to 500 ℃ results in enlarged dimples (3-4 μm) on the fracture surfaces. Little differences in fracture morphologies can be found in both the pure AlSi10Mg and TiB_2/AlSi10Mg deposits at higher annealing temperatures. Additionally, well-bonded fractured TiB_2 particles (as shown

in Figure 4-24j) can be noted throughout the matrix, which indicates that the matrix efficiently transmitted the applied load to the TiB_2 particles. Figure 4-25c and d illustrate the fracture models for the annealed composite samples at micro-scale and submicron scale.

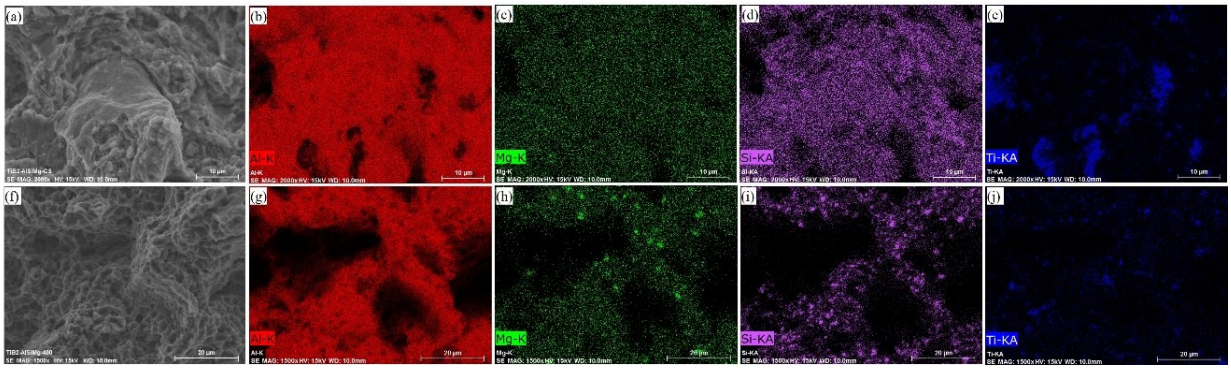

Figure 4-24 Fracture morphologies and EDS mapping of the TiB_2/AlSi10Mg-CT2 composite samples in as-sprayed state and annealed at 400 ℃.

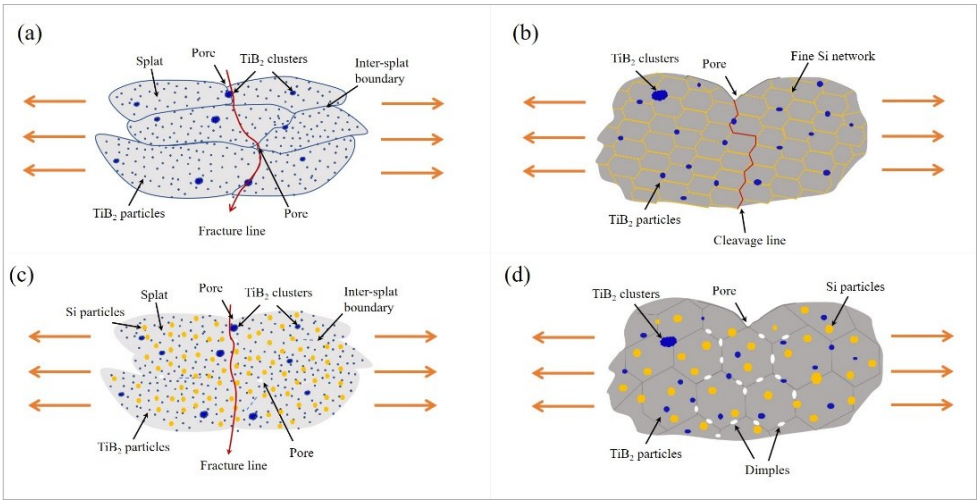

Figure 4-25 Schematic of the fractural model for as-sprayed and annealed composite deposits at micro-scale and submicron-scale: (a) micro-scale and (b) submicron-scale fracture model of the as-sprayed composite deposit; (c) micro-scale and (d) submicron-scale fracture model of the annealed composite deposit.

4.4 The effect of FSP process

4.4.1 Phase composition

Figure 4-26a and b display the XRD patterns of the CSed and FSP treated (FSPed) pure AlSi10Mg-CT2 and TiB_2/AlSi10Mg-CT2 composite deposits. The composition phases, including α-Al, Si, and Mg_2Si, in the as-sprayed deposit were well preserved in the FSPed samples. In addition to these three phases, peaks corresponding to the TiB_2 phase can be observed on the composite patterns. Moreover, XRD patterns of the AlSi10Mg and TiB_2/AlSi10Mg composite samples show that Si peaks of FSPed samples have higher intensities than those in as-sprayed states, but they are independent of processing passes. This indicates a significant decrease of Si solid solubility in Al caused by the thermal effect during FSP, as the temperature in the stir zone (SZ) can be of the order of 80 % of the melting temperature of the Al alloys [15]. A similar observation was also revealed for the annealed samples (Figure 4-6).

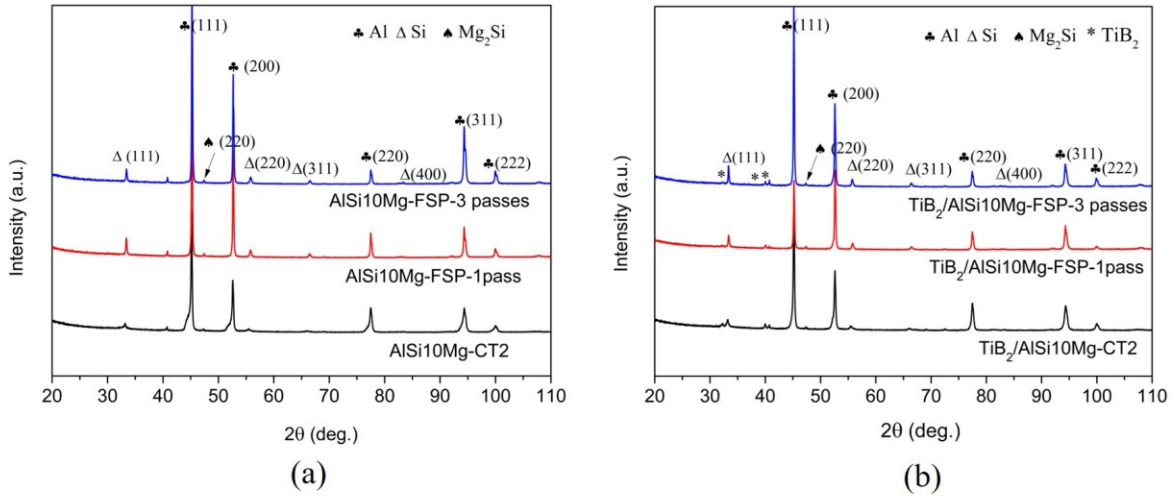

Figure 4-26 XRD patterns of the CSed and FSPed deposits: (a) AlSi10Mg-CT2; (b) TiB_2/AlSi10Mg-CT2.

4.4.2 Microstructure evolution

Figure 4-27a and b display the etched cross-sectional overviews of the CSed AlSi10Mg deposits after one pass and three passes FSP treatments, respectively. The SZ appears as a half-basin shape. It is evident that this nugget zone is free of defects such as keyholes, cracks, or tunnels. A sharp boundary is visible between the SZ and the unprocessed as-sprayed deposits. On the contrary, the boundary on the retreating side is obscure. A similar observation can be found on the surface morphologies, as illustrated in Figure 4-29. Some whiter regions appear on the top, right, and bottom of the SZ, where the materials undergo greater plastic deformation and the thermal effect. Moreover, such a white region also appears in the center of the SZ after three passes of the FSP treatment. As shown in Figure 4-28 and Figure 4-30, a similar morphology evolution can also be observed in the FSPed TiB_2/AlSi10Mg composite deposits. However, a part of composite deposit was stirred into the substrate, especially for the composite deposit after multi-FSP treatment. This is because the composite deposits are about 0.5 mm thinner and the press amount of the pin was not well controlled during the FSP operation.

Figure 4-31 shows the SEM images of the FSPed AlSi10Mg deposit in different regions (A, B, C, and D) as marked in Figure 4-27a. As shown in Figure 4-31a, evident inter-splat boundaries and small pores can be seen in the as-sprayed pure AlSi10Mg deposit. Figure 4-31b shows a typical morphology of the thermomechanical affected zone (TMAZ), where the inter-splat boundaries tend to disappear. However, some small pores are still present along the material flow direction. As shown in the magnified SEM image (Figure 4-32b), eutectic Si networks are broken into ultrafine individual Si particles in this region. The SZ is characterized by a dense structure with uniformly distributed Si particles (Figure 4-32c). The average particle size of the Si phase was measured as approximately 0.42 μm, showing slight growth compared to that of the as-sprayed state. Figure 4-33 shows the microstructure of AlSi10Mg deposit after repeating the FSP treatment for three passes. The Si particles within the SZ become larger, and their number and density decrease significantly. This phenomenon is more evident in the whiter regions, as shown in Figure 4-33c. The coarsening of the Si phase observed in SZ is similar to annealing heat treatment effect, as the deposits experienced extensive plastic deformation and a large amount of heat was generated during the FSP process, especially in the case of three passes. Indeed, it was reported that the temperature in the SZ can reach as high as 400-480 ℃ [16].

The FSPed TiB_2/AlSi10Mg composites show similar evolution in the inter-splat boundary and Si phase (Figure 4-34 and Figure 4-35). Interestingly, the TiB_2 clusters presented in the as-sprayed composite deposits are broken into smaller sized particles after the FSP treatment. As shown in Figure 4-34c, the remarkably refined TiB_2 particles are uniformly dispersed in the SZ. The finer distribution can be attributed to the vigorous stirring action of the rotating tool that forced the particles into the grains. Less segregation or clusters of particles is observed in Figure 4-34c and d. Similar fragmentation of SiC and Al_2O_3 particles were reported in the literature on FSP of AMCs [17, 18]. However, a few TiB_2 clusters can still be observed in the TMAZ zone as the effect of the shear force in this zone is not strong enough to redistribute the particles. By examining five SEM images of each case, the volume fractions of the TiB_2 particles in CSed and FSPed composites were counted. The volume fraction of the TiB_2 particles in FSPed composite yields an average value of 3.8 vol.%, slightly lower than that of the as-sprayed state (4.1 vol.%). The decrease is because some nanosized TiB_2 particles (less than 200 nm) cannot be counted by using this method. However, these refined and uniform distributed TiB_2 particles play an important role in enhancing the mechanical properties of the composite.

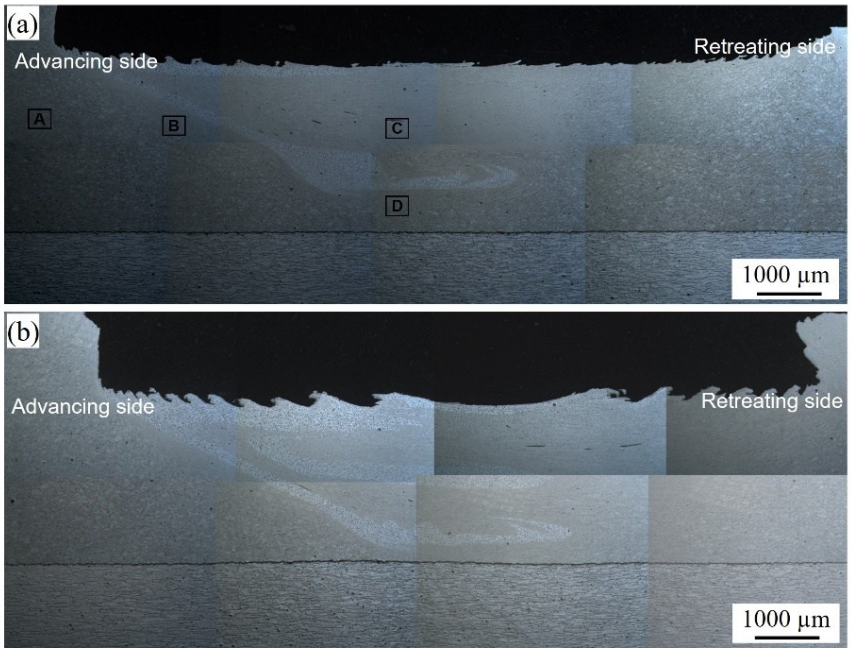

Figure 4-27 Optical micrographs showing the cross-section of the FSPed AlSi10Mg deposits: (a) 1 pass; (b) 3 passes.

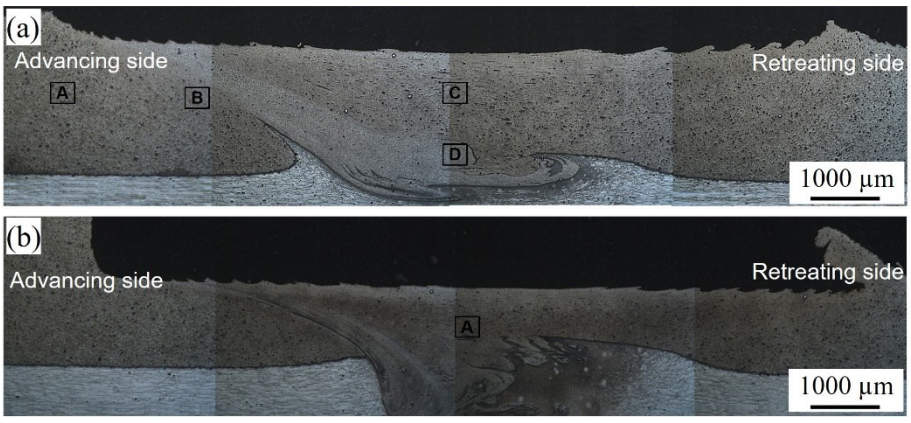

Figure 4-28 Optical micrographs showing the cross-section of the FSPed TiB_2/AlSi10Mg deposits: (a) 1 pass; (b) 3 passes.

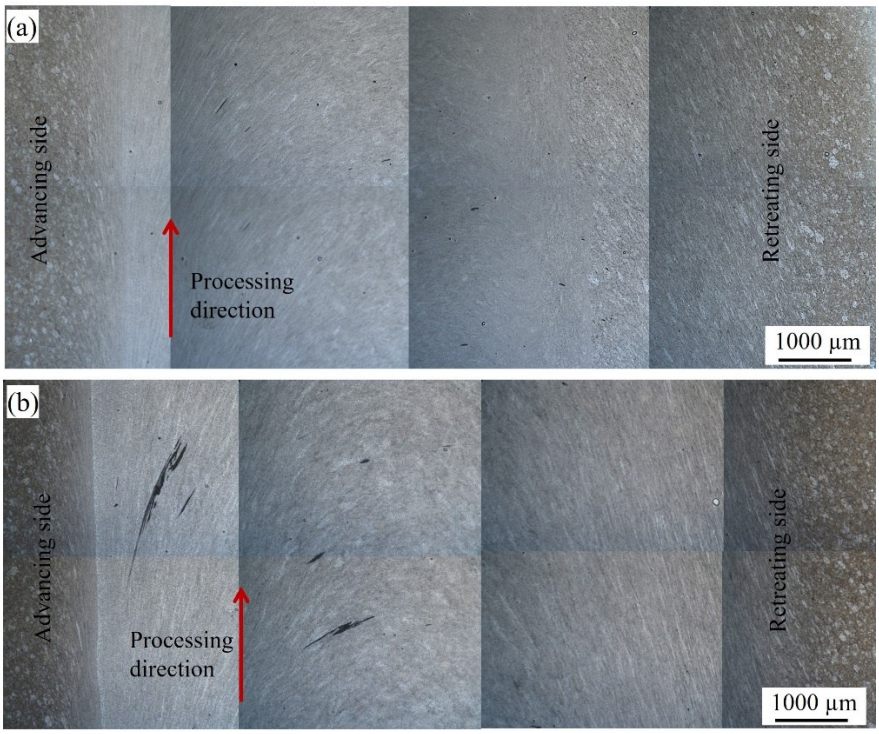

Figure 4-29 Optical micrographs showing the surface morphologies of the FSPed AlSi10Mg deposits: (a) 1 pass (b) 3 passes.

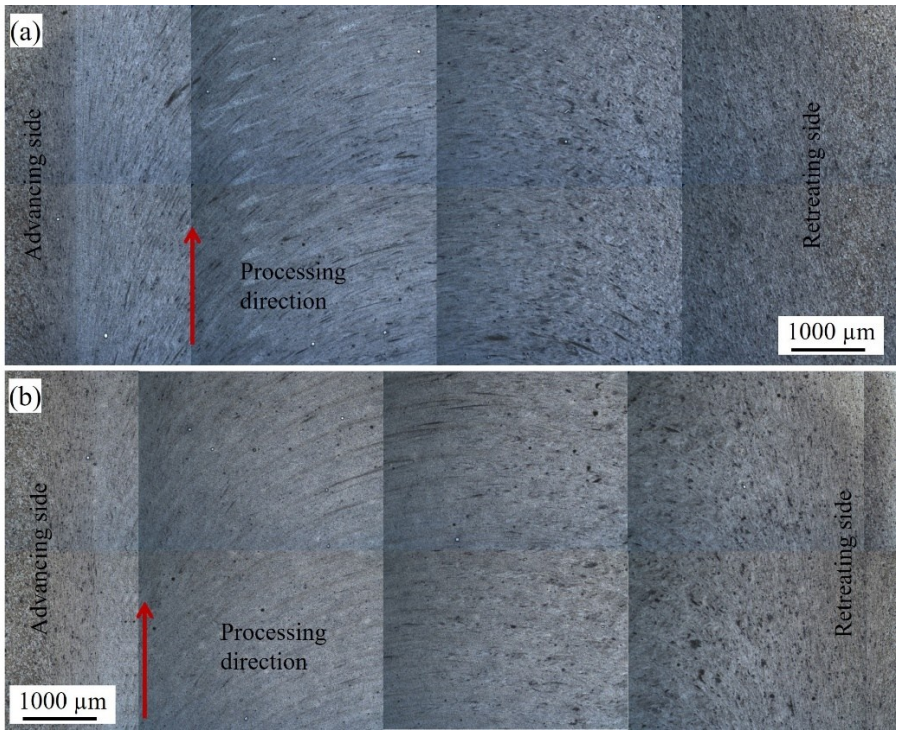

Figure 4-30 Optical micrographs showing the surface morphologies of the FSPed TiB_2/AlSi10Mg deposits: (a) 1 pass; (b) 3 passes.

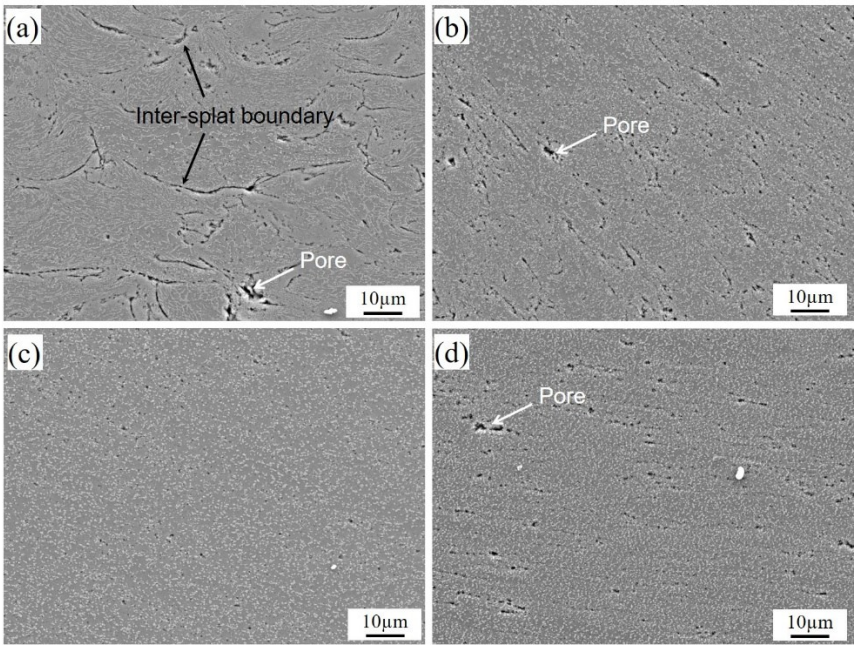

Figure 4-31 SEM images of the FSPed AlSi10Mg deposit in different regions corresponding to the A, B, C and D as marked in Figure 4-27.

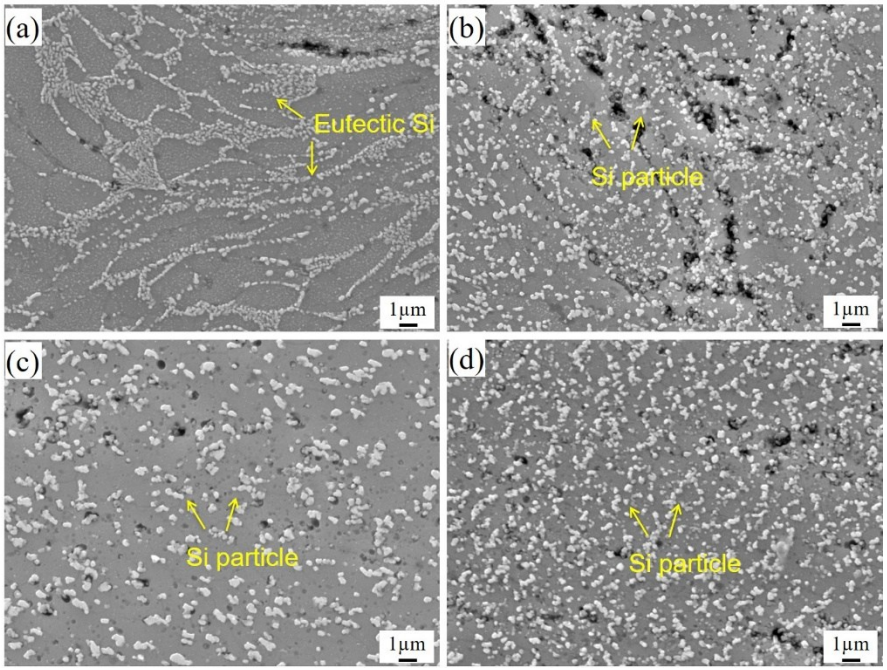

Figure 4-32 Magnified SEM images of the cross-section of the FSPed AlSi10Mg deposits in different regions corresponding to the A, B, C and D as marked in Figure 4-27a.

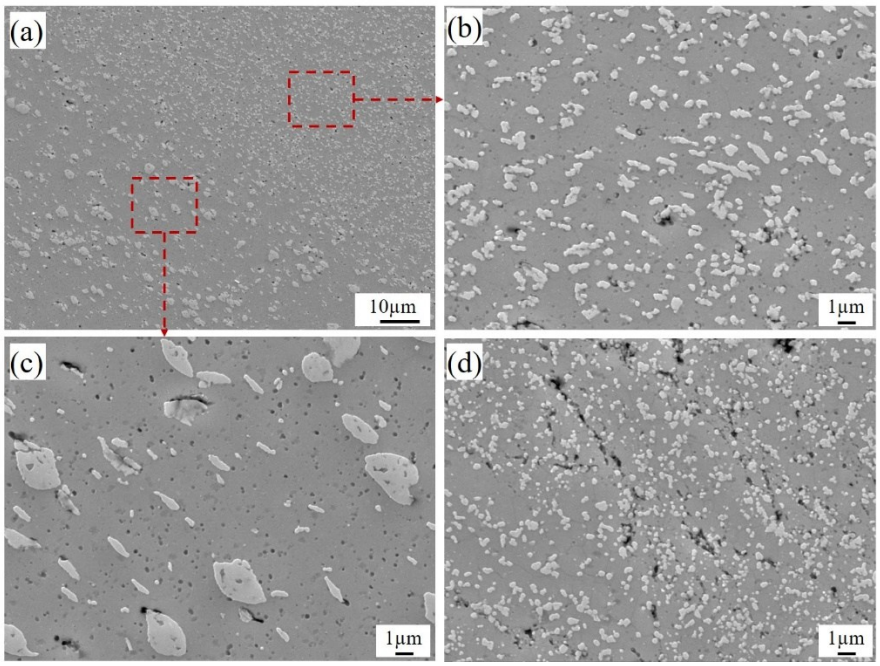

Figure 4-33 Magnified SEM images of the FSPed AlSi10Mg deposits in different regions as marked in Figure 4-27b.

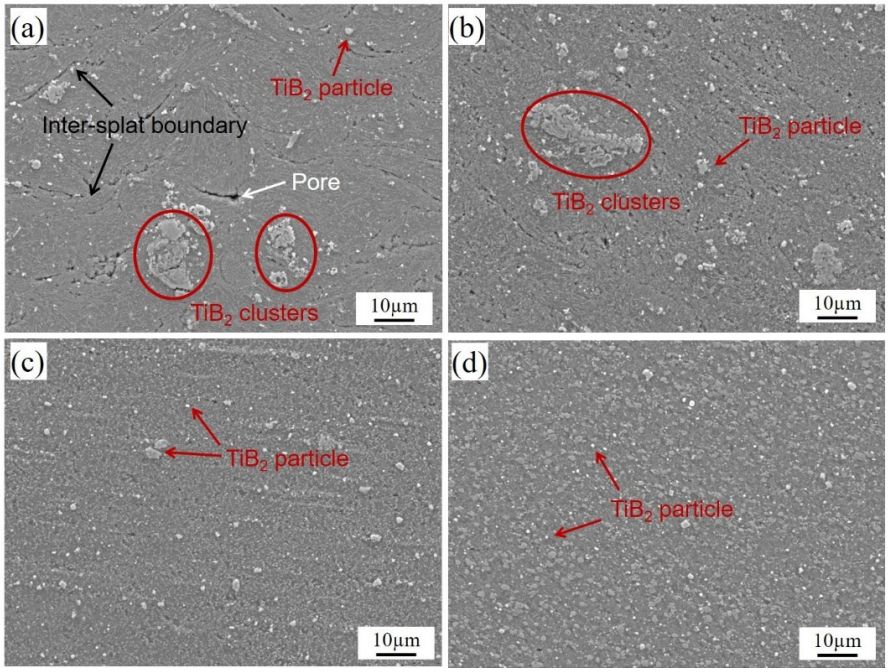

Figure 4-34 SEM images of the cross-section of the FSPed TiB_2/AlSi10Mg deposits in different regions corresponding to the A, B, C and D as marked in Figure 4-28a.

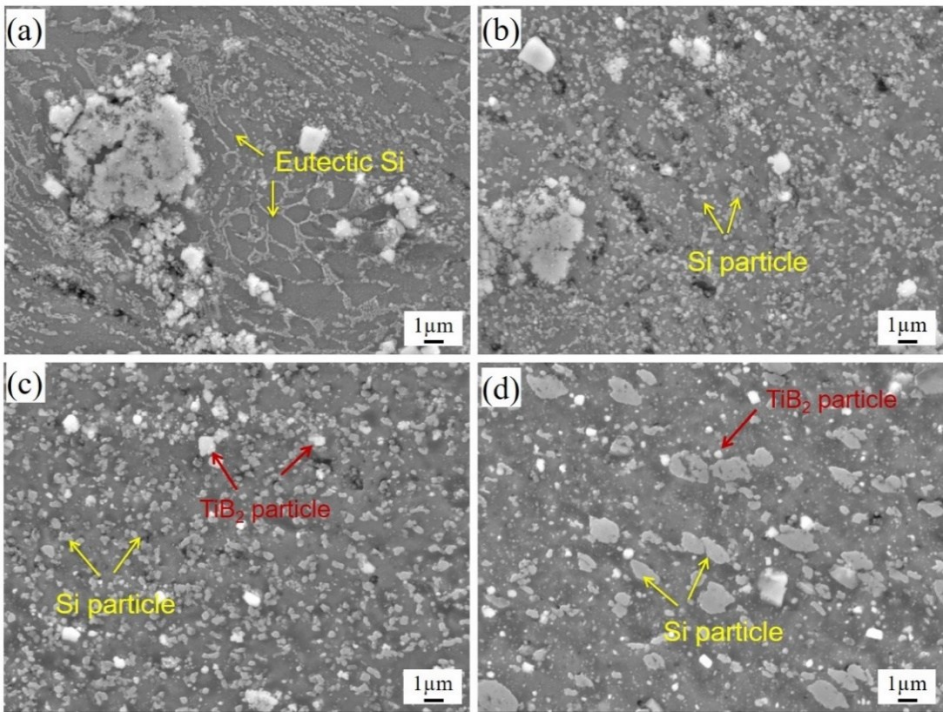

Figure 4-35 Magnified SEM images of the cross-section of the FSPed TiB_2/AlSi10Mg deposits in different regions corresponding to the A, B, C and D as marked in Figure 4-28a.

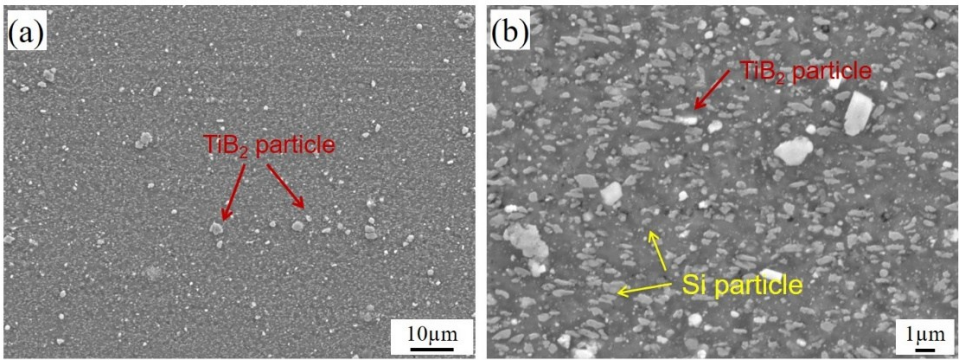

Figure 4-36 SEM images of the cross-section of the FSPed TiB_2/AlSi10Mg deposits in SZ as marked in Figure 4-28b.

TEM micrographs of the CSed and FSPed TiB_2/AlSi10Mg-CT2 composite samples are presented in Figure 4-37. As shown in Figure 4-37a, the as-sprayed composite microstructure is characterized by equiaxed grains, which is indicative of the interior particle region. These equiaxed grains have an average size of about 450 nm. However, it should be noted that the grain size in the highly deformed region could be much smaller. A large number of Si nanoparticles, marked by yellow arrows, are dispersed into the Al matrix. The magnified micrograph in Figure 4-37b shows that these Si particles are less than 50 nm, and most of them are located at the GBs. Besides, as highlighted by the red arrows, the TiB_2 particles are almost cubic or polyhedral in morphology with the size ranging from several tens to several hundreds of nanometers. It can be noticed that the TiB_2 particles are primarily distributed at the GBs. In the interior particle region, the lack of dislocations inside the Al grains seems to indicate that dislocation density in the initial composite deposit is low.

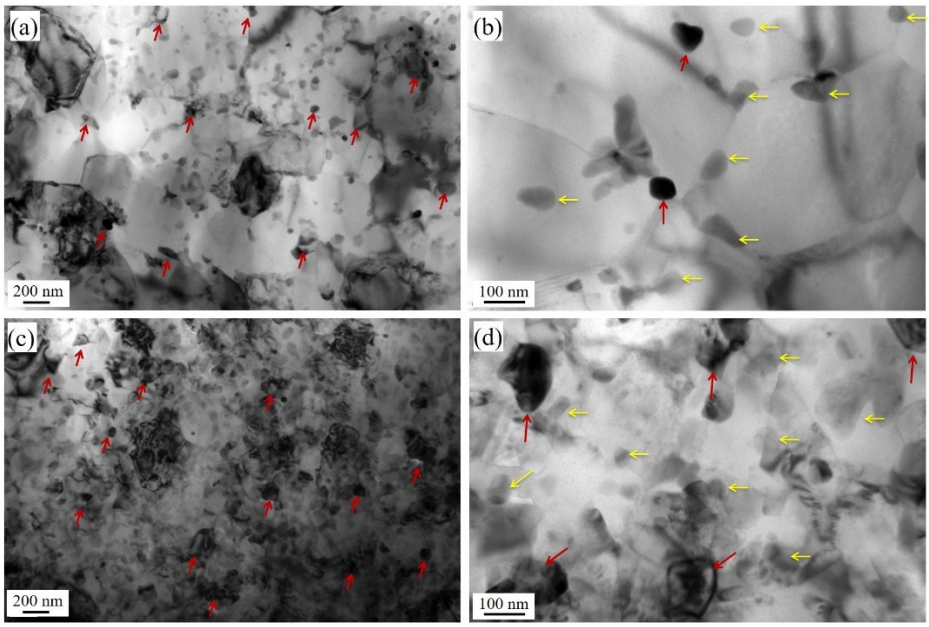

Figure 4-37 TEM bright-field (BF) images of CSed and FSPed TiB_2/AlSi10Mg-CT2 composite samples; (b) and (d) are the magnified views.

After the FSP treatment, the composite sample is characterized by fine equiaxed Al grains, having a size in range of 250-350 nm, as illustrated in Figure 4-37c. The creation of fine equiaxed grains is attributed to intense plastic deformation followed by dynamic recrystallization. The strain rate at the contact surface of the tool pin and the processed material can attain a value of 80 s^{-1}, which is much larger than many conventional deformation approaches (0.1-10 s^{-1}) [17, 19]. The strain rate of this magnitude contributes to grain refinement. As highlighted in Figure 4-37d, after the FSP treatment, the Si nanoparticles, as well as the TiB_2 nanoparticles, are distributed not only along the GBs but also inside the Al grains. It is well understood that eutectic Si can be rejected from the supersaturated Al matrix to form small Si particles due to the thermal softening effect as a result of the friction between the working tool and the material surface. The FSPed sample revealed a slight growth of Si particles compared to the as-sprayed state. Besides, the FSP altered the intergranular distribution of TiB_2 particles in the CSed composite into intragranular distribution. The finer distribution can be attributed to the vigorous stirring action of the rotating tool that forced the TiB_2 particles into the grains [17]. These uniformly distributed TiB_2 nanoparticles tend to restrict the dynamic recrystallization and slow down grain growth by pinning the movement of GBs and sub-boundaries.

4.4.3 Microhardness

Figure 4-38 illustrates the microhardness values measured on a horizontal line across the cross-section of the FSPed samples. The microhardness evolution for FSPed samples can be divided into three typical zones: the heat-affected zone (HAZ), TMAZ, and SZ. A continuous decrease in microhardness can be observed from the unaffected region to HAZ, TMAZ, and finally SZ with the lowest values. The asymmetry of microhardness in the advancing side and the reversing side is because the microstructure on the reversing side was influenced by the following FSP path, while the advancing side was free of other FSP path. Therefore, the microhardness on the advancing side is much higher and close to the bulk value (176 $HV_{0.1}$). The removal of the work hardening effect is the primary factor that should be responsible for such significant decrease in microhardness in the HAZ, TMAZ, and SZ regions. Besides, it can be noted that in the same position for these zones, the multi-pass treated samples possess slightly lower values compared to single-pass treated samples, which suggests that more thermal effect was produced after three passes of the FSP treatment. The effect of high heat in the HAZ region changed the

characteristic properties associated with softening of the matrix due to coarsening of the Si precipitates and increased grain size. Increasing the FSP passes results in lower microhardness. Moreover, the microhardness of the composite deposits in the SZ possess is about 110 ± 3 $HV_{0.1}$, much higher than that of the pure AlSi10Mg deposit (87 $HV_{0.1}$) due to the presence of TiB_2 nanoparticles. This fact may result from the combined effect of grain refinement and reinforcement of TiB_2 particles, which may offset a part of softening effect due to Si phase coarsening in SZ region.

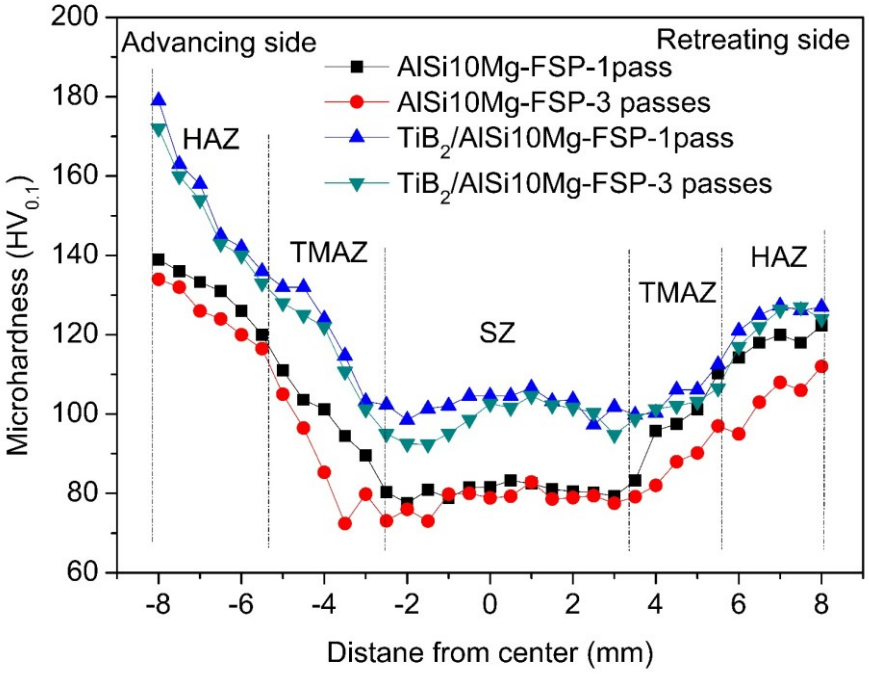

Figure 4-38 Microhardness values of FSPed AlSi10Mg and TiB_2/AlSi10Mg composite samples.

4.4.4 Tribological property

The tribological performance of the AlSi10Mg-CT2 and TiB_2/AlSi10Mg-CT2 composite deposits before and after FSP treatment is presented in Figure 4-39. As illustrated in Figure 4-39a and b, the COFs of both deposits show an unstable initial state (run-in), which then become steady after about 80 m and 50 m sliding distance for pure AlSi10Mg and TiB_2 reinforced composite deposits, respectively. This observation once again indicates that the addition of TiB_2 particles is beneficial for the formation of tribofilm, thereby reaching a stable stage earlier than the unreinforced AlSi10Mg deposits. A sharp increase in the COF at the final stage observed in AlSi10Mg-CT1 deposit is absent in the case of the CT2 deposits, which suggests a better inter-splat bonding state for the CT2 deposits. Besides, the CT2 deposits possess lower COF values and a reduced wear rate compared to the CT1 deposits. This could mainly due to the enhanced microhardness and improved inter-splat bonding. Generally, the TiB_2/AlSi10Mg composite deposits exhibit better wear performance compared to the unreinforced AlSi10Mg deposits.

FSP treatment seems to have little effect on wear performance for both pure AlSi10Mg and TiB_2/AlSi10Mg composite samples, as the COF values and wear rates remain essentially unchanged after FSP treatments. In general, a significant decrease in microhardness after FSP treatment can result in a higher wear rate. However, the elimination of defects and precipitation of Si particles after FSP treatment may improve the wear performance of the FSPed samples. As for the TiB_2/AlSi10Mg composite samples, the redistribution and refinement of TiB_2 particle are also beneficial for the

improvement of the wear performance. The worn surface morphologies in Figure 4-40 revealed the combined adhesive and abrasive wear mechanisms of the CSed and FSPed samples.

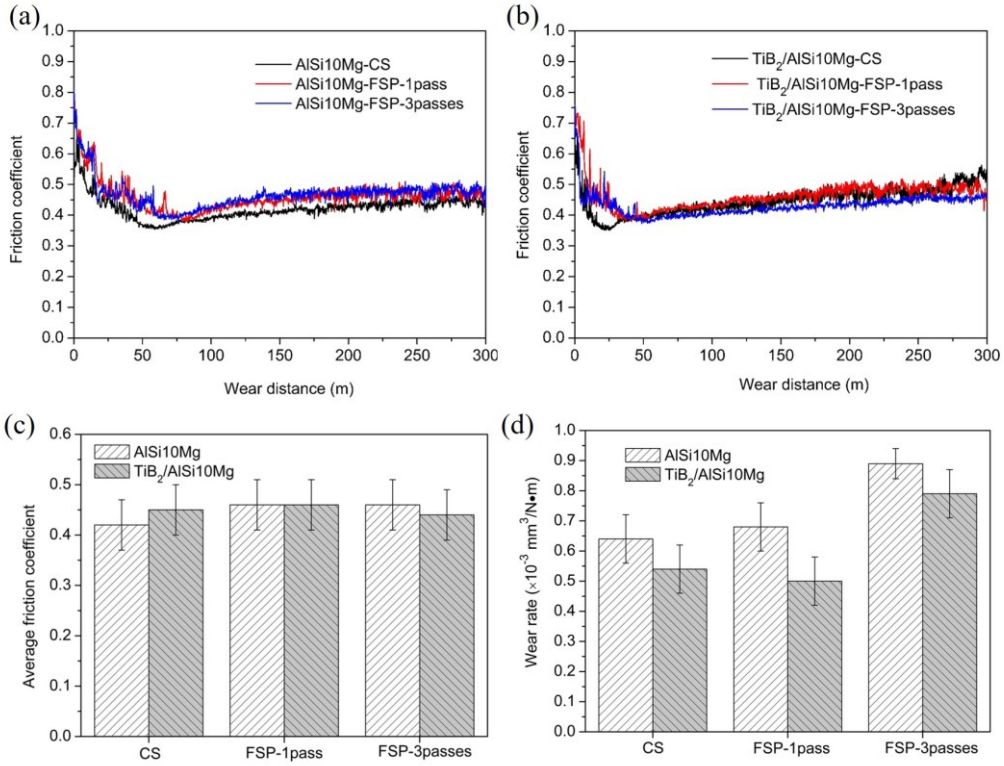

Figure 4-39 Friction coefficient vs. sliding wear distance for FSPed (a) AlSi10Mg-CT2 and (b) TiB_2/AlSi10Mg-CT2 composite deposits. (c) and (d) display the average COF and wear rate values of the CSed and FSPed samples.

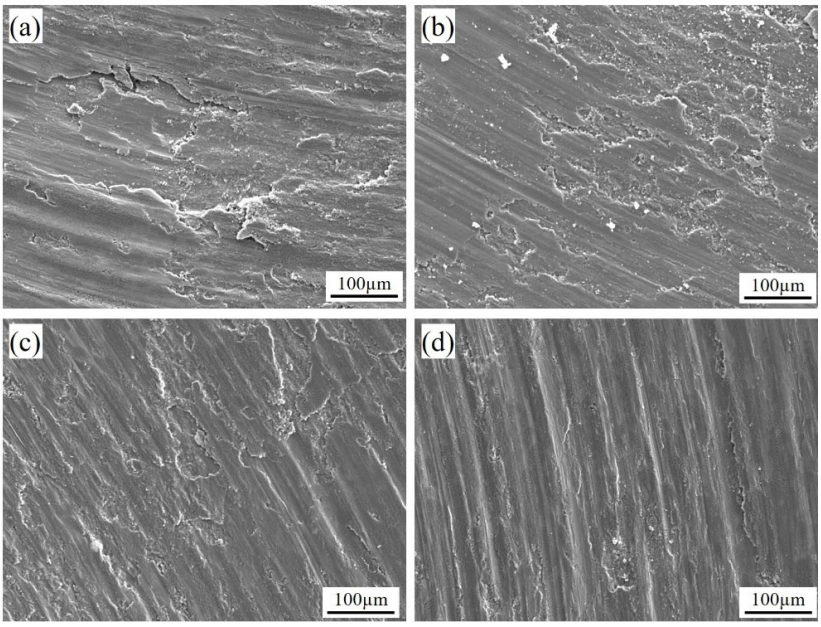

Figure 4-40 The worn morphologies of CSed and FSPed pure AlSi10Mg-CT2 and TiB_2/AlSi10Mg-CT2 deposits: (a) AlSi10Mg-CT2; (b) TiB_2/AlSi10Mg-CT2; (g) AlSi10Mg-FSP-1 pass; (d) TiB_2/AlSi10Mg-FSP-1 pass.

4.4.5 Tensile property

Figure 4-41a shows a representative stress-strain curve of the pure AlSi10Mg and TiB_2/AlSi10Mg composite deposits before and after FSP treatments. The UTS and elongation values are summarized in Figure 4-42a and b, respectively. In the as-sprayed state, both the pure AlSi10Mg and TiB_2/AlSi10Mg composite deposits exhibit completely a brittle feature with almost no ductility. Significant improvement in ductility while maintaining high strength was achieved in the FSPed samples. The UTS and elongation of the pure AlSi10Mg deposit after one pass treatment reached about 295 MPa and 21%, respectively. Comparatively, the FSPed TiB_2/AlSi10Mg composite deposits possess an UTS value of 365 MPa, which is 23.7% higher than that of the unreinforced sample. Meanwhile, the composite deposits possess a slightly lower elongation of 16%. As shown in Figure 4-43, the TiB_2/AlSi10Mg composite deposits in this work exhibit superior mechanical properties compared with other AMCs fabricated or post-treated by the FSP process. It is noteworthy that unlike the mutual repulsion of strength versus ductility for most structural materials, a simultaneous enhancement in both strength and ductility has been achieved in the FSPed TiB_2/AlSi10Mg composite deposit, which has always been the merits pursued by material scientists for P-AMCs. According to Yang. et al. [18, 20], FSP was applied to treat the CSed Al_2O_3/2024Al composites produced from micron-sized mixture powders. However, the FSPed composite deposits presented very limited improvement in tensile strength (290 MPa) and ductility (4.9%). This is mainly because of the presence of largescale reinforced particles (micron-sized) and poor reinforcement/matrix interfacial bonding within the composite, which are negative factors hampering the improvement of tensile properties. In this study, these two weaknesses can be resolved by using the in-situ TiB_2 reinforced composite powder. The superior property of the FSPed composite deposits are mainly attributed to the homogenous distribution of reinforcement, matrix grain refinement, and robust interfacial bonding.

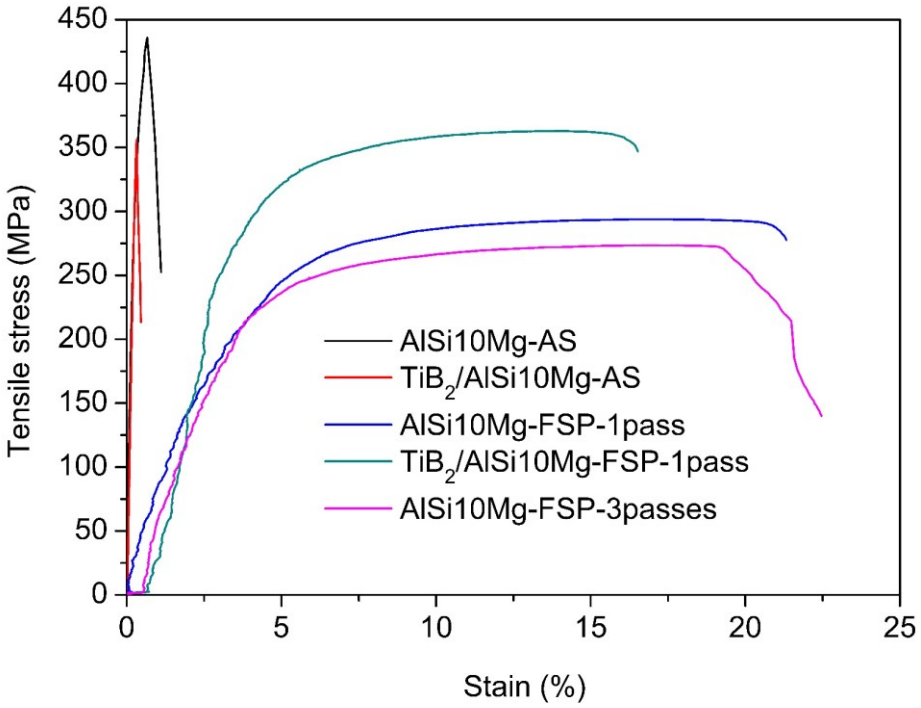

Figure 4-41 Tensile stress-strain curves for pure AlSi10Mg and TiB_2/AlSi10Mg composites in as-sprayed state and FSPed with different passes.

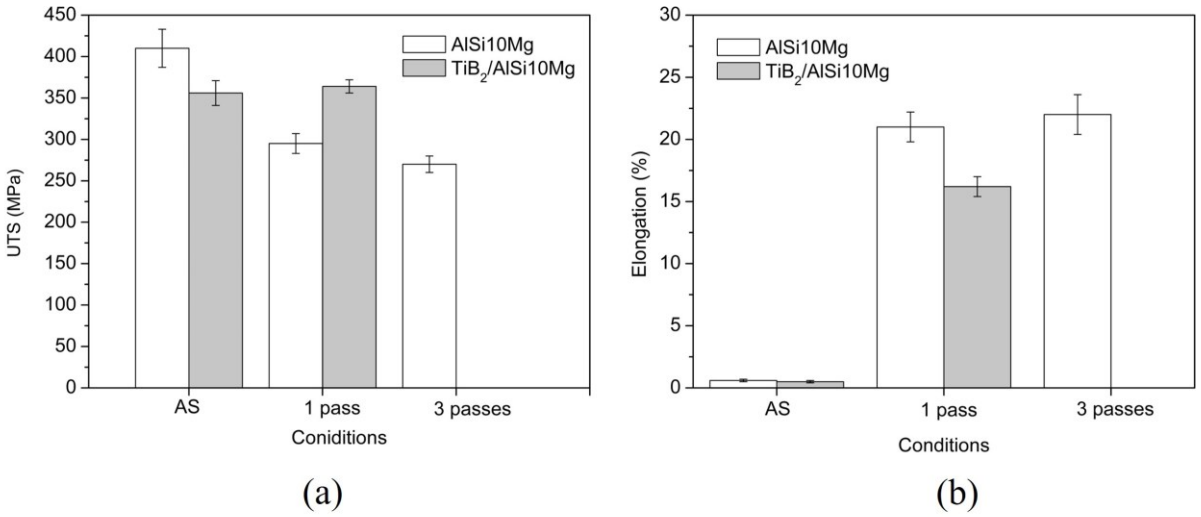

Figure 4-42 (a) and (b) summarize the UTS and elongation values of the tensile specimens, respectively.

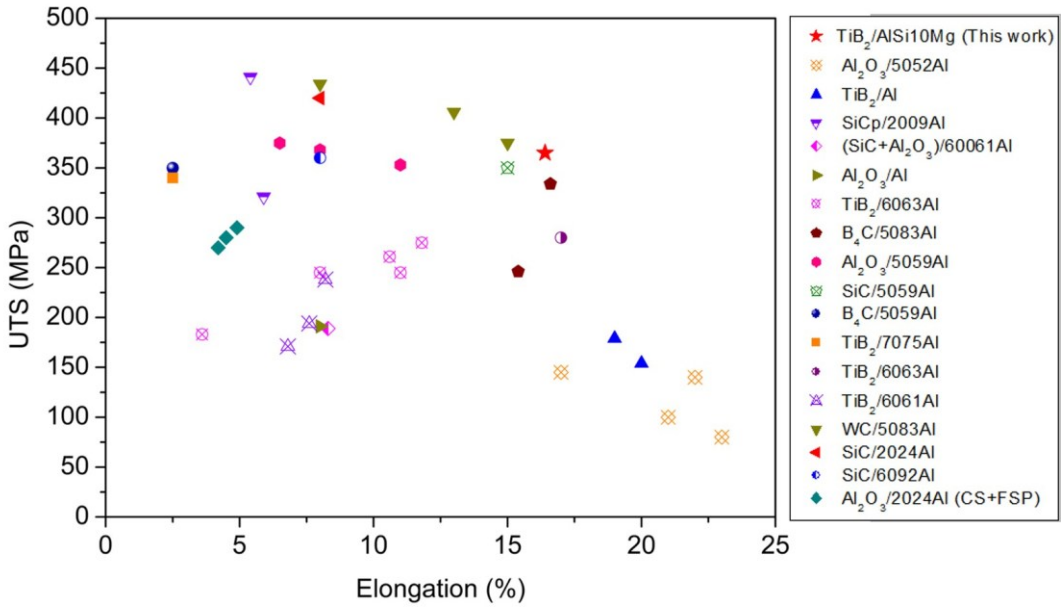

Figure 4-43 Comparison of the UTS and elongation of the FSPed TiB_2/AlSi10Mg composite deposits with other FSP fabricated Al matrix composites [21-26] [17, 20, 27-34].

Figure 4-44 shows the typical fracture surfaces of tensile samples for the AlSi10Mg and TiB_2/AlSi10Mg composite after FSP treatment. It is completely different from the brittle fracture morphology of the as-sprayed deposits (see Figure 4-22 and Figure 4-23), the fracture surfaces of the FSPed tensile samples are characterized by numbers of small dimples. When the pure AlSi10Mg samples were FSPed for one pass, equiaxed dimples with an average size of approximately 0.75 μm were observed across the whole fracture surface (see Figure 4-44b), indicating a highly ductile fracture. The dimple size is related to the grain size, as GBs can act as sites for crack nucleation and, therefore, control the size of the dimples. At higher magnification, these dimples contain ultrafine Si precipitates (as marked by the red arrow in Figure 4-44c). Hence, the rupture is ductile and occurs by decohesion between the Si precipitate and the Al matrix. As shown in Figure 4-44e and f, fine dimples are noticeable on the fracture surface of the composite deposits after FSP treatment, which is similar to that of the

FSPed AlSi10Mg sample. Apart from the ultrafine Si particles, some well-bonded and fractured TiB_2 particles are also observed on the fracture surface. These results give evidence of strong interfacial bonding between the Al matrix and the TiB_2 particles. A ductility feature with larger dimples can be observed on the fracture surface of the pure AlSi10Mg samples after FSP treatment for three passes, as illustrated in Figure 4-44h and i. The enlarged dimples suggest gain growth when repeating the FSP passes.

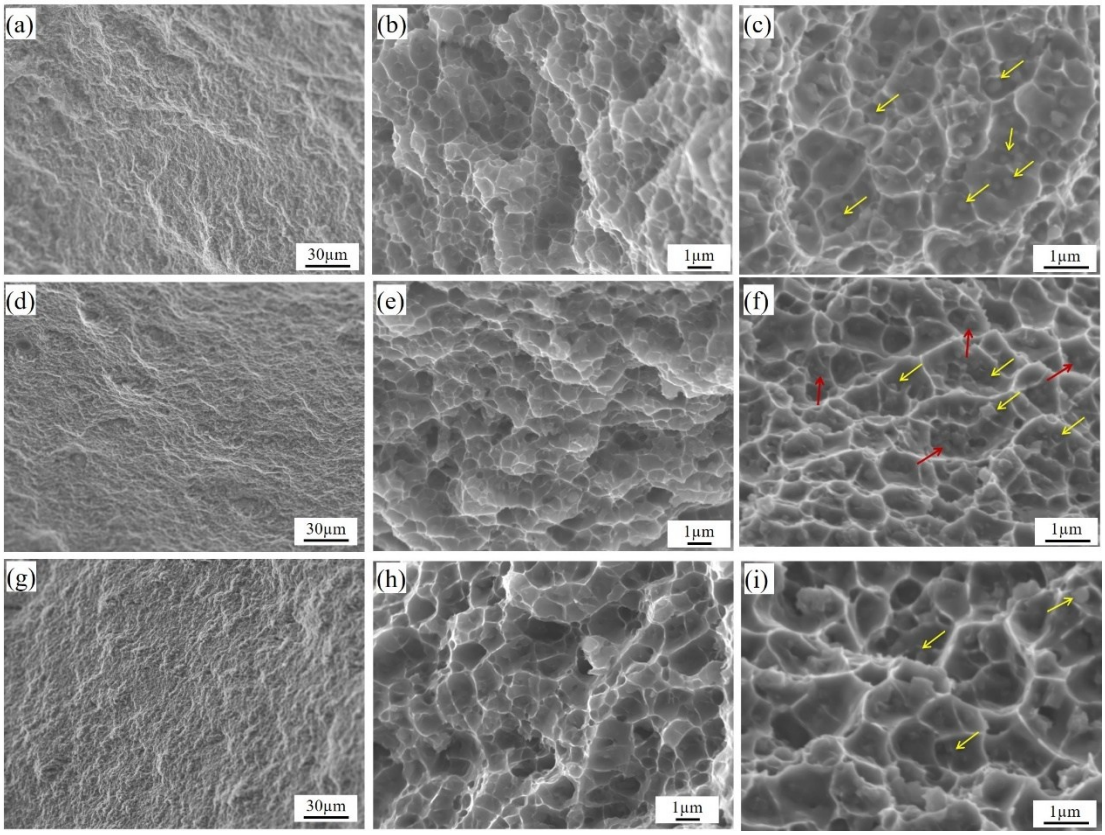

Figure 4-44 SEM micrographs of the tensile fracture surface of the FSPed AlSi10Mg and TiB_2/AlSi10Mg composites with different magnifications: (a-c) AlSi10Mg-FSP-1 pass; (d-f) TiB_2/AlSi10Mg-FSP-1 pass; (g-i) AlSi10Mg-FSP-3 passes.

4.4.6 Strength mechanisms

Significant improvement in the tensile properties of the FSPed samples is mainly because the interior defects, such as pores and poor inter-splat boundaries, presented in the as-sprayed state can be effectively eliminated by FSP treatment. Considering that a fracture could primarily take place around these defects, it is vitally important to obtain a fully dense and defect-free structure in the FSPed samples. It should be emphasized that the FSP treatment altered the inter-splat bonding conditions from prominent interlocking or partially metallurgical bonding in the as-spray state to fully metallurgical bonding. Thus, the brittle appearance fracture mode in the as-sprayed condition is shifted to the ductile dominated fracture after FSP treatment.

Moreover, the FSPed TiB_2/AlSi10Mg composites possess higher tensile strength in comparison with the unreinforced pure AlSi10Mg sample. First, a more uniform and refined structure was produced in the FSPed samples due to the dynamic recrystallization, which, in turn, can increase the tensile strength of the samples. Compared to the FSPed pure AlSi10Mg samples, the addition of TiB_2 nanoparticles, on the one hand, provides new sites for recrystallization; on the other hand, they can pin the movement of GBs, which can reduce the rate of grain growth. This pinning effect leads to the

refinement of grains, which contributes to the strengthening effect resulting based on Hall-Petch mechanisms. EBSD characterization will be carried out to determine the grain size evolution after FSP treatment.

Besides, the homogenized and refined TiB_2 particles produced by the FSP treatment are beneficial for both strength and ductility enhancement. Because the TiB_2 clusters in the as-sprayed composite deposits will result in stress concentration, this will promote the rupture, degrading ductility severely. According to the Orowan strengthening mechanism, strengthening of the composites is attributed to the interaction between the reinforcement particles and the motion of dislocations in the matrix. Normally, the size of reinforcements should be smaller than 1 μm to initiate this strengthening mechanism [26]. As revealed by TEM micrographs (see Figure 4-37c and d), both the nanosized TiB_2 particles and Si particles are distributed homogeneously in the matrix of the FSPed composites, which can further increase the contribution of the Orowan strengthening effect. However, since the size and the content of Si particles are basically the same in both the FSPed pure AlSi10Mg and TiB_2/AlSi10Mg composite samples, it is believed that the Orowan strengthening by Si particles is the same. Therefore, only the Orowan strengthening effect produced by TiB_2 particles is responsible for the improved strength of the composites compared to the pure AlSi10Mg samples.

Finally, a load-bearing mechanism resulting from strong interface bonding between the TiB_2 nanoparticles and Al matrix is also responsible for the improved tensile strength of the composite. Previous studies have reported that the in-situ formed TiB_2 particles have a good bonding interface with the Al matrix [35], suggesting an effective load transfer from matrix to nanoparticles. On the other hand, the composite failure is associated with particle cracking and void formation in the matrix. Particle cracking by the propagation of an internal defect is given by the Giffith equation [36]:

$$\sigma_f = \left(\frac{2E\gamma}{\pi C}\right)^{1/2} \qquad (4\text{-}1)$$

where σ_f is the stress on the particle, γ is the fracture surface energy, E is Young's modules of the particle, and C is the internal crack length. Since very fine and uniformly distributed TiB_2 particles were obtained in the FSPed composite samples, the internal crack length C is short, and the stress on the particle is high. The decrease in particles cracking would improve the ductility. Therefore, uniform dispersion of nano-sized TiB_2 particles in the grain interior is an effective approach to increase the strength and simultaneously improve the ductility of the composites, because they can generate, pin down, and thus accumulate dislocations within the grains [37-39].

4.5 Summary

In this chapter, a novel gas-atomized composite powder reinforced with in-situ TiB_2 particles was used as the feedstock to fabricate TiB_2/AlSi10Mg composite deposits by the CS process. Then, the influence of post-treatments, including heat treatment and FSP, on the microstructure and mechanical properties was investigated. For comparison, the as-sprayed AlSi10Mg deposits were treated in the same conditions. The following conclusions can be drawn:

(1) The CSed deposits display a fully dense structure with the cellular-like network of eutectic Si particles embedded in the Al matrix. Apart from the uniformly distributed TiB_2 nanoparticles, some clusters on a micrometer scale were also present in the CSed TiB_2/AlSi10Mg composite deposits. This inhomogeneous distribution of the particles derives from the gas-atomized composite powder.
(2) With the increase in the annealing temperature from 200 °C to 500 °C, the size of the Si particles increased to several micrometers, whereas their number decreased significantly. According to

the XRD and EDS analyses, there were no other new phases other than Al, Si, Mg_2Si and TiB_2 detected in the CSed and annealed samples.

(3) The microhardness showed a decreasing trend with the increase in the heat treatment temperature and duration of time, mainly due to the elimination of work hardening effect, grain growth and coarsening of Si phase. Nevertheless, the composite deposit exhibited an inhabitation of reduction in microhardness because of the hindering effect of the dislocation movement via nanosized hard TiB_2 during heat treatment.

(4) The tensile tests showed that both the as-sprayed AlSi10Mg and TiB_2/AlSi10Mg composite deposits possessed high tensile strength but almost no ductility. Comparatively, relatively lower tensile strength was obtained for the composite samples even though they have a denser structure and higher microhardness than the pure AlSi10Mg deposit. This could be attributed to the presence of TiB_2 clusters on the deformed splats surface, which are detrimental for metallic bonding between particles, thus resulting in an easier fracture during the tensile test.

(5) Significant improvement in ductility but a reduction in tensile strength was obtained for the annealed samples mainly due to the improved interfacial bonding between the deformed splats and grain growth after the annealing treatment, respectively. Besides, the annealed composite samples possess higher UTS but lower ductility compared to the unreinforced pure AlSi10Mg samples.

(6) FSP improves the distribution of TiB_2 particles and refines the particles as well. Based on the TEM observation, the FSP treatment altered the intergranular distribution of TiB_2 particles in the CSed composite into intragranular distribution. Significant grain refinement was achieved via dynamic recrystallization in the FSPed samples. The addition of TiB_2 particles can pin the movement of GBs which retards grain growth and results in a finer structure of the composite sample.

(7) A simultaneous enhancement in both strength and ductility of the CSed TiB_2/AlSi10Mg composite deposits has been achieved by FSP treatment. The strengthening mechanisms are related to the homogenous distribution of reinforcements, matrix grain refinement, and robust interfacial bonding. Increasing the FSP passes results in a lower tensile strength due to the coarsening of the Si phase and grain growth.

References of Chapter IV

[1] Xiao-Tao Luo, Ying-Kang Wei, Yan Wang, Chang-Jiu Li, Microstructure and mechanical property of Ti and Ti6Al4V prepared by an in-situ shot peening assisted cold spraying, Mater. Des., 85 (2015), 527-533.
[2] Xinliang Xie, Chaoyue Chen, Yingchun Xie, Zhongming Ren, Eric Aubry, Gang Ji, Hanlin Liao, A novel approach for fabricating Ni-coated FeSiAl soft magnetic composite via cold spraying, J. Alloys Compd., 749 (2018), 523-533.
[3] Renzhong Huang, Michiyoshi Sone, Wenhua Ma, Hirotaka Fukanuma, The effects of heat treatment on the mechanical properties of cold-sprayed coatings, Surf. Coat. Technol., 261 (2015), 278-288.
[4] Kang Yang, Wenya Li, Xiawei Yang, Yaxin Xu, Achilles Vairis, Effect of heat treatment on the inherent anisotropy of cold sprayed copper deposits, Surf. Coat. Technol., 350 (2018), 519-530.
[5] Krystian Zyguła, Bartłomiej Nosek, Hubert Pasiowiec, Norbert Szysiak, Mechanical properties and microstructure of AlSi10Mg alloy obtained by casting and SLM technique, World Scientific News, 104 (2018), 462-472.
[6] Yanfeng Han, Xiangfa Liu, Xiufang Bian, In situ TiB2 particulate reinforced near eutectic Al–Si alloy composites, Composites Part A, 33 (2002), 439-444.
[7] Z Chen, J Li, Andras Borbely, G Ji, SY Zhong, Y Wu, ML Wang, HW Wang, The effects of nanosized particles on microstructural evolution of an in-situ TiB2/6063Al composite produced by friction stir processing, Mater. Des., 88 (2015), 999-1007.
[8] Aaron Christopher Hall, DJ Cook, RA Neiser, TJ Roemer, DA Hirschfeld, The effect of a simple annealing heat treatment on the mechanical properties of cold-sprayed aluminum, J. Therm. Spray Technol., 15 (2006), 233-238.
[9] Shuo Yin, Jan Cizek, Xingchen Yan, Rocco Lupoi, Annealing strategies for enhancing mechanical properties of additively manufactured 316L stainless steel deposited by cold spray, Surf. Coat. Technol., 370 (2019), 353-361.
[10] Shuo Yin, Pasquale Cavaliere, Barry Aldwell, Richard Jenkins, Hanlin Liao, Wenya Li, Rocco Lupoi, Cold spray additive manufacturing and repair: Fundamentals and applications, Addit. Manuf., 21 (2018), 628-650.
[11] T Laha, Y Chen, D Lahiri, Arvind Agarwal, Tensile properties of carbon nanotube reinforced aluminum nanocomposite fabricated by plasma spray forming, Composites Part A, 40 (2009), 589-594.
[12] B Yu, J Tam, W Li, HJ Cho, J-G Legoux, D Poirier, JD Giallonardo, U Erb, Microstructural and bulk properties evolution of cold-sprayed copper coatings after low temperature annealing, Materialia, 7 (2019), 100356.
[13] Sathyapal Hegde, K Narayan Prabhu, Modification of eutectic silicon in Al–Si alloys, J. Mater. Sci., 43 (2008), 3009-3027.
[14] XP Li, XJ Wang, Martine Saunders, Alexandra Suvorova, LC Zhang, YJ Liu, MH Fang, ZH Huang, Timothy B Sercombe, A selective laser melting and solution heat treatment refined Al–12Si alloy with a controllable ultrafine eutectic microstructure and 25% tensile ductility, Acta Mater., 95 (2015), 74-82.
[15] Rajiv S Mishra, ZY Ma, Friction stir welding and processing, Mater. Sci. Eng., R, 50 (2005), 1-78.
[16] CG Rhodes, MW Mahoney, WH Bingel, RA Spurling, CC Bampton, Effects of friction stir welding on microstructure of 7075 aluminum, Scripta Mater., 36 (1997),
[17] HB Michael Rajan, I Dinaharan, S Ramabalan, ET Akinlabi, Influence of friction stir processing on microstructure and properties of AA7075/TiB2 in situ composite, J. Alloys Compd., 657 (2016), 250-260.
[18] Kang Yang, Wenya Li, Pengliang Niu, Xiawei Yang, Yaxin Xu, Cold sprayed AA2024/Al2O3 metal matrix composites improved by friction stir processing: Microstructure characterization, mechanical performance and strengthening mechanisms, J. Alloys Compd., 736 (2018), 115-123.

[19] Rajiv S Mishra, SX McFadden, NA Mara, AK Mukherjee, Murray W Mahoney, High strain rate superplasticity in a friction stir processed 7075 Al alloy, (1999),
[20] Kang Yang, Wenya Li, Chunjie Huang, Xiawei Yang, Yaxin Xu, Optimization of cold-sprayed AA2024/Al2O3 metal matrix composites via friction stir processing: Effect of rotation speeds, J. Mater. Sci. Technol., 34 (2018), 2167-2177.
[21] M Sharifitabar, A Sarani, S Khorshahian, M Shafiee Afarani, Fabrication of 5052Al/Al2O3 nanoceramic particle reinforced composite via friction stir processing route, Mater. Des., 32 (2011), 4164-4172.
[22] Devinder Yadav, Ranjit Bauri, Friction stir processing of Al-TiB 2 in situ composite: effect on particle distribution, microstructure and properties, Journal of Materials Engineering and Performance, 24 (2015), 1116-1124.
[23] D Wang, BL Xiao, QZ Wang, ZY Ma, Friction stir welding of SiCp/2009Al composite plate, Mater. Des., 47 (2013), 243-247.
[24] A Devaraju, A Kumar, A Kumaraswamy, B Kotiveerachari, Influence of reinforcements (SiC and Al2O3) and rotational speed on wear and mechanical properties of aluminum alloy 6061-T6 based surface hybrid composites produced via friction stir processing, Mater. Des., 51 (2013), 331-341.
[25] JF Guo, J Liu, CN Sun, S Maleksaeedi, G Bi, MJ Tan, J Wei, Effects of nano-Al2O3 particle addition on grain structure evolution and mechanical behaviour of friction-stir-processed Al, Mater. Sci. Eng., A, 602 (2014), 143-149.
[26] SM Ma, Peipei Zhang, Gang Ji, Z Chen, GA Sun, SY Zhong, Vincent Ji, HW Wang, Microstructure and mechanical properties of friction stir processed Al–Mg–Si alloys dispersion-strengthened by nanosized TiB2 particles, J. Alloys Compd., 616 (2014), 128-136.
[27] Narayana Yuvaraj, Sivanandam Aravindan, Fabrication of Al5083/B4C surface composite by friction stir processing and its tribological characterization, Journal of materials research and technology, 4 (2015), 398-410.
[28] S Sahraeinejad, H Izadi, M Haghshenas, AP Gerlich, Fabrication of metal matrix composites by friction stir processing with different particles and processing parameters, Mater. Sci. Eng., A, 626 (2015), 505-513.
[29] Mohammad Narimani, Behnam Lotfi, Zohreh Sadeghian, Investigating the microstructure and mechanical properties of Al-TiB2 composite fabricated by Friction Stir Processing (FSP), Mater. Sci. Eng., A, 673 (2016), 436-442.
[30] V Kishan, Aruri Devaraju, K Prasanna Lakshmi, Influence of volume percentage of NanoTiB2 particles on tribological & mechanical behaviour of 6061-T6 Al alloy nano-surface composite layer prepared via friction stir process, Defence Technology, 13 (2017), 16-21.
[31] Guoqiang Huang, Wentao Hou, Yifu Shen, Evaluation of the microstructure and mechanical properties of WC particle reinforced aluminum matrix composites fabricated by friction stir processing, Mater. Charact., 138 (2018), 26-37.
[32] Ali Hosseinzadeh, Guney Guven Yapici, High temperature characteristics of Al2024/SiC metal matrix composite fabricated by friction stir processing, Mater. Sci. Eng., A, 731 (2018), 487-494.
[33] Omar S Salih, Hengan Ou, Xingguo Wei, W Sun, Microstructure and mechanical properties of friction stir welded AA6092/SiC metal matrix composite, Mater. Sci. Eng., A, 742 (2019), 78-88.
[34] Atul Kumar, Kaushik Pal, Suhrit Mula, Simultaneous improvement of mechanical strength, ductility and corrosion resistance of stir cast Al7075-2% SiC micro-and nanocomposites by friction stir processing, Journal of Manufacturing Processes, 30 (2017), 1-13.
[35] Xiao Peng Li, Gang Ji, Z Chen, Ahmed Addad, Y Wu, HW Wang, Jef Vleugels, Jan Van Humbeeck, Jean-Pierre Kruth, Selective laser melting of nano-TiB2 decorated AlSi10Mg alloy with high fracture strength and ductility, Acta Mater., 129 (2017), 183-193.

[36] XC Tong, AK Ghosh, Fabrication of in situ TiC reinforced aluminum matrix composites, J. Mater. Sci., 36 (2001), 4059-4069.
[37] Dongshuai Zhou, Feng Qiu, Qichuan Jiang, The nano-sized TiC particle reinforced Al–Cu matrix composite with superior tensile ductility, Mater. Sci. Eng., A, 622 (2015), 189-193.
[38] Gaohui Wu, Xi Wang, Longtao Jiang, Boran Ma, A nanostructural design to produce high ductility of high volume fraction SiCp/Al composites with enhanced strength, Mater. Des., 61 (2014), 141-145.
[39] Dongshuai Zhou, Feng Qiu, Qichuan Jiang, Simultaneously increasing the strength and ductility of nano-sized TiN particle reinforced Al–Cu matrix composites, Mater. Sci. Eng., A, 596 (2014), 98-102.

Chapter V Cold spraying of TiB_2/AlZnMgCu composites

5.1 Introduction

In this chapter, a gas-atomized AlZnMgCu (7075Al) composite powder reinforced with in-situ nanosized TiB_2 particles was used as the feedstock to fabricate composite coating or parts by cold spraying (CS). First, the plastic deformation of the pure 7075Al and TiB_2/7075Al composite particles were studied by a combination of single-particle deposition experiments and Finite Element Analysis (FEA) simulation using ABAQUS. Single-particle compression tests were conducted to obtain the Johnson-Cook (JC) parameters of the feedstocks. The effect of the CS processing conditions (i.e. particle velocity and temperature, and gas type) on the microstructure evolution of the as-sprayed samples was investigated in terms of X-ray diffraction (XRD), scanning electron microscopy (SEM), transmission electron microscopy (TEM), and electron backscatter diffraction (EBSD). Mechanical performance of the CSed composite, including adhesion strength, microhardness, wear performance, and tensile properties, was evaluated. Moreover, the corrosion behavior of the CSed and annealed deposits in the NaCl solution was investigated in terms of immersion, potentiodynamic polarization, and impedance spectroscopy tests. The corrosion mechanisms were analyzed based on the results of electrochemical tests and microstructure observation. Furthermore, different post heat treatments were applied to further improve the mechanical performance of the as-sprayed deposits. The microstructure evolution especially the precipitation behavior and the related mechanical performance after heat treatment, was investigated in detail. Last, the strengthening mechanisms relating to microstructural evidence were discussed.

5.2 Particle impact velocity and temperature simulation

CS deposition was performed on 7075Al-T6 plate substrates under three different processing conditions. The main processing parameters used for CS deposition are listed in Table 5-1.

Table 5-1 The main CS processing parameters for the pure 7075Al and TiB_2/7075Al composite powder feedstocks. (This table is also given in Chapter 2).

Conditions	Nozzle	Propelling gas	Carrier gas	Gas pressure (MPa)	Gas temperature (°C)	CS system
C1	SiC-1	Air	Ar	3.0	550	CGT-3000
C2	SiC-2	N_2	N_2	5.0	500	Impact 5/8
C3	PBI-3	He	He	1.8	320	LERMPS

Particle impact velocity and temperature are the most important factors in determining the bonding behaviour and the quality of the deposits. In this work, the relevant numerical simulation work was carried out using Fluent/Ansys for a better understanding. Figure 5-1a and b display the contours of particle velocity and particle temperature along the nozzle's central line under different processing conditions. Here, an average particle size of 33 μm and 37 μm corresponding to pure 7075Al particle and TiB_2/7075Al composite particle respectively were used for this simulation. It is obvious that the processing conditions significantly affect the particle velocity and temperature. As can be seen from Figure 5-1c, the particle velocity of the pure 7075Al increases from 632 m/s to 695 m/s, while the particle temperature decreases from 353 ºC to 290 ºC as the processing condition changes from C1 to

C2. In the case of C3, a sharp increment in particle velocity (850 m/s) was achieved using He gas. Previous studies have proved that higher gas pressure, higher gas temperature, or lower gas molecular weight causes better gas flow acceleration through a de-Laval nozzle [1]. Thus, a higher particle impact velocity was obtained using He gas. Besides, it can be noted that the composite particle possesses a slightly lower particle velocity, but a similar particle temperature compared to the case using the pure 7075Al particle due to its slightly larger particle size and slightly higher density.

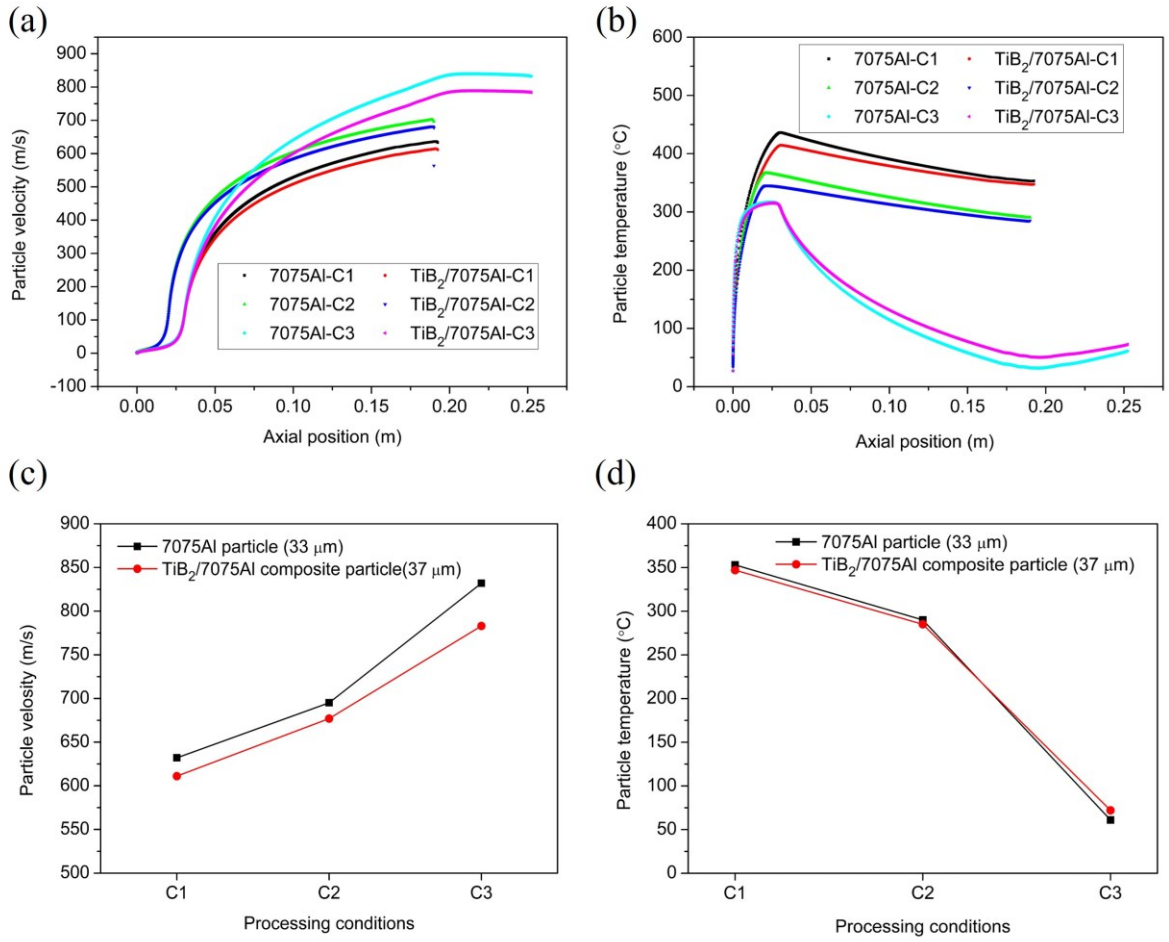

Figure 5-1 (a) Particle velocity and (b) particle temperature along the nozzle central line; (c) and (d) show particle impact velocity and particle impact temperature as a function of processing conditions, respectively. An average particle size of 33 μm and 37 μm corresponding to pure 7075Al and TiB_2/7075Al composite particle respectively were used for this simulation.

5.3 Single particle deposition

5.3.1 Single particle compression test

Single particle compression tests were carried out to obtain the mechanical properties of the pure 7075Al and TiB_2/7075Al composite particles, which are critically important for better understanding the plastic deformation behavior of the particles during CS deposition. In this work, 10 'good' particles for both pure 7075Al and TiB_2/7075Al composite powders, which are spherical and have similar sizes (from 40–55 μm), were selected for this compression tests. Figure 5-2 shows the raw force-displacement data of the pure 7075Al particles and TiB_2/7075Al composite particles obtained from the particle compression tests. As shown from the force-displacement variations, these tested particles exhibit similar deformation behaviors since the particles similar in size were selected for this compression test.

It can be noted that the smaller particle (e.g. the #1 pure 7075Al particle) yields at an earlier stage compared to the larger ones. The deformation behavior of the TiB_2/7075Al composite particle exhibits a higher consistency compared to that of the pure 7075Al particle. The concept of nominal stress vs nominal strain, as formulated in Eq. (2-4), was applied to fully filter out the effect of particle size on particle deformation behavior. Figure 5-3 a and b display the variations of nominal stress-strain of the pure 7075Al particle and TiB_2/7075Al composite particle, respectively. Clearly, the composite particle possesses a higher strength compared to the pure 7075Al particle. Furthermore, the deformation behavior of both the 7075Al and TiB_2/7075Al composite particles in the elastic deformation stage is basically the same, but the deformation behavior of particles in the subsequent plastic deformation stage exhibits a greater dispersion, especially for the pure 7075Al particles. This may be due to the fact that pure 7075Al particles are characterized by uneven grain size and morphology, as shown in Figure 2-11.

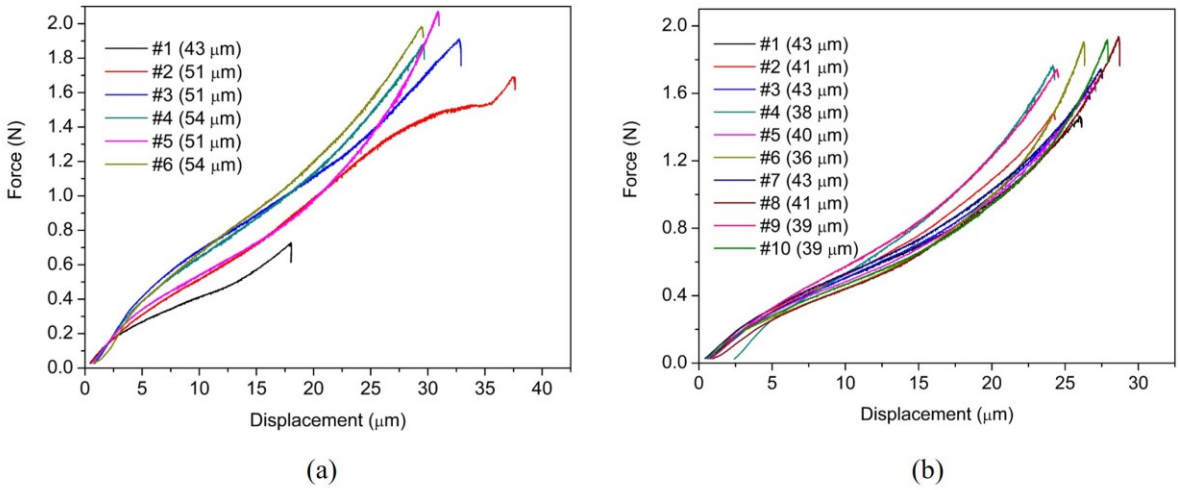

Figure 5-2 Raw force-displacement data of pure 7075Al particles and TiB_2/7075Al composite particles obtained from single particle compress experiment.

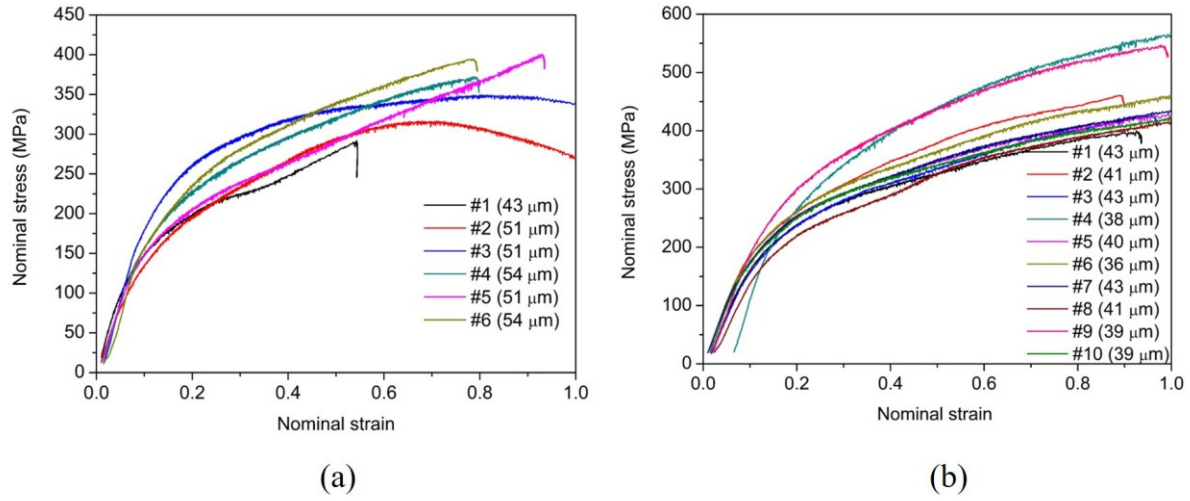

Figure 5-3 Nominal stress-strain converted from force-displacement data: (a) 7075Al particles; (b) TiB_2/7075Al composite particle.

Figure 5-5 presents the ultimate tensile strength (UTS) values of the pure 7075Al and TiB_2/7075Al composite particles obtained from the semi-empirical formula of Eq. (2-6). The TiB_2/7075Al composite particle has an average UTS value of 557.0 MPa, showing a 15.6% increment compared to that of pure

7075Al particle (481.8 MPa). In addition, the microhardness measurements on the cross-section of the initial powders revealed average value of 71 $HV_{0.015}$ and 84 $HV_{0.015}$ for the pure 7075Al and TiB_2/7075Al composite powders, respectively. Furthermore, nanoindentation tests were performed on the cross-section of the polished particles. Compared to the pure 7075Al particle, micromechanical properties of the composite particle show a remarkable increase of 26.1% for elastic modulus (E) and 10.9% for nanohardness. The enhanced UTS, E, microhardness and nanohardness values may result from the uniform distribution of TiB_2 nanoparticles and the refined grain size of the composite particle.

The typical nominal stress-strain curves obtained from force-displacement data are fitted into Eq. (2-5). Examples of the 7075Al particle and TiB_2/7075Al composite particle are displayed in Figure 5-4. The obtained fitting parameters, a, b and c, are subsequently used to work out the JC parameters, using the procedure explained in Section 2.7. The fitting of other particles was done in the same way, and the results for the pure 7075Al and TiB_2/7075Al composite particles are listed in Table 5-2 and Table 5-3, respectively. The average JC parameters obtained for pure 7075Al are as follows: A = 166.7 MPa, B = 439.2 MPa, and n = 0.14; while those obtained for the composite particle are as follows: A = 359.1 MPa, B = 384.1 MPa, and n = 0.31. These JC parameters will be used for FEA simulation of particle plastic deformation behavior in the next section.

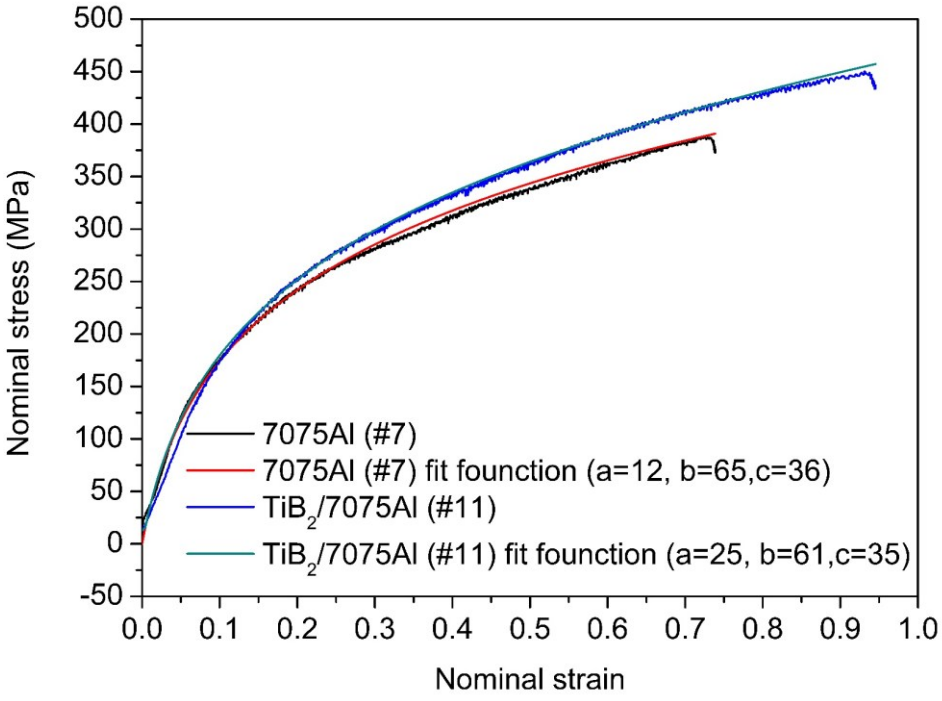

Figure 5-4 Variations of the nominal stress vs. strain for a 7075Al particle comparing with the fit function.

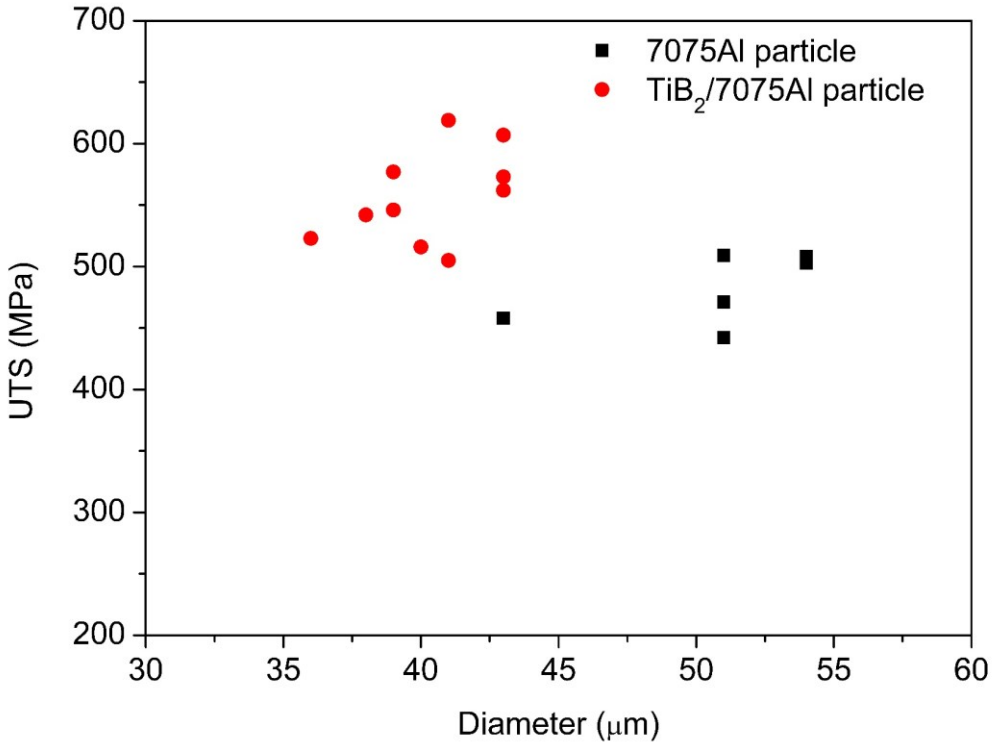

Figure 5-5 UTS values of the pure 7075Al and TiB_2/7075Al composite particle as a function of particle diameter.

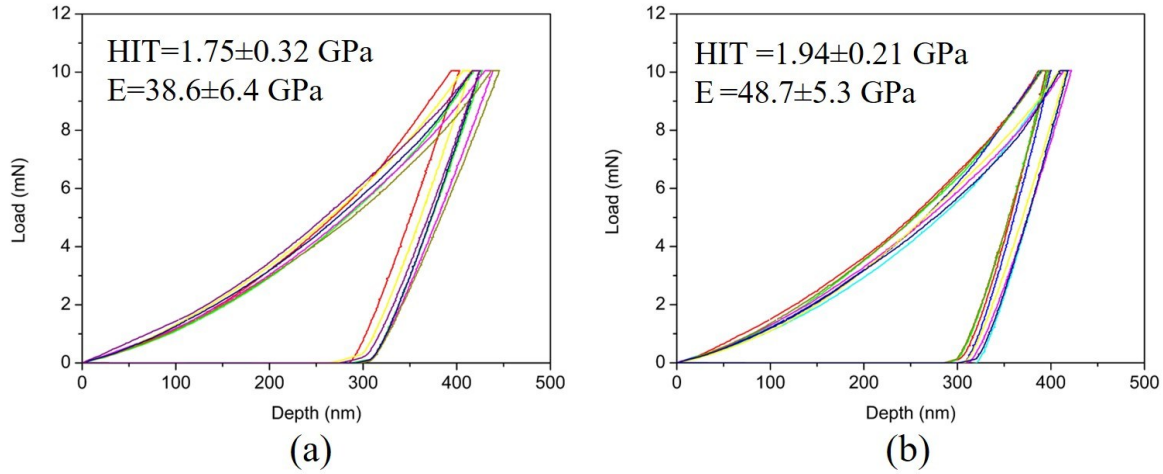

Figure 5-6 Nanoindentation performance of the (a) pure 7075Al particle and (b) TiB_2/7075Al composite particle.

Table 5-2 Summary of the UTS values and A, B, n parameters of the pure 7075Al particle obtained from single particle compression tests.

	Diameter (μm)	UTS (MPa)	E (GPa)	A (MPa)	B (MPa)	n
Average		481.8±26.3	1.62±0.22	166.7±20.6	439.2±26.5	0.14±0.04
#1	43	458	1.452	150	400	0.095
#2	51	442	1.353	140	440	0.180
#3	51	509	1.993	180	430	0.095
#4	54	508	1.658	190	475	0.185
#5	51	471	1.493	150	420	0.100
#6	54	503	1.793	190	470	0.190

Table 5-3 Summary of the UTS values and A, B, n parameters of the TiB_2/7075Al composite particle obtained from single particle compression tests.

	Diameter (μm)	UTS (MPa)	E (MPa)	A (MPa)	B (MPa)	n
Average		557.0±35.9	1.82±0.19	359.1±76.7	384.1±88.6	0.31±0.09
#1	43	607	1.715	380	375	0.190
#2	41	619	1.905	385	475	0.350
#3	43	562	1.660	450	308	0.400
#4	38	542	2.149	364	439	0.497
#5	40	516	1.776	293	369	0.207
#6	36	523	1.825	439	215	0.312
#7	43	573	1.703	250	500	0.200
#8	41	505	1.529	275	430	0.330
#9	39	546	2.151	280	455	0.260
#10	39	577	1.755	475	275	0.360

5.3.3 Particle deformation behavior

The FEA simulation of particle plastic deformation behavior was performed based on the JC parameters obtained from single particle compression tests. The simulated particle impact velocities and temperatures in different processing conditions, as listed in Table 5-4, were used for the FEA simulation. Other mechanical and thermal properties of the particles and substrates are given in Table 2-6. The aim of this study is to evaluate the influence of processing conditions, substrate material, and the addition of TiB_2 nanoparticles on the plastic deformation behavior of the composite particle. Relative soft Al (45 $HV_{0.3}$) and hard 7075Al-T6 (158 $HV_{0.3}$) plates were used as the substrate materials. A particle size of 35 μm was used for both the pure 7075Al and TiB_2/7075Al composite particles.

Table 5-4 The simulated particle impact velocities and temperatures under different conditions were used for the FEA simulation.

Conditions	Velocity (m/s)	Temperature (℃)
C1	632	353
C2	695	290
C3	832	61

The contours of equivalent plastic strain (PEEQ) and temperature of the individual 7075Al and TiB_2/7075Al composite particles deposited onto soft pure Al substrates under different processing conditions are displayed from Figure 5-7 to Figure 5-9. Obviously, the particles and the pure Al substrates experienced different deformation features under different conditions. In the case of C1, when the particles impact onto the soft Al substrate with a high impact temperature but a relatively low velocity, both the particle and substrate experienced extensive plastic deformation (see Figure 5-7). It is also noted that localized plastic deformation occurs at the periphery of the contact interface, where the temperature is much higher than that of the inner part of the particle due to plastic dissipation-induced adiabatic temperature rise. As a result, prominent metal jets are formed at the rims of both the deformed splat and substrate. The composite particle seems to be less deformed and exhibits less prominent metal jets compared to the pure 7075Al particle due to its higher strength. Compared to C1, both the pure 7075Al and TiB_2/7075Al composite particles in C2 experience less plastic deformation, and thus resulting a lower localized plastic strain and temperature (see Figure 5-8). Consequently, less prominent metal jets are formed compared to the case of C1. The composite particle is slightly less deformed than the pure 7075Al particle, demonstrating a similar behavior as the case of C1.

When the particle impact velocity is increased to 832 m/s (C3), both the pure 7075Al and TiB_2/7075Al composite particles were embedded into the soft Al substrates (see Figure 5-9). In this case, most of the initial kinetic energy is dissipated by the soft Al substrate. Therefore, the substrate experiences intensive deformation with evident metal jets forming at the rim of the crater. Comparatively, the relatively hard 7075Al and TiB_2/7075Al composite particles experience less plastic deformation. Similar to the case of C1, slightly greater plastic deformation and more prominent metal jets occurred to the pure 7075Al particle than those of the TiB_2/7075Al composite particle. The maximum temperature in these highly deformed zones of the particle is lower than that in the cases of C1 and C2 due to the reduced thermal softening effect of the initial powder. Therefore, it is believed that the enhanced thermal softening effect caused by the increasing initial temperature is also helpful for the metallic interface bonding between the particle and substrate.

The contours of PEEQ and temperature of the individual 7075Al and TiB_2/7075Al composite particles after impacting on hard 7075Al-T6 substrates under different conditions are presented from Figure 5-10 to Figure 5-12. In these cases, the relatively soft 7075Al particle or TiB_2/7075Al composite particle absorbs most of the kinetic energy and results in a more intensive deformation, while the hard 7075Al-T6 substrate deforms slightly. Compared to the cases of the pure Al substrate, the particles experience much greater plastic deformation with prominent metal jets formed at the periphery of the deformed particle. A higher impact temperature results in a higher localized temperature, while a higher impact velocity can lead to a greater localized plastic strain. In these cases, the deformation behavior of the TiB_2/7075Al composite particle is similar to that of the pure 7075Al particle.

From the above simulation results, we can conclude that the particle impact velocity and temperature, as well as the mechanical properties of the particles and substrates are important in

determining the particle plastic deformation behavior. More detailed investigation on these aspects will be carried out using the individual particle deposition experiments in the following section.

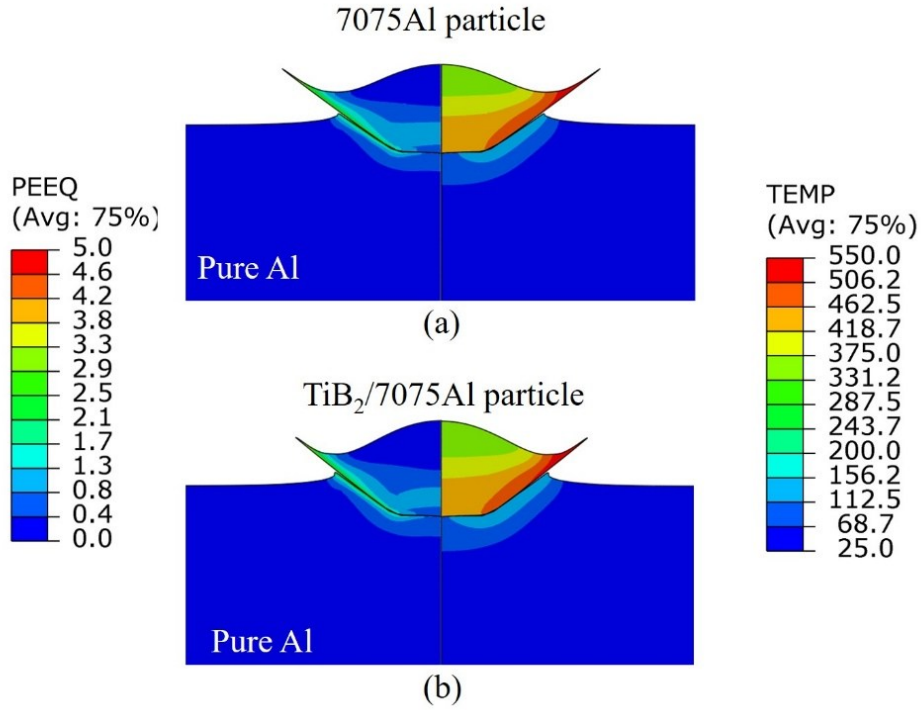

Figure 5-7 Distribution of effective plastic strain (PEEQ) (on the left-hand side) and temperature (on the right-hand side) of the single (a) 7075Al and (b) TiB_2/7075Al composite particles deposited onto pure Al substrate in C1.

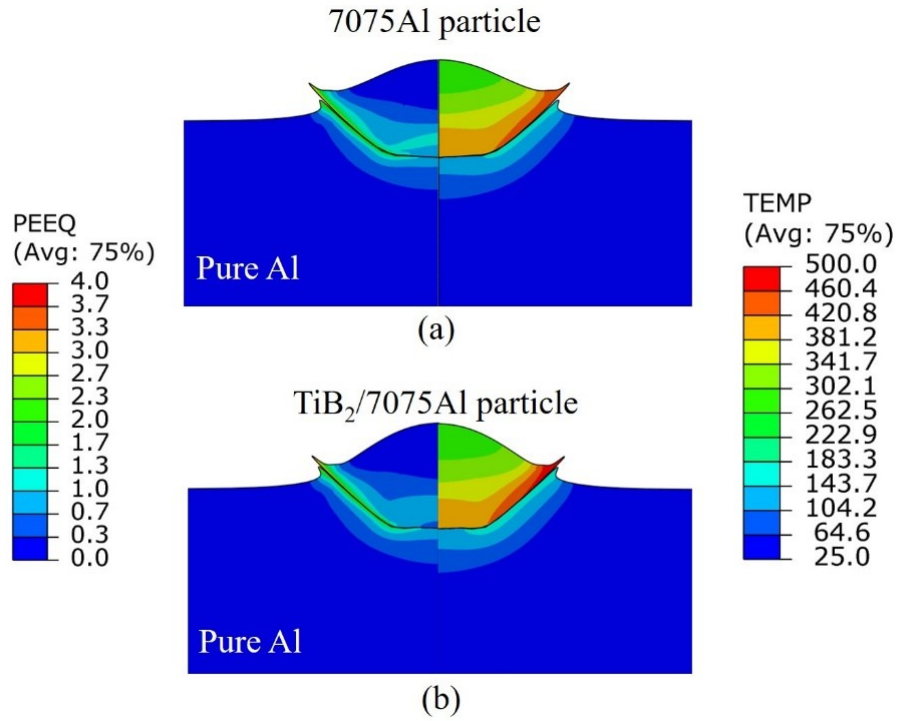

Figure 5-8 Distribution of PEEQ (on the left-hand side) and temperature (on the right-hand side) of the single (a) 7075Al and (b) TiB_2/7075Al composite particles deposited onto pure Al substrate in C2.

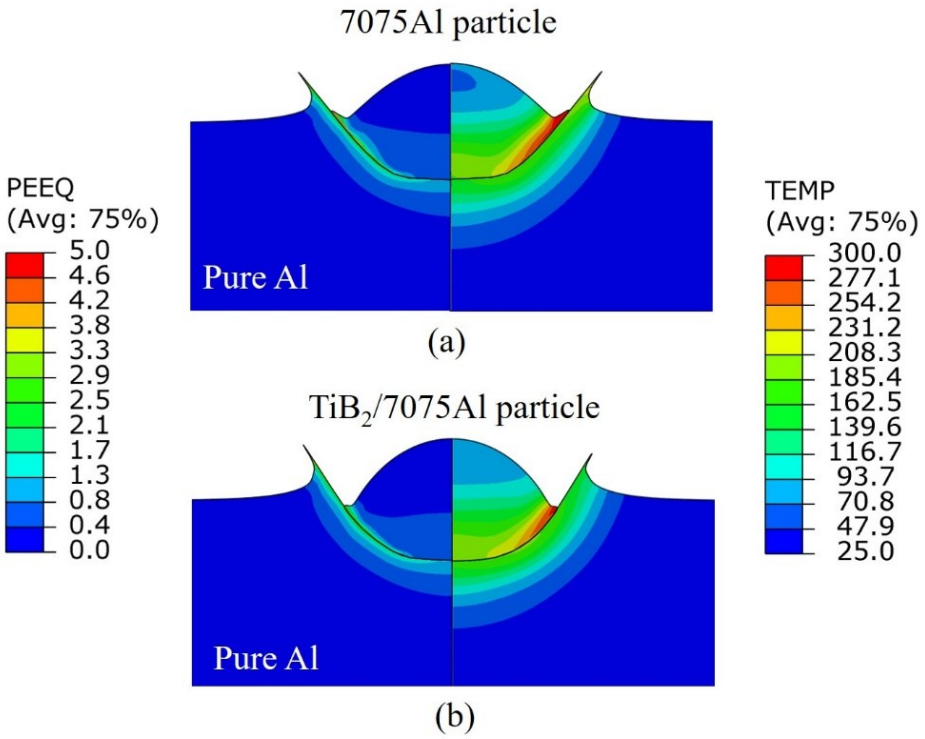

Figure 5-9 Distribution of PEEQ (on the left-hand side) and temperature (on the right-hand side) of the single (a) 7075Al and (b) TiB_2/7075Al composite particles deposited onto pure Al substrate in C3.

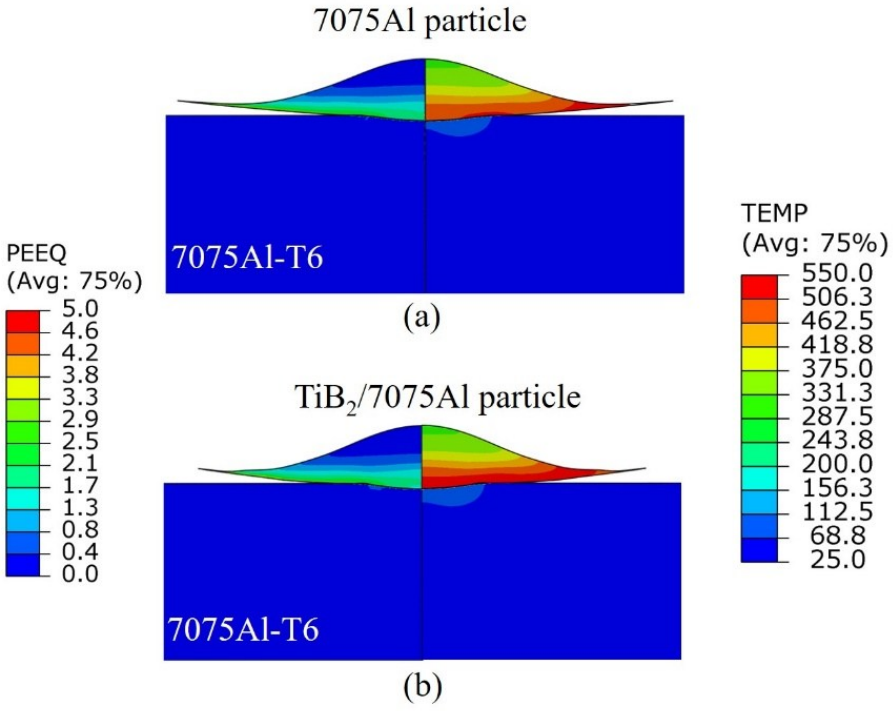

Figure 5-10 Distribution of PEEQ (on the left-hand side) and temperature (on the right-hand side) of the single (a) 7075Al and (b) TiB_2/7075Al composite particles deposited onto 7075Al-T6 substrate in C1.

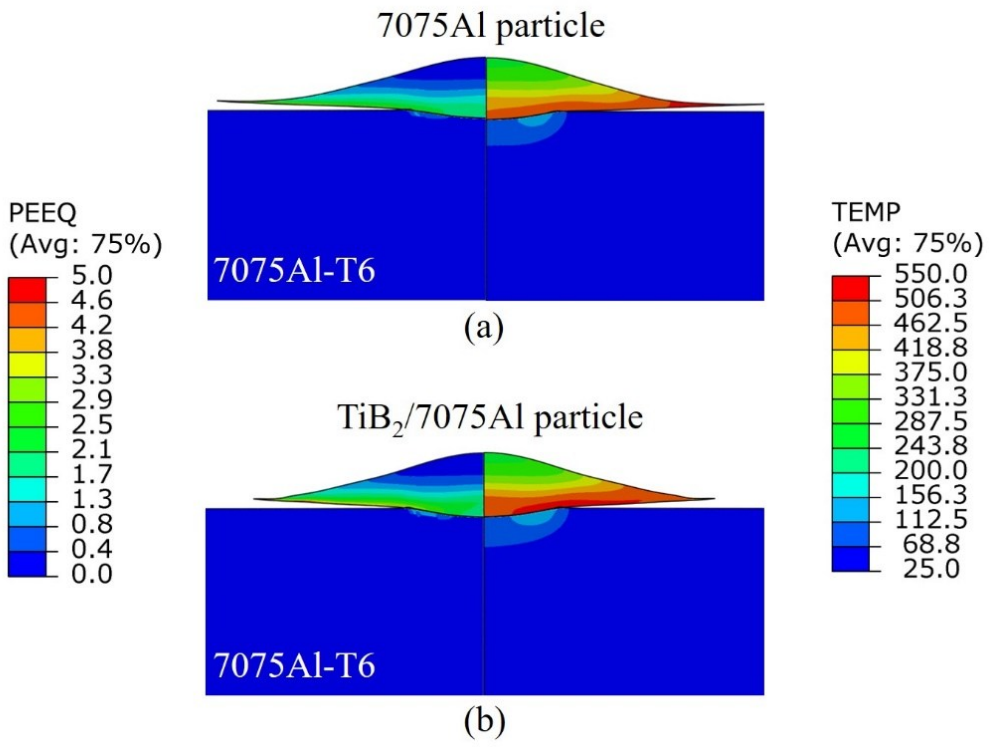

Figure 5-11 Distribution of PEEQ (on the left-hand side) and temperature (on the right-hand side) of the single (a) 7075Al and (b) TiB_2/7075Al composite particles deposited onto 7075Al-T6 substrate in C2.

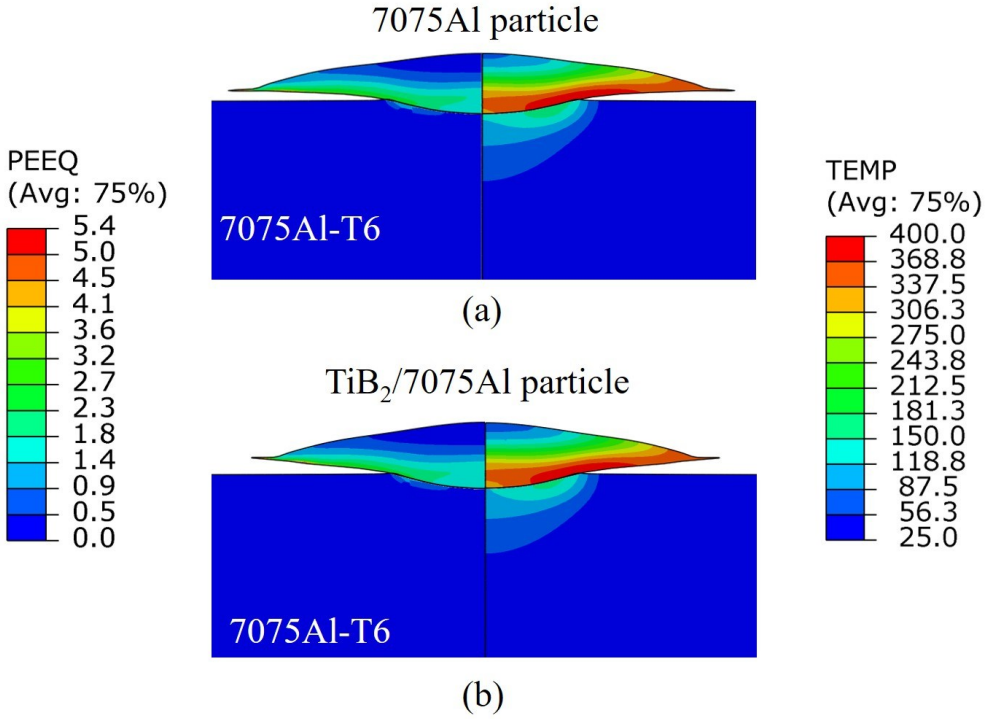

Figure 5-12 Distribution of PEEQ (on the left-hand side) and temperature (on the right-hand side) of the single (a) 7075Al and (b) TiB_2/7075Al composite particles deposited onto 7075Al-T6 substrate in C3.

5.3.3 Single particle deposition experiments

The deposition experiments on individual splats were performed to understand the deposition behavior of pure 7075Al and TiB_2/7075Al composite particles by comparing with the FEA simulation results. Figure 5-13a and d show the surface morphologies of the Al substrate after the impact of several individual pure 7075Al and TiB_2/7075Al composite particles under C1. As for the pure 7075Al particle deposition, some particles were successfully attached to the substrate following the impact, while craters were formed due to the particle rebounding and unsuccessful bonding with the substrate. Comparatively, fewer craters are observed in the case of TiB_2/7075Al composite particle. This fact indicates the increased deposition (DE) for the composite particle in C1.

Figure 5-13b and c display the surface and cross-sectional morphologies of a single splat of the pure 7075Al particle. Clearly, the 7075Al particle experienced severe plastic deformation accompanying the formation of metal jets at the rim of the deformed particle. The TiB_2/7075Al composite particle seems to experience less plastic deformation and resulting less evident metal jets compared to the pure 7075Al particle, which consistent with our simulation results (Figure 5-7). In addition, as shown in the etched cross-sectional morphologies in Figure 5-13c and f, the grains inside both the pure 7075Al particle and TiB_2/7075Al composite particle undergo different degrees of deformation, with high-level deformation at the particle-substrate contact regions but relatively low-level deformation at the center and top of the particles. The grains of the TiB_2 reinforced composite particle are less deformed compared to those of pure 7075Al particle. The grains at the top of the composite particle retain an equiaxed morphology, which is similar to that of the initial composite powder.

Figure 5-14 shows the surface and cross-sectional morphologies of single 7075Al and TiB_2/7075Al composite splats deposited onto the Al substrate in C3. In this case, almost no craters resulting from rebounding particles are seen on the surface of the substrates, demonstrating an enhanced DE in C3. These particles are embedded deeper into the pure Al matrix, forming an obvious metal jet at the rim of the particle. A much higher impact velocity can result in a greater plastic deformation of the deposited particles as well as the substrate, producing enhanced metallic bonding between the deformed particle and the substrate. The etched cross-sectional morphologies confirm that the grains inside both the deformed 7075Al and TiB_2/7075Al composite splats are highly deformed, especially in the case of the pure 7075Al deposit.

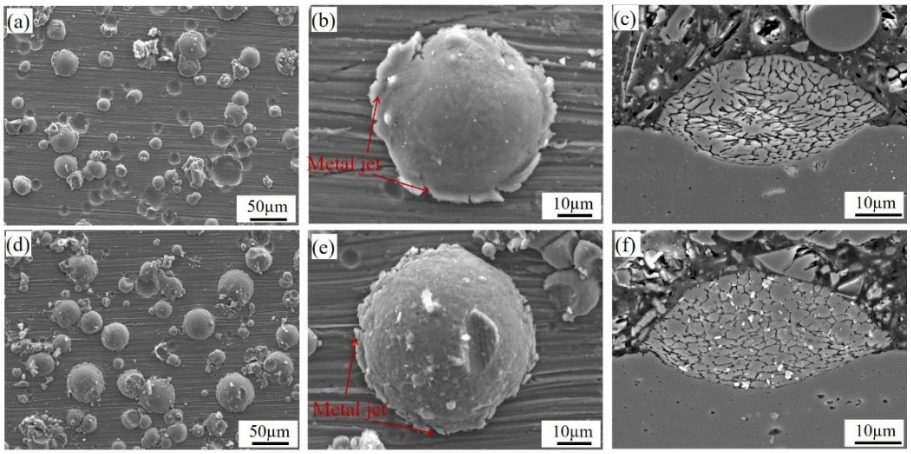

Figure 5-13 Surface and cross-sectional morphologies of single 7075Al and TiB_2/7075Al composite splats deposited onto Al substrate at C1: (a-c) 7075Al; (d-f) TiB_2/7075Al composite.

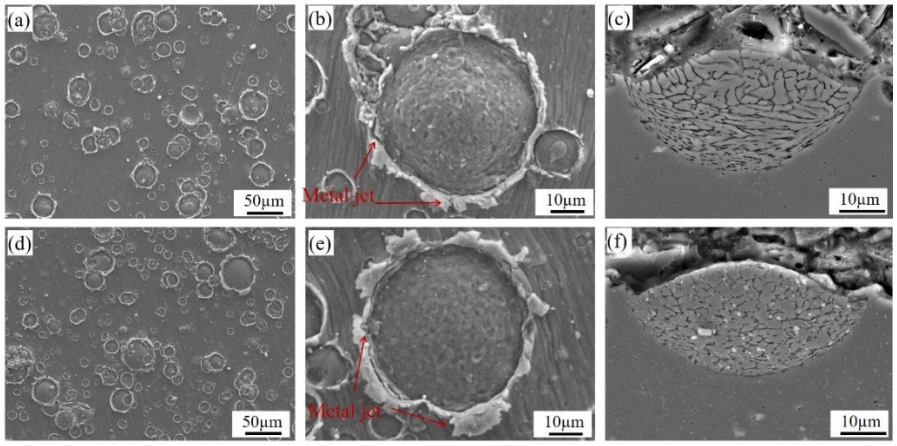

Figure 5-14 Surface and cross-section morphologies of single 7075Al and TiB_2/7075Al composite splats deposited onto Al substrate in C3: (a-c) 7075Al; (d-f) TiB_2/7075Al composite.

Moreover, the pure 7075Al and TiB_2/7075Al composite particles were deposited into different substrates (pure Al and 7075Al-T6) in C1 to investigate the influence of substrate properties on the deformation behavior of the particles. As shown in Figure 5-15, the particles deposited onto 7075Al-T6 substrate deform more greatly than those deposited onto the pure Al substrate when the same processing parameters are used (Figure 5-13). In this case, metal jets are clearly observed at the rim of the flattened splats after impacting on the surface of the relatively hard 7075Al-T6 substrate. However, the substrate itself experienced less plastic deformation as its hardness is higher. The deformed particle morphology consistent will the simulation results in Figure 5-10. The grains inside the particles are extensively deformed, particularly in the highly deformed interfacial regions. Compared to the pure 7075Al particle, the TiB_2 reinforced composite particle has a lower DE as more craters are left on the substrate surface. This is likely due to the fact that the composite particle has higher microhardness and strength compared to the unreinforced 7075Al particle.

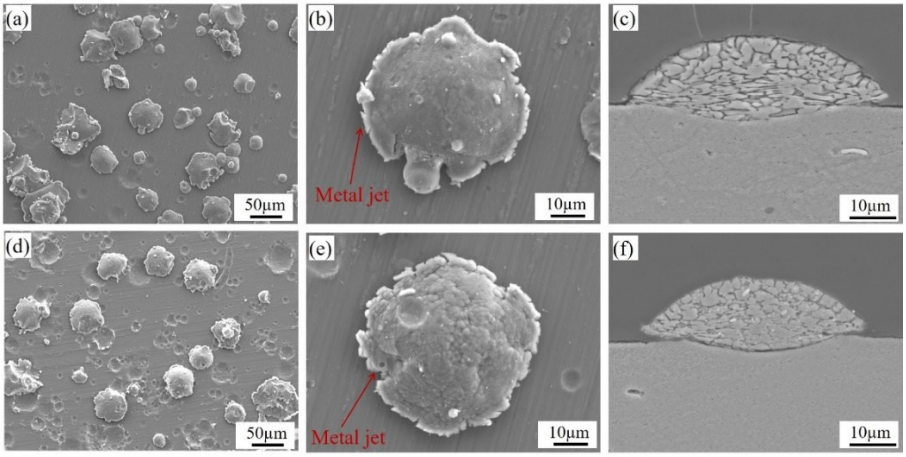

Figure 5-15 Surface and cross-section morphologies of single 7075Al and TiB_2/7075Al composite splats deposited onto Al substrate in C1: (a-c) 7075Al; (d-f) TiB_2/7075Al composite.

The semi-semi-empirical equations developed by Assadi et al. [2] was used to estimate the critical velocity of the pure 7075Al and TiB_2/7075Al composite particles, which is expressed below:

$$v_{crit} = \sqrt{\frac{F_1 \cdot 4 \cdot \sigma_{TS} \cdot (1 - \frac{T_i - T_R}{T_m - T_R})}{\rho} + F_2 \cdot c_p \cdot (T_m - T_i)} \qquad (5\text{-}1)$$

where ρ is the density of the material, c_p is the specific heat of the material, T_m, T_i, T_R are related to the melting point, particle impact temperature, and reference temperature (25℃), respectively. The calibration factors (F_1= 1.2 and F_2=0.3) are represent the mechanical and thermal parts of the material. σ_{TS} is the tensile strength of the particle; Here, average values of 482 MPa and 557 MPa are used for the pure 7075Al particle and TiB_2/7075Al composite particle. In C1, the v_{crit} values for pure 7075Al particle and TiB_2/7075Al composite particle with a size of 25 μm are estimated to be 654 m/s and 687 m/s, respectively. The increased v_{crit} for the composite particle decrease the DE.

The consistency of the experimental and FEA simulation results indicates the validity of these JC parameters of the particles obtained using single particle compression tests, although strain rate in the compression tests are much lower as compared to that in CS. In fact, the effectiveness of this method for the applications of CS deposition has been verified on the testing of pure Cu and CoNiCrAlY powders by H. Assadi et al. [3]. The UTS of particles as determined under quasi-static conditions could also be used to predict the particle deformation behavior or even the critical velocity for bonding during CS deposition, which is beneficial for better understanding the coating formation and even the final mechanical properties of the coatings.

5.4 Phase composition and microstructure evolution

Thick pure 7075Al and TiB_2/7075Al composite coatings were deposited on 7075Al-T6 plate substrates using three different processing conditions (C1, C2, and C3). The phase composition and microstructure evolution were characterized using XRD, SEM, EBSD and TEM.

5.4.1 Phase composition

The XRD patterns of the starting powders and CSed components processed under different conditions are presented in Figure 5-16. Apart from the α-Al and TiB_2 phases, there is no significant difference in the XRD patterns between the powders and the corresponding deposited components, suggesting that no (or limited) formation of new phases occurred during the CS processes. It seems that the increased gas propelling temperature did not affect the phase composition of the components, even at the highest gas temperature of 550 °C used in C1.

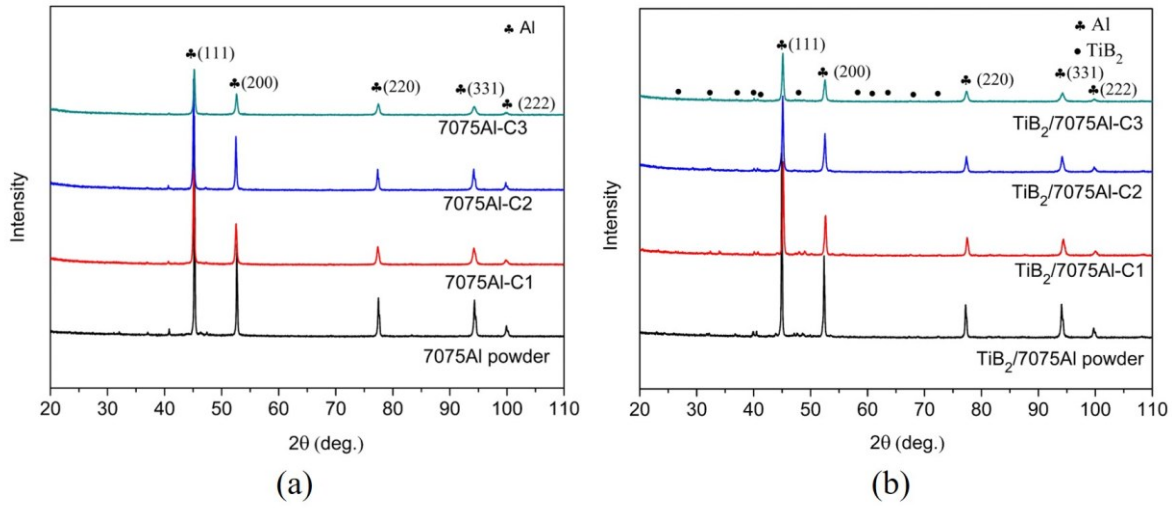

Figure 5-16 XRD patterns of the initial feedstocks and as-sprayed components: (a) 7075Al and (b) TiB_2/7075Al composite.

5.4.2 Microstructure evolution

Figure 5-17 displays the surface morphologies of the 7075Al and TiB_2/7075Al composite components deposited under C1 and C3. Different deposition features of the overview morphology are observed for different processing conditions. Regarding the C1 deposits, a large number of craters were left on the surfaces of the 7075Al and TiB_2/7075 Al composite samples after impact due to particle rebounding and unsuccessfully bonding with the previously deposited layers. As can be seen from the magnified views (Figure 5-17e and f), metal jets were not obviously observed at the rim of the deformed splats in either deposits. As seen in the C3 deposits presented in Figure 5-17c and d, only a few craters were left on both coating surfaces, indicating an enhanced DE. Furthermore, the magnified views in Figure 5-17g and h clearly reveal that both the 7075Al and TiB_2/7075Al composite particles experienced great plastic deformation and exhibited prominent metal jets at the rim of these largely deformed splats. The enhanced particle deformation, DE and metal jet of the deposited particles should be attributed to the increased particle impact velocity by using He as the propellant gas.

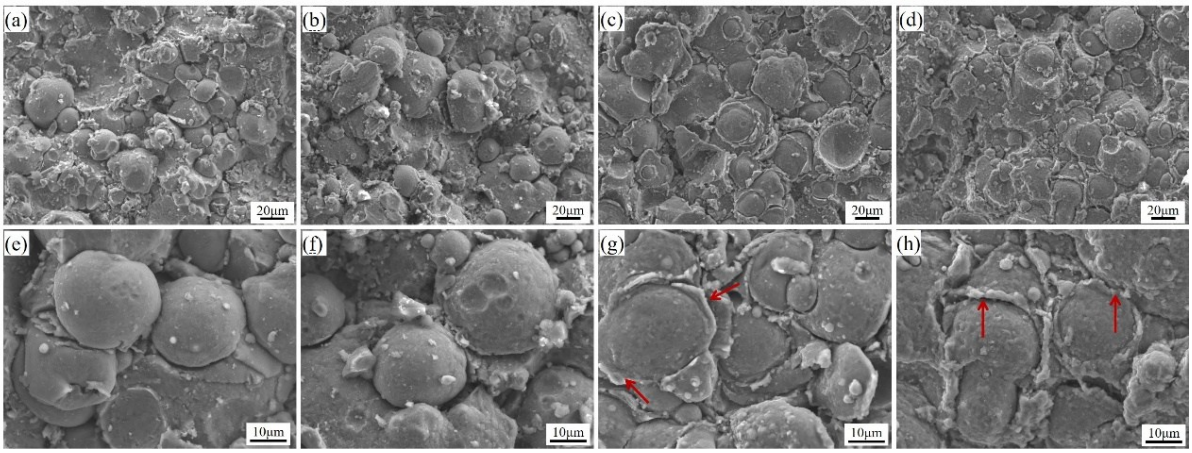

Figure 5-17 Surface morphologies of the 7075Al and TiB_2/7075Al composite particles deposited at C1 and C3: (a) and (e) 7075Al-C1; (b) and (f) TiB_2/7075Al-C1; (c) and (g) 7075Al-C3; (d) and (h) TiB_2/7075Al-C3.

Figure 5-18 shows the cross-sectional morphologies of the 7075Al and TiB_2/7075Al composite deposits in different processing conditions. Both deposits present a fully dense structure except for some small pores located at interparticle regions for both C1 deposits. The composite deposit seems to be denser than the pure 7075Al component. The back scattered electron (BSE/SEM) images in Figure 5-19 confirm this observation. The porosity evolution for both deposits from C1 to C3 is given in Figure 5-20. As the processing condition changes from C1 to C3, the porosities of the 7075Al and TiB_2/7075Al composite decrease from 0.68% and 0.49% to about 0.15% and 0.12%, respectively. Another obvious feature is that the particles undergo varying degrees of deformation under different conditions. In order to better evaluate particle deformation behaviours, flattening ratio measurements were performed, and the results are presented in Figure 5-21. The flattening ratio of the particle was obtained by measuring the longest length of the particle over the shortest length of the particle. Since both the initial powders display near-spherical shapes, their flattening ratios were calculated to be about 1.15, which is close to 1.0. In the case of C1, the average flattening ratios of the pure 7075Al and TiB_2/7075Al composite particles were measured to be 2.50 and 2.32, showing an increment of about 117.4% and 101.7% compared to the initial powders, respectively. As the particle velocity increases from C1 to C3, the flattening ratios of both deformed particles gradually increase, indicating a greater particle deformation at a higher particle velocity. In the case of C3, both deposits present a ‘curly’ structure with a large number of elongated and refined grains at the interparticle boundaries.

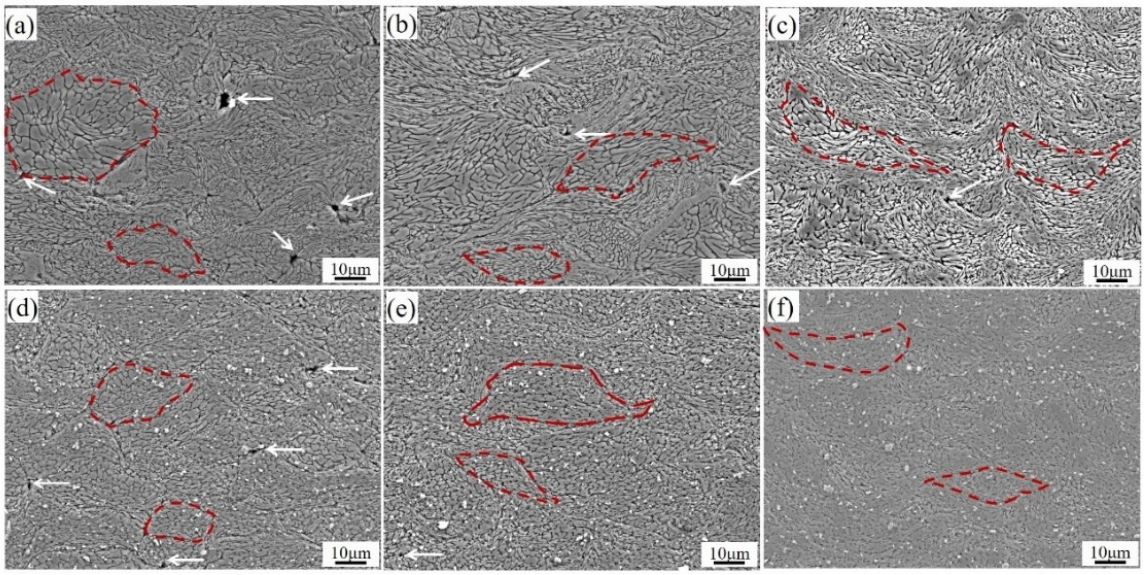

Figure 5-18 Cross-sectional SEM images of the CSed (a-c) 7075Al deposits and (b-d) TiB_2/7075Al composite deposits at different processing parameters: (a) 7075Al-C1, (b) 7075Al-C2, (c) 7075Al-C3, (d) TiB_2/7075Al-C1, (e) TiB_2/7075Al-C2, (f) TiB_2/7075Al-C3. The pores and the typical deformed particles were indicated by white arrows and red dashed outlines, respectively.

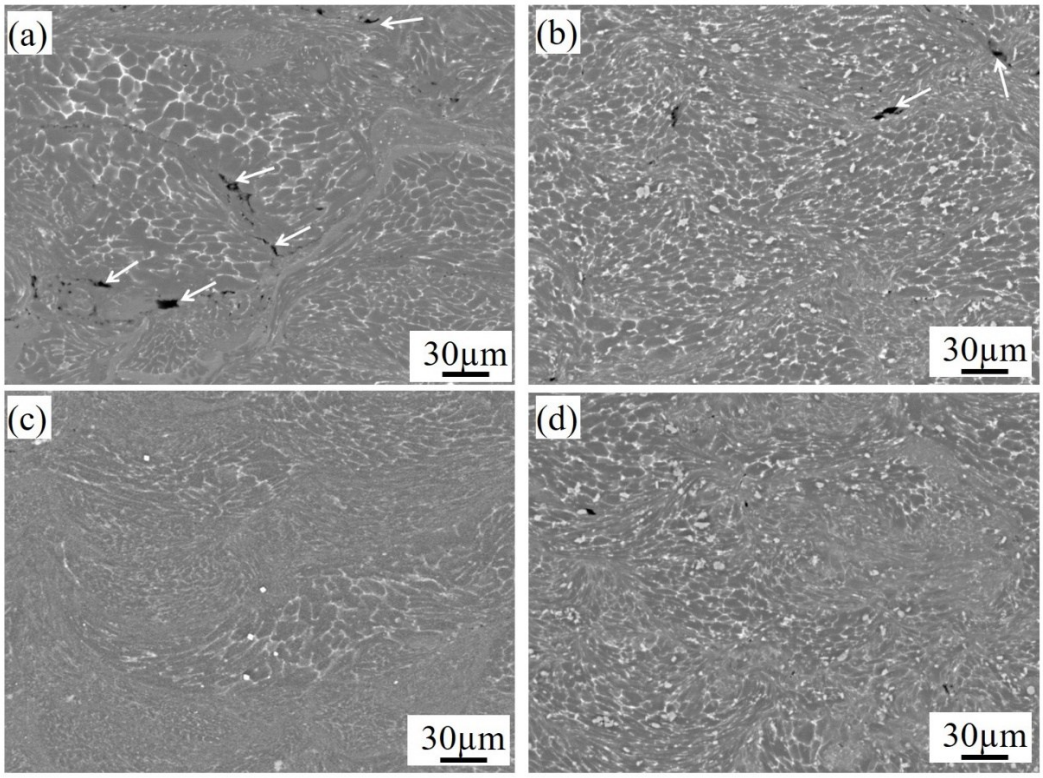

Figure 5-19 BSE/SEM micrographs of the microstructure of the (a, c) 7075Al and (b, d) TiB_2/7075Al composite coatings: (a) 7075Al-C1, (b) TiB_2/7075Al-C1, (c) 7075Al-C3, (d) TiB_2/7075Al-C3. The white arrows indicate pores in the coatings.

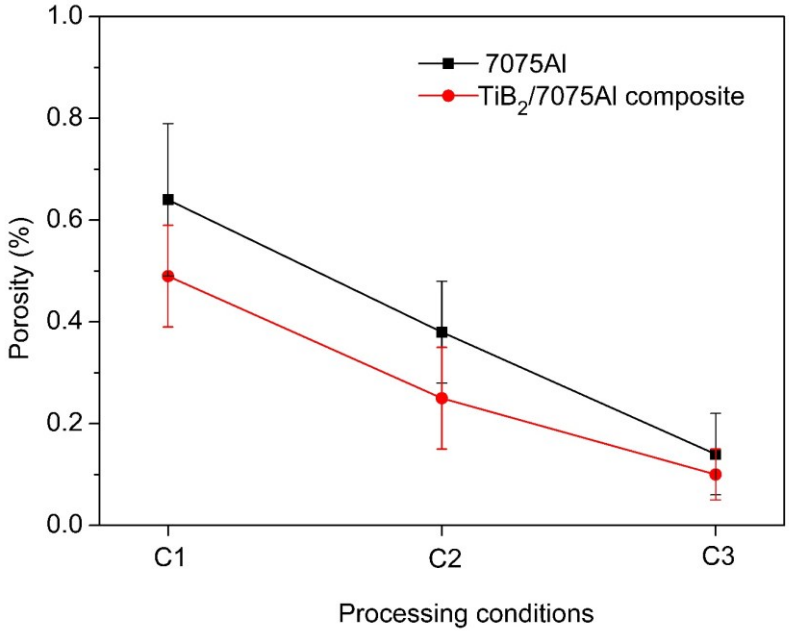

Figure 5-20 Porosity evolution of the 7075Al and TiB_2/7075Al composite deposits in different processing conditions.

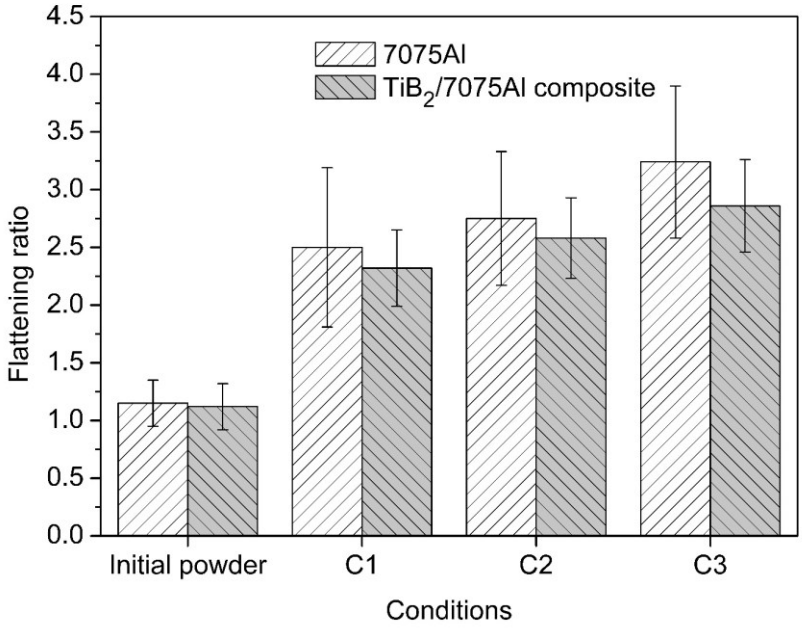

Figure 5-21 Particle flattening ratio evolution of the pure 7075Al and TiB_2/7075Al composite particle under different processing conditions.

The element contrast from the BSE/SEM images in Figure 5-19 reveal some solute segregation (e.g. Zn, Mg, Cu) at grain boundaries (GBs), which is originated from the gas-atomized powder. Furthermore, as illustrated in SEM images (Figure 5-18 (d-f), and Figure 5-22a) and EDS mapping (Figure 5-22c), ultrafine TiB_2 particles (and also nanosized TiB_2 particles, but not identifiable at this scale) are uniformly dispersed in the Al matrix. As shown in the magnified SEM image (Figure 5-22b), irregular TiB_2 particles dispersed not only inside the deformed particles but also along the interparticle boundaries. Figure 5-22e shows the size distribution of TiB_2 particles in the composite components analyzed by Image J. These in-situ formed TiB_2 particles present a wide particle size distribution from 100 nm to 1.5

μm, while most of them were lower than 700 nm. The measurement of the volume fraction of TiB_2 particles in the composite deposits was performed on five SEM images using Image J, yielding a value of 4.2 vol.%. However, it should be noted that nanosized TiB_2 particles (< 100 nm) are not counted by this method due to the limitation of spatial resolution using SEM.

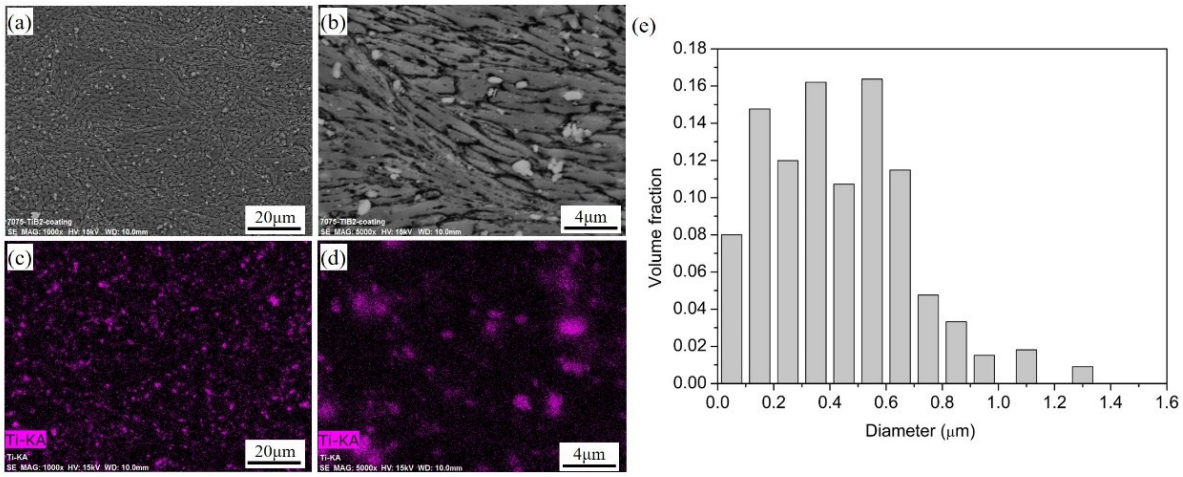

Figure 5-22 SEM morphologies (a, b) and the corresponding EDS maps of Ti (c, d) of the TiB_2/7075Al-C2 deposit; (e) TiB_2 particle size distribution obtained from SEM images.

SEM/EBSD characterization was performed to further investigate the microstructure evolution of the CSed pure 7075Al and TiB_2/7075Al composite components obtained in different processing conditions. As for the 7075Al-C1deposit (see Figure 5-23a and b), the ultrafine grains are located at interparticle boundary regions, while some large grains with sizes and structures similar to the initial 7075Al powder still remained in the center of the deformed splats. According to Kang et al. [4], these ultrafine grains should be attributed to dynamic recrystallization caused by the extremely high strain-rate (up to 10^9 s^{-1}) of plastic deformation at the interparticle regions. However, the heterogeneous microstructure suggests a limited plastic deformation of the entire pure 7075Al particle due to a relatively low particle impact velocity at C1. Nevertheless, the average grain size of this pure 7075Al deposit was measured to be 0.958 μm, much smaller than that of the initial powder, which clearly demonstrates the grain refinement effect. As can be seen from Figure 5-23d and e, a more uniform structure with a smaller average grain size (0.739 μm) was obtained at C3 compared to C1. However, this deposit shows a relatively lower indexing rate compared to that of C1 because greater residual strain stress was generated and retained in this deposit, especially at the highly deformed interparticle boundary regions. Therefore, it can be concluded that a higher particle impact velocity leads to greater plastic deformation of the particle, and thus greater grain refinement of the deposit.

As shown in Figure 5-23g and j, the microstructure evolution of the TiB_2/7075Al composite is similar to that of the pure 7075Al deposit. This means that the interior of the splat maintains a grain size and structure similar to that of the initial powder, while the interparticle boundaries experienced more evident deformation. A slightly greater grain refinement effect of the composite is observed at C3 due to the greater plastic deformation of the highly accelerated particles. For both the C1 and C3 conditions, the grain sizes of the composite deposits are much smaller than those of the pure 7075Al deposits, mainly as a result of the finer initial structure in the composite feedstock. Therefore, it can be concluded that both the structure of initial powder and the processing conditions play important roles in determining the final structure of the deposit. It should be noticed that the actual average grain size of these deposits should be smaller than the above statistical value due to the following two reasons: i) some small grains located at the interparticle boundaries failed to be detected by the back scattered electron due to the high residual stain stress retained within these highly deformed areas; and ii) grains smaller than 200 nm were

excluded from our finial statistical results because EBSD characterization was performed at a scanning step of 100 nm.

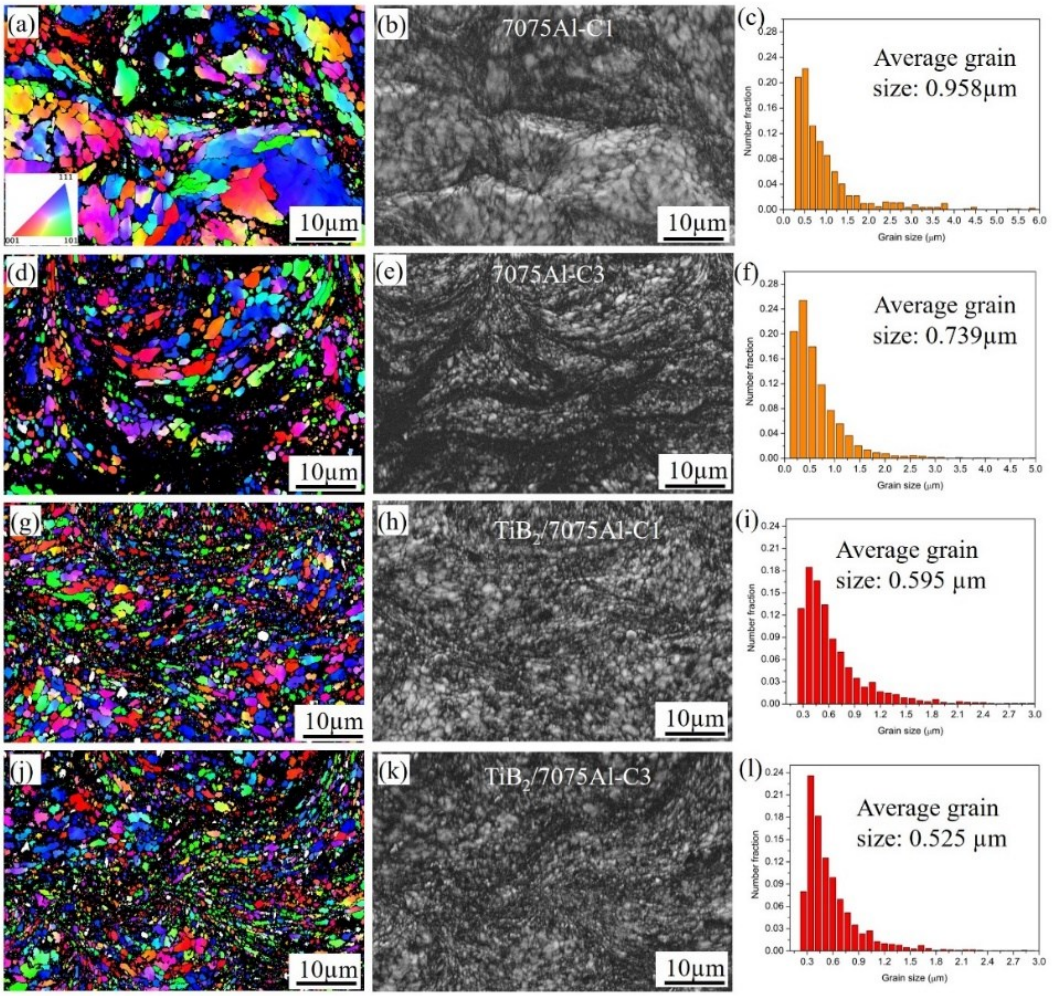

Figure 5-23 SEM/EBSD characterization of the cross-section of the CSed (a-f) pure 7075Al and TiB_2/7075Al composite deposits in different processing conditions: (a-c) 7075Al-C1; (d-f) 7075Al-C3; (g-i) TiB_2/7075Al-C1; (j-l) TiB_2/7075Al-C3. The first column displays gain orientation maps, and the middle column presents the band contrast. The last column shows gain size distribution of the Al matrix (the TiB_2 phase was eliminated).

Figure 5-24 shows the TEM bright-field (BF) images of the characteristic regions of the TiB_2/7075Al-C1 deposit. Figure 5-24a shows the structure of particle's interior region, where grains experienced slight deformation but are still in relatively large size. The average grain size in this region is measured to be about 1.2 μm, which is slightly smaller than that of the initial composite powder (1.6 μm). This observation suggests that such a low level of deformation in this region is not enough to result in evident grain refinement. However, as illustrated in Figure 5-24c, gains at the inter-splat boundary regions are highly deformed, forming a finer structure. Apart from the elongated grains, some equiaxed grains with a size less than 200 nm are also present. These fine grains are free of dislocations, which may be a result of dynamic recrystallization during CS deposition. Closer observation on the interior region (Figure 5-24b) reveals that a few fine precipitates are dispersed in the Al matrix. The precipitates are present in two forms: one is in a needle-like or rod-like shape (as marked by red arrows) and precipitate inside the deformed gains, and the other has an oval shape (as marked by yellow arrows) and is primary located along the GBs. As shown in Figure 5-24d, only the oval-shaped precipitates are observed along the GBs in the inter-splat boundary regions. It is clearly observed in Figure 5-25a and b

that the precipitates prefer to form along the sub-grain boundaries. As shown in Figure 5-24 and Figure 5-25, nanosized TiB_2 particles (indicated by blue arrows) appear to be primarily dispersed along the GBs of the Al matrix.

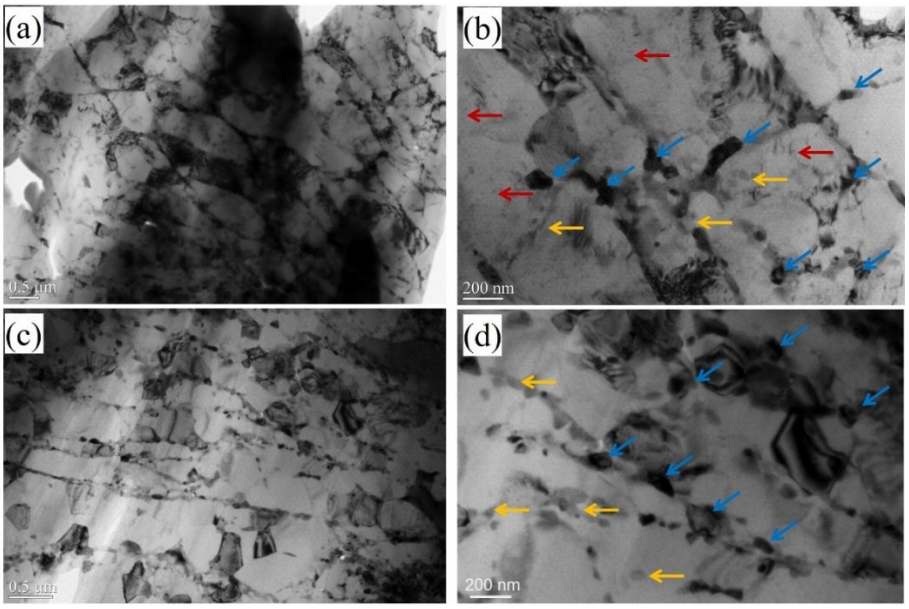

Figure 5-24 TEM micrographs of the TiB_2/7075Al-C1 deposit in different regions: (a) and (b) particle interior; (c) and (d) near interparticle boundaries. Red arrows show needle-like precipitates dispersed in the Al matrix, while the yellow arrows indicate the spherical precipitates. The blue arrows indicate the in-situ formed TiB_2 nanoparticles in the Al matrix.

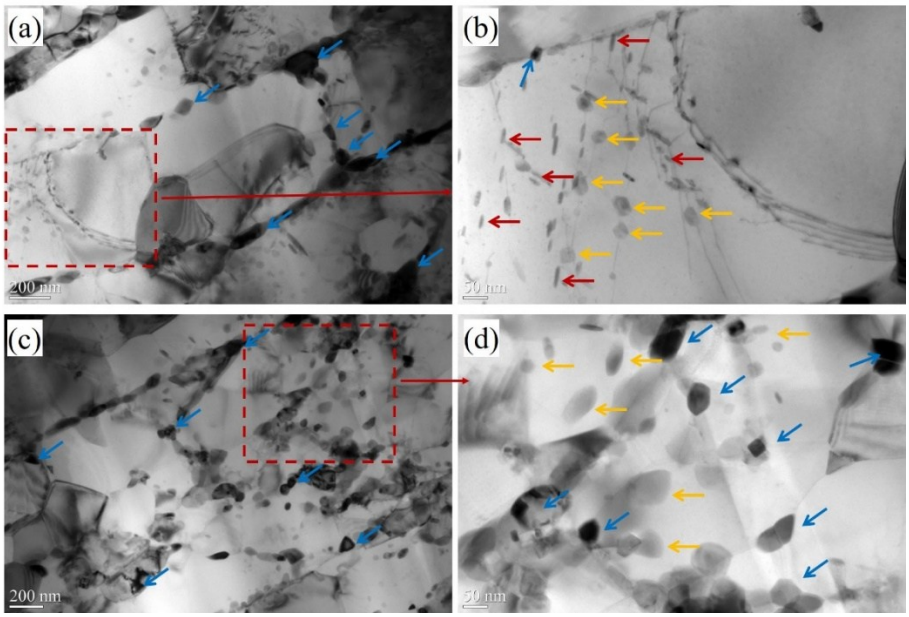

Figure 5-25 TEM micrographs of the TiB_2/7075Al-C1 deposit showing the precipitate structure. (b) and (d) the magnified micrographs within red dashed boxes of (a) and (c), respectively. Red arrows show needle-like precipitates dispersed in the Al matrix, while the yellow arrows indicate the spherical precipitates. The blue arrows indicate the in-situ formed TiB_2 nanoparticles in the Al matrix.

Figure 5-25 shows the TEM micrographs of the characteristic regions of the TiB_2/7075Al-C3 deposit. In the interior particle, as illustrated in Figure 5-26a and b, it can be clearly observed that plenty of precipitates are distributed throughout the grain interior. These precipitates are presented in two forms,

which are similar to the case of the C1 deposit. However, a greater number of precipitates are present in the C3 sample compared to the C1 sample. Another feature can be clearly noted is that the interior grains are dominated by the rod-like precipitates rather than the oval-shaped precipitates. Dislocation networks (marked by white dotted circles) can also be observed in the largely deformed Al matrix, especially around the in-situ formed nanosized TiB_2 particles. It was reported that the formation of the dislocation networks may be caused by the presence of a high density of fine precipitates in the grain interiors and nanosized TiB_2 particles at GBs, which can help pin and hinder the rapid migration of the dislocations [5].

As shown in Figure 5-26c and d, a laminar structure with a transverse spacing of 50–200 nm can be observed in the interparticle interface regions, where grains are heavily deformed during deposition. In these regions, unlike the case of the interior particle region, the fine, needle-like precipitates are rarely present within the elongated Al grain interiors. On the contrary, a number of spherical precipitates with relatively larger sizes can be observed at the lamellar boundaries. As revealed in Figure 5-27, precipitation behaviour is found to be related to the laminar grain size. In small-sized grains, as illustrated in Figure 5-27c, only spherical precipitates appear to be located at GB, while in large-sized laminar grains, a large number of precipitates are distributed throughout the laminar grains. In addition, in contrast to smaller grains, large-sized grains have more internal defects, e.g. dislocations and dislocation loops.

Figure 5-26e and f display the interparticle region structures, which feature smaller equiaxed grains with few dislocations. The observation of these ultrafine grains at the interparticle interface again provides evidence for the dynamic recrystallization mechanism during high strain-rate impact [4]. However, few precipitates can be observed within these newly formed grains. It should be noticed that little change in the distribution and structure of TiB_2 particles are found in these three typical regions.

Precipitation in 7075Al is well understood, whereby the primary precipitates in this alloy are η ($MgZn_2$) [6], η' ($MgZn_2$) [7], $Mg(Zn, Cu, Al)_2$ and T phase ($(Al, Zn)_{49}Mg_{32}$) [8]. According to previous studies [9-11], the metastable phase η' has a plate shape with a size range of 10-30 nm. The equilibrium phase η has a needle-like shape with a size range of 40–80 nm, while the $Mg (Zn, Cu, Al)_2$ and T phases are usually presented in a spherical shape. Therefore, it is reasonable to speculate that the needle-like or rod-like precipitates formed at the grain interior of the CSed TiB_2/7075Al composite would correspond to the η' and η phase, while the spherical precipitates located at lamellar boundaries are most probably correspond to the T phase or $Mg(Zn, Cu, Al)_2$). Precipitation behaviour was also reported in the CSed pure 7075Al coating by M.R. Rokni et al. [10]. However, the formation mechanism of these two kinds of precipitates could be different, and more detailed TEM characterization is required to further determine these precipitates.

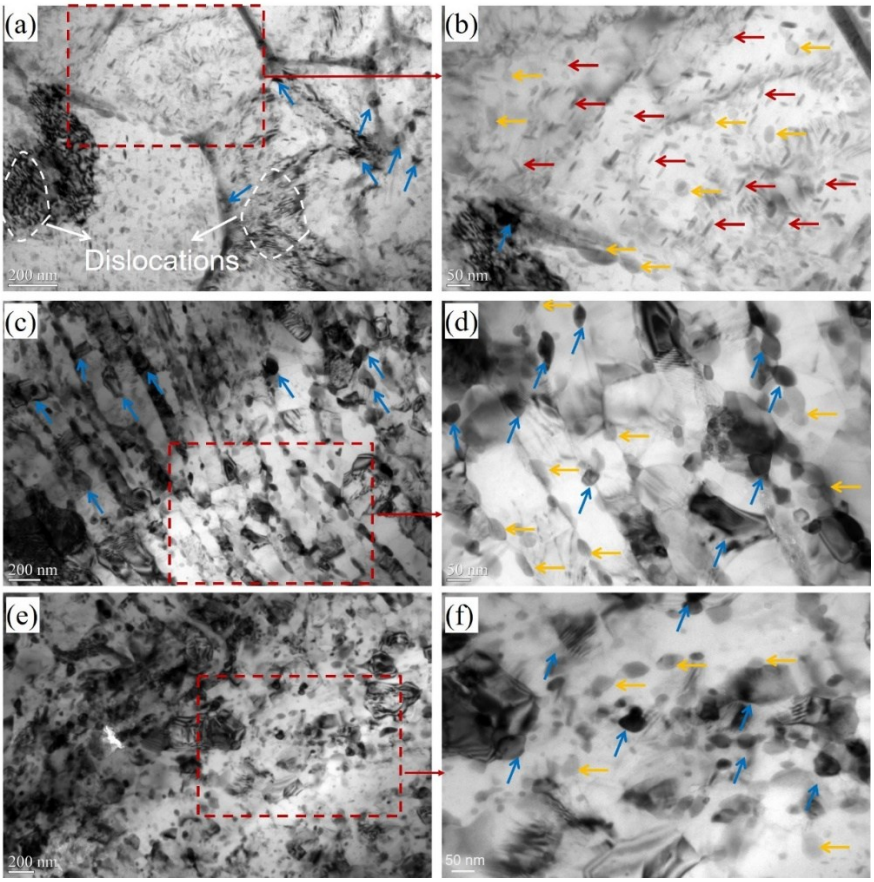

Figure 5-26 TEM micrographs of the TiB_2/7075Al-C3 deposit showing precipitate structures in (a) particle interior, (b) interparticle boundaries with pancake structures and (c) interparticle boundaries with ultrafine grain structures. (b), (d) and (f) are the magnified micrographs within red dashed boxes of (a), (c) and (e), respectively.

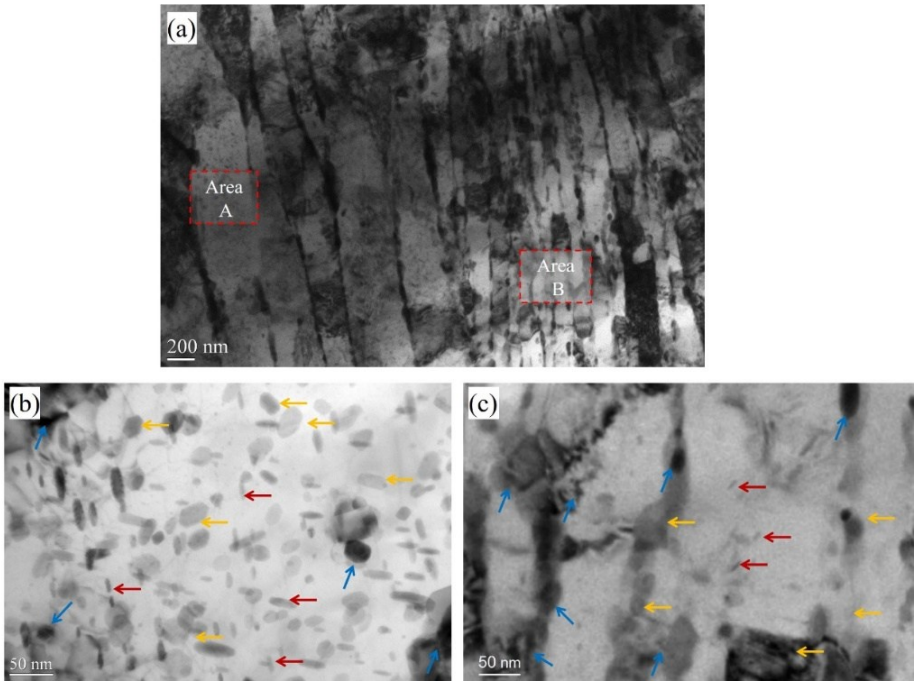

Figure 5-27 TEM micrographs of the TiB_2/7075Al-C3 deposit showing a pancake structure. (b) and (c) are the corresponding magnified micrographs of area A and B in (a), respectively.

Generally, the precipitation sequence in Al-Zn-Mg based alloys during artificial aging is described as: supersaturated solution → η' phase→ η phase [9, 12]. Such a phase transition path is seldom completed during natural aging. The TEM images in Figure 5-25and Figure 5-26 revealed that η'/ η precipitates are formed in the Al matrix, especially in the highly deformed C3 sample. The formation of these needle-like or rod-like precipitates should be related to the severe plastic deformation of the particles during CS deposition. It has been reported that the severe interaction of dislocations as a result of a high strain-rate provides plenty nucleation sites for precipitation within the grain interior [9, 10]. The He-processed particle had much higher impact velocity and experienced greater plastic deformation compared to that in the case of C1. The enhanced plastic deformation in the case of C3 increases dislocation density and vacancy concentration, the volume fraction of sub-grain boundaries, and hence the effective diffusion coefficients of solutes [12, 13]. As a result, a remarkably higher density of precipitates formed in the C3 deposit compared to C1 sample, as illustrated in Figure 5-26a. However, it is unclear if the small precipitates are η or η' precipitates, and more detailed characterization on this is necessary.

Since the precipitates along GBs are larger in size and have a near-spherical shape, their formation mechanisms may be different from those formed inside the grains. GB segregation in the as-received powder particles can be retained in the CS deposition, resulting in a high supersaturation of solute elements at GBs. According to previous studies, the severe plastic deformation during high-pressure torsion process of 7075Al at room temperature resulted in the formation of so-called “non-equilibrium” GBs. Such non-equilibrium GBs served as fast diffusion paths of solute atoms and hence promoted the growth of the precipitates in the GBs. Therefore, these spherical precipitates located at GBs are likely to nucleate from such a highly supersaturated solid solute at GBs during deposition [10].

5.5 Mechanical properties of the cold sprayed deposits

5.5.1 Microhardness

Figure 5-28 shows the microhardness evolution of the CSed 7075Al and TiB_2/7075Al composite deposits in different processing conditions. The as-sprayed deposits exhibit significant increase in microhardness compared to the initial powder. This is because the work hardening, and grain refinement effect produced during CS deposition. It is evident that the microhardness of both deposits increases as the processing condition changes from C1 to C3. The increased microhardness at C2 and C3 can be attributed to the increased particle impact velocity, which leads to a greater plastic deformation, the enhanced work hardening effect and grain refinement (Figure 5-23). The average microhardness value of the 7075 Al-C1 deposit (118 ± 6 $HV_{0.3}$) is in good agreement with that reported by Rokni et al. (115 ± 9 $HV_{0.3}$) [10], while the value obtained at C3 (146 ± 8 $HV_{0.3}$) is close to that reported by Meydanoglu et al. (136 ± 10.5 $HV_{0.3}$) [14]. Moreover, the composite deposit possesses a higher microhardness compared to the unreinforced 7075Al deposit for each condition. Microhardness increases of about 20.3%, 17.6%, and 13.0% were obtained for the composite deposits compared to the pure 7075Al deposits in C1, C2, and C3, respectively. This result indicates that for the as-sprayed composites, in addition to the work hardening and grain refinement effect, the uniformly distributed nanosized TiB_2 particles also play an important role in the enhancement of microhardness. The reinforced mechanisms will be discussed later.

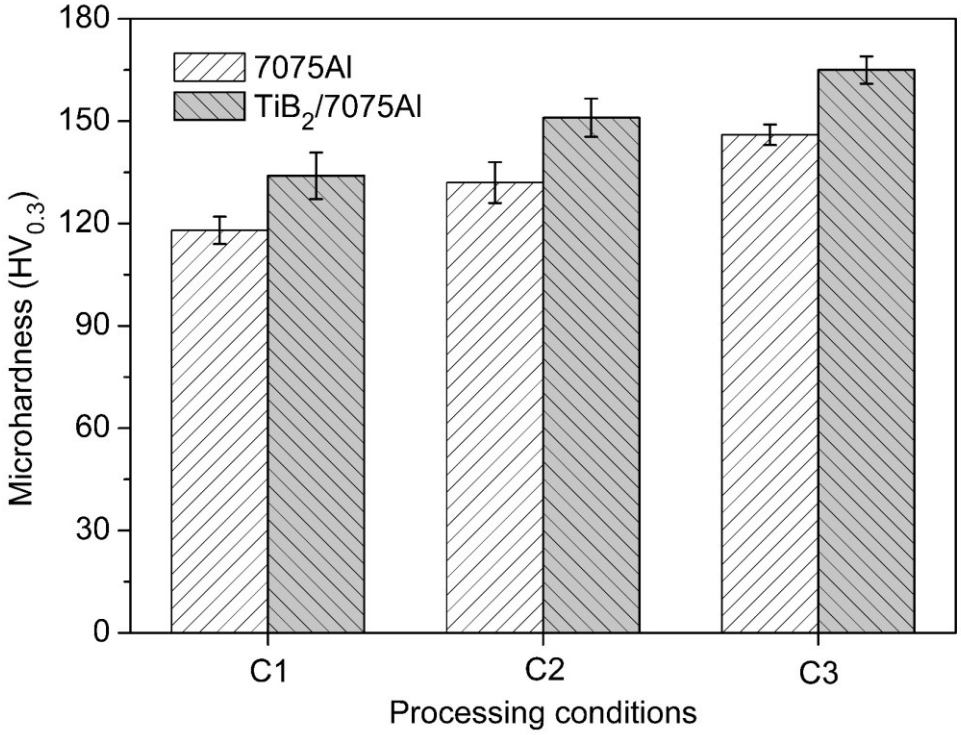

Figure 5-28 Microhardness evolution of the pure 7075Al and TiB_2/7075Al composite deposits in different processing conditions.

5.5.2 Bonding strength

The adhesion strengths between the coating and substrate in different processing conditions were measured, and the values are displayed in Figure 5-29. An examination of the specimens revealed that the failure occurred at the coating–substrate interface. The composite coating has a similar adhesion strength value compared to the pure 7075Al coating in C1, which indicates that the presence of TiB_2 nanoparticles has little effect on the adhesion strength between the coating and substrate. In general, the addition of ceramic particles can increase the adhesion strength of the coating by CS of the mixed powders, as the micron-sized hard ceramic particles can enhance the deformation of the soft metal particles and the bonding between the particle and the substrate [15, 16]. However, when the volume fraction of the ceramic particles reaches a high level, the bonding strength remains stable or even starts to decrease, because the presence of micron-sized particles reduced the surface area available for the Al matrix to deform around the surface irregularities of the substrate and bond to the latter [17]. As revealed in Chapter 4, TiB_2/AlSi10Mg composite deposit possesses a lower bonding strength compared to the pure AlSi10Mg deposit due to the presence of TiB_2 clusters on the particle surface. However, TiB_2 nanoparticles in this study are smaller and most of them are uniformly distributed inside the particles, thereby having little effect on the mechanical interlocking and metallurgical bonding between the composite coating and the substrate. Furthermore, based on our FEA simulation and single particle deposition experiments, the pure 7075Al particle and TiB_2/7075Al composite particle experienced similar plastic deformation behavior when impacting on the relative hard 7075Al-T6 substrates. Therefore, both deposits exhibit similar adhesion strength.

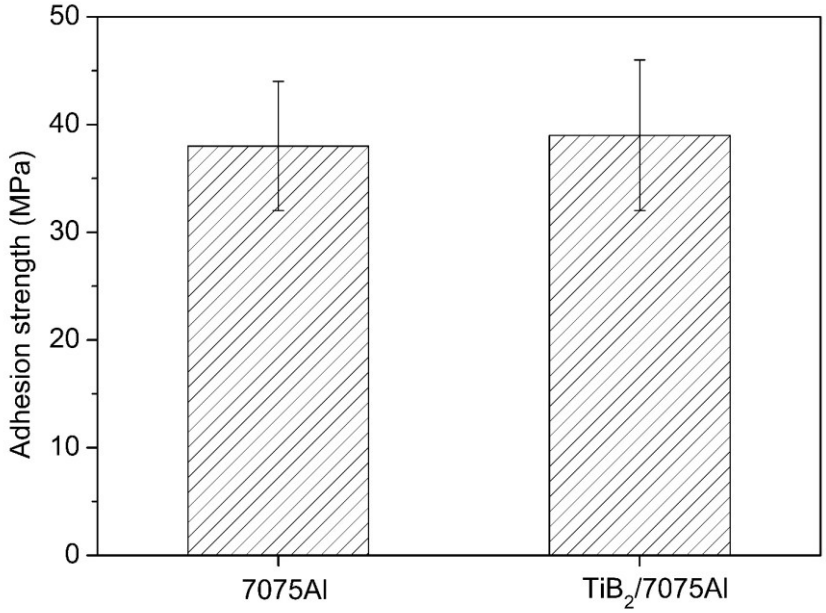

Figure 5-29 Adhesion strength evolution of 7075Al and TiB_2/7075Al composite in C1.

5.5.3 Tribological performance

The coefficient of friction (COF) versus wear distance for pure 7075Al and TiB_2/7075Al composite coatings was plotted in Figure 5-30a. At the beginning, the COF of both coatings show an unstable initial plateau, and then become steady and lower after 50 mm sliding time, which indicates a relatively steady-state wear mechanism. Similar behavior of the COF has been reported by K. Spencer et al. [18]. During the dry sliding test, the formation of a surface tribolayer can promote wear resistance against the counterpart, leading to a stable and low COF value. The TiB_2-reinforced Al coatings have a higher COF value than the unreinforced coatings, but are independent of the processing conditions (Figure 5-30b). In addition, the composite coatings exhibited slightly higher wear resistance compared to the unreinforced coating. The wear rates for both coatings decrease as the processing conditions change from C1 to C3, which incorporates well with the microhardness tendency. The improved wear resistance of the composite coating can be associated with (a) the increase in the load bearing capacity of the material, (b) the improved cohesion of splats and the higher density of the coating, and (c) increase in the hardness.

Typical wear tracks from the 7075Al and TiB_2/7075Al composite coatings are shown in Figure 5-31. The appearance of the track shows signs of smearing and adhesive wear, but there is also some evidence of abrasive wear. The obvious appearance of extrusion and plastic deformation of Al matrix is observed, meanwhile, it exhibits a little wear debris on the worn surfaces, suggesting that the adhesion between coating and sliding ball might be the dominant wear behavior at the initial stage. Besides, the wear debris was a mixture of light colored material similar to that of the coating, but also dark debris suggesting some oxidation of the wear debris. The Al_2O_3 counter ball was worn partially flat and there was some Al adhered to the surface. The EDS results (Figure 5-31c and f) demonstrate that a higher content of oxygen distributes on the worn surfaces during the sliding process. In addition, the EDS mapping of wear tracks of the composite coating also clearly presents a uniform distribution of TiB_2 particles in the Al matrix.

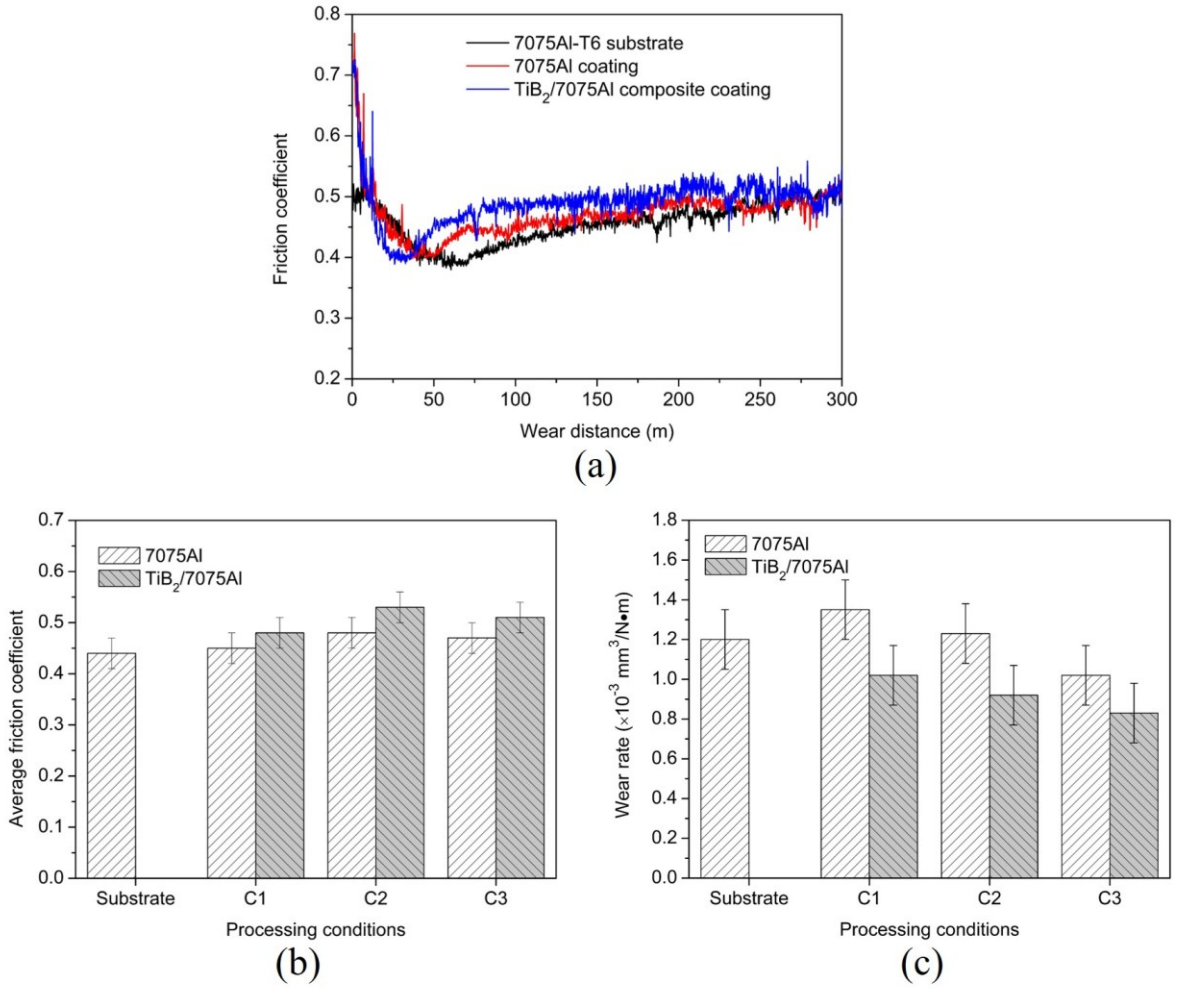

Figure 5-30 (a) Coefficient of friction versus wear distance; (b) and (c) average friction coefficients and wear rates at diffident processing conditions.

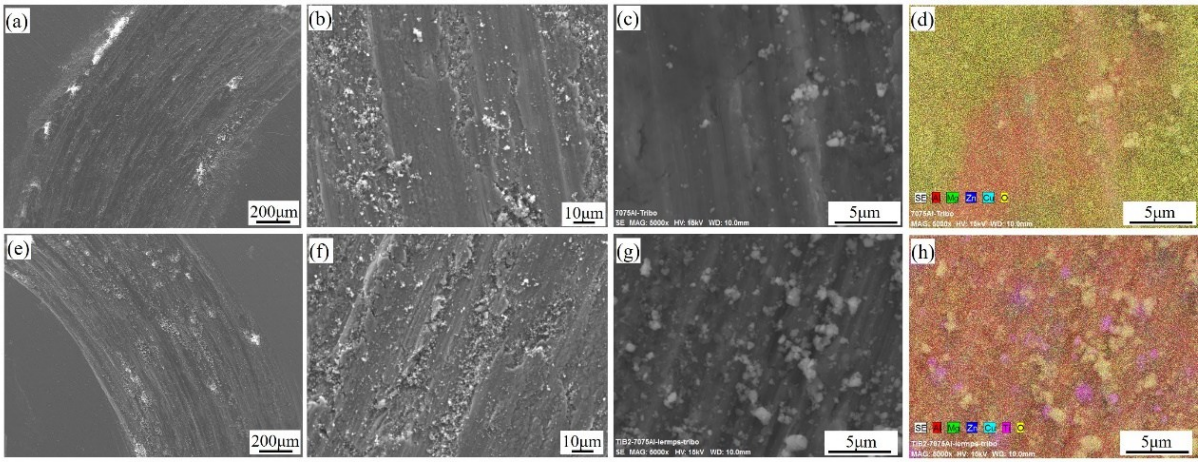

Figure 5-31 Overviews, magnified views and EDS mapping of the worn morphologies of CSed (a-d) 7075Al-C1 and TiB_2/7075Al-C1composite coatings.

5.5.4 Tensile strength

The values of ultimate tensile strength (UTS) and elongation of the as-sprayed 7075Al and TiB_2/7075Al composite deposits under different processing conditions are summarized in Figure 5-32a

and b, respectively. The C2 samples exhibit the lowest UTS value and almost no elongation, while the C1 and C3 samples show slightly improved UTS. The composite samples possess higher UTS values compared to those of the pure 7075Al deposits. However, both the as-sprayed deposits exhibit typical brittle behaviour. The elongation values of the as-sprayed samples are lower than 2.0 %, even for those of the He-processed samples. The highest UTS value of the composite component reaches 350 MPa with an elongation of 1.2% at C3.

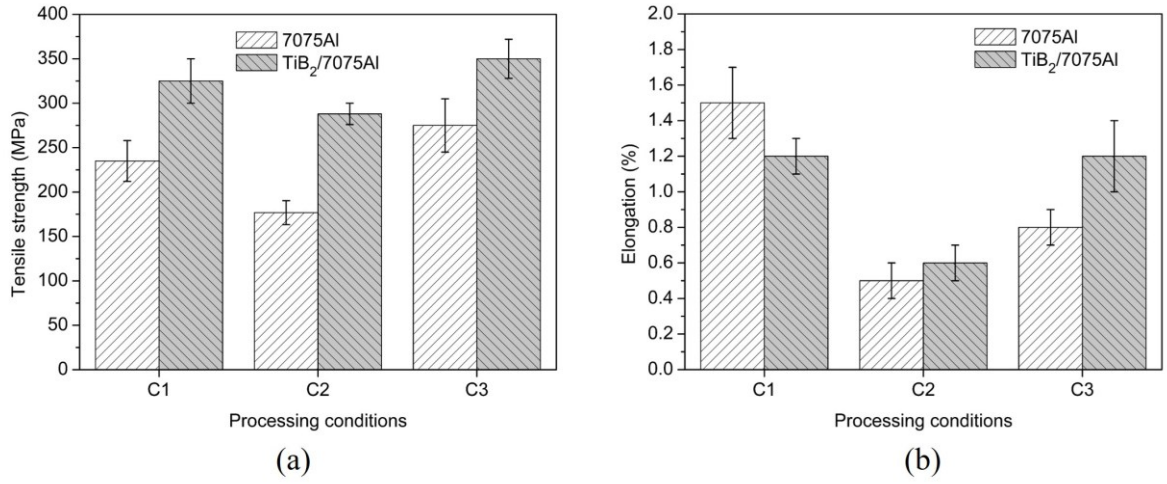

Figure 5-32 Variation of (a) tensile strength and (b) elongation of the as-sprayed 7075Al and TiB_2/7075Al composite samples in different processing conditions.

Figure 5-33 shows the fracture surface of the as-sprayed TiB_2/7075Al composite samples obtained in different processing conditions. As shown in Figure 5-32a, the fracture surface of the TiB_2/7075Al-C1 deposit demonstrates a typical cleavage feature. Some dimples are found in the interparticle boundaries, where greater plastic deformation and recovery occurred. In the case of C2 (Figure 5-33b), fracture takes place along the splats' interface rather than through them, and almost no dimples are observed on the surface, displaying a brittle rupture. As shown in Figure 5-33c, the fracture surface of the He-processed composite sample displays a curly structure with some fracture occurring through the deformed splats. This observation confirms the robust metallic bonding at the severely deformed interface regions due to the occurrence of ASI and the metal jet [19]. As marked in Figure 5-33a_1-c_1, some interior defects or pores can be seen within the deposits.

Generally, a higher impact velocity leads to enhanced plastic deformation and metallic bonding of the deformed splats. Consequently, the decreased grain size and enhanced work hardening effect as well as the metallic bonding resulted in higher microhardness and tensile strength for both the pure 7075Al and TiB_2/7075Al composite in C2 and C3. However, tensile tests reveal that the C1 samples possess higher UTS and elongation values compared to those of the C2 samples, even though a higher particle impact velocity and lower porosity was achieved in C2. As indicated from our FEA simulation results (see Figure 5-10 and Figure 5-11), a higher particle impact temperature is beneficial for the occurrence of ASI at local interparticle regions during deposition [20] [21]. The soften effect produced from a relatively high particle impact temperature can enhance the metallurgical bonding at C1. Therefore, some dimples are observed at interparticle boundaries from the fracture surface (Figure 5-33a), which are absent in C1 and C3. The above results reveal that the metallurgical bonding between deformed splats is the most important factor that determines the final tensile properties of the CS samples. Heat treatment is a commonly used but effective method to improve their mechanical properties by improving

the interparticle bonding and curing the defaults. Therefore, appreciate heat treatments on these CSed samples will be carried out in the following section.

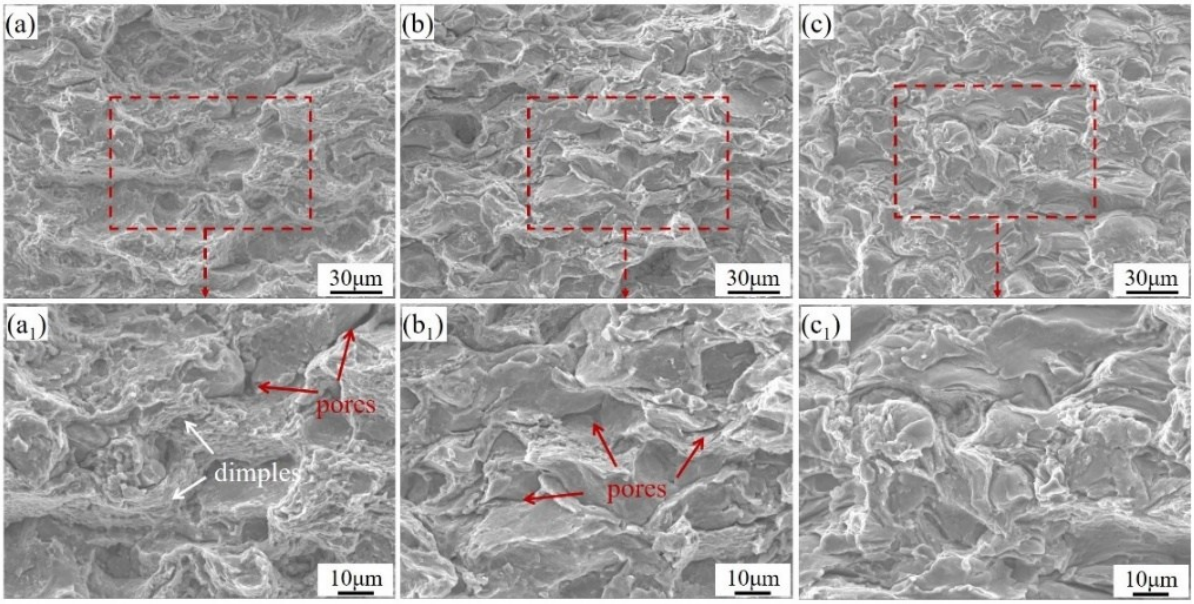

Figure 5-33 Fracture morphologies of the as-sprayed TiB_2/7075 Al composite tensile samples fabricated using different processing conditions: (a) C1; (b) C2; (c) C3. (a_1), (b_1) and (c_1) are the magnified images of the red dashed area in (a), (b) and (c), respectively.

5.6 Corrosion properties of the cold sprayed deposits

In order to study the influence of processing conditions on the saltwater corrosion behavior of the CSed coatings, the C1 and C3 samples were selected for electrochemical corrosion tests in terms of immersion, potentiodynamic polarization, and impedance spectroscopy. In addition, the C3 samples were annealed at different conditions to investigate the effect of annealing treatments on the corrosion behavior of CSed coating.

5.6.1 Immersion studies

A comparison of surface morphologies of the 7075Al-T6 bulk, 7075Al coatings and TiB_2/7075Al composite coatings before and after immersion in either 0.1 M or 0.6 M NaCl for 7 days is given in Figure 5-34. The first column in Figure 5-34 displays the surface morphologies of the samples before immersion. Contrary to the relatively smooth surface of the bulk 7075Al, the CSed coatings show evident swearing scratch marks from sample preparation. In Figure 5-34b, after immersion in a 0.1 M NaCl solution for 7 days, the scratch marks become obscure, indicating the occurrence of general corrosion during immersion. Meanwhile, some signs of local corrosion as well as some productions are found from the bulk surface. After immersion in a 0.6 M NaCl solution for 7 days, more severe local corrosion can be seen on the surface. However, the bulk material shows no sign of pitting after immersion in either a 0.1 M or 0.6 M NaCl solution.

As seen in Figure 5-34e, after immersing the 7075Al-C1 coating in a 0.1 M NaCl for 7 days, the scratch marks all disappeared, and some individual pits are seen on the corroded surface. The pits are commonly observed for the 7075Al alloy immersed in the NaCl solution. It is clear that circular areas are formed around the obvious pits (black arrow). According to previous studies [22, 23], these areas are cathodic protection zones (CPZs), which are the surface regions required as cathodes to support the anodic dissolution taking place in the pit. Therefore, in the CPZs, corrosion is largely suppressed.

Normally, the pit size is much smaller than the CPZs. When immersed in 0.6 M NaCl for 7 days, some large, irregular shaped pits, even caves (with a diameter of 100-200 μm) are observed on the corroded surface of the coating, as shown in Figure 5-34f. Around these large pits, there are many corrosion products, which are oxygen-rich, most likely oxides or hydroxides. These pits are believed to originate from the anodic dissolution of the matrix around the constituent particles at the GBs. Anodic dissolution of the matrix around Cu- and Fe- rich constituent particles has been previously reported for 7075Al [22]. As corrosion proceeds and the matrix gradually dissolves, these pits become larger and larger and finally form the irregular shaped caves. The formation of these large pits is quite dangerous for the application of these coatings. In the case of He-processed 7075Al coating, similar pit features can be seen on the corroded surface after immersion in either 0.1 M or 0.6 M NaCl solution. The results imply that pit seems easily form in the CSed 7075Al coating.

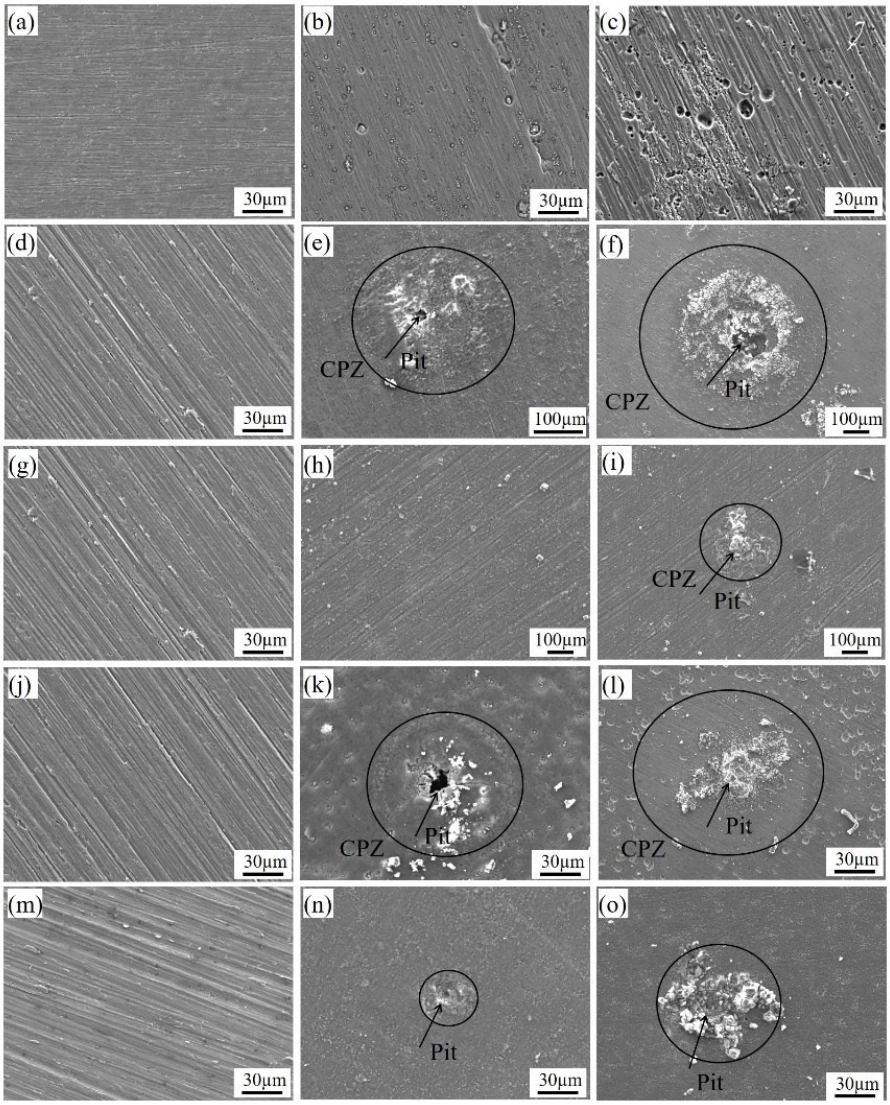

Figure 5-34 SEM images of the 7075Al bulk, 7075 Al and TiB_2/7075Al composite coatings before (first row) and after open circuit immersion in 0.1 M (middle row) and 0.6 M (third row) NaCl for 7 days: (a-c) 7075Al bulk; (d-f) 7075Al-C1; (g-i) TiB_2/7075Al-C1; (j-l) 7075Al-C3; (m-o) TiB_2/7075Al-C3.

However, the TiB_2/7075Al composite coatings exhibit entirely different features when compared to the pure 7075Al coating and the bulk material. After immersion in 0.1 M NaCl for 7 days, scratch marks are still visible on the corroded surface, as shown in Figure 5-34h. Meanwhile, few pits can be observed. Instead, a thin oxide film formed on the corroded surface after immersion, which can protect

the surface from corrosion. When the solution concentration is increased to 0.6 M, some traces of scratch marks can still be observed. Moreover, only a few small pits are found on the corroded surface in this case. The TiB_2/7075Al-C3 composite sample also proves these observations. Compared to the TiB_2/7075Al-C1 composite coating, pit seems to form slightly more easily in the case of the C3 coating either in 0.1 M or 0.6 M NaCl. Nevertheless, large, irregular shaped pits or caves are not formed on the composite coatings. These results indicate that the composite coating possesses a much better corrosion resistance in a static corrosion condition (without an applied current) compared to the pure 7075Al coating.

5.6.2 Open circuit potential and polarization studies

Typical polarization curves for the bulk 7075Al-T6 alloy, CSed pure 7075Al and TiB_2/7075Al composite coatings obtained in different conditions are displayed in Figure 5-35. The values of corrosion potential (E_{corr}) and corrosion current densities (I_{corr}) obtained from the polarization curves are listed in Table 5-5. The E_{corr} can be regarded as the thermodynamic performance, representing the corrosion tendency of the material; a higher E_{corr} value indicates a lower tendency for corrosion. And I_{corr}, as a kinetic factor, can directly reflect the corrosion rate of the material. A higher I_{corr} value signifies a higher corrosion rate. Figure 5-35a depicts the results of polarization experiments in a 0.1 M NaCl solution. It is clear that the bulk 7075Al possesses the highest E_{corr} of about -0.736 V and lowest I_{corr} of 2.25 E-6 A/cm^2 as compared to both the pure 7075Al and TiB_2/7075Al composite coatings, indicating that the bulk material has higher corrosion resistance than both the as-sprayed pure 7075Al and TiB_2/7075Al composite coatings in a 0.1 M NaCl solution. For each CS processing condition, the average E_{corr} value of the composite coating is higher than that of the pure 7075Al coatings, suggesting that TiB_2/7075Al samples are highly corrosive from the view of corrosion thermodynamics. Moreover, from the view of corrosion kinetics, the I_{corr} of the composite coating is higher than that of the pure 7075Al coating, which indicates a higher corrosion rate for the composite coating. In addition, within the error, there is no significant difference in corrosion potential among C1 and C3 deposits tested in a 0.1 M NaCl solution. However, one can notice that the corrosion rates for C3 deposits were estimated to be slightly higher than those of the C1 deposits, as I_{corr} values of the C3 deposits are slightly higher.

Figure 5-35b depicts the results of polarization experiments in a 0.6 M NaCl solution. All the samples behave more active when increase the chloride concentration. Again, the bulk material represents the lowest I_{corr} compared to all the coatings, implying the best corrosion resistance among the samples in a 0.6 M NaCl solution; while its E_{corr} is higher than that of the pure 7075Al coating but lower than that of composite coating. For each condition, the composite coating possesses a higher E_{corr} than that of the pure 7075Al, indicating a low corrosive from the view of corrosion thermodynamics. A higher I_{corr} compared to the pure 7075Al coating indicates a higher corrosion rate of the composite coating. Furthermore, the C3 samples exhibit lower E_{corr} and higher I_{corr} values compared to the C1 samples. For the pure 7075Al coating, E_{corr} drops from -0.916 V to -0.941V, while the I_{corr} increases from 4.02 E-5 A/cm^2 to 7.89E-5 A/cm^2. For the TiB_2/7075Al composite coating, E_{corr} drops from -0.848 V to -0.898 V, while the I_{corr} increases from 8.13E-5 A/cm^2 to 17.5E-5 A/cm^2, which is about ten times higher than the bulk material. The C3 samples show a significant decrease in corrosion resistance.

Through the above polarization analysis, we can conclude that the order of corrosion resistance is bulk material, C3 coatings, and C1 coatings. Meanwhile, the TiB_2/7075Al composite coating seems to have a lower corrosion tendency but a higher corrosion rate than the unreinforced 7075Al deposit.

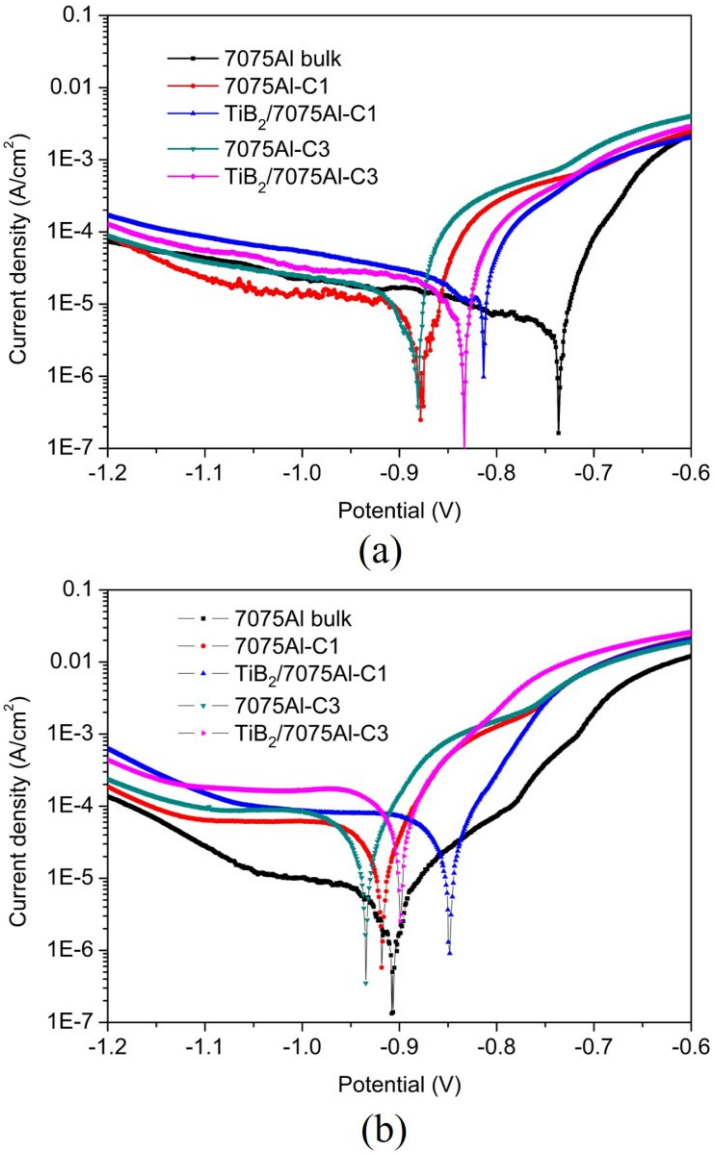

Figure 5-35 Corrosion behavior of the bulk 7075Al , CSed 7075Al coatings and TiB_2/7075Al composite coatings obtained at C1 and C3 in a solution of (a) 0.1 M and (b) 0.6 M NaCl as determined by potentiodynamic polarization.

Table 5-5 Results of potentiodynamic corrosion tests in 0.1 M and 0.6 M NaCl solutions.

Material	E_{corr} (V)		I_{corr} (A/cm^2)	
	0.1 M	0.6 M	0.1 M	0.6 M
7075Al Bulk	-0.736	-0.908	0.225E-5	1.55E-5
7075Al-C1	-0.878	-0.916	2.56E-5	4.02E-5
TiB_2/7075Al-C1	-0.813	-0.848	4.19E-5	8.13E-5
7075Al-C3	-0.880	-0.941	3.06E-5	7.89 E-5
TiB_2/7075Al-C3	-0.833	-0.898	4.24E-5	17.5E-5

5.6.3 Electrochemical impedance studies

Electrochemical impedance spectroscopy (EIS) tests were performed in a 0.6 M NaCl solution at open circuit potential to further illustrate the corrosion behavior of the CSed 7075Al and TiB_2/7075Al composite coatings. Figure 5-36 shows the experimental Nyquist and bode plots for the bulk and CSed coatings. Nyquist plots of all these samples include two separate semicircles, which indicate two capacitance loops and two time constants. As seen in Figure 5-36, the amplitudes of the semicircles follow this order: bulk 7075Al-T6 >7075Al-C1>7075Al-C3> TiB_2/7075Al-C1> TiB_2/7075Al-C3. In Nyquist diagrams, the greater the diameter of the capacitive loop is, the lower the corrosion rate of the test sample will be [24]. Therefore, the bulk 7075Al-T6 exhibits the lowest corrosion rate among all the samples. It is evident that the addition of TiB_2 particles decreases the corrosion resistance of the composite coating. Moreover, the C1 deposits show better corrosion resistance than the C3 samples. The EIS measurements are consistent with the polarization results.

Taking into account the typical EIS plots, an electrical equivalent circuit (EEC) with two time constants is proposed as shown in Figure 5-37. In the EEC, R_s is solution resistance; R_{ct} is the charge transfer resistance across the double layer at the electrolyte/coating (electrode) interface in parallel with the constant phase element CPE_{dl}, which corresponds to the medium frequency range; R_{film} accounts for the oxide film dissolution/diffusion through a barrier oxide layer at the inter-splat boundary interface, which is due to the penetration of the electrolyte into the coatings. R_{film} is parallel with the constant phase element CPE_{film} which corresponds to the low-frequency range.

The values for the circuit elements required to fit the EIS data are given in *Table* 5-6. R_{ct} is an important parameter that is directly dependent on the active protection provided by the coating. It is evident that the R_{ct} of bulk 7075Al is much higher than that of other coatings. Compared to the pure 7075Al coating, a slight decrease of R_{ct} is observed for the TiB_2/7075Al composite coating. While the C1 coating possesses a higher value than that of C3 sample. A similar tendency is found for R_{film}. According to previous studies [25, 26], the sum of R_{ct} and R_{film} can be used to characterize corrosion resistance. It can be seen that the corrosion resistance follows the order: bulk 7075Al >7075Al-C1>7075Al-C3>TiB_2/7075Al-C1> TiB_2/7075Al-C3, which again is consistent with the polarization results.

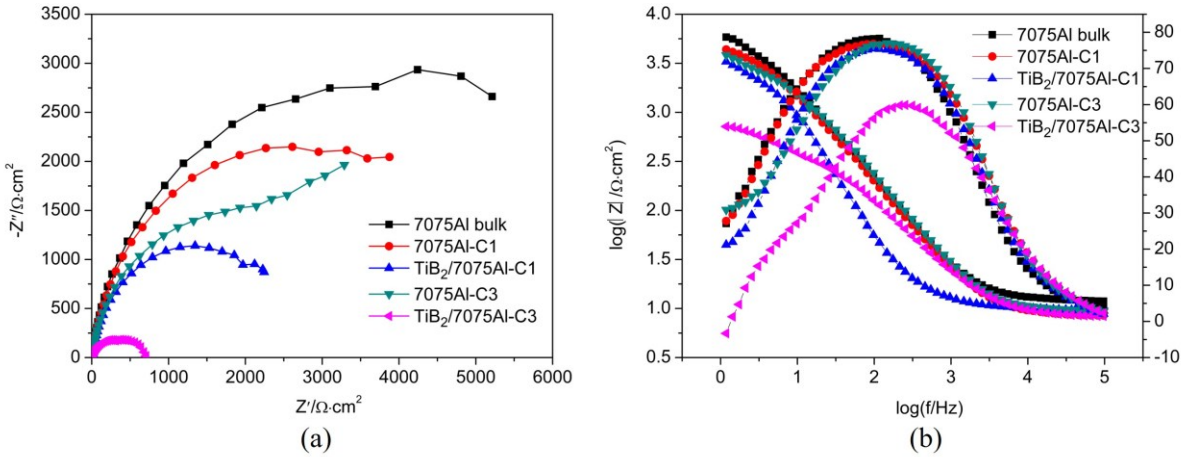

Figure 5-36 Experimental and simulated (a) Nyquist and (b) Bode plots of the bulk 7075Al, and CSed 7075Al and TiB_2/7075Al composite coatings.

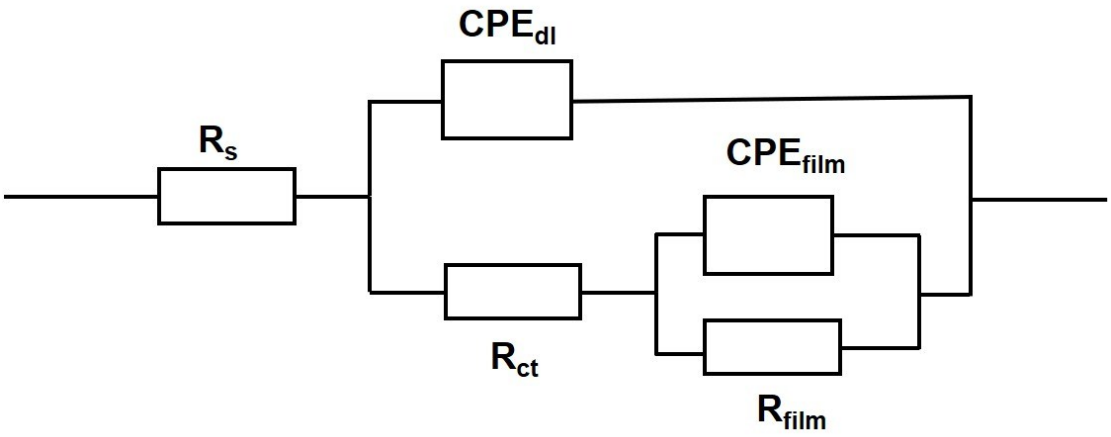

Figure 5-37 Electrical equivalent circuits used to fit the EIS data.

Table 5-6 Fitted EIS parameters for the bulk and as-sprayed coatings.

Sample	Rs (Ω cm^2)	CPE$_{dl}$ (10^{-4}F cm^{-2})	n_{dl} (Ω cm^2)	R_{ct} (KΩ cm^2)	CPE$_{film}$(10^{-4}F cm^{-2})	n_{film}	R_{film}(KΩ cm^2)	R_{ct}+R_{film} (KΩ cm^2)
Bulk 7075Al	12.85	0.07	0.93	1.41	0.05	0.54	4.33	5.74
7075Al-C1	9.12	0.07	0.91	0.53	0.04	0.82	3.82	4.35
TiB_2/7075Al-C1	8.70	0.08	0.91	0.40	0.05	0.87	1.99	2.39
7075Al-C3	10.18	0.06	0.93	0.18	0.19	0.94	2.26	2.44
TiB_2/7075Al-C3	9.31	0.07	0.82	0.15	0.20	0.66	0.41	0.61

5.6.4 Effect of annealing treatment on the corrosion behavior of the CSed coatings

Electrochemical corrosion tests were performed on the annealed 7075Al-C3 and TiB_2/7075Al-C3 composite coatings in a 0.6 M NaCl solution to investigate the effect of annealing treatments on the corrosion behavior of CSed coatings. Annealing treatments were performed using two different conditions: one was performed at 230 ℃ for 6 h, the samples of which refer to HT1; and the other was performed at 412 ℃ for 4 h, the samples of which of which refer to HT2. The polarization curves of the CSed and annealed coatings in a 0.6 M NaCl solution are given in Fig. 10. The E_{corr} and I_{corr} values obtained from the polarization curves are listed in Table 5-7. It is clear that after annealing treatment at 230 ℃ for 6 h, both the pure 7075Al and TiB_2/7075Al composite coatings show a significant decrease in I_{corr} and a slight increase in E_{corr} compared to the as-sprayed coatings. This result indicates an enhanced corrosion resistance of both coatings after HT1 annealing treatment. However, when the samples were annealed using HT2, the I_{corr} of the pure 7075Al coating increases from 1.06 E-5 A/cm^2 to 29.2 E-5 A/cm^2, while the I_{corr} of the TiB_2/7075Al composite coating increases from 6.04 E-5 A/cm^2 to 69.8E-5 A/cm^2. Such an increase in I_{corr} significantly lowers their corrosion resistance. The above results clearly show that the annealing treatment can significantly influence the corrosion behavior of the CSed coatings.

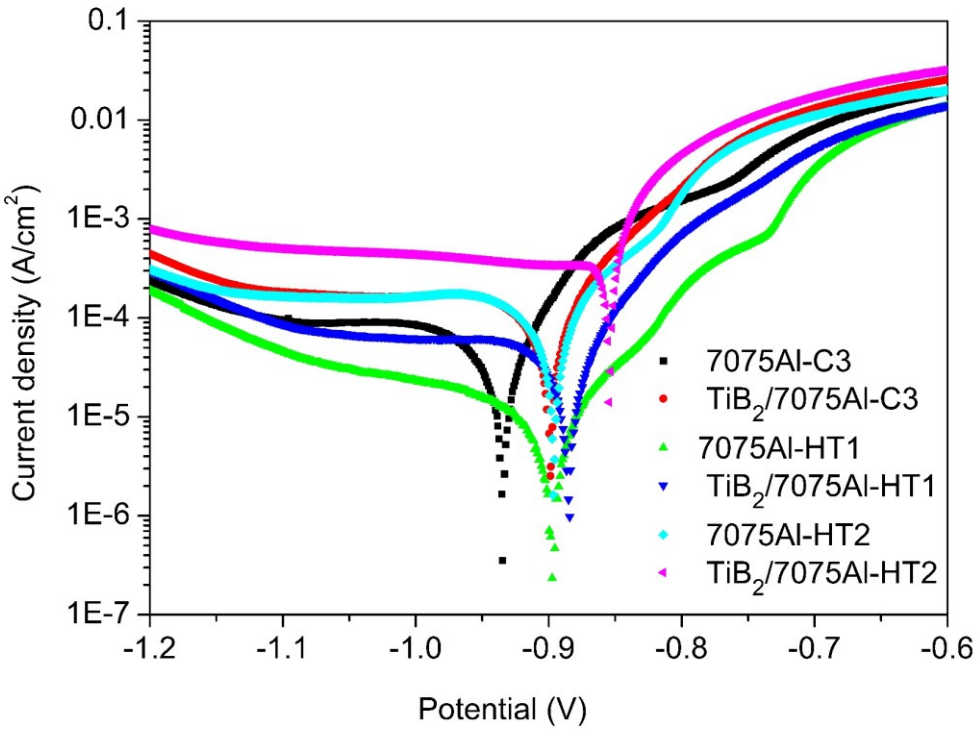

Figure 5-38 Potentiodynamic polarization curves of the CSed and annealed coatings. HT1 refers to annealing procedure of 230 ℃ for 6 h, while HT2 refers to annealing procedure of 412 ℃ for 4 h.

Table 5-7 Results of potentiodynamic corrosion tests of the annealed samples in a 0.6 M NaCl solution.

Samples	E_{corr} (V)	I_{corr} (A/cm^2)
7075Al-C3	-0.941	7.89 E-5
TiB_2/7075Al-C3	-0.898	17.5E-5
7075Al-HT1	-0.882	1.06E-5
TiB_2/7075Al-HT1	-0.884	6.04E-5
7075Al-HT2	-0.896	29.2E-5
TiB_2/7075Al-HT2	-0.854	69.8E-5

5.6.5 Corrosion mechanisms

In this study, the influence of processing parameters and annealing treatments on saltwater corrosion behavior of the CSed pure 7075Al coating and TiB_2/7075Al composite coating were investigated exhaustively using Tafel polarization, EIS, and immersion tests. Additionally, the effect of nanosized in-situ TiB_2 particles on the corrosion behavior of the coatings was also examined in detail. Through the experimental analysis, the following three general conclusions are drawn: i) the bulk 7075Al-T6 sample shows the best corrosion resistance followed by the C1 coatings and C3 coatings; ii) the TiB_2/7075Al composite coatings show lower corrosion tendency in a static state but a worse dynamic corrosion resistance compared to the pure 7075Al coatings; iii) A low-annealing temperature treatment is beneficial for the corrosion resistance of the as-sprayed coating, however, a high-annealing temperature treatment results in significant decrease in the corrosion resistance. Combining with

microstructural evolutions, the corrosion mechanisms of the CSed and annealed composite coatings are discussed, which may help further improve and optimize the corrosion resistance.

Generally, the detailed microstructure is decisive factor of the corrosion resistance of the materials whose chemical compositions are the same [27]. As reported by previous studies [22, 28], the bulk 7075-T6 sample produced from hot-rolling process exhibited a homogenous structure with micron-sized grains, which is beneficial for its corrosion resistance in a saltwater solution. However, the as-sprayed pure 7075Al and TiB_2/7075Al composite coatings are formed though plastic deformation and bonding of the individual particles, leaving a plenty of inter-particle boundaries, which provide active reaction zones for pitting corrosion. As a result, the corroded surface morphologies of the samples after immersion tests revealed a pitting corrosion mechanism for both the CSed pure 7075Al and TiB_2/7075Al composite coatings. The corrosion resistance of the CSed coatings are largely reduced compared to the 7075Al-T6 bulk.

In addition, previous studies revealed that both the porosity and the degree of plastic deformation of the particles also play important roles in determining the corrosion behavior of CSed Al coatings [22, 29]. On the one hand, according to S.Ngai et al. [22], limited particle deformation and a high degree of resultant porosity in the N_2-processed coating can have a higher corrosion rate compared to the He-processed coating due to the formation of severe micro-crevice corrosion and irregular network pitting on the corroded surface. Therefore, a porous structure can significantly lower the corrosion resistance of the coating. On the other hand, according to studies of K.Balani et al. [29] and O.Meydanoglu et al. [14], the presence of more active sites for corrosion as a result of a high degree of deformation may lead to higher corrosion current density of the coatings. In this study, using He as the propellant gas can effectively accelerate the particles to a much higher impact velocity and thus greater particle deformation and a denser structure compared to the air-processed coatings (see Figure 5-18 and Figure 5-23). Therefore, a greater deformation generated in the C3 coatings can promote more active sites for corrosion, resulting in rapid corrosion kinetics. In addition, according to the EBSD and TEM results (see Figure 5-23 and Figure 5-26), a large number of recrystallized grains appear at the inter-splat boundaries, which further reduces the corrosion resistance [30, 31], especially for the C3 samples. Moreover, the high density of fine η'/η precipitates resulted from severe plastic deformation, were distributed homogeneously within the matrix of C3 deposits. The dislocations in the GBs also provided heterogeneous nucleation sites for the η precipitates, which are noted as being anodic to the Al alloy matrix [32]. Consequently, the precipitates in the GBs became smaller and tended to a form relatively continuous distribution, worsening the corrosion resistance because of the continuous attack coverage of GBs [33]. In summary, the presence of relatively higher porosities in the C1 coatings yet display better corrosion resistance compared to the C3 coatings. These results indicate that the degree of plastic deformation plays much more important role in determining the corrosion behavior of the coatings when a relatively low porosity is present in the coatings.

Based on the above analysis, both the level of particle plastic deformation and the area fraction of inter-particle boundaries can influence the corrosion resistance of the as-sprayed coatings. Therefore, annealing treatments, as one of the most important methods in healing the defects of the CSed coatings, were applied to optimize the coatings' corrosion performance. After a low-temperature annealing treatment (230 ℃/6 h), the samples demonstrate the optimum corrosion resistance performance, as a result of the strain stress relief and dislocation elimination, reducing the active sizes. As a result, the corrosion resistance is increased. However, after a high-temperature annealing treatment (412 ℃/4 h), the corrosion resistance was the worst compared to either the as-sprayed coatings or the low-temperature annealed coatings. Generally, the corrosion resistance could be improved by further eliminating CS defects, such as dislocations and inter-splat boundaries using a high-temperature annealing treatment.

However, on the other hand, a high-temperature treatment can lead to remarkable grain growth and more continuous precipitates located at GBs for the C3 deposits [34], which are detrimental for the corrosion resistance. Therefore, when we consider the use of heat treatment to improve the corrosion performance of the CSed coatings, we need to balance many aspects of microstructure changes, such as defects, precipitation, and grain size.

Moreover, our experimental results show that the addition of nano-TiB_2 has a significant influence on the corrosion behavior of the coatings. On the one hand, the immersion tests show that the addition of nano-TiB_2 particles in the 7075Al composite leads to stable oxide films and fewer pits on the corroded surface. Meanwhile, relatively lower E_{corr} values of the composite coatings also indicates a lower corrosion tendency from the view of corrosion thermodynamics compared to those of the pure 7075Al coating. These results indicate a better corrosion resistance of the composite coating in a static state due to the fact that the quality of a passive oxide layer is better than the non-reinforced samples. After immersion in an NaCl solution, oxidation of Al leads to a formation of a protective oxide layer on the surface of the specimens. This oxide layer protects the underlying surface from further corrosion attack. In the TiB_2/7075Al composite, TiB_2 particles on the exposed surface form an oxide layer of $TiO_2 \cdot H_2O$ after immersion in the saltwater solution at room temperature [35]. On the other hand, higher I_{corr} values and much lower R_{ct} values of the composite coating clearly display higher corrosion rates compared to those of the pure 7075Al coating. The literature suggests that the TiB_2 particle is semi-conductive in nature, as it has an electrical resistivity of approximately 15×10^{-6} ohm·cm [36, 37]. Hence, this corrosion behavior of the composites may be due to the galvanic coupling effect between a noble reinforcement (TiB_2) and the much more active Al matrix [37]. This fairly large potential difference between Al and TiB_2 (about 252 mV) can be considered as the cause of galvanic corrosion, especially in the potentiodynamic polarization and EIS tests, where extra current was applied. The presence of galvanic effect between TiB_2 and Al can serve as a cathode site for oxygen reduction or hydrogen. As a result, corrosion progress mainly occurs at GBs with a large amount of TiB_2 particulates and continues into the composite inner. Localized dissolution at the matrix/TiB_2 interfacing producing a localized acidic environment increases the matrix dissolution beneath the oxide layer to form blisters. In favorable conditions, these blisters enlarge and rupture to form a new open pit. Similar corrosion behavior was also reported in the in-situ TiB_2/Al, and in-situ TiB_2/Al-4%Cu, as well as the in-situ TiB_2/AlSi composite systems produced from stir casting [36, 37].

5.7 Effect of heat treatments on microstructure and mechanical properties

5.7.1 Microstructure evolution after heat treatment

As shown in Figure 5-39, the microstructure of the deposits after T6 treatment (470 ℃/70 min solution followed by water quenching and 121 ℃/24 h aging) is dramatically different from that of the as-spray state. The first obvious feature is that the inter-splat boundaries in the as-spayed state disappear or become obscure after T6 treatment as a result of atom diffusion and recrystallization. Moreover, some large pores are still observed in the T6 treated samples. The porosity measurements based on analysis of SEM images reveal that the porosities of the pure 7075Al and TiB_2/7075Al composite samples after T6 treatment are slightly lower than those in the as-spray state, which is shown in Figure 5-40. The T6 composite samples possess lower porosity values than do the pure 7075Al deposits.

Moreover, a more uniform grain structure with a larger grain size (several micrometers) is observed in the samples after T6 treatment. Almost all the ultrafine grains located in the largely deformed regions disappeared and showed remarkable growth after T6 treatment. Clearly, the grain size of the composite

deposit is much smaller than that of the pure 7075Al deposit. Meanwhile, the composite deposits exhibit an equiaxed structure, while an elongated grain structure can still be seen within the pure 7075Al deposits. As shown in Figure 5-39 (d-f), the nanosized TiB_2 particles are uniformly dispersed within the composite deposits.

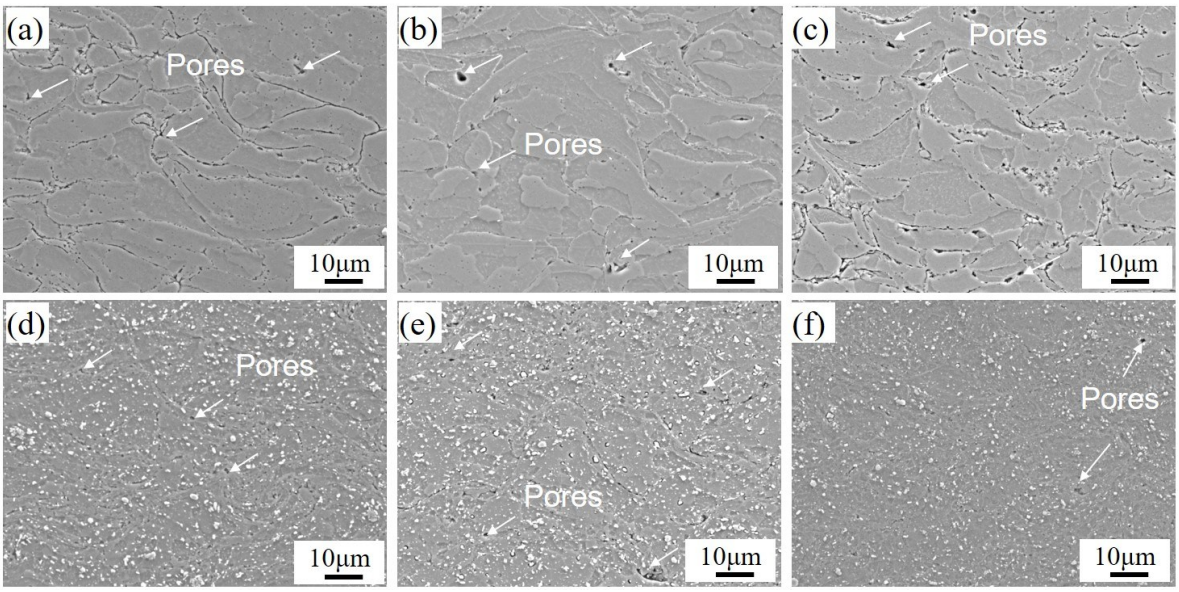

Figure 5-39 Cross-sectional SEM images of the pure 7075Al and TiB_2/7075Al composite deposits after T6 treatment: (a) 7075Al-C1, (b) 7075Al-C2, (c) 7075Al-C3, (d) TiB_2/7075Al-C1, (e) TiB_2/7075Al-C2, (f) TiB_2/7075Al-C3. The pores were indicated by white arrows.

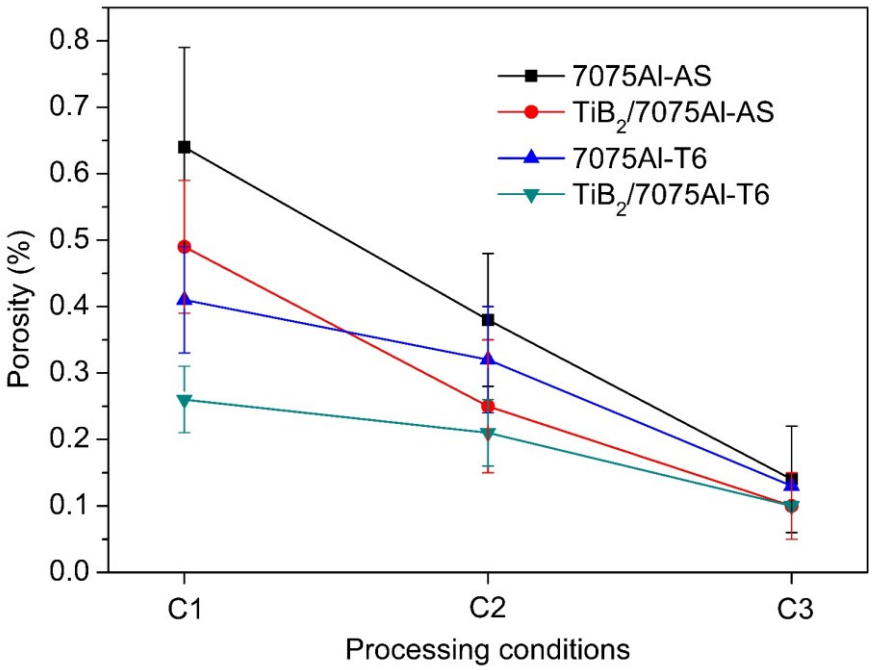

Figure 5-40 Porosity evolution of the deposits after T6 treatment.

In order to further improve the interfacial bonding between splats, the 7075Al-C2 and TiB_2/7075Al-C2 composite deposits were heat-treated by extending the solution duration to 4 h or by adding an annealing treatment (412 ℃ for 4 h) prior T6 treatment. The optical and SEM morphologies of the

deposits heat treated in different conditions are shown in Figure 5-41, Figure 5-43 and Figure 5-44. Compared to the T6 samples, the pure 7075Al deposits after heat treatment with a solution duration for 4 h or pre-annealing at 412 ℃ for 4 h exhibit more significant grain growth, while a significant difference is not found for the composite deposits. It can be noticed that some white needle-like as well as some micron-sized spherical precipitates can be found in both pure 7075Al and TiB_2/7075Al composite deposits after heat treatments. According to the EDS mapping results (Figure 5-45 and Figure 5-46), these needle-like precipitates are mainly composed of Mg, while the spherical precipitates are mainly composed of Cu. However, it is still difficult to determine the specific phases from the EDS mapping results. More detailed studies need to be carried out using TEM.

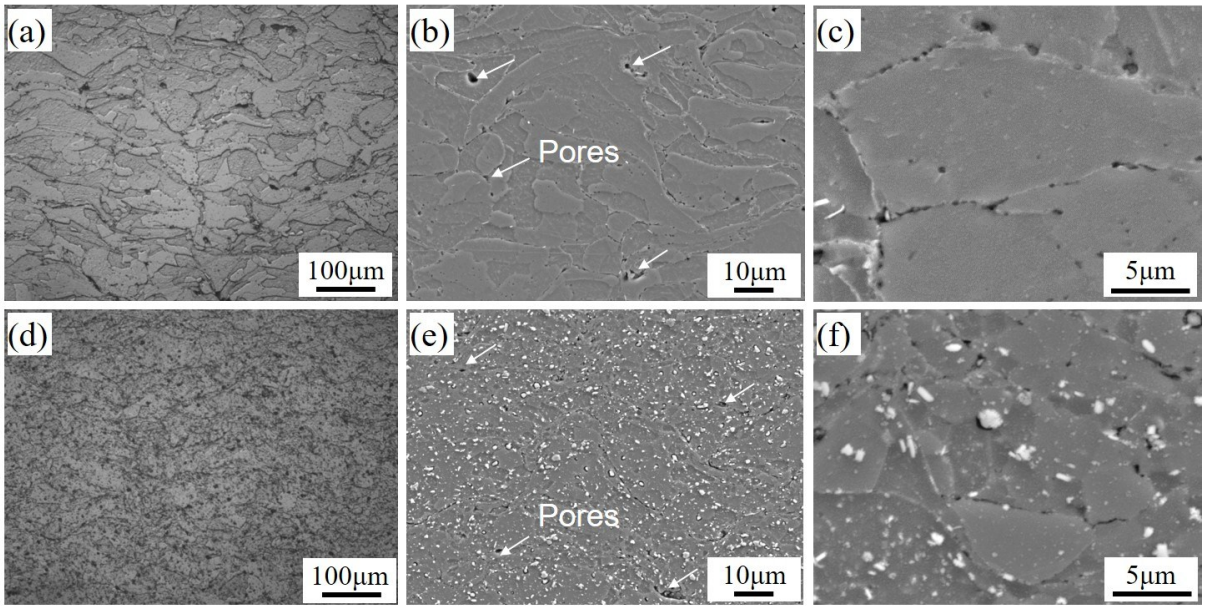

Figure 5-41 Optical and SEM micrographs of the etched cross-section of the (a-c) pure 7075Al-C2 and (d-f) TiB2/7075Al-C2 composite deposits after T6 treatment. (a) and (d) optical micrographs; (b, c) and (e, f) are the SEM images.

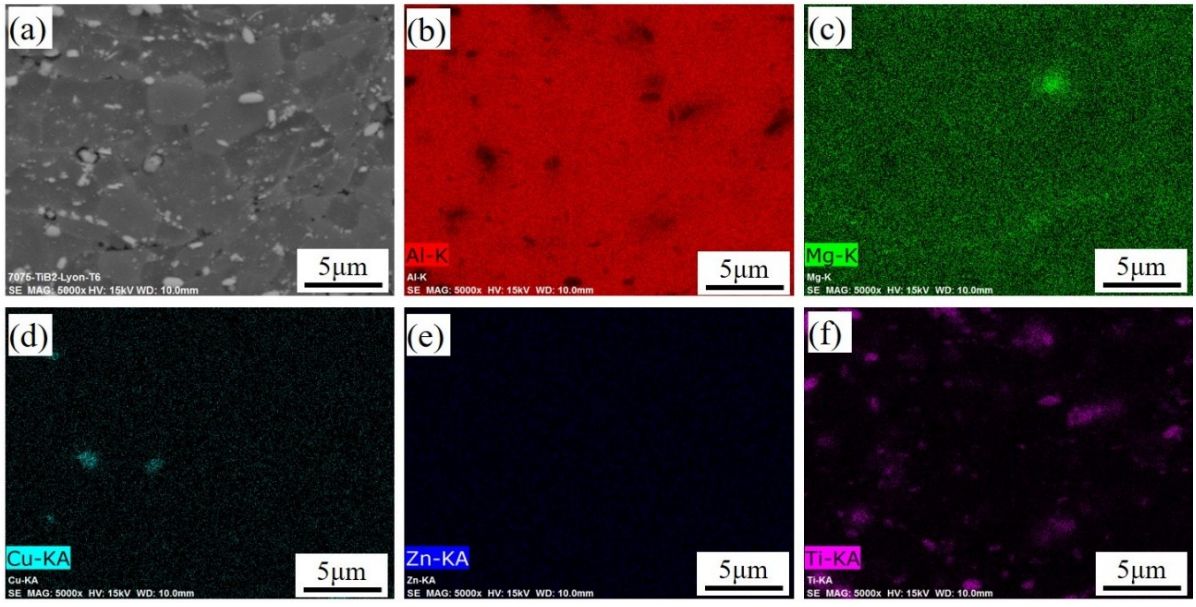

Figure 5-42 EDS mapping of the cross-section of the TiB_2/7075Al composite deposit after T6 treatment.

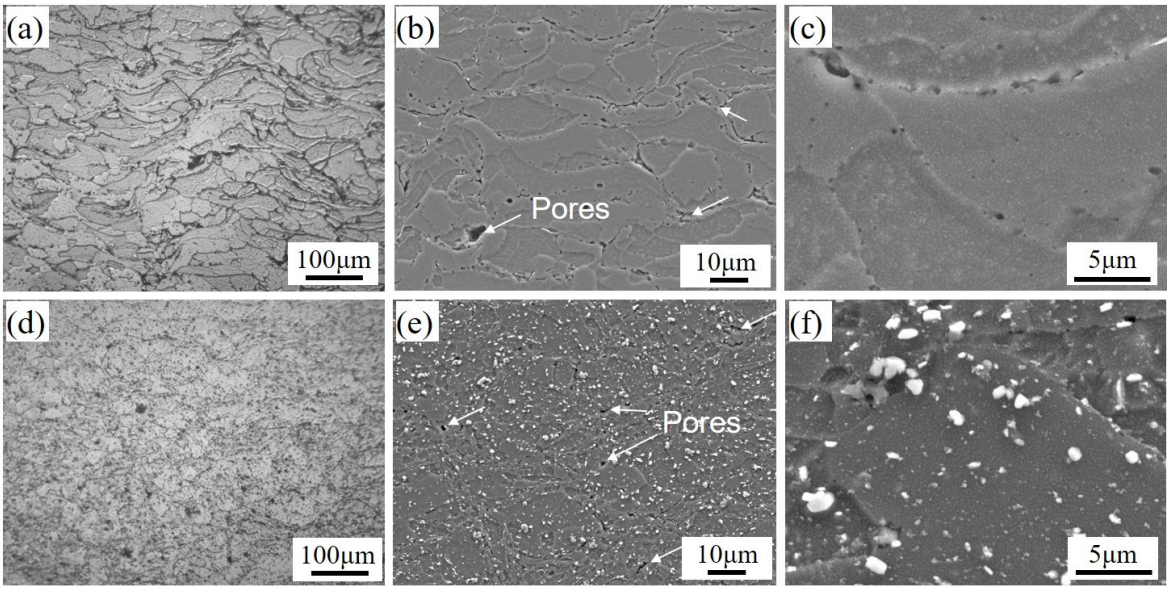

Figure 5-43 Optical and SEM micrographs of the etched cross-section of the (a-c) pure 7075Al-C2 and (d-f) TiB_2/7075Al-C2 composite deposits after 470 ℃/4 h (water quenching) +121 ℃/24 h treatment. (a) and (d) are the optical micrographs; (b, c) and (e, f) are the SEM images.

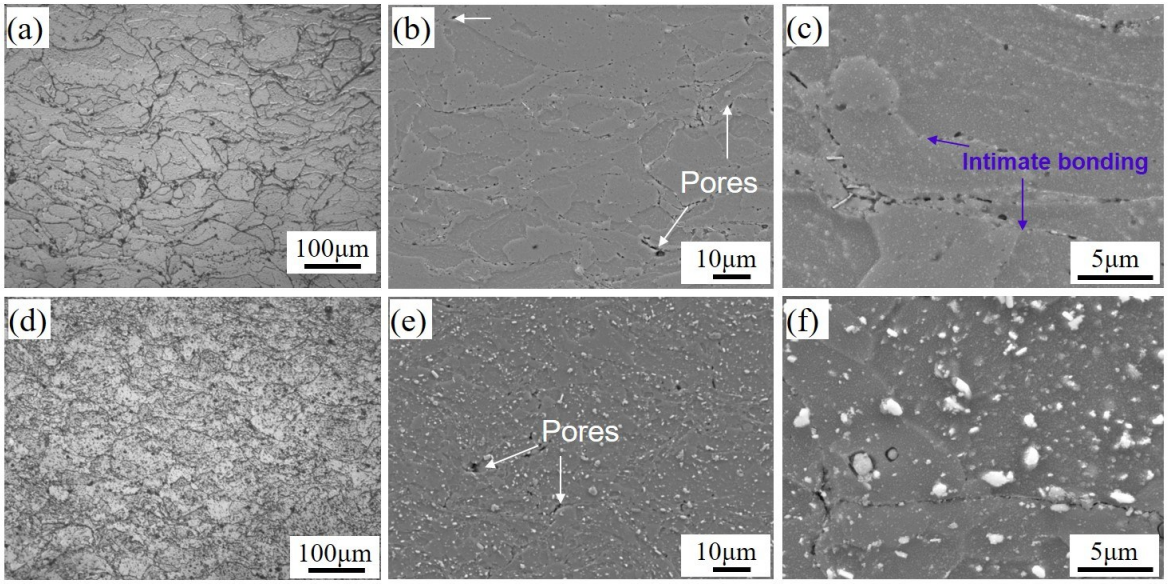

Figure 5-44 Optical and SEM micrographs of the etched cross-section of the (a-c) pure 7075Al-C2 and (d-f) TiB_2/7075Al-C2 composite deposits after 412 ℃/4 h+T6 treatment. (a) and (d) are the optical micrographs; (b, c) and (e, f) are the SEM images.

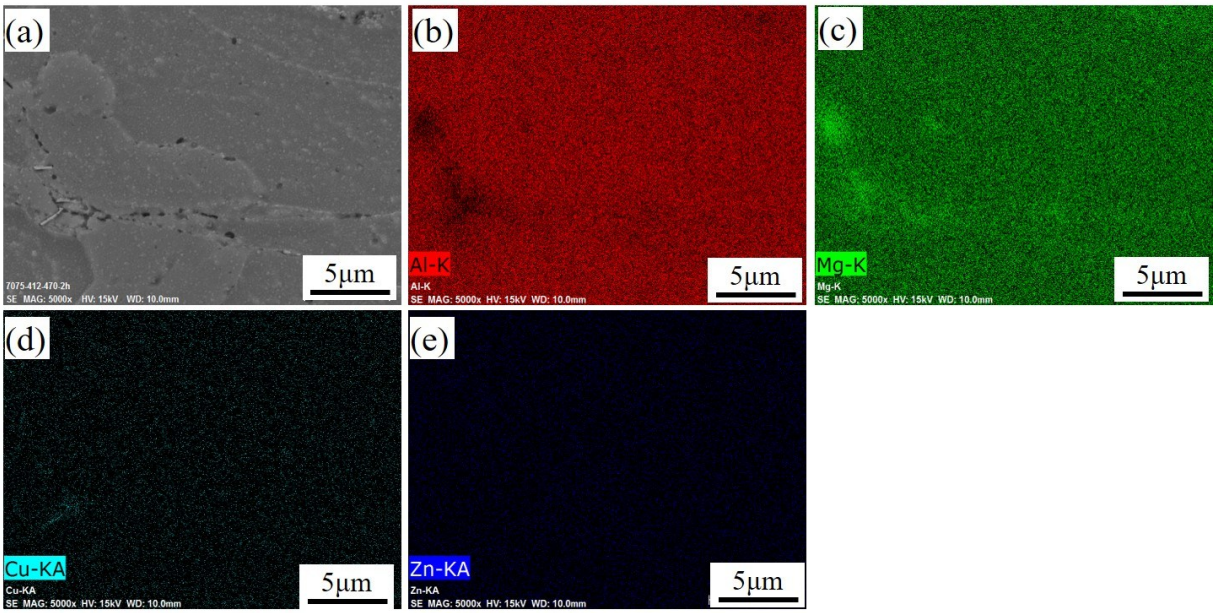

Figure 5-45 EDS mapping of the cross-section of the pure 7075Al-C2 deposit after 412 ℃/4 h + T6 treatment.

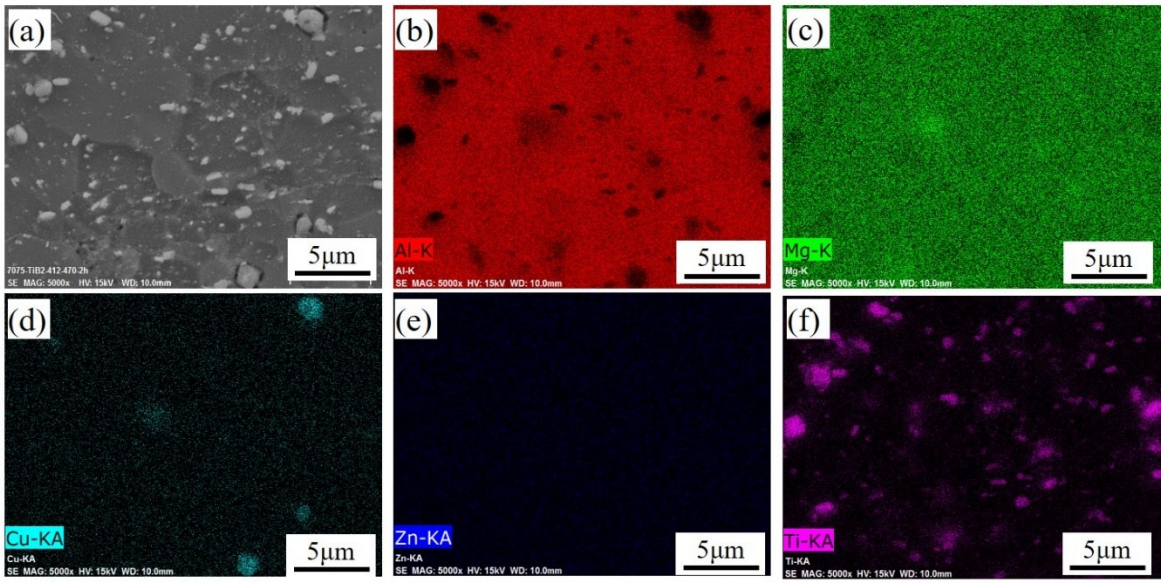

Figure 5-46 EDS mapping of the cross-section of the TiB_2/7075Al-C2 composite deposit after 412 ℃/4 h+T6 treatment.

Figure 5-47 shows the EBSD characterization of the pure 7075Al-C1 and TiB_2/7075Al-C1 composite deposits after T6 treatment. Compared to the microstructure of as-sprayed deposits (Figure 5-23), both the pure 7075Al and TiB_2/7075Al composite deposit show a significant grain growth after T6 treatment. The average grain sizes of the pure 7075Al and composite deposits after T6 treatment are measured to be about 9.4 μm and 4.3 μm, respectively, which demonstrates approximately a tenfold increase compared to the as-spray state. However, a number of fine grains with a size less than 2 μm can be still observed in some specific regions of the composite deposit, where recrystallization and ultrafine grain nucleation could occur during CS deposition. It was reported that the uniformly distributed TiB_2 particle can inhibit grain growth as it can block the migration and movement of GBs [38, 39]. Another distinct feature from the as-sprayed samples is that the T6 samples show high-quality contrast maps and very clear GBs, which indicate little residual stress after T6 treatment.

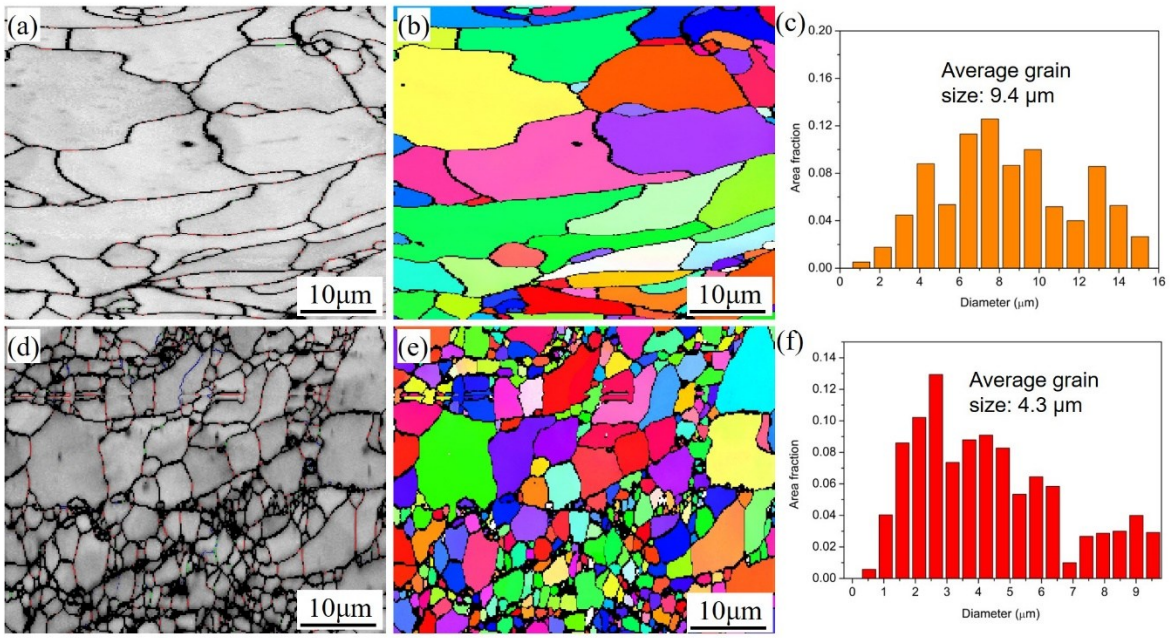

Figure 5-47 EBSD characterization of the (a-c) pure 7075Al-C1 and (d-f) TiB_2/7075Al-C1 composite deposits after T6 treatment: (a) and (d) band contrast; (b) and (e) IPF mapping; (c) and (f) grain size distribution.

Figure 5-48a shows the TEM BF images of the TiB_2/7075Al-C1 composite sample after T6 treatment. The microstructure features equiaxed large grains (>500 nm), of which no dislocation lines but a high number density of nano precipitates can be observed. As can be seen from the magnified TEM images in Figure 5-48b, these precipitates are of a near-spherical shape with sizes are in the range of 10–60 nm, which have been confirmed to be η phase based on previous studies [40]. These nano precipitates will contribute significantly to the enhancement of the mechanical properties of the composite, as well as the pure 7075Al deposits (the TEM results are not shown here). However, as illustrated in Figure 5-48c and d, the T6 treated TiB_2/7075Al-C3 composite sample displays a completely different structure compared to the TiB_2/7075Al-C1 sample. It can be noted that few precipitates are formed within the grain matrix, while some dislocation walls are still visible. This phenomenon indicates that the abundant η/ η' precipitates formed during CS deposition is dissolved into the Al matrix during the solution treatment, but new phases cannot be precipitated during the aging treatment. Normally, dissolution and re-precipitation could take place when repeating the solution and aging treatment for the 7075Al alloy. However, in the case of the TiB_2/7075Al-C3 composite, precipitation is suppressed using T6 treatment. More attention will be paid on the chemical composition and stability of the precipitates formed during CS deposition to look insight into the reasons why the precipitation phase is suppressed during T6 treatment.

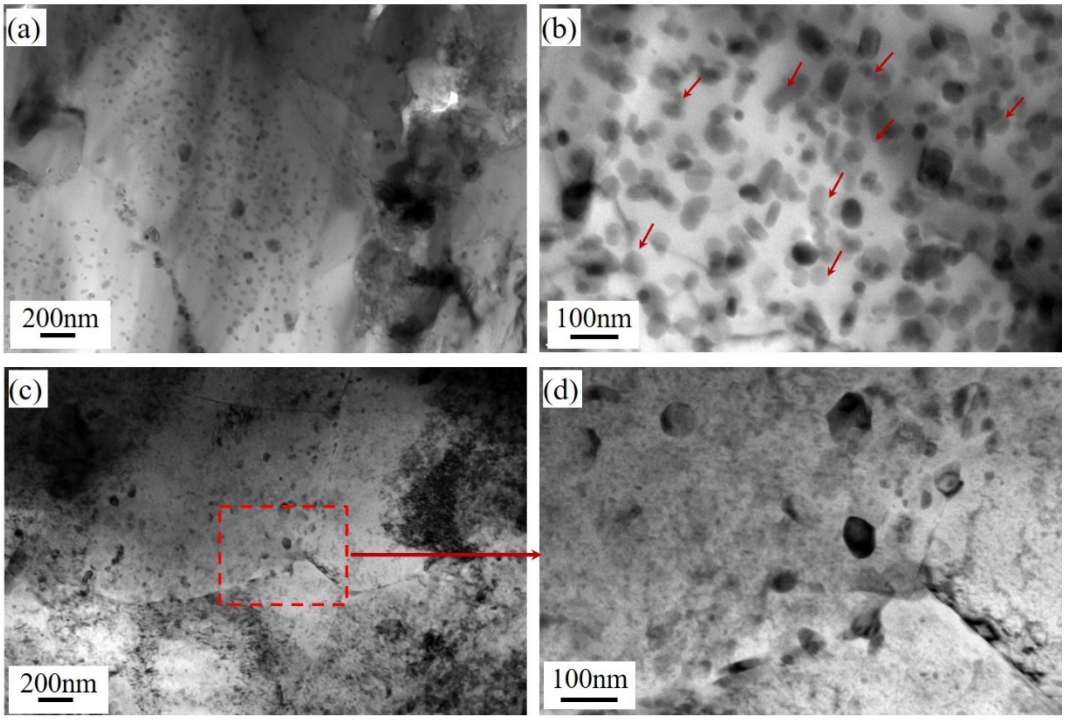

Figure 5-48 TEM micrographs of the (a, b) TiB_2/707Al-C1 and (c, d) TiB_2/707Al-C3 composite samples after T6 treatment.

5.7.2 Mechanical properties after heat treatment

Microhardness tests were conducted on the cross-section of the polished samples and the average values are given in Table 5-8. Both the pure 7075Al and TiB_2/7075Al composite deposits show significant microhardness enhancement after T6 treatment. The microhardness of pure 7075Al-C1 and C2 deposits after T6 treatment reach 156 $HV_{0.3}$ and 158 $HV_{0.3}$, showing an increment of 32.2% and 19.7% compared to those in the as-sprayed state, respectively. A higher value of 178 $HV_{0.3}$ was obtained for the TiB_2/7075Al-C1 and C2 composite deposits after T6 treatment, which shows an increment of 14.0% compared to that of T6 treated pure 7075Al deposits and increments of 32.8% and 17.9% compared to those of TiB_2/7075Al-C1 and C2 composite deposits in as-sprayed states. In the cases of C1 and C2 deposits, the microhardness after T6 treatment seems to be independent of the initial state of the deposit (C1 or C2). However, an unexpected phenomenon was found in the case of C3 deposits, where the microhardness of the pure 7075Al and TiB_2/7075Al composite deposits decreased from 146 $HV_{0.3}$ and 165 $HV_{0.3}$ to 140 $HV_{0.3}$ and 138 $HV_{0.3}$, respectively. The T6 treatments are useless for improving the microhardness of the C3 deposits.

The influence of aging time on the microhardness evolution of the C1 and C3 deposits was investigated by using oil bath heating. Prior to aging treatments, the samples were solution treated at 470 ℃ for 70 min under an Ar protective atmosphere followed by water quenching. The microhardness evolution of the deposits as a function of aging time is presented in Figure 5-49. The average microhardness values of pure 7075Al-C1 and TiB_2/7075Al-C1 composite deposits after solution treatment (without aging) are about 136 $HV_{0.3}$ and 156 $HV_{0.3}$, respectively, which are slightly higher than those in as-sprayed states. These results indicate that a part of precipitates is already formed during water quenching or the natural aging period. Then the values increase gradually with the increase of aging time as the precipitation gradually increases. The microhardness of the pure 7075Al deposit reaches the highest value of 175 $HV_{0.3}$ after it has been aging for 28 h, while the highest value (196 $HV_{0.3}$) of the composite deposit is obtained for an aging duration of 24 h. Afterwards, their

microhardness values decreased gradually until 40 h, which should be attributed to the coarsening of the precipitates. When the aging time is further prolonged from 40 h to 48 h, both the deposits exhibit a slight decrease in microhardness.

Table 5-8 The properties of the deposits after heat treatment at different conditions.

Material	Heat treatment conditions	Porosity (%)	Microhardness ($HV_{0.3}$)	UTS (MPa)	Elongation (%)
7075Al-C1	T6	0.41±0.08	156±5	360±45	2.8±0.8
TiB_2/7075Al-C1	T6	0.26±0.05	179±6	448±54	2.1±0.4
7075Al-C2	T6	0.32±0.08	158±8	342±36	1.3±0.5
TiB_2/7075Al-C2	T6	0.21±0.05	178±7	403±46	1.1±0.4
7075Al-C3	T6	0.22±0.06	140±4	-	-
TiB_2/7075Al-C3	T6	0.14±0.03	138±3.6	-	-
7075Al-C2	470 ℃/4h+121℃/24h	0.46±0.08	159±6	-	-
TiB_2/7075Al-C2	470 ℃/4h+121℃/24h	0.35±0.06	181±4.2	-	-
7075Al-C2	412 ℃/4 h+T6	0.49±0.08	162±5	346±39	2.2±0.8
TiB_2/7075Al-C2	412 ℃/4 h+T6	0.38±0.08	191±4.3	411±52	1.8±0.6
7075Al-C3	412 ℃/4 h	0.21±0.06	128±3.1	225±40	6.4±1.2
TiB2/7075Al-C3	412 ℃/4 h	0.15±0.03	142±3.5	275±38	8.8±1.4

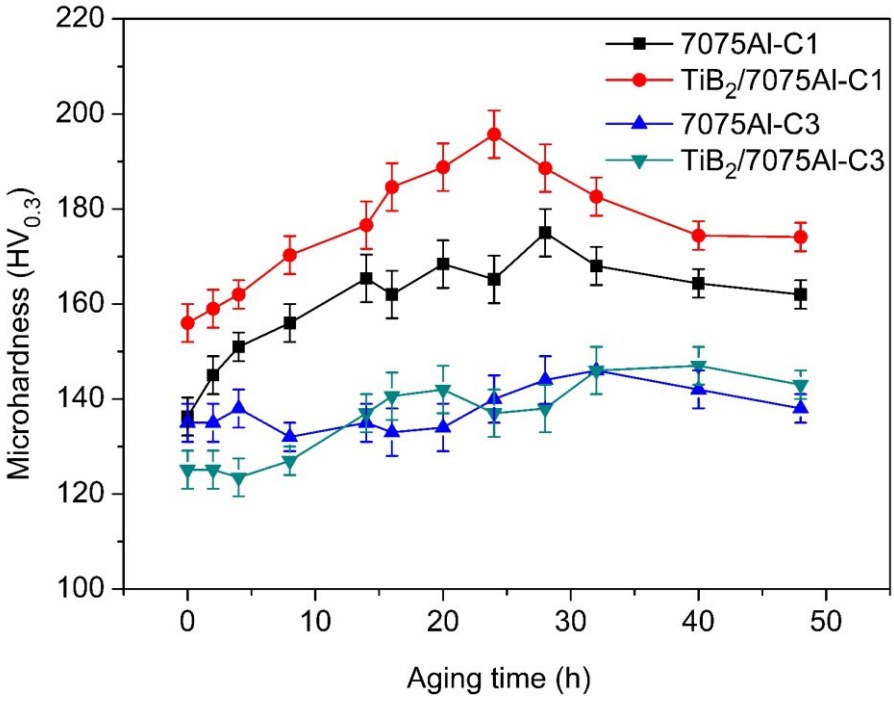

Figure 5-49 Microhardness evolution of the deposits as a function of aging duration.

However, a completely different microhardness evolution is found for the C3 deposits. The microhardness of both deposits seems to be independent of aging time. Further, the microhardness values of both deposits are much lower than those in the as-sprayed states. Moreover, the composite

deposits possess similar or even lower values than those of pure 7075Al-C3 deposits. One possible reason for this phenomenon is that the precipitation was completed or nearly completed during the CS deposition in C3. As presented in Figure 5-26c and d, an extensive precipitates are already formed during the CS deposition as a result of severe plastic deformation. These precipitates were dissolved into the Al matrix but failed to precipitate out after aging treatment. The removal of work hardening effect and grain growth during solution treatment also result in the decrease of microhardness. Therefore, the microhardness of the C3 deposits cannot be affected by extending the aging time.

The tensile tests of the deposits after heat treatments were carried out, and their UTS and elongation values are summarized in Table 5-8. Compared to the as-sprayed samples, both the pure 7075Al and TiB_2/7075Al composite deposits (C1 and C2) exhibit slight improvement in tensile strength and elongation after T6 treatment. The UTS and elongation of the TiB_2/7075Al-C1 composite reach 448 MPa and 2.1%, respectively. Lower tensile properties with a UTS of 403 MPa and an elongation of 1.4% were obtained for the T6 treated C2 deposits. Nevertheless, the enhancement in the mechanical performance of the CSed deposits using T6 treatment is still very limited. In order to further enhance the particle-particle bonding by atom diffusion, the C2 deposits were annealed at 412 ℃ for 4 h followed by T6 treatment. However, the tensile tests show only a slight improvement in UTS and elongation by adding the annealing procedure compared to those only using T6 treatment.

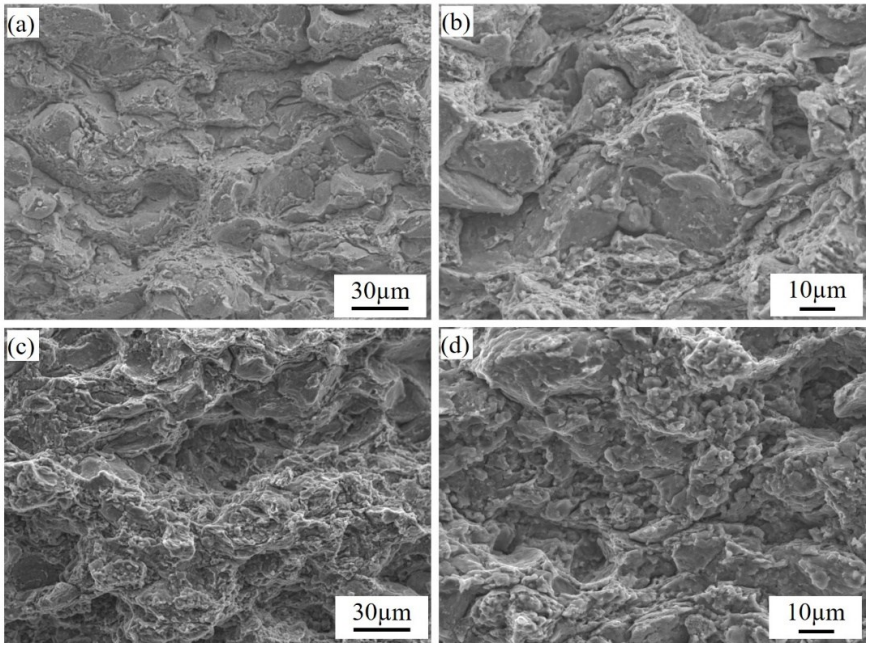

Figure 5-50 The fracture morphologies of the TiB_2/7075Al composite deposits after T6 treatment: (a) and (b) TiB_2/7075Al-C1; TiB_2/7075Al-C2.

SEM observation of the tensile fractured surface was performed to further understand the fracture mechanisms of the deposits after heat treatments. Figure 5-50 presents the fracture morphologies of the TiB_2/7075Al-C1 and C2 composite deposits after T6 treatment. It can be noticed that fractures primarily occurred through intergranular, but some fractures still took place along the inter-splat boundaries, which are similar to the fracture morphologies observed from the as-sprayed deposits. In comparison with the as-sprayed samples, more dimples are observed on the fractured surface of the T6 treated samples implies the enhancement of interface bonding by atom diffusion during T6 treatment. However, T6 treatment still failed to heal some poorly bonded regions or pores, which are the initial sites for fracturing or cracking during the tensile test. However, fewer dimples but more defects observed on the fractured surface of the T6 treated C2 deposit (Figure 5-50c and d) could lead to lower tensile properties.

Moreover, as shown in Figure 5-51, the deposit after pre-annealing and T6 treatments presents a similar facture morphology compared to that of theT6 state, which suggests that extending heat treatment duration does not effectively improve the tensile properties of the deposits. Nevertheless, the quality of the as-sprayed deposits is also important to achieve good mechanical performance of the final components.

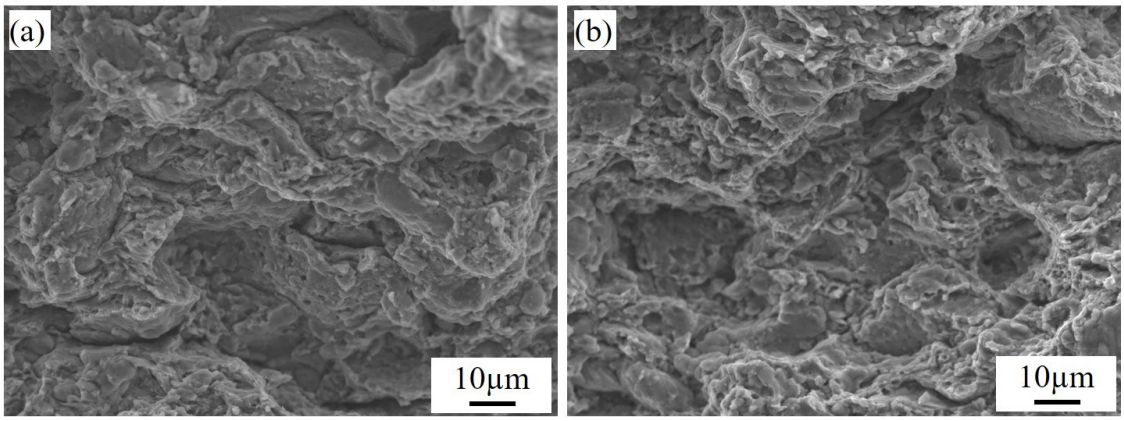

Figure 5-51 The fracture morphologies of the TiB_2/7075Al composite deposits after 412 ℃/4 h + T6 treatment: (a) 7075Al-C2; (b) TiB_2/7075Al-C2.

It is worth noticing that T6 treatments performed on the C3 deposits failed as a number of large bubbles formed not only on the surface but also in the center of the tensile samples after the solution and water quenching treatments. The morphologies of these bubbles are shown in Figure 5-52. It can be clearly observed from the cross-sectional view that the deposits split from the middle and arch upward to form a large gap or cavity with a diameter as large as 500 μm. Moreover, as shown in Figure 5-52b, some small gaps or pores are also observed around the large bubbles. The top-view after polishing with SiC papers presents a lot of individual fractured particles within such a large cavity. There are three possible factors for the formation of such large bubbles. First, residual stress is released during the heat treatment or water quenching. Second, certain elements like Zn or Mg evaporate during the high temperature solution treatment to form bubbles. Third, He dissolved in the deposit during the CS process escapes to form bubbles after high temperature treatment.

In order to verify these assumptions, a series of heat treatments on the C3 deposits having a of size of (15×15 μm) were performed using different conditions, as listed in Table 5-9. The experimental results show that the bubbles formed independently of the furnace atmosphere and quenching medium, which represents different cooling rate. However, it was found that bubbles started to form when the heat treatment temperature was increased to 450 ℃. Therefore, it is speculated that stress released during heat treatment may not be the cause of the bubble formation. Furthermore, the C1 samples were also heat treated using the same conditions for comparison, but no bubbles were found. Therefore, the second factor-evaporation of certain elements like Zn or Mg during solution treatment, can be eliminated.

One possible hypothesis for the formation of these obvious bubbles within the heat treated samples is that the He atoms would dissolve into the solid deposits during CS processing, and then they would escape and aggregate after high temperature treatment. Because the C3 samples were processed under a completely enclosed He atmosphere system, the fresh metals of the deformed particles as a result of ASI were exposed to such a He atmosphere. The small He atoms would embed in the fresh metals and be trapped at vacancies because of their high binding energy [41]. The embedded He atoms would migrate and aggregate to form bubbles when the samples were heat treated at a relative high temperature. Further investigation will be carried out to evaluate whether He could be dissolved in the deposit and lead to the formation of the bubble after high-temperature treatment.

Another possible reason for the formation of these bubbles could be the moisture of the powder. During production, storage or handling of the powder, moisture is deposited on the powder surface. According to Weingarten et. al [42], the hydrogen amount strapped in the powder material can reach as high as 14.8 ml/100g. The hydrogen is stored in the coating along with the powder particles. As the heating temperature increases, the strength of the Al alloy decreases, and the coating is fractured by the explosion of the hydrogen gas, forming big bubbles. Big bubbles only observed on the He-processed samples after heat treatment. This possibly due to the fact that the He-processed samples are so dense that the hydrogen cannot escape from the coatings at low temperature. However, the C1 and C2 samples have some pores which can provide channels for the hydrogen during heat treatment. As a result, big bubbles are not observed in these samples. Therefore, more tests are needed to measure the hydrogen contents of the powder as well as the coatings.

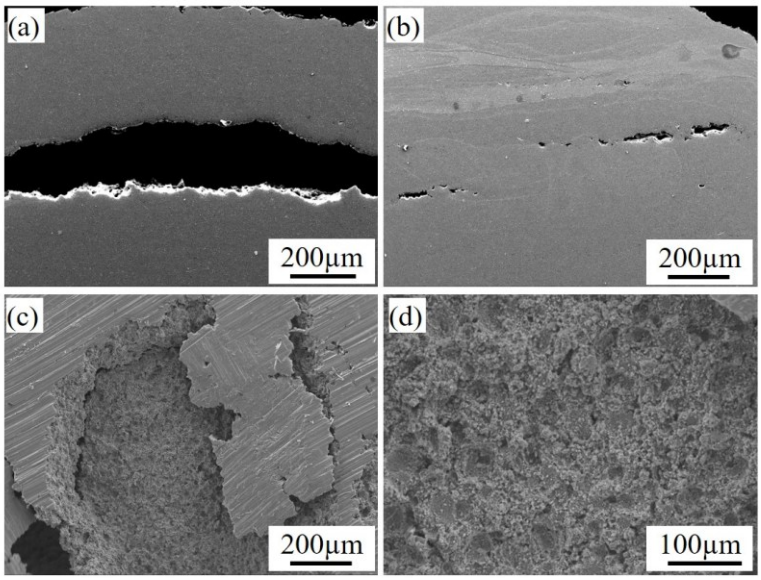

Figure 5-52 SEM morphologies of the TiB_2/7075Al-C3 composite deposit after T6 treatment.

Table 5-9 Summary of the effect of heat treatments on bubble formation of C3 deposits.

HT conditions	bubbles	Remarks
470 ℃/70 min + water quenching (Ar atmosphere)	Yes	
470 ℃/70 min + air cooling (Ar atmosphere)	Yes	
470 ℃/70 min + furnace cooling (Ar atmosphere)	Yes	
470 ℃/70 min + air cooling (vacuum)	Yes	
460 ℃/70 min + water quenching (Ar atmosphere)	Yes	
450 ℃/70 min + water quenching (Ar atmosphere)	Yes	Small bubbles
440 ℃/70 min + water quenching (Ar atmosphere)	No	

5.8 Reinforced mechanisms

The microhardness and tensile tests show that the composite components possess higher microhardness and tensile strength compared to the unreinforced pure 7075Al deposits (Figure 5-28). The microhardness and strength increments of the composite deposits may be mainly attributed to the following three factors: 1) the composite deposits possess a denser structure than the unreinforced 7075Al deposits; 2) grain refinement due to the presence of TiB_2 nanoparticles during the gas atomization and static recovery resulting from severe plastic deformation during CS deposition; and 3) the strengthening effect of uniformly distributed nanosized TiB_2 particles in Al matrix.

The strengthening effect resulting from grain refinement (Hall-Petch equation) can be expressed as follows:

$$\Delta H_{Hall-Petch} = k\left(d^{-\frac{1}{2}} - d_o^{-\frac{1}{2}}\right) \qquad (5\text{-}2)$$

Where k is the Hall-Petch slope (a constant), and d and d_o are the average grain size of the TiB_2/7075Al composite and the unreinforced 7075Al deposit, respectively. According to the previous study [43], the Hall-Petch slope k of 7075Al alloy is ~0.12 MPa/$\sqrt{m}$ when only the grain size effect is considered. Based on the previous EBSD analysis, the average grain sizes of the CS composite samples were measured to be around 0.695 μm and 0.525 μm for C1 and C3, respectively, which are much smaller than those of as-sprayed pure 7075Al deposits. The values related to grain refinement strengthening for the unreinforced 7075Al alloy and TiB_2/7075Al composite are 35.8 HV (122 MPa) and 42.0 HV (144 MPa) at C1, and 40.8 HV (139 MPa) and 48.5 HV (165 MPa) at C3, respectively. Therefore, it is obvious that grain refinement is one of the primary mechanisms for improving the microhardness and strength of the as-sprayed composite samples.

Additionally, the uniformly distributed nanosized TiB_2 particles play an important role in the enhancement of microhardness and strength in the as-sprayed composite samples. The increment of microhardness or strength resulting from Orowan strengthening can be described by the Orowan-Ashby equation [44]:

$$\Delta H_{Orowan} = \frac{0.13Gb}{\lambda}\ln\left(\frac{D}{2b}\right) \qquad (5\text{-}3)$$

where G is the matrix shear modulus (~26.9 GPa for the 7075Al matrix) [44], b is the Brugers vector (0.286 nm) [45], D is the average diameter of the reinforcement (~300 nm), and λ is the interparticle spacing, which can be expressed as follows [44]:

$$\lambda = D\left[\left(\frac{1}{2V_P}\right)^{1/3} - 1\right] \qquad (5\text{-}4)$$

where V_p is the volume fraction of reinforced particles (~4.2 vol.% TiB_2).

Combining Eq. (5-3) and (5-4), an increase of 4.7 HV (15.8 MPa) is obtained in the present TiB_2/7075Al composite due to the Orowan strengthening effect. In addition, the formation of nanosized precipitates in the TiB_2/7075Al composite can further enhance the microhardness and strength due to the Orowan strengthening mechanism, especially for the samples after solution aging treatment. Nevertheless, the as-sprayed and heat-treated samples still exhibit very low ductility values even though pre-annealing followed by the T6 treatment was applied. This could be mainly attributed to the fact that the defects such as pores and poor inter-splat bonding within the deposits were not successfully eliminated using heat treatment. Therefore, the initial bonding state of the CSed deposits plays a decisive role in the final mechanical properties. Unfortunately, heat treatment of the He-processed samples was

not successful as many bubbles formed within the samples. Our future works will focus on the formation mechanism of these bubbles.

5.9 Summary

A novel gas-atomized 7075Al composite powder reinforced with nanosized in-situ TiB_2 particles was used as the feedstock to fabricate composite components by CS. The investigation of the processing conditions and heat treatment on composite component porosity, microstructure, and mechanical properties was carried out, and pure 7075Al deposits were also fabricated for comparison. Besides, the corrosion behavior of the CSed composite coatings was investigated exhaustively using Tafel polarization, electrochemical impedance spectroscopy and immersion tests under 0.1 M and 0.6 M NaCl solutions. Particle plastic deformation behavior was investigated by combining single particle deposition experiments and FEA simulation. Furthermore, the influence of heat treatment on the microstructure and mechanical properties was also studied. The main conclusions are as follows:

(1) Fully dense and thick TiB_2/7075Al composite deposits with uniformly distributed nanosized TiB_2 particles were successfully fabricated by CS.
(2) Phase analysis in terms of XRD shows that as-fabricated samples possess a well-retained phase composition compared to the feedstock powders; However, TEM analysis reveals that nanosized precipitates are formed inside the severely deformed grains as well as at the GBs. A greater plastic deformation resulting from a higher particle impact velocity could result in a remarkably higher density of precipitates in the C3 deposit.
(3) A higher particle impact velocity and temperature lead to a denser structure and greater particle deformation, enhancing metallic bonding between deformed splats and grain refinement. Consequently, higher microhardness, lower wear rate, and higher tensile strength were acquired. The addition of TiB_2 nanoparticles improves the microhardness, wear resistance and tensile strength of the composite deposits, but makes no difference to the adhesion strength.
(4) The fracture morphologies of the as-sprayed composite samples display a brittle feature, which indicates limited metallurgical bonding at the deformed splats even though He was used as the propelling gas.
(5) Electrochemical tests revealed that the TiB_2/7075Al composite coatings possess a lower corrosion tendency from the view of corrosion thermodynamics, which is considered to be primarily due to the TiB_2 particles on the exposed surface forming a defective oxide layer of $TiO_2 \cdot H_2O$ after immersion in the saltwater solution. However, galvanic corrosion between noble TiB_2 reinforcements and the more active Al matrix results in a higher corrosion rate of the composite coating compared to the pure 7075Al coating.
(6) Relatively greater plastic deformation of the particles in the He-processed samples (C3 deposits) results in inferior corrosion resistance compared to the air-processed samples due to the greater generation of defects and precipitates within the samples. A low-temperature annealing treatment is beneficial for the corrosion resistance of the CSed coating due to the reduced dislocations. However, evident grain growth produced by a high-temperature annealing treatment can have a detrimental effect on the corrosion resistance of the coatings.
(7) FEA simulation and single particle deposition revealed that compared to the pure 7075Al particle, the TiB_2/7075Al composite particle experienced less plastic deformation when impacting onto the pure Al substrate, but few differences were found when they were sprayed onto 7075Al-T6 substrate. The plastic deformation behaviour of the particles depends on the impact velocity and temperature, as well as the hardness of the substrates.
(8) The microhardness of the 7075Al-C1 and TiB_2/7075Al-C1 composite deposits can be largely improved by solution-aging treatment due to the formation of abundant precipitates in the Al

matrix. However, the precipitation behavior of the C3 samples was suppressed during solution-aging treatment, probably because the precipitates formed as a result of severe plastic deformation during CS deposition are stable and could not re-dissolve well into the matrix to form a saturated solid solution. However, more detailed characterizations are necessary to further investigate the related precipitation mechanisms.

(9) In addition, it was found that applying post-heat treatments did not significantly improve the tensile properties, and a brittle feature was still observed on the fractured surface of the heat-treated tensile samples. Interestingly, some large bubbles are presented in the He-processed deposits after the solution treatment. However, the formation mechanisms of these bubbles are still unknown.

(10) The grain refinement effect and Orowan strengthening mechanism result from the uniform distribution of TiB_2 nanoparticles and the precipitation of η/η´ should be responsible for the improved microhardness and strength of the TiB_2/7075Al composite.

References of Chapter V

[1] Shuo Yin, Pasquale Cavaliere, Barry Aldwell, Richard Jenkins, Hanlin Liao, Wenya Li, Rocco Lupoi, Cold spray additive manufacturing and repair: Fundamentals and applications, Addit. Manuf., 21 (2018), 628-650.
[2] Tobias Schmidt, Frank Gärtner, Hamid Assadi, Heinrich Kreye, Development of a generalized parameter window for cold spray deposition, Acta Mater., 54 (2006), 729-742.
[3] H Assadi, I Irkhin, H Gutzmann, F Gärtner, M Schulze, M Villa Vidaller, T Klassen, Determination of plastic constitutive properties of microparticles through single particle compression, Advanced Powder Technology, 26 (2015), 1544-1554.
[4] Kicheol Kang, Juyeon Won, Gyuyeol Bae, Sangmin Ha, Changhee Lee, Interfacial bonding and microstructural evolution of Al in kinetic spraying, J. Mater. Sci., 47 (2012), 4649-4659.
[5] CY Dan, Z Chen, G Ji, SH Zhong, Y Wu, F Brisset, HW Wang, V Ji, Microstructure study of cold rolling nanosized in-situ TiB2 particle reinforced Al composites, Mater. Des., 130 (2017), 357-365.
[6] R Ferragut, A Somoza, A Tolley, Microstructural evolution of 7012 alloy during the early stages of artificial ageing, Acta Mater., 47 (1999), 4355-4364.
[7] DeIasi Richard, Philip N Adler, Calorimetric studies of 7000 series aluminum alloys: I. Matrix precipitate characterization of 7075, Metallurgical Transactions A, 8 (1977), 1177-1183.
[8] George E Totten, D Scott MacKenzie, Handbook of aluminum: vol. 1: physical metallurgy and processes, CRC press, 2003.
[9] A Deschamps, F De Geuser, Zenji Horita, S Lee, G Renou, Precipitation kinetics in a severely plastically deformed 7075 aluminium alloy, Acta Mater., 66 (2014), 105-117.
[10] MR Rokni, CA Widener, GA Crawford, Microstructural evolution of 7075 Al gas atomized powder and high-pressure cold sprayed deposition, Surf. Coat. Technol., 251 (2014), 254-263.
[11] YH Zhao, XZ Liao, Z Jin, RZ Valiev, Yu T Zhu, Microstructures and mechanical properties of ultrafine grained 7075 Al alloy processed by ECAP and their evolutions during annealing, Acta Mater., 52 (2004), 4589-4599.
[12] Yidong Zhang, Shenbao Jin, Patrick W Trimby, Xiaozhou Liao, Maxim Y Murashkin, Ruslan Z Valiev, Jizi Liu, Julie M Cairney, Simon P Ringer, Gang Sha, Dynamic precipitation, segregation and strengthening of an Al-Zn-Mg-Cu alloy (AA7075) processed by high-pressure torsion, Acta Mater., 162 (2019), 19-32.
[13] Keiichiro Oh-Ishi, Kaveh Edalati, Hyoung Seop Kim, Kazuhiro Hono, Zenji Horita, High-pressure torsion for enhanced atomic diffusion and promoting solid-state reactions in the aluminum–copper system, Acta Mater., 61 (2013), 3482-3489.
[14] Onur Meydanoglu, Bertrand Jodoin, E Sabri Kayali, Microstructure, mechanical properties and corrosion performance of 7075 Al matrix ceramic particle reinforced composite coatings produced by the cold gas dynamic spraying process, Surf. Coat. Technol., 235 (2013), 108-116.
[15] JM Shockley, HW Strauss, RR Chromik, N Brodusch, R Gauvin, E Irissou, J-G Legoux, In situ tribometry of cold-sprayed Al-Al2O3 composite coatings, Surf. Coat. Technol., 215 (2013), 350-356.
[16] Yongshan Tao, Tianying Xiong, Chao Sun, Huazi Jin, Hao Du, Tiefan Li, Effect of α-Al2O3 on the properties of cold sprayed Al/α-Al2O3 composite coatings on AZ91D magnesium alloy, Appl. Surf. Sci., 256 (2009), 261-266.
[17] Qiang Wang, Kevin Spencer, Nick Birbilis, Ming-Xing Zhang, The influence of ceramic particles on bond strength of cold spray composite coatings on AZ91 alloy substrate, Surf. Coat. Technol., 205 (2010), 50-56.
[18] K Spencer, DM Fabijanic, M-X Zhang, The use of Al–Al2O3 cold spray coatings to improve the surface properties of magnesium alloys, Surf. Coat. Technol., 204 (2009), 336-344.

[19] Mica Grujicic, CL Zhao, WS DeRosset, D Helfritch, Adiabatic shear instability based mechanism for particles/substrate bonding in the cold-gas dynamic-spray process, Mater. Des., 25 (2004), 681-688.
[20] Shuo Yin, Xiaofang Wang, Xinkun Suo, Hanlin Liao, Zhiwei Guo, Wenya Li, Christian Coddet, Deposition behavior of thermally softened copper particles in cold spraying, Acta Mater., 61 (2013), 5105-5118.
[21] Yingchun Xie, Marie-Pierre Planche, Rija Raoelison, Philippe Hervé, Xinkun Suo, Pengjiang He, Hanlin Liao, Investigation on the influence of particle preheating temperature on bonding of cold-sprayed nickel coatings, Surf. Coat. Technol., 318 (2017), 99-105.
[22] Sieglind Ngai, Tungwai Ngai, Florian Vogel, William Story, Gregory B Thompson, Luke N Brewer, Saltwater corrosion behavior of cold sprayed AA7075 aluminum alloy coatings, Corros. Sci., 130 (2018), 231-240.
[23] JJ Pang, FC Liu, J Liu, MJ Tan, DJ Blackwood, Friction stir processing of aluminium alloy AA7075: microstructure, surface chemistry and corrosion resistance, Corros. Sci., 106 (2016), 217-228.
[24] Yan Liu, Shuyi Li, Yaming Wang, Huiyuan Wang, Ke Gao, Zhiwu Han, Luquan Ren, Superhydrophobic and superoleophobic surface by electrodeposition on magnesium alloy substrate: wettability and corrosion inhibition, Journal of colloid and interface science, 478 (2016), 164-171.
[25] Kang Yang, Wenya Li, Yaxin Xu, Xiawei Yang, Using friction stir processing to augment corrosion resistance of cold sprayed AA2024/Al2O3 composite coatings, J. Alloys Compd., 774 (2019), 1223-1232.
[26] Yongshan Tao, Tianying Xiong, Chao Sun, Lingyan Kong, Xinyu Cui, Tiefan Li, Guang-Ling Song, Microstructure and corrosion performance of a cold sprayed aluminium coating on AZ91D magnesium alloy, Corros. Sci., 52 (2010), 3191-3197.
[27] Ying-Kang Wei, Xiao-Tao Luo, Yi Ge, Xin Chu, Guo-Sheng Huang, Chang-Jiu Li, Deposition of fully dense Al-based coatings via in-situ micro-forging assisted cold spray for excellent corrosion protection of AZ31B magnesium alloy, J. Alloys Compd., 806 (2019), 1116-1126.
[28] Alexandre Goloborodko, Tsutomu Ito, Xiaoyong Yun, Yoshinobu Motohashi, Goroh Itoh, Friction stir welding of a commercial 7075-T6 aluminum alloy: grain refinement, thermal stability and tensile properties, Mater. Trans., 45 (2004), 2503-2508.
[29] Kantesh Balani, T Laha, Arvind Agarwal, J Karthikeyan, N Munroe, Effect of carrier gases on microstructural and electrochemical behavior of cold-sprayed 1100 aluminum coating, Surf. Coat. Technol., 195 (2005), 272-279.
[30] Jinghui Li, Fuguo Li, Xinkai Ma, Jiang Li, Shan Liang, Effect of grain boundary characteristic on intergranular corrosion and mechanical properties of severely sheared Al-Zn-Mg-Cu alloy, Mater. Sci. Eng., A, 732 (2018), 53-62.
[31] HC Fang, FH Luo, KH Chen, Effect of intermetallic phases and recrystallization on the corrosion and fracture behavior of an Al-Zn-Mg-Cu-Zr-Yb-Cr alloy, Mater. Sci. Eng., A, 684 (2017), 480-490.
[32] Joachim Wloka, Theo Hack, Sannakaisa Virtanen, Influence of temper and surface condition on the exfoliation behaviour of high strength Al–Zn–Mg–Cu alloys, Corros. Sci., 49 (2007), 1437-1449.
[33] Hao Wang, Chengyi Ning, Yihui Huang, Zhenya Cao, Xiaoxiao Chen, Wenwu Zhang, Improvement of abrasion resistance in artificial seawater and corrosion resistance in NaCl solution of 7075 aluminum alloy processed by laser shock peening, Optics and Lasers in Engineering, 90 (2017), 179-185.
[34] Jin-Feng Li, Zhuo-wei Peng, Chao-Xing Li, Zhi-Qiang Jia, Wen-jing Chen, Zi-Qiao Zheng, Mechanical properties, corrosion behaviors and microstructures of 7075 aluminium alloy with various aging treatments, Transactions of Nonferrous Metals Society of China, 18 (2008), 755-762.
[35] BS Coving Jr, SD Cramer, JP Carter, David Schlain, Corrosion of titanium diboride, Journal of the Less Common Metals, 41 (1975), 211-224.

[36] DS Sekhawat, M Chakraborty, UK Chatterjee, Materials Science Forum, Trans Tech Publ, 2005, pp. 449-452.
[37] HH Sun, D Chen, XF Li, NH Ma, HW Wang, Electrochemical corrosion behavior of Al–Si alloy composites reinforced with in situ TiB2 particulate, Materials and corrosion, 60 (2009), 419-423.
[38] CS Ramesh, S Pramod, R Keshavamurthy, A study on microstructure and mechanical properties of Al 6061–TiB2 in-situ composites, Mater. Sci. Eng., A, 528 (2011), 4125-4132.
[39] TV Christy, N Murugan, S Kumar, A comparative study on the microstructures and mechanical properties of Al 6061 alloy and the MMC Al 6061/TiB2/12p, Journal of Minerals and Materials Characterization and Engineering, 9 (2010), 57.
[40] MR Rokni, CA Widener, VK Champagne, GA Crawford, SR Nutt, The effects of heat treatment on 7075 Al cold spray deposits, Surf. Coat. Technol., 310 (2017), 278-285.
[41] Christian Weingarten, Damien Buchbinder, Norbert Pirch, Wilhelm Meiners, Konrad Wissenbach, Reinhart Poprawe, Formation and reduction of hydrogen porosity during selective laser melting of AlSi10Mg, J. Mater. Process. Technol., 221 (2015), 112-120.
[42] Cuncai Fan, Qiang Li, Jie Ding, Yanxiang Liang, Zhongxia Shang, Jin Li, Ruizhe Su, Jaehun Cho, Di Chen, Yongqiang Wang, Helium irradiation induced ultra-high strength nanotwinned Cu with nanovoids, Acta Mater., 177 (2019), 107-120.
[43] Kaka Ma, Haiming Wen, Tao Hu, Troy D Topping, Dieter Isheim, David N Seidman, Enrique J Lavernia, Julie M Schoenung, Mechanical behavior and strengthening mechanisms in ultrafine grain precipitation-strengthened aluminum alloy, Acta Mater., 62 (2014), 141-155.
[44] Fei Chen, Zongning Chen, Feng Mao, Tongmin Wang, Zhiqiang Cao, TiB2 reinforced aluminum based in situ composites fabricated by stir casting, Mater. Sci. Eng., A, 625 (2015), 357-368.
[45] He Li, Xiaoming Wang, Lihua Chai, Haijing Wang, Ziyong Chen, Zhilei Xiang, Tounan Jin, Microstructure and mechanical properties of an in-situ TiB2/Al-Zn-Mg-Cu-Zr composite fabricated by Melt-SHS process, Mater. Sci. Eng., A, 720 (2018), 60-68.

Conclusions and perspectives

The objective of this study is to develop new routes for manufacturing Al matrix composites (AMCs) strengthened with nano reinforcements by cold spraying (CS). In order to achieve balanced strength-ductility of the cold sprayed AMCs, efforts have been dedicated from the aspects of composite powder preparation, processing parameters optimization, and post-treatments. The effect of CS processing conditions (i.e. particle impact velocity and temperature, gas type) on microstructure evolution of the as-sprayed composite samples was investigated in terms of X-ray diffraction (XRD), scanning (SEM) and transmission electron microscopy (TEM), and electron backscatter diffraction (SEM/EBSD). The adhesion strength, wear performance, corrosion properties as well as the mechanical performance including microhardness and tensile properties of CSed composites were evaluated. The particle plastic deformation behaviour and the formation mechanisms of composite deposits were investigated with the assist of single-particle compression tests and FEA simulation. Moreover, the influence of heat treatments and friction stir processing (FSP) on the microstructure evolution and mechanical properties of the cold sprayed AMCs were investigated. The details of the conclusions are listed below:

1. Fabrication of CNTs/Al composite coating via CS

(1) In the case of CNTs/Al composite powder produced by HSD process, CNTs were uniformly coated on the surface of Al particles without serious damages to CNTs during powder preparation. However, the dispersion of CNTs onto Al particle surface could prevent the particles from metallic bonding during CS deposition, resulting in a dramatic decrease of deposition efficiency and a low strength of the composite coating.

(2) In the case of CNTs/Al composite powder produced by the SSBM process, uniform distribution of CNTs into Al matrix was achieved, but the CNTs were slightly damaged during processing. The microhardness of CNTs/Al composite coating produced from SSBM powders reached as high as 133 $HV_{0.1}$, showing a significant improvement compared with the pure Al coating.

(3) The strengthening mainly resulted from grain boundary hardening due to the nanocrystalline structure and hardening by CNTs. In addition, according to the XRD and Raman analysis, the brittle Al_4C_3 phase was not formed in both CNTs/Al composite coatings.

(4) The combination of FEA simulation and experimental results demonstrates that the dense lamellar structure at the microscale results from the self-alignment behavior of flaky particles and the enhanced peening effect during deposition. The flaky shaped particle experience less plastic deformation and thus weaker interfacial bonding and lower adhesion strength compared to the spherical particle.

(5) The phase composition as well as the structural integrity of CNTs were well preserved in the composite samples annealed at lower temperatures. The new Al_4C_3 phase starts to form in the highly fractured CNTs regions as the annealing temperature rises up to 500 ℃. A duration of annealing time can also facilitate the nucleation and growth of Al_4C_3 phase.

(6) A slight decrease of microhardness was observed on the annealed SSBM CNTs/Al composites. This should be explained by the limited grain growth Zener drag and solute drag phenomena during heat treatment.

(7) The tensile tests on the as-sprayed SSBM CNTs/Al composite presents a brittle feature, with the fracture primarily occurred along the weak inter-splat interface. A slight improvement in both UTS and elongation was obtained after annealing treatment as a result of enhanced interfacial bonding and defects healing effect.

2. Fabrication of TiB_2/AlSi10Mg composite coating via CS

(1) The CSed deposits display a fully dense structure with the cellular-like network of eutectic Si particles embedded in the Al matrix. Apart from the uniformly distributed TiB_2 nanoparticles, some clusters on the micrometer scale were also presented in the CSed TiB_2/AlSi10Mg composite deposits. This inhomogeneous distribution of the particles derives from the gas-atomized composite powder.

(2) With the increase in the annealing temperature from 200 °C to 500 °C, the size of the Si particles increased to several micrometers, whereas their number decreased significantly. According to the XRD and EDS analyses, there were no other new phases other than Al, Si, Mg_2Si and TiB_2 detected in the CSed and annealed samples.

(3) The microhardness showed a decreasing trend with the increase of the heat treatment temperature and duration of time, mainly due to the elimination of work hardening effect and growth of Si phase. Nevertheless, the composite deposit exhibited an inhabitation of this reduction because of the hindering effect on dislocation movement via nanosized hard TiB2 during heat treatment.

(4) The tensile tests showed that both the as-sprayed AlSi10Mg and TiB_2/AlSi10Mg composite deposits possessed high tensile strength but almost no ductility. Comparatively, relatively lower tensile strength was obtained for the composite samples even though they have a denser structure and higher microhardness than the pure AlSi10Mg deposit. This could be attributed to the presence of TiB_2 clusters on the deformed splats surface, which are detrimental for metallic bonding between particles, thus resulting in an easier fracture during the tensile test.

(5) Significant improvement in ductility but a reduction in tensile strength was obtained for the annealed samples mainly due to the improved interfacial bonding between the deformed splats and grain growth after the annealing treatment, respectively. Besides, the annealed composite samples possess higher UTS but lower ductility compared to the unreinforced pure AlSi10Mg samples.

(6) FSP improves the distribution of TiB_2 particles and refines the particles as well. Based on the TEM observation, the FSP treatment altered the intergranular distribution of TiB_2 particles in the CSed composite into intragranular distribution. Significant grain refinement was achieved via dynamic recrystallization in the FSPed samples. The addition of TiB_2 particles can pin the movement of GBs which retards grain growth and results in a finer structure of the composite sample.

(7) A simultaneous enhancement in both strength and ductility of the CSed TiB_2/AlSi10Mg composite deposits has been achieved by FSP treatment. The strengthening mechanisms are related to the homogenous distribution of reinforcements, matrix grain refinement, and robust interfacial bonding. Increasing the FSP passes results in a lower tensile strength probably due to the coarsening of the Si phase and grain growth.

3. Fabrication of TiB_2/AlZnMgCu composite coating via CS

(1) Fully dense and thick TiB_2/7075Al composite deposits with uniformly distributed nanosized TiB_2 particles were successfully fabricated by CS.

(2) Phase analysis in terms of XRD shows that as-fabricated samples possess a well-retained phase composition compared to the feedstock powders; However, TEM analysis reveals that nanosized precipitates are formed inside the severely deformed grains as well as at the GBs. A greater plastic deformation resulting from a higher particle impact velocity could result in a remarkably higher density of precipitates in the C3 deposit.

(3) A higher particle impact velocity and temperature lead to a denser structure and greater particle deformation, enhancing metallic bonding between deformed splats and grain refinement. Consequently, higher microhardness, lower wear rate, and higher tensile strength were acquired. The addition of TiB_2 nanoparticles improves the microhardness, wear resistance and tensile

strength of the composite deposits, but makes no difference to the adhesion strength.

(4) The fracture morphologies of the as-sprayed composite samples display a brittle feature, which indicates limited metallurgical bonding at the deformed splats even though He was used as the propelling gas.

(5) Electrochemical tests revealed that the TiB_2/7075Al composite coatings possess a lower corrosion tendency from the view of corrosion thermodynamics, which is considered to be primarily due to the TiB_2 particles on the exposed surface forming a defective oxide layer of $TiO_2 \cdot H_2O$ after immersion in the saltwater solution. However, galvanic corrosion between noble TiB_2 reinforcements and the more active Al matrix results in a higher corrosion rate of the composite coating compared to the pure 7075Al coating.

(6) Relatively greater plastic deformation of the particles in the He-processed samples (C3 deposits) results in inferior corrosion resistance compared to the air-processed samples due to the greater generation of defects and precipitates within the samples. A low-temperature annealing treatment is beneficial for the corrosion resistance of the CSed coating due to the reduced dislocations. However, evident grain growth produced by a high-temperature annealing treatment can have a detrimental effect on the corrosion resistance of the coatings.

(7) FEA simulation and single particle deposition revealed that compared to the pure 7075Al particle, the TiB_2/7075Al composite particle experienced less plastic deformation when impacting onto the pure Al substrate, but few differences were found when they were sprayed onto 7075Al-T6 substrate. The plastic deformation behaviour of the particles depends on the impact velocity and temperature, as well as the hardness of the substrates.

(8) The microhardness of the 7075Al-C1 and TiB_2/7075Al-C1 composite deposits can be largely improved by solution-aging treatment due to the formation of abundant precipitates in the Al matrix. However, the precipitation behavior of the He-preocessed samples was suppressed during solution-aging treatment, probably because the precipitates formed as a result of severe plastic deformation during CS deposition are stable and could not re-dissolve well into the matrix to form a saturated solid solution. However, more detailed characterizations are necessary to further investigate the related precipitation mechanisms.

(9) In addition, it was found that applying post-heat treatments did not significantly improve the tensile properties, and a brittle feature was still observed on the fractured surface of the heat-treated tensile samples. Interestingly, some large bubbles are presented in the He-processed deposits after the solution treatment. However, the formation mechanisms of these bubbles are still unknown.

(10) The grain refinement effect and Orowan strengthening mechanism result from the uniform distribution of TiB_2 nanoparticles and the precipitation of η/η' should be responsible for the improved microhardness and strength of the TiB_2/7075Al composite.

From the investigation of these three different composite systems, some general conclusions can be drawn:

(1) Fully dense and thick composite deposits with uniformly distributed nanosized reinforcements were successful fabricated by cold spraying. The as-sprayed deposits exhibited high tensile strength but very low elongation.

(2) The powder preparation method takes an important role in determining the quality of the as-sprayed deposits and the final mechanical properties.

(3) Heat treatment alone cannot significantly improve the mechanical properties of the CSed composites, especially for the ball-milled CNTs/Al system and high strength 7075Al system.

(4) FSP is an effective method in improving the mechanical properties of the CSed composites.

In perspective, some ideas for improvement can complement the current study:

(1) As for the cold sprayed CNTs/Al composite systems, our experimental results have proved that post annealing treatments or CS processing parameter optimization are not effective methods to improve their tensile properties. More attention should be paid on composite powder design and other post-treatment methods such as hot rolling and FSP.

(2) FSP was proved to be an effective method in curing the cold sprayed defects, redistributing the reinforcements as well refining both the ceramic particle size and matrix grain size. However, the thermal effect generated from the FSP process can lead to the coarsening of the Si phase, which can significantly reduce the tensile strength of the composite. Therefore, process optimization is necessary to further improve the mechanical properties of the cold sprayed composites. In addition, more attempts on hybrid additive manufacturing (CS+FSP) will be made to fabricate AMCs with high performance.

(3) The state or quality of the cold sprayed deposit itself has a very great effect on the subsequent heat treatment and thus the final mechanical performance of the composite. Therefore, more experiments need to be done to further study the relationship between processing parameters, particle deformation, inter-splat bonding and precipitation behaviour of the Al alloy and AMCs.

(4) It is interesting to note that the precipitation behaviour of the 7075Al alloy depends on the degree of plastic deformation during CS deposition. The formation of the precipitates during CS could further affect the precipitation behaviour during the solution aging treatment. More detailed characterization will be carried out by TEM to identify the precipitate phases and their formation mechanisms.

(5) Interestingly, bubbles were found inside the He-processed samples after heat treatments. However, the formation mechanisms of such bubbles are not clear yet.

Abstract

This study aims to develop new routes for manufacturing Al matrix composites (AMCs) strengthened with nano reinforcements by using a solid-state cold spraying (CS) process. Three different AMCs, CNTs/Al, TiB_2/AlSi10Mg and TiB_2/AlZnMgCu (7075Al), were successfully fabricated through CS of the composite powders prepared using different approaches. The microstructure evolution of the cold sprayed composite samples was investigated using X-ray diffraction (XRD), scanning electron microscopy (SEM), transmission electron microscopy (TEM), and electron backscatter diffraction (EBSD). The adhesion strength, wear performance, and corrosion properties as well as the mechanical performance, including microhardness and tensile properties of cold sprayed composites were evaluated. The particle plastic deformation behaviour and the formation mechanisms of composite deposits were investigated through the use of single particle compression tests and Finite Element Analysis (FEA) simulation. Moreover, the influence of heat treatments and friction stir processing (FSP) on the microstructure evolution and mechanical properties of the cold sprayed AMCs was investigated.

Experimental results revealed that uniform distribution of CNTs in the Al matrix was achieved by using shift speed ball milled (SSBM) composite powders. However, the tensile tests on cold sprayed SSBM CNTs/Al composite revealed a brittle feature, with the fracture occurring along the weak inter-splat interface and through intergranular. A slight improvement in both ultimate tensile strength and elongation was obtained after annealing treatment as a result of enhanced interfacial bonding and a defect-healing effect. Fully dense and thick TiB_2/AlSi10Mg and TiB_2/7075Al composite components were obtained by CS of gas-atomized composite powders reinforced with in-situ TiB_2 particles. The presence of poor inter-splat bonding and TiB_2 clusters on the deformed splats surface results in a brittle fracture of the cold-sprayed TiB_2/AlSi10Mg composites. Significant improvement in ductility but a reduction in tensile strength was obtained for the annealed TiB_2/AlSi10Mg samples mainly due to the improved interfacial bonding between the deformed splats and the grain growth after annealing treatment, respectively. A simultaneous enhancement in both strength and ductility was achieved through FSP treatment. The strengthening mechanisms are related to the homogenous distribution of reinforcements, matrix grain refinement, and robust interfacial bonding. In the case of the TiB_2/7075Al composite, nanosized TiB_2 particles are uniformly distributed in Al matrix. Higher particle impact velocity and temperature lead to a denser structure and greater particle deformation, enhancing metallic bonding between deformed splats and grain refinement. Consequently, higher microhardness and tensile strength were acquired. However, electrochemical tests revealed that the greater plastic deformation in the He-processed samples results in inferior corrosion resistance compared to the air-processed samples due to the greater generation of defects such as strain stress and dislocations. The microhardness can be greatly improved by heat treatment due to the formation of abundant precipitates in the Al matrix. However, little improvement in tensile properties was found by applying post-heat treatments, and a brittle feature was still observed on the fracture surface of the heat-treated TiB_2/7075Al tensile samples.

Keywords: Cold spray; Nano reinforcements; Metal matrix composite; Mechanical properties; Heat treatment

Résumé

Cette étude vise à développer de nouvelles voies pour la fabrication de composites à matrice d'aluminium (AMC) renforcés de nano-renforcements par un procédé de cold spray (CS) à l'état solide. Trois AMC différents, notamment les NTC/Al, TiB_2/AlSi10Mg et TiB_2/7075Al, ont été fabriqués avec succès par CS de poudres composites préparées selon différentes approches. L'évolution de la microstructure des échantillons composites après projection a été étudiée en termes de diffraction des rayons X (DRX), de microscopie électronique à balayage (MEB) et de microscopie électronique à transmission (MET) et de diffraction d'électrons rétrodiffusion (EBSD). La force d'adhérence, les performances d'usure, les propriétés de corrosion ainsi que les performances mécaniques, y compris la microdureté et les propriétés de traction des composites, ont été évaluées. Le comportement de la déformation plastique des particules et les mécanismes de formation des dépôts composites ont été étudiés à l'aide d'essais de déposition à une seule particule et de simulation FEA. De plus, l'influence des traitements thermiques et du traitement par friction-malaxage (FSP) sur l'évolution de la microstructure et les propriétés mécaniques des AMC ont été étudiées.

Les résultats expérimentaux ont révélé que la distribution uniforme des NTC dans la matrice d'Al était obtenue en utilisant des poudres composites broyées à la vitesse de balle (SSBM). Cependant, les essais de traction sur le composite de NTC/Al SSBM présentent une caractéristique fragile, la fracture se produisant le long de l'interface faible entre les éclaboussures et à travers l'intergranulaire. Une légère amélioration de la résistance ultime à la traction (UTS) et de l'allongement a été obtenue après traitement de recuit en raison d'une liaison interfaciale améliorée et d'un effet de guérison des défauts. Des composants composites TiB_2/AlSi10Mg et TiB_2/7075Al totalement denses et épaisses ont été obtenus par CS de poudres composites renforcées par des particules de TiB_2 in situ, qui se forme pendant l'atomisation du gaz. La présence de fabile liaisons entre les particules et la présence de grappes de TiB_2 à la surface des splats déformés entraîne une rupture fragile des composites TiB_2/AlSi10Mg. Une amélioration significative de la ductilité mais une réduction de la résistance à la traction ont été obtenues après le traitement thermique, principalement en raison de la amélioration de liaison interfaciale entre les splat déformés et la croissance des grains, respectivement. Le traitement FSP a permis d'améliorer simultanément la résistance et la ductilité des composites TiB_2/AlSi10Mg. Les mécanismes de renforcement sont liés à la répartition homogène des renforcements, au raffinage du grain de la matrice et à la liaison interfaciale robuste. Dans le cas du composite TiB_2/7075Al, les particules de TiB_2 nanométriques sont uniformément réparties dans la matrice d'Al. Une vitesse d'impact et une température de particule plus élevées conduisent à une structure plus dense et à une déformation plus importante des particules, renforçant la liaison métallique entre les lamelles déformées et l'affinage du grain. En conséquence, une microdureté et une résistance à la traction supérieures ont été obtenues. Cependant, des tests électrochimiques ont révélé qu'une déformation plastique plus importante dans les échantillons fabriqués par He entraînait une résistance à la corrosion inférieure à celle des échantillons fabriqués par air en raison de la génération plus importante de défauts. La microdureté peut être largement améliorée par traitement thermique en raison de la formation de précipités abondants dans la matrice d'Al. Cependant, les traitements thermique n'ont pas guère beaucoup d'amélioration des propriétés de résistance à la traction, et une caractéristique fragile a encore été observée sur la surface de rupture des échantillons de traction TiB_2/7075Al traités thermiquement.

Mots clés : Projection à froid ; Nano renforcement ; Composit à matrice métallique ; Propriétée mécaniques ; Traitment thermique

Publications (12 publications of international journals (two of them are under review), 7 presentations in international conferences)

International journals

[1] **Xinliang Xie**, Yu Ma, Chaoyue Chen, Gang Ji, Christophe Verdy, Zhe Chen, Sheng Yuan, Bernard Normand, Shuo Yin, Hanlin Liao. Cold spray additive manufacturing of metal matrix composites (MMCs) using a novel nano-TiB_2-reinforced 7075Al powder. ***Journal of Alloys and Compounds,*** 819 (2020).

[2] **Xinliang Xie**, Chaoyue Chen, Yu Ma, Yingchun Xie, Hongjian Wu, Gang Ji, Eric Aubry, Zhongming Ren, Hanlin Liao, Influence of annealing treatment on microstructure and magnetic properties of cold sprayed Ni-coated FeSiAl soft magnetic composite coating, ***Surface and Coating Technolology***, 374 (2019), 476-484.

[3] **Xinliang Xie**, Chaoyue Chen, Gang Ji, Run Xu, Zhanqiu Tan, Yingchun Xie, Zhiqiang Li, Hanlin Liao, A novel approach for fabricating a CNT/AlSi composite with the self-aligned nacre-like architecture by cold spraying, ***Nano Materials Science***, 1 (2019), 137-141.

[4] **Xinliang Xie**, Chaoyue Chen, Yingchun Xie, Eric Aubry, Zhongming Ren, Gang Ji, Hanlin Liao, Comparative investigation of microstructure and properties of Ni-coated FeSiAl soft magnetic composite coatings produced by cold spraying and HVOF, ***Surface and Coating Technology***, 371 (2019), 224-234.

[5] **Xinliang Xie**, Chaoyue Chen, Yingchun Xie, Zhongming Ren, Eric Aubry, Gang Ji, Hanlin Liao, A novel approach for fabricating Ni-coated FeSiAl soft magnetic composite via cold spraying, ***Journal of Alloys and Compouds***, 749 (2018), 523-533.

[6] Chaoyue Chen, **Xinliang Xie* (corresponding author)**, Yingchun Xie, Marie-Pierre Planche, Sihao Deng, Gang Ji, Eric Aubry, Zhongming Ren, Hanlin Liao, Cold spraying of thermally softened Ni-coated FeSiAl composite powder: Microstructure characterization, tribological performance and magnetic property, ***Materials & Design***, 160 (2018), 270-283.

[7] Chaoyue Chen, **Xinliang Xie (Joint first authors)**, Yingchun Xie, Xincheng Yan, Chunjie Huang, Sihao Deng, Zhongming Ren, Hanlin Liao, Metallization of polyether ether ketone (PEEK) by copper coating via cold spray, ***Surface and Coating Technology***, 342 (2018), 209-219.

[8] **Xinliang Xie**, Ying Chun Xie, Zhan Qiu Tan, Chao Yue Chen, Jiang Wang, Zhi Qiang Li, Xiao Peng Li, Gang Ji, Han Lin Liao, ***Materials Science Forum***, Trans Tech Publ, 2018, pp. 2173-2177.

[9] Chaoyue Chen, Yingchun Xie, **Xinliang Xie**, Xingchen Yan, Renzhong Huang, Jiang Wang, Zhongming Ren, Sihao Deng, Hanlin Liao, Effects of substrate heat accumulation on the cold sprayed Ni coating quality: Microstructure evolution and tribological performance, ***Surface and Coating Technology***, 371 (2019), 185-193.

[10] Hongjian Wu, **Xinliang Xie**, Meimei Liu, Chaoyue Chen, Hanlin Liao, Yicha Zhang, SihaoDeng, A new approach to simulate coating thickness in cold spray, ***Surface and Coating Technology,*** 2019,

[11] **Xinliang Xie**, Bilel Hosni, Chaoyue, Chen, Gang Ji, Zhe Chen, Hongjian Wu, Christophe Verdy, Qingdong Zhong, Omar EI Kedim, Hanlin Liao. Corrosion behavior of cold sprayed 7075Al composite coating reinforced with in-situ nanosized TiB_2 particles. ***Corrosion Science*** (under review).

[12] **Xinliang Xie,** Chaoyue Chen, Zhe Chen, Gang Ji, Hongjian Wu, Longtao Liu, Zhongming Ren, Christophe Verdy, Hanlin Liao Microstructure and mechanical properties of in-situ TiB_2 particle reinforced AlSi10Mg composite components produced by cold spray additive manufacturing, ***Journal of Materials Science & Technology*** (under review).

International Conferences

[1] **Xinliang Xie,** Chaoyue Chen, Hongjian Wu, Christophe Verdy, Zhe Chen, Gang Ji, Hanlin Liao, Balanced strength-ductility in cold sprayed metal matrix composite via powder design, process

optimization and post treatment, Les Rencontres Internationales de la Projection Thermique, Forschungszentrum Jülich, Germany, December 11-13, 2019.

[2] **Xinliang Xie**, Bilel Hosni, Hanlin Liao, Zhe Chen, Omar EI Kedim, Qingdong Zhong, Hongjian Wu, Christophe Verdy, Gang JI. Corrosion behavior of cold sprayed 7075Al composite coating reinforced with in-situ nanosized TiB_2 particles. 1st International Conference on Corrosion Protection and Application. Chongqing, China, October 10 -12, 2019.

[3] **Xinliang XIE**, Chaoyue CHEN, Zhe CHEN, Hongjian WU, Haowei WANG, Gang JI, Hanlin LIAO, Microstructure and mechanical properties of in-situ nano-TiB_2 particle reinforced AlSi10Mg composite components produced by cold spraying. International Thermal Spray Conference, YoKohama, Japan, May 25-29, 2019.

[4] **Xinliang XIE**, Chaoyue CHEN, Yingchun XIE, Zhanqiu TAN, Zhiqiang LI, Gang JI, Hanlin LIAO Synthesis of carbon nanotube reinforced Al matrix composites via cold spray deposition. International Thermal Spray Conference, Orlando, USA, May 7-10, 2018.

[5] **Xinliang XIE**, Yingchun XIE, Zhanqiu TAN, Chaoyue CHEN, Zhiqiang LI, Pengxiao LI, Gang JI, Hanlin LIAO, Additive manufacturing of a CNT/Al6Si composite with the nanolaminated architecture via cold spray deposition, PROCESSING & MANUFACTURING OF ADVANCED MATERIALS: Processing, Fabrication, Properties, Paris, France, July 8-13, 2018.

[6] **Xinliang XIE**, Hanlin LIAO, Zhanqiu TAN, Chaoyue CHEN, Zhiqiang LI, Gang JI. Fabrication of Al matrix composites via cold spraying-process, structure and properties, 25th Congress of International Federation for Heat Treatment and Surface Engineering, Xi'an, China, September 11-14, 2018.

[7] **Xinliang XIE**, Chaoyue CHEN, Yingchun XIE, Zhongming REN, Gang JI, Hanlin LIAO, Preparation and characterization of Ni-coated Fe-Si-Al soft magnetic composites via cold spraying, Rencontres Internationales de la Projection Thermique), Limoges, France, December 6-8, 2017.

SPIM

■ École doctorale SPIM - Université de Technologie Belfort-Montbéliard
F - 90010 Belfort Cedex ■ tél. +33 (0)3 84 58 31 39
■ ed-spim@univ-fcomte.fr ■ www.ed-spim.univ-fcomte.fr

utbm
université de technologie
Belfort-Montbéliard